

ABSTRACT

Title of dissertation: **OPTICAL NANOFIBER FABRICATION AND ANALYSIS TOWARDS COUPLING ATOMS TO SUPERCONDUCTING QUBITS**

Jonathan Hoffman, Doctor of Philosophy, 2014

Dissertation directed by: Professor Luis Orozco
Department of Physics

We describe advancements towards coupling superconducting qubits to neutral atoms. To produce a measurably large coupling, the atoms will need to be on the order of a few micrometers away from the qubit. A consequence of combining superconducting qubits and atoms is addressing their operational constraints, such as the deleterious light effects on superconducting systems and the magnetic field sensitivity of superconducting qubits. Our group proposes the use optical-nanofiber-based optical dipole traps to confine atoms near the superconductor. Optical nanofibers (ONFs) have high-intensity evanescent waves that require less power than equivalent standard dipole traps.

This thesis focuses on the fabrication and analysis of the behavior of ONFs. First we present the construction of the pulling apparatus. We outline the necessary steps for a typical pull, detailing the cleaning and alignment process. Then we examine the quality of the fibers by measuring their transmission and comparing our results to other reported measurements, demonstrating a two-order of magnitude

decrease in loss.

Next we present the modal evolution in ONFs using simulations and spectrogram analysis. We identify crucial elements to improve the transmission and demonstrate understanding of the modal dynamics during the pull.

Then we study higher-order modes (HOMs) with ONFs using the first excited TE_{01} , TM_{01} , and HE_{21} modes. We demonstrate transmissions greater than 97% for 780 nm light when we launch the first excited LP_{11} family of modes through fibers with a 350 nm waist. This setup enables us to launch these three modes with high purity at the output, where less than 1% of the light is coupled to the fundamental mode.

We then focus on the identification of modes on the ONF waist. First we use Rayleigh scattering to identify the modal content of an ONF. Bulk optics can convert the modes in the ONF, and we observe the controllable conversion of superpositions of modes. Finally, we use an evanescently-coupled tapered optical fiber probe that allows for the identification of the fundamental mode beating with HOMs and compare the results to simulations.

OPTICAL NANOFIBER FABRICATION AND ANALYSIS
TOWARDS COUPLING ATOMS TO SUPERCONDUCTING
QUBITS

by

Jonathan Hoffman

Dissertation submitted to the Faculty of the Graduate School of the
University of Maryland, College Park in partial fulfillment
of the requirements for the degree of
Doctor of Philosophy
2014

Advisory Committee:

Professor Luis A. Orozco, Chair/Advisor
Professor Steven L. Rolston, Co-Advisor
Professor Mario Dagenais, Dean's Rep
Professor Frederick C. Wellstood
Professor Christopher J. Lobb
Dr. Fredrik Fatemi
Professor William D. Phillips

© Copyright by
Jonathan Hoffman
2014

Dedication

To my parents and their endless quest to ensure my happiness and well-being.

Acknowledgments

This thesis is the culmination of six years of work and I could not have done it without the support of my friends, family, and coworkers. I would like to start by thanking my family. My parents always allowed me the freedom to pursue whatever interests I had. They were only concerned with my happiness and encouraged me to search for a major that piqued my curiosity. My sister is always there for me, even if it is to inform me my opinion is wrong, often before I state it.

Being a part of the Atoms on SQUIDs team has provided me the opportunity to work with wonderful people.

First, I must thank my advisor Professor Luis Orozco. His tireless dedication to and enthusiasm for science and education are the traits I admire most in him. Over the last five years he has always provided an open door for questions and a willingness to help. I am fortunate to have an advisor I can rely on to send me thesis edits within a few hours regardless of the time I sent them, be it midday or midnight. I must also thank Luis for years of spoiling me and all of his students with excellent dinners whether they were home-cooked meals or at a restaurant.

I owe a great deal to my co-advisor, Professor Steve Rolston. Your excellent physical intuition has provided me with an opportunity to learn your approach to physics. Whenever we have a result that contradicts your intuition we often joke that we must have made a mistake and more often than not, we have. I truly appreciate his openness to discussion, be it science or general life advice.

I thank Professor Frederick Wellstood for his dedication to the project and

taking the time to understand all results, even if they are outside his field. If he is satisfied with my reasoning I can be confident that it is sound.

I have to thank Professor Christopher Lobb for introducing me to the Atom's on SQUIDs project. His insight is only surpassed by his good humor. More so than anything else, as an insomniac, I am envious of his ability to sleep during meetings. Yet somehow, he always has a better idea of what's going on than I do.

I am incredibly grateful for my collaboration with Dr. Fredrik Fatemi. His knowledge and intuition for optics has placed me in an unbelievably lucky position and I am appreciative for everything he has taught me. Thank you for working with me, even though your ten-year-old son solves a Rubik's cube 28 years faster than I can.

Jeffrey Grover and I have worked together on this project nearly from its inception. I have probably spent more time with him than any other human being over the last 5 years. I am very lucky to have you as a coworker and friend. Your superb knowledge of science and current experiments is invaluable and you never give yourself enough credit for your abilities. I will always appreciate your ability to keep everything in perspective and I was lucky to have a lab mate that understood what the truly important things are in life.

Most of the work in this thesis was done in collaboration with Sylvain Ravets. I have met few people with his drive and no one else with his ability to get things done. It is impressive. The long hours pulling fibers, in the unreasonably hot clean room (at least cleanish room), were undercut by your humor and enthusiasm for problem solving. I think few people quite understand how far a few feet can feel,

especially after the hundredth or so failed attempt at carrying a small piece of glass across those few feet. Thank you for all the help and the friendship that we share, it's some sort of the best.

Pablo Solano's calm demeanor, genuine interest, and physical intuition make him a pleasure to work with. I can say with confidence that I'm leaving the project in better hands. My back thanks you for reminding me that we are physicists and not weightlifters when I had the idea to lift the 100 kg granite slab.

Peter Kordell was an undergraduate that did not deserve the slight of being called an undergraduate. His dedication to working through the poorly documented FIMMPROP led to great results producing dispersion curves and beautiful mode evolution simulations.

It was serendipitous that I fell into my housing situation my first year of graduate school. I should probably come clean and admit that I spent two minutes looking for housing before my first year: approximately one minute emailing Andres to tell him of my interest in rooming together and a promise that I would help look for housing, and the other minute emailing Matt to express my interest in the place he found. Sorry Andres, I never looked for housing, I was just efficient at emailing.

The timing of these emails was fortuitous, since I ended up living with some of my closest friends in graduate school. Andres, Matt, and later Anjor and I not only worked through many assignments together, but with two almost proposals and two almost adoptions I think that almost makes us family. Their friendship along with David, Rangga, Eric, Evan, and Rufus really helped create a tight-knit community that I will always cherish. Rufus' relentless drive is something I aspire to and his

continual outwitting of me pushes me to be more creative and strategically minded.

The person I owe the greatest deal of gratitude to is Kristen Voigt. No, I didn't forget you, I just wanted to build a bit of tension while you read this. There is no way for me to adequately express the extent of my appreciation and love for you. I don't know how I would have gotten through the last few years without your support, affection, and organization. I'm pretty hopeless at organization. Thank you, you are the most wonderful person I will ever know.

As per Eric's request I acknowledge spongebob square pants. Not his help just his existence as a comedic entity for children.

If you actually read my thesis, thank you for (potentially) bringing this document past the average readership of publications at four reads.

This work was supported by the NSF through the PFC at the JQI.

Table of Contents

List of Figures	x
List of Abbreviations	xiii
1 Introduction	1
1.1 Quantum computing background	1
1.1.1 Physical examples	2
1.1.2 DiVincenzo criteria	3
1.2 Atoms coupled to superconducting qubits	4
1.2.1 The interaction and its realization	6
1.2.2 Proof of principle	7
1.2.3 Constraints	11
1.3 Optical nanofibers	12
1.3.1 Intensity profile and trapping potential	12
1.4 Thesis overview	16
2 Optical nanofiber fabrication	18
2.1 Introduction	18
2.2 Experimental setup	20
2.2.1 The fiber-pulling apparatus	20
2.2.2 Transmission monitoring setup	27
2.3 Algorithm	28
2.3.1 Motor control	33
2.3.2 Measurement of the flame width	34
2.4 The pulling process	37
2.4.1 Cleaning procedure	37
2.4.2 Alignment procedure	38
2.5 Results	40
2.5.1 Microscopy validation	40
2.5.2 Transmission	43
2.5.3 Spectrogram analysis	50
2.6 Power Measurements	51

2.7	Dust studies	52
2.8	Conclusion	57
3	Optical nanofiber spectrogram analysis	59
3.1	Introduction	59
3.2	Motivation and construction overview	60
3.3	Modal evolution	61
3.3.1	Modes in a cylindrical waveguide	61
3.4	Adiabaticity in fibers	68
3.4.1	Adiabaticity criterion	68
3.4.2	Transmission of a tapered fiber section	71
3.4.3	Genetic algorithm	74
3.4.4	Fully adiabatic fiber	74
3.4.5	Utilizing non-adiabaticity	78
3.5	Analysis of transmission signal	83
3.5.1	Single mode section	85
3.5.2	From single mode to multimode	85
3.5.3	Single mode again	89
3.6	Spectrograms	90
3.6.1	Modeling the pull	93
3.6.2	Identifying the modes	93
3.7	Applications of the quality of the pull	98
3.7.1	Internal parameters: algorithm input parameters	99
3.8	Understanding the losses	104
3.8.1	Losses	104
3.8.2	Coupling to higher-order modes	105
3.8.3	Rayleigh scattering	105
3.8.4	Systematic effects	106
3.9	Conclusion	106
4	Efficient guidance of higher-order modes	108
4.1	Introduction	108
4.2	Mode propagation in an optical fiber	110
4.2.1	First family of excited modes	110
4.2.1.1	Adiabaticity condition	112
4.2.2	Experimental setup	113
4.2.3	Results	115
4.2.3.1	Varying the fiber type	116
4.2.3.2	Transmission measurements	117
4.2.3.3	Spectrograms	119
4.2.3.4	Imaging the fiber output	120
4.2.3.5	Varying the angle	121
4.2.4	Conclusion	125

5	Higher-order mode identification and control	126
5.1	Introduction	126
5.2	IDIOM	126
5.3	Rayleigh scattering measurements	127
5.3.1	Theory	128
5.3.2	Experimental setup	135
5.3.3	Experimental results	139
5.3.3.1	Mode identification	139
5.3.3.2	Mode control	143
5.3.4	Surface scattering and mode cutoffs	150
5.3.5	Optical fiber probe	159
5.3.6	Photodiode motor jog	164
5.4	Conclusion	170
6	Conclusions and Outlook	171
6.1	Hybrid System	172
6.2	ONF studies	174
A	Fiber Modes	177
A.1	Cylindrical coordinates	177
A.2	Maxwell's Equations	178
A.3	Cylindrically symmetric dielectric waveguide	179
A.4	Two layer step index fiber	182
A.4.1	Boundary Conditions	184
A.4.2	The propagation constant and fiber modes	186
A.4.3	Solving for the propagation constants	187
A.4.4	Quasilinear polarization	192
A.5	Power Normalization	195
A.5.1	HE_{lm} and EH_{lm} mode normalizations	196
	Bibliography	201

List of Figures

1.1	Lumped-element LC resonator	8
1.2	HFSS simulation of the lumped-element LC resonator magnetic field .	9
1.3	Aluminum on sapphire lumped element resonator	10
1.4	Fiber trap geometry, intensity profile, and trapping potential	13
2.1	A schematic of the fiber pulling setup and photograph.	22
2.2	An image of the flame nozzle.	26
2.3	Transmission monitoring setup for the fundamental mode.	27
2.4	Physical model of taper linking process.	32
2.5	Measurement of the effective flame size	36
2.6	Fiber alignment image of left and right fiber clamps.	39
2.7	Measured vs simulated profile for a three angle microfiber.	42
2.8	SEM image of an ONF.	43
2.9	Normalized transmission during the pull for the fundamental mode. .	45
2.10	Loss in dB/mm vs fiber radius comparing previous groups results with our ONFs.	47
2.11	Spectrogram of transmission.	50
2.12	Transmission and spectrogram comparison for an uncleaned fiber. .	53
2.13	Core- to cladding-guidance transition simulated in FIMMPROP . .	56
3.1	Schematic of the stretched fiber and calculated intensity profile. . .	63
3.2	Dispersion relations for various modes inside the fiber.	67
3.3	Adiabatic criterion for a fiber taper presented as taper angle vs radius.	70
3.4	FIMMPROP simulation of transmission in a section of fiber taper (from 25.5 to 23.5 μ m).	72
3.5	Optimal adiabatic tapers calculated with the genetic algorithm for 99.90% and 99.99% transmission.	76
3.6	Optimal taper profile using the genetic algorithm for 99.90% and 99.99% transmission.	77
3.7	Simulation of fiber profile for 99.99% transmission with optimized length given by the genetic algorithm.	79
3.8	Mode evolution for a 2 mrad linear fiber down to 250 nm radius. . .	82

3.9	Transmission through a 2 mrad fiber as a function of time during the manufacturing process and corresponding waist radius evolution.	84
3.10	Detailed view of the transmission of the 2 mrad pull shown in Fig. 3.9.	86
3.11	Schematic showing modal evolution in the transition region.	88
3.12	Simulation of fiber stretch for fiber sample 1.a	91
3.13	Transmission spectrogram of a 2 mrad pull.	92
3.14	Flow chart of spectrogram overlap process	94
3.15	Simulated taper profile from step N and $\beta_i(r(z))$	95
3.16	Simulation of the differences between the fundamental mode and the first four excited modes of family one.	96
3.17	Identification of the modes beating for the 2 mrad tapered fiber spectrogram	97
3.18	Normalized transmission through the fiber as a function of time during the manufacturing process for a two-angle pull from 2 to 0.75 mrad taper.	100
3.19	Spectrogram of the transmission data and mode identification overlap for the two-angle pull.	101
3.20	Study of the asymmetry of a two-angle pulled fiber.	103
4.1	Effective indices of refraction vs V number with corresponding HOMs.	112
4.2	Experimental setup for HOM efficient guidance	113
4.3	HOM transmission as a function of initial fiber radius and spectrogram	116
4.4	HOM core-cladding transition	120
4.5	HOM transmission as a function of taper angle and FIMMPROP simulation	122
5.1	Beat length vs ONF radius	130
5.2	Inverse beat length vs ONF radius	131
5.3	Inverse beat frequency simulation for $r_w = 390 \text{ nm}$ with $\Omega = 1 \text{ mrad}$ taper.	132
5.4	HOM transverse mode profiles	133
5.5	HOM interference mode profile	134
5.6	HOM identification experimental setup	135
5.7	Rayleigh Scattering mode identification imaging system	137
5.8	HOM 50x montage transverse polarization	140
5.9	Rayleigh Scattering depicting HOMs leaking transitioning from core to cladding modes.	141
5.10	Scattered power along ONF waist	142
5.11	Scattered power vs position and FFT for two input polarizations.	145
5.12	Conversion of HE_{21} and TM_{01} to HE_{21} and TE_{01} as a function of half-wave plate angle	146
5.13	Conversion of HE_{21} and TM_{01} to HE_{21} and TE_{01} longitudinal and transverse components as a function of half-wave plate angle	147
5.14	Contrast in the relative frequency band for HOM mode conversion	148
5.15	Pure mode conversion as a function of half-wave plate angle	149

5.16	HE_{21} cutoff observable in Rayleigh scattering intensity	151
5.17	Rayleigh scattering vs position and Spectrogram for $\Omega = 0.5$ mrad and $r_w = 300$ nm ONF	154
5.18	HOM spectrogram overlap and radius extraction.	157
5.19	HOM spectrogram overlap and radius extraction with TM_{01} mode.	158
5.20	Image of fiber probe setup	160
5.21	Power collected through fiber probe as a function of position along ONF waist.	161
5.22	FFT of power collected using the fiber probe.	162
5.23	Probe power collected on a PD while jogging the motors.	165
5.24	Spectrogram of data from Fig. 5.23.	166
5.25	FFT of power collected from ONF waist from 5.23 and table of extracted beat frequencies.	167
5.26	Spectrogram with overlap.	168
5.27	Measured vs Simulated radius and deviation from simulation.	169
6.1	Hybrid quantum system setup	173
6.2	Γ_{1D} calculation	175
A.1	Cylindrically symmetric waveguide, with constant layers of index of refraction.	179
A.2	Two layer cylindrically symmetric waveguide	182
A.3	Determining the HE_{1m} and EH_{1m} propagation constants	188
A.4	Determining the TE_{0m} and TM_{0m} propagation constants	189
A.5	Effective indices of refraction vs V number	190
A.6	Region of closest approach for n_{eff}	192
A.7	HE_{11} Intensity with quasilinear polarization.	193
A.8	Ratio of power in an annulus surrounding an ONF.	194

List of Abbreviations

Ω	the fiber taper angle
APD	avalanche photodiode
FC	fiber channel / ferrule connector
FWHM	full width at half maximum
HOM	Higher-order mode, specifically TE_{01} , TM_{01} , and HE_{21}
HWHM	half width at half maximum (3 dB point)
HWP	half-wave plate
JC	Jaynes-Cummings
JQI	Joint Quantum Institute
L_w	length of the fiber waist
MOT	magneto-optical trap
NISP	Nanoscale Imaging Spectroscopy and Properties Laboratory
NIST	National Institutes of Standards and Technology
NSF	National Science Foundation
ONF	Optical nanofiber
PBS	Polarizing beam splitter
PC	Polarization controller
PM	polarization maintaining
PZT	piezo-electric transducer
QED	quantum electrodynamics
QWP	quarter-wave plate
Rb	Rubidium
r_w	radius of the optical nanofiber waist
SEM	scanning electron microscope
SS	Stainless steel
UHV	ultra-high vacuum

Chapter 1: Introduction

1.1 Quantum computing background

The field of quantum computation arguably began with Feynman’s paper [1] on quantum simulation. While the Deutsch-Jozsa algorithm [2] was the first example of a quantum algorithm that outperformed classical computation, it was Peter Shor’s work [3] concerning prime factorization that garnered widespread interest. This work gave quantum computation national security implications since the widely used RSA encryption, a public key encryption named after Rivest, Shamir, and Adleman, relies on the difficulty involved in factoring large numbers into primes. With the advent of quantum error correction codes [4–7] the feasibility of quantum computation, while still daunting, significantly improved.

Although Shor’s [3] and Grover’s [8] algorithms give credence to the potential application of a quantum processor the concept of quantum simulation [1, 9, 10] is of fundamental interest in physics. Full control of a qubit, understanding of all its interactions, manipulating and measuring it is a worthy study on its own, and opens insights into our understanding of physical phenomena. Analog and Digital quantum simulators can be used to study classically intractable problems [11]. A fully functioning quantum computer, one that could run Shor’s or Grover’s algorithm,

might not be necessary for these types of problems. In principle, a quantum simulator could study specific Hamiltonians, modeling various physical systems such as quantum magnetism [12–15] and high-temperature superconductivity [16–18].

1.1.1 Physical examples

There are a wide variety of physical incarnations of qubits, each with its own benefits and limitations. Some qubits exhibit better isolation from their environment, having longer coherence times, while others have fast gate times, or more straightforward means of scalability. Examples include atoms [19–21], ions [22–24], electrons on helium [25], superconducting qubits [26,27], NV centers [28] and Phosphorus donors in Silicon-28 [29].

Many of these systems have seen great advances in the last decade. For instance, the ground state hyperfine splitting in a Rb atomic qubit was demonstrated to have a 2 second coherence time in 2004 [19]. Addressing a singular ^{13}C nucleus near an NV center [28] has shown coherence times on the order of seconds. Recently, the longest observed coherence time was measured in Ionized Phosphorus Donors in Silicon-28. Exhibiting a room temperature coherence time of 39 minutes, and a coherence time in excess of 180 minutes at cryogenic temperatures [29].

Qubits based on Josephson junctions have seen remarkable advances in the last decades with the development of the charge [30], phase [31–33], and flux qubits [34–36]. Later the development of circuit Quantum Electrodynamics (cQED) [37], Transmons [38], Fluxonium [39], and Transmons in 3D cavities [40], have seen the

coherence times improve by about five orders of magnitude [27].

Despite major advancements in all of these systems it is not clear that any single qubit currently satisfies the DiVincenzo criteria [41, 42] : a set of conditions describing the necessary qualities this qubit must satisfy in order to construct a universal quantum computer.

1.1.2 DiVincenzo criteria

Briefly, a quantum computer according to DiVincenzo [41, 42] will need:

1. Scalability and well defined Hilbert Space: A quantum computer requires full knowledge of the energy level structure of a given quantum system. Having a well-defined two level system, a qubit, allows the system to be controllably addressed and manipulated.
2. Initialization: It is necessary to be able to place a qubit in a predefined initial state. This allows for calculations to begin with known conditions.
3. Long coherence time relative to gate operation time: The time scale of information loss to the environment, decoherence, must be long relative to the time it takes to perform an operation. In this way, the quantum computer can perform many operations before control of the qubit is lost. Furthermore, decoherence can lead to errors in calculations over time.
4. Universal set of quantum gates: A quantum computer must be able to perform a controllable sequence of unitary operations that are functionally complete, a

set of operations that can be used reach any desired state in the computational Hilbert space.

5. Qubit specific strong measurement: Finally, it is necessary to measure final state of each qubit with high fidelity.

DiVincenzo also developed two requirements for quantum communication:

1. Stationary to flying qubits: This conversion allows for the concept of computation nodes for computation and the ability to convert and send the result elsewhere.
2. Transmission of flying qubits: Conversion of a stationary to flying qubit is not quite stringent enough a condition, the flying qubit must be capable of being transported successfully to another site.

1.2 Atoms coupled to superconducting qubits

The idea behind a hybrid quantum processor is to exploit the best aspects of different types of qubits. Our group proposes a scheme to couple the ground state hyperfine transition of neutral ^{87}Rb atoms to a superconducting (SC) qubit. Atomic systems exhibit excellent isolation from the environment [19], while condensed matter systems benefit from technological developments in microfabrication, leading to a scalable qubit architecture [43].

For the ease of discussion here we will use a flux qubit, but the ultimate SC qubit may be a transmon, fluxonium, or other qubit and is not important for

the conceptual understanding of the system. A flux qubit consists of one or more Josephson junctions in a micrometer-sized superconducting loop [35, 44, 45]. The supercurrent can exist in a superposition of clockwise and counterclockwise flow. Many designs involve three or more junctions with one junction smaller than the others and chosen so that its Josephson inductance dominates the geometrical loop inductance. We can use the magnetic field from this SQUID loop to drive the atomic transition. The flux qubit can possess a relatively long coherence time, on the order of 10 μ s [46] at the flux degeneracy point in a four-junction SQUID [47], and a tunability range of over a GHz [48].

The atomic qubit in our approach consists of two magnetic sublevels on one of the hyperfine ground state manifolds of ^{87}Rb , between the $|5S_{1/2}; F = 1\rangle$ and $|5S_{1/2}; F = 2\rangle$ states. These states are separated by about 6.83 GHz and one of the Zeeman pairs forms a clock transition that is insensitive to magnetic field to first order.

We note that there are similar proposals that focus on creating a memory by coupling ions [43, 49, 50], neutral atoms [51, 52], or molecules [53, 54] to a SC stripline resonator [55]. Nitrogen-vacancy (NV) centers have taken a prominent role in these designs because of the ease with which these natural ion traps integrate with SC systems [56]. Recent results demonstrate strong coupling of NV centers to a stripline resonator [25, 57]. It is worth noting that most other proposals involving neutral atoms and superconducting circuits focus on magnetic traps to confine the atoms [52, 58–60] rather than optical traps.

1.2.1 The interaction and its realization

A flux qubit in its excited state can induce magnetic dipole transitions in the ground state hyperfine manifold of ^{87}Rb . The coupling occurs via the interaction Hamiltonian, $-\sum_i \boldsymbol{\mu}_i \cdot \mathbf{B}$, where $\boldsymbol{\mu}_i$ is the magnetic dipole moment of the i th individual atom, and \mathbf{B} is the magnetic field from the SC qubit. To calculate the strength of the coupling we must first determine the strength of the magnetic field.

Assuming that only geometrical inductance is present the average magnetic field associated with a single microwave photon is:

$$B = \sqrt{\frac{\mu_0 \hbar \omega}{2V_{\text{eff}}}}, \quad (1.1)$$

where ω is the frequency of the photon, μ_0 the permeability of free space, and V_{eff} the effective mode volume. We take the effective mode volume for a square SQUID loop with $10 \text{ } \mu\text{m} \times 10 \text{ } \mu\text{m}$ sides and width of $5 \text{ } \mu\text{m}$ to be about $10 \times 10^{-16} \text{ m}^3$, assuming the field is confined within 5 micrometers above and below the loop. For a photon at 6.8 GHz this gives a magnetic field of about 10 nT, which for the typical moment of $\mu = 1.4 \times 10^{10} \text{ Hz/T}$ gives a coupling strength of roughly 100 Hz for one atom.

The field associated with a single quantum flux, $\Phi_0 = h/2e = 2 * 10^{-15} \text{ T m}^2$, in a loop of this size corresponds to 0.2 Gauss, a much higher value than the single photon. The coupling of one magnetic flux to the atomic magnetic moment would be lowered by some geometric factor determined by the specific shape of the magnetic field obtaining a single flux coupling larger than 100 Hz. Further understanding of

the field distribution and the inductance of the SQUID will help narrow the range of this number.

1.2.2 Proof of principle

As a proof of principle, our short-term goal is to first couple atoms to a high-Q lumped-element superconducting LC resonator, tuned to the ^{87}Rb hyperfine splitting [61]. The SC resonator affords a few advantages over a SC qubit. First, the fabrication of the SC resonator is simpler. There are fewer production steps necessary and resonators less sensitive and less prone to destruction than a qubit. Second, the length of the inductor can be made relatively long (about 1 mm). This length is beneficial because it increases the possible number of trapped atoms and therefore the coupling strength. Here, the interaction results from a (Cavity QED) Jaynes-Cummings Hamiltonian and the coupling strength of the system scales with the square root of the number of atoms. Having many atoms trapped in a small volume is difficult so if the length of the inductance line, which carries the magnetic field, can be made long, we can potentially increase the number of atoms and therefore the coupling strength.

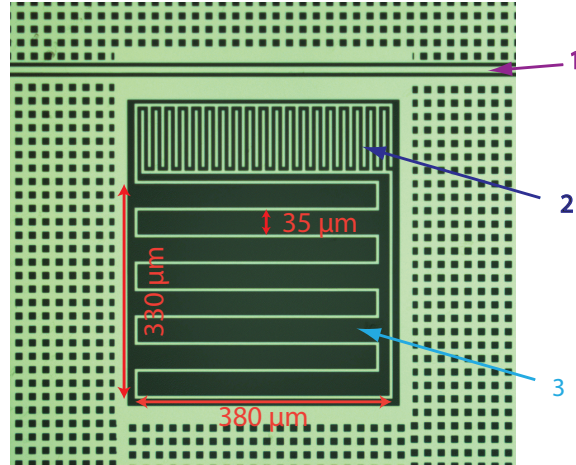


Figure 1.1: Lumped-element LC resonator. 1: microwave transmission line. 2: interdigitated capacitor. 3: meandering inductor.

Figure 1.2.2 shows our 2010 design for a thin-film lumped-element LC superconducting resonator. This niobium resonator consists of a meandering inductor and an interdigitated capacitor coupled to a transmission line. At $T=12$ mK and on resonance at 6.863 GHz, the transmission through the microwave line decreases by 1.5 dB, and the loaded quality factor is 40,000. We simulate the electromagnetic fields of the SC resonator with the software package, High Frequency Structure Simulator (HFSS), to determine the position of maximal magnetic field and uniformity.

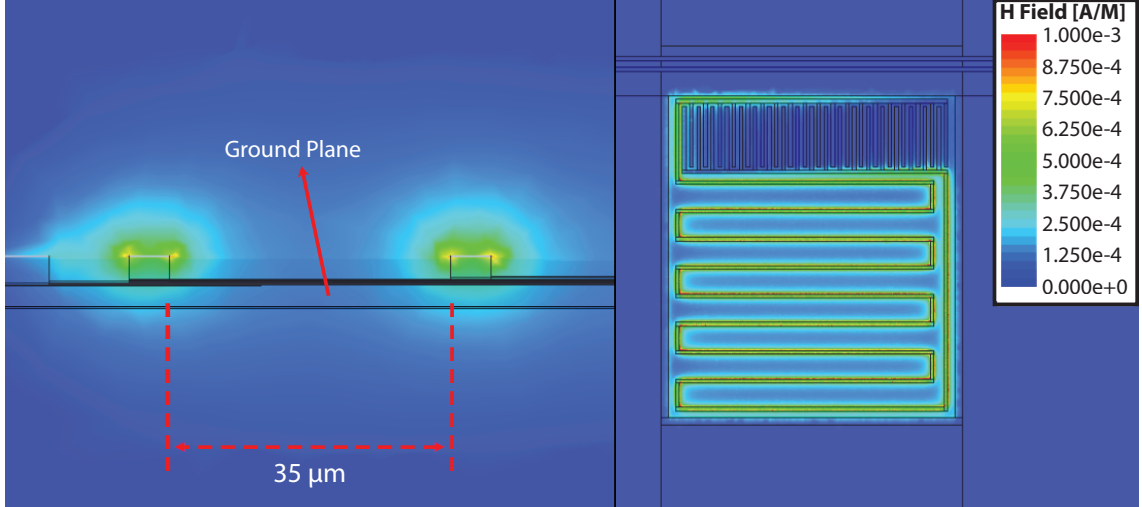


Figure 1.2: Results from a HFSS simulation of the magnetic field produced by the lumped-element LC resonator.

The coupling strength of an atom to the resonator depends on the specific geometry but may not reach the single photon value that we estimate for the SQUID. It would be lower by an order of magnitude, for example, if the resonator inductor is ten times longer than the SQUID. Figure 2, shows that the magnetic field outside of the SC for the early design. The magnetic field lines encircle the edges of the meandering inductor. We estimate the effective mode volume of this LC resonator to be around $1 \times 10^{-13} \text{ m}^3$, which yields a coupling on the order of 10 Hz per atom. For this estimate, we assume the atoms to be about $10 \mu\text{m}$ above the SC surface, independent of the device being a SQUID or lumped resonator [62].

The strongest interaction will occur if the resonator is on resonance with the hyperfine splitting of ^{87}Rb . Fabricating a resonator with a resonance that overlaps

with on the Rb hyperfine splitting is challenging [61], making an *in situ* tuning technique desirable. In Ref. [61] we employ an Al pin as a frequency tuner by placing it above the inductor and using a piezo-electrically driven stage to change the inductance of the resonator. Using this method, we demonstrate tuning of the resonator within 2 kHz (well within the bandwidth of the resonator) of the hyperfine splitting in ^{87}Rb , with only minor degradation of the Q due to the tuning mechanism [61].

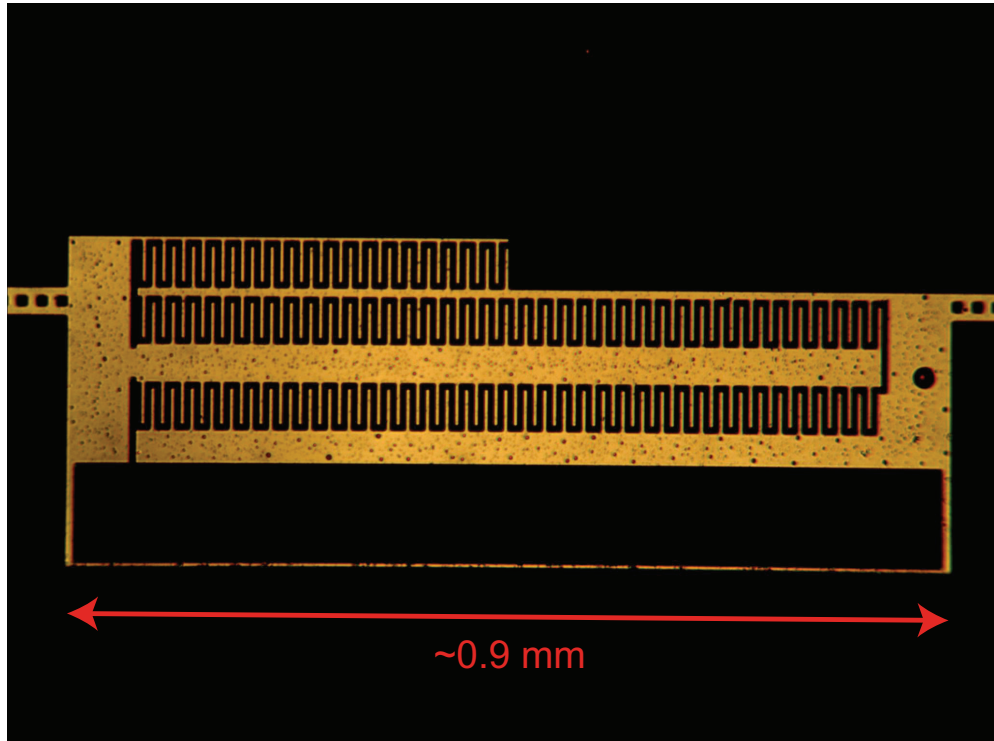


Figure 1.3: Aluminum on Sapphire lumped element resonator fabricated by J. Hertzberg [64].

Fig. 1.2.2 shows the 2013 resonator design that J. B. Hertzberg developed [64]. This design increases the inductor line length from a few hundred micrometers to nearly a millimeter. At 13 mK this resonator has a resonance of 6.140651 GHz with a high power Q of over 257,000. Eventually one could even imagine using the LC resonator as an impedance matcher between the atoms and a SC qubit.

1.2.3 Constraints

The resonator operates inside a Triton 200 Cryofree Dilution Refrigerator from Oxford Instruments at 12 mK. The 200 μW cooling power of the mixing chamber and degradation of the quality factor of SC resonators in the presence of light or a strong magnetic field present an unusual set of constraints for trapping atoms. In particular, these design constraints make the magneto-optical trap (MOT) and a conventional optical dipole trap difficult to implement [63]. Also, studies of light interaction with SC circuits shows tight light constraints leading to quasiparticle formation and degradation of Q [64–67].

These constraints necessitate a unique atomic trap. With this in mind we wish to use a trap that requires no magnetic field and minimizes the dissipated or scattered optical power from the atomic trap. One way to reduce the power is to use an optical dipole trap that has a small mode field area. To realize this we seek to employ an evanescent wave-based dipole trap outside an optical nanofiber whose diameter is smaller than the wavelength of input light [68–71], see Fig. 1.4.

1.3 Optical nanofibers

ONFs can be tailored to have tightly bound evanescent fields, see Sec. 1.3.1 and Appendix A. The tight confinement of the mode field allows us to achieve the same field strength for significantly less input power when compared to a conventional optical dipole trap formed by focusing a gaussian beam. Furthermore, unlike a gaussian beam, which will expand more rapidly the tighter the focus, we do not face the same design limitations with ONFs: as long as there is waveguide the light will propagate without expending radially. Also, incredibly low losses are achievable with ONFs, see Chap 2, making them an ideal candidate for the hybrid system. Finally, ONFs offer a simple geometry that is well-suited for coupling atoms to SC qubits.

1.3.1 Intensity profile and trapping potential

Figure 1.4 (a) Shows the ONF trapping schematic [72]. We couple linearly polarized red- and blue-detuned light from the D2 transition in ^{87}Rb into an ONF. The red-detuned light is orthogonally polarized to the blue-detuned light, to minimize light shifts on the atomic levels [69, 71, 73]. Red-detuned light is also launched through the fiber output to create a standing wave on the fiber waist, forming a 1D lattice on either side of the fiber.

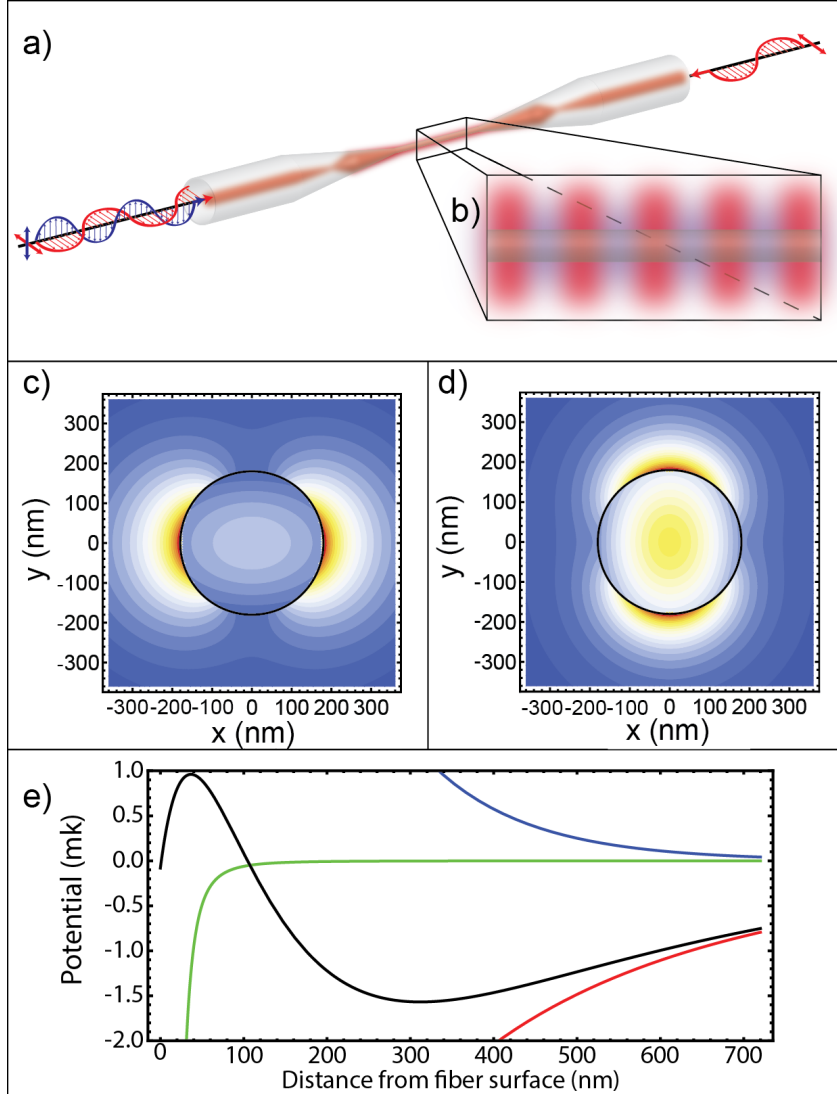


Figure 1.4: (a) The trapping schematic for a two-color ONF optical dipole trap. (b) An inset showing the red- and blue-detuned light surrounding the ONF waist. (c) The intensity profile for horizontally polarized 1064 nm light launched into an 180 nm radius waist ONF. Where the color scale indicates increasing intensity from blue to red. (d) The intensity profile for vertically polarized 730 nm nm light propagating on an 180 nm radius waist ONF. (e) The trapping potential taken along a slice of the abscissa from the fiber surface with 7.5 mW at 730 nm and 4.5 mW in a standing wave configuration for 1064 nm light.

The inset in Fig. 1.4 (b) shows the ONF waist with the evanescent wave formed by the trapping fields. Here we can see the two lattices that form around the ONF waist on either side. Notice that the red- and blue-detuned light have different decay lengths from the ONF surface, see Appendix A.

Figure 1.4 (c) shows the intensity profile for a 1064 nm horizontally polarized red-detuned input beam on a 180 nm radius ONF. The black circle represents the cladding-air boundary of the ONF. Similarly, Fig. 1.4 (d) displays the intensity profile for a 730 nm vertically polarized blue detuned input beam for a 180 nm radius ONF. The intensity profiles inside and outside the fiber are [70, 74]

$$|E_{in}|^2 = g_{in} [J_0^2(hr) + uJ_1^2(hr) + fJ_2^2(hr) + (uJ_1^2(hr) - f_p J_0(hr)J_2(hr)) \cos[2(\phi - \phi_0)]] \quad (1.2)$$

$$|E_{out}|^2 = g_{out} [K_0^2(qr) + wK_1^2(qr) + fK_2^2(qr) - (wK_1^2(qr) - f_p K_0(qr)K_2(qr)) \cos[2(\phi - \phi_0)]] \quad (1.3)$$

where J_n and K_n are Bessel functions of the first and second kinds of order n respectively, r is the radius from the center of the fiber, and g is a normalization constant. The terms h, q, f, f_p and w , given explicitly in [70], are functions that depend on the fiber radius and the propagation constant β of the input field.

The intensity outside the fiber falls off with a characteristic decay length proportional to $q = \sqrt{\beta^2 - k^2}$ (see Fig. 1.4), where k is the free space wave vector. In Fig. 1.4 (c) and (d) we observe the difference in decay lengths: the 1064 nm intensity has longer decay length than the 730 nm intensity. Furthermore, there is a discontinuity across the cladding-air boundary. This occurs because the ra-

dial and longitudinal components of the electric field for the fundamental mode are discontinuous, see Appendix A.

Light shifts due to the optical power can be problematic for this type of trap, and the shifts include contributions from the longitudinal component of the electric field [75]. This longitudinal component, which is inherent to the fundamental mode of a fiber, leads to vector light shifts [71, 73, 75, 76]. In our scheme the standing wave formed by the counter-propagating red-detuned beam cancel the longitudinal component of the electric field, making the blue-detuned light the only source of vector light shifts. In fact, at the trapping site along the horizontal axis of the red-detuned beam, the longitudinal component from the blue-detuned light is zero in this configuration. We also note that Refs. [71, 73] employ a trap which significantly reduces light shifts in a Cs based ONF trap by finding wavelengths that minimize or cancel the effect, the so called magic wavelengths [77, 78].

Fig. 1.4 (e) shows the trapping potential realized by sending two color light, red- and blue-detuned from the D_2 transition of Rb, through the fiber, with 7.5 mW at 730 nm and 4.5 mW at 1064 nm light in a standing wave configuration . Here, we take a slice of the potential along the abscissa from the fiber surface. The red curve corresponds to the attractive red-detuned light, the blue curve correspond to the repulsive blue-detuned light, the green curve is the van der Waals potential, and the black curve is the total potential. We see this forms a trap that is more than one mK deep at a few hundred nanometers from the fiber surface.

As a result of the close proximity of the atoms to the fiber surface means we must include the van der Waals interaction in the trapping potential. We do

not, however, use the exact van der Waals interaction between an atom and a nanowire [79] but instead treat the system as if the atoms were located next to an infinite dielectric, where the C_3 coefficient is $8.46 \times 10^{-49} \text{ J} \cdot \text{m}^3$ [80, 81]. Given the distances of atoms from the fiber surface, it appears that we may be in a cross-over region between the van der Waals and Casimir-Polder regimes [105].

Changing the radius of the fiber, the wavelengths of the red- and blue-detuned beams, and the relative powers of the two-color trap allows us to change the trapping distance of the atoms from the fiber surface. This distance plays a critical role in atom-light interactions and explains why ONFs are of interest in atomic physics. The optical depth (OD) per atoms can reach 10% in certain configurations and these type of traps allow for studies of long-range interactions [82].

1.4 Thesis overview

This thesis focuses on the fabrication of ONFs for coupling atoms to superconducting qubits. In Chapter 2 we present the ONF fabrication process with particular attention to obtaining high transmission and adiabatic tapering for reducing light losses. Here we will discuss the entire fabrication process and algorithm and report on measurements comparing results to simulation. We demonstrate that following this process yields the lowest loss ONFs reported. In Chapter 3 we discuss modal analyses of ONFs using simulations and spectrogram analysis. Using a genetic algorithm we produce tighter bounds on ONF taper geometries that yield desired transmission. Furthermore, using simulations we can identify the entire modal evolution

during a fiber taper using a spectrogram analysis. We next present studies of HOM guidance in Chapter 4, in which we demonstrate the highest reported transmission of HOMs through ONFs. Chapter 5 discusses modal identification techniques for HOMs on the ONF waist using Rayleigh scattering and evanescent coupling with tapered fiber probes. Finally, Chapter 6 includes a brief conclusion and outlook followed by an Appendix discussing the mode structure in an ONF.

Chapter 2: Optical nanofiber fabrication

2.1 Introduction

Optical nanofibers have seen widespread use in science and engineering applications during the last thirty years [83, 84]. The tight confinement of the evanescent field around the optical nanofiber [70], unique light geometries provided by the fiber modes [72, 85, 86], low loss, and promise of improved atom-light interaction [69, 71, 87–89] have led to increased interest in the physics community. Optical micro- or nanofibers are used for sensing and detection [90, 91], and coupling light to resonators [91–96], NV centers [97], or photonic crystals [98–100]. Optical nanofiber fabricated systems can be connected to an existing fiber network to provide applications in quantum information science [101].

The development of atom traps around optical nanofibers affords new avenues of research [69–71] including hybrid qubit systems. These qubits can benefit from high transmission nanofibers through a reduction in unwanted stray light fields produced from non adiabatic mode excitation and reduced laser power requirements. Here we present the tools and procedures necessary to create ultrahigh transmission nanofibers.

Some previous work focuses on the effect of the post-pull environment concern-

ing the humidity and air purity [102]. Here we focus on the critical pre-pull steps necessary to achieve an ultrahigh transmission, before handling the known environmental effects. Following the protocols described below we have produced fibers with 99.95 % transmission when launching the fundamental mode. We have also launched higher-order modes [103, 104] through the fabrication process below and achieve transmissions of greater than 97% for the first family of excited modes, see Chap. 4. This level of transmission requires a thorough optimization of the pulling algorithm and fiber cleaning procedure. In this chapter we describe our technique and the apparatus that produces fibers that we will use in a series of experiments towards building a hybrid quantum system [105, 106].

Our pulling technique is based on an existing methodology [84]. It requires two pulling motors and a stationary oxyhydrogen heat source. This flame brushing method allows us to reliably produce optical nanofibers with controllable taper geometries and a uniform waist. With our setup the waist can vary in length from 1 to 100 mm, and we can achieve radii as small as 150 nanometers [107–111]. Rather than sweep the flame back and forth over the fiber, we keep the flame stationary; this action reduces the creation of small air currents, which could lead to nonuniformities on the fiber waist and is equivalent to transforming to the rest frame of the flame. This approach is applicable to other pulling techniques as well, so there would be no need to scan a heat source.

Other common techniques for optical nanofiber production make use of micro-furnaces, fusion splicers, chemical etchants, and CO₂ lasers [112–117]. Chemical etching generally produces lower transmission than other heat and pull methods and

offers less control over the shape of the taper and the length of the waist. A CO₂ laser produces high-transmission optical nanofibers but the final diameter is limited by the power and focus of the laser. Here we present, to the best of our knowledge, result on ONF fabrication; with the highest reported transmission, corresponding to a loss of 2.6×10^{-5} dB/mm for the fundamental mode [84,118], with controllable taper geometries and long fiber waists. These fibers were specifically developed to be suitable for meeting constraints of use in cryogenic environments [105].

2.2 Experimental setup

This sections describes the details of the experimental setup. Our work follows the originally Mainz and currently Vienna group [111].

2.2.1 The fiber-pulling apparatus

The fiber-puller apparatus (see Fig. 2.1 and Table 2.1) consists of a heat source that brings the glass to a temperature greater than its softening point (1585° C for fused silica [119]) and two motors that pull the fiber from both ends. We use two computer-controlled motors, Newport XML 210 (fiber motors), mounted to a precision-ground granite slab with dimensions 12" × 48" × 4", flat to 3.81 μm on average. The granite slab serves two purposes: it's weight suppresses vibrations and it provides a flat surface. The weight of the granite slab, exceeding 100 kg, damps the recoil from the fiber motors as they change direction at the end of every pull step. Without a flat surface the motors will not work to specification, leading to

distortion of the ONF during the pull: the pitch or yaw of the motor can vary the distance between the fiber and the flame, changing the effective size of the flame and pulling the fiber in unintended directions (negating any pre-pull alignment), see Fig. 2.1(b). The motors are mounted to the granite by L-bracket adapters designed to not deform the motors from the the granite surface. The granite is mounted on an optical breadboard at three points so that surface imperfections of the optical table do not distort the granite slab.

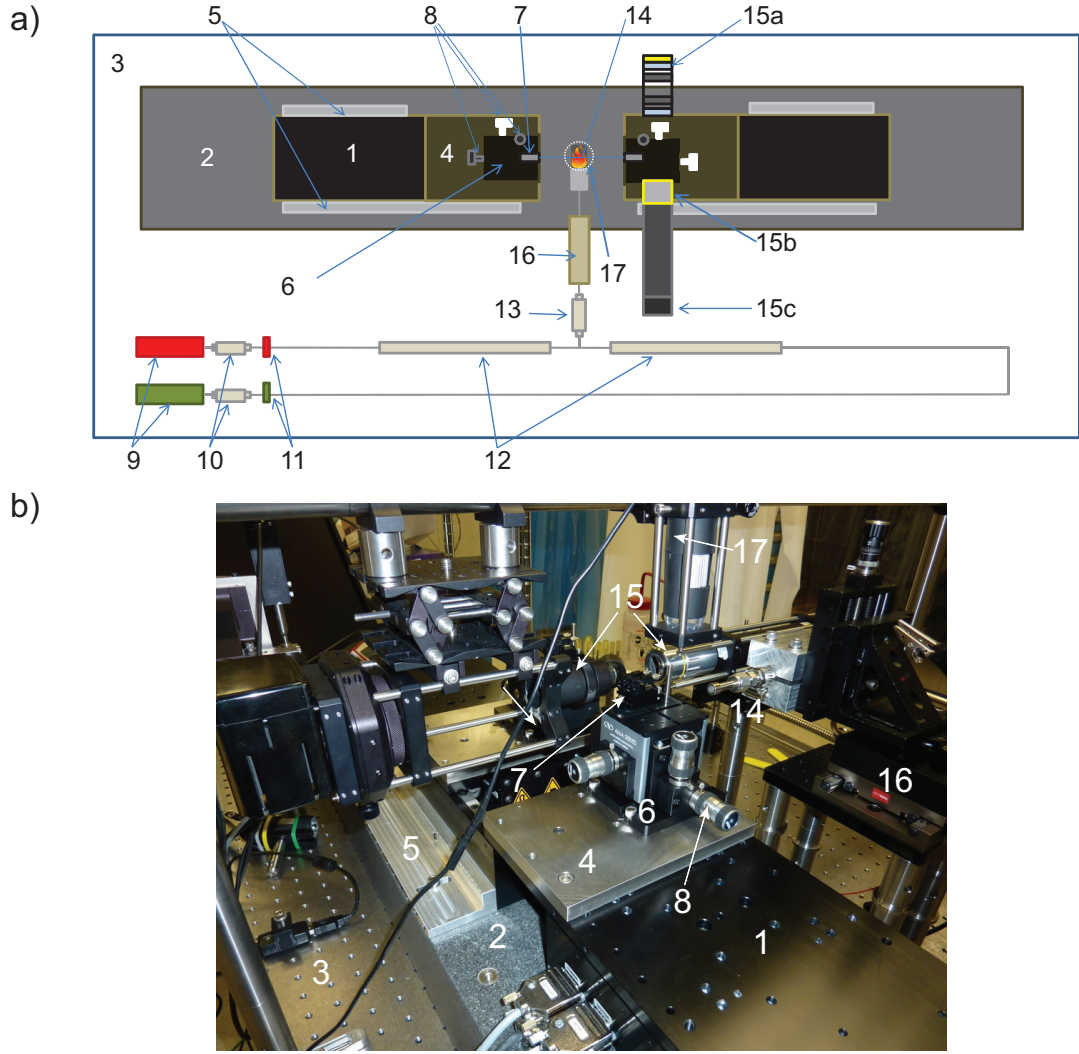


Figure 2.1: (a) A schematic of the fiber pulling setup (view from above). (b) An image of the pulling apparatus. 1) Fiber motors. 2) Granite slab. 3) Optical breadboard. 4) Adapter plates. 5) L brackets. 6) XYZ fiber alignment flexure stages. 7) Fiber holders. 8) Adjustment screws. 9) Gas flow meters. 10) Filters. 11) Valves. 12) Pipes. 13) Filter. 14) Nozzle. 15) (a) Illumination system, (b) Optical microscope, and (c) CCD. 16) Flame positioning stepper motor. 17) 2 MP USB microscope positioned orthogonally to the fiber. The entire apparatus is inside a cleanroom rated to ISO Class 100.

The fiber motors have 210 mm of motion with a minimum step size of 0.01 μm and an on-axis accuracy of $3 \pm 1.5 \mu\text{m}$ (1 in Fig. 2.1). The resolution of the motors is much smaller than any other relevant length scale in our system, although the accuracy is not less than the fiber radius. This is sufficient for the motors to be suitable for pulling ONFs. The fiber motors are controlled with a Newport XPS controller, which allows us to implement trajectories with a relatively constant acceleration, resulting in jerkless motion during each step of the pull.

Item	Part	Description
1	Newport XML 210	Computer-controlled high precision motor
2	Granite slab	12" \times 48" \times 4", Flat to 3.81 μ m
3	Newport VH3660W	3' x 5' workstation
4	Adapter Plate	Adapts metric XML 210 to 466A
5	L brackets	Adapts XML 210 to granite
6	Newport 466A	Compact XYZ fiber alignment flexure stages
7	Newport 466A-710	Double arm bare fiber holder double V-grooves
8	Newport DS-4F	High precision adjuster
8	Newport AJS100-0.5	High precision small knob adjustment screw
9	Omega FMA 5400/5500	Gas flow meters
10	Swagelok SS-4F-7	Particulate filter, 7 micron pore size
11	Swagelok SS-4P4T	Valve to close the flow of gas
12	Swagelok SS-FM4SL4SL4-12	Stainless steel flexible tubing
13	GLFPF3000VMM4	"Mini Gaskleen filter" from Pall
14	Custom SS nozzle	29, 200 μ m holes in a 1x2 mm ² array
15	Optical microscope	Microscope objective, CCD, and illumination system
15a	Illumintation System	Kohler illumination system
15b	Mitutoyo M Plan APO 10X	Microscope objective, 0.28 NA
15c	Flea2G CCD camera	2448 x 2048 pixels, 3.45 x 3.45 μ m ² pixels
16	Thorlabs DRV014	50 mm Trapezoidal Stepper Motor Drive
17	USB microscope	200x, 2 MP USB microscope
18	Platinum wire	Platinum catalyst to ignite flame
19	Clean room	ISO class 100 cleanroom

Table 2.1: List of equipment parts for the pulling apparatus.

We attach Newport 466A flexure stages (6 in Fig. 2.1) with a Newport 466A-710 fiber clamp (7 in Fig. 2.1) to the XML 210 (1 in Fig. 2.1). We position the v-grooves of the fiber clamp on each stage at the minimum separation allowed by the parameters of a given pull, which is typically 3 cm. Separating the fiber clamps at the minimum distance minimizes the fiber sag during the pull, which can result in the ONF breaking during the pulling process. The v-grooves of the fiber clamps on the left and right fiber motors must be aligned within a few micrometers to achieve a high transmission. We align the v-grooves using Newport DS-4F (8 in Fig. 2.1) and AJS100-0.5 (8 in Fig. 2.1) micrometers, attached to the flexure stages to allow for three axis translation and use an *in situ* optical microscope (15(a)-(c) in Fig. 2.1).

The optical microscope includes a Mitutoyo M Plan APO 10X infinity-corrected objective and a Point Grey Flea2G CCD camera (15(a)-(c) in Fig. 2.1). The Flea2G has 2448×2048 pixels, each having an area of $3.45 \mu\text{m} \times 3.45 \mu\text{m}$ pixels. With this long working distance microscope objective each pixel corresponds to $0.345 \mu\text{m} \times 0.345 \mu\text{m}$ in the image. We illuminate the microscope with a Köhler illumination system composed of a thermal light source, two condenser lenses, and two apertures.

We use an oxyhydrogen flame to heat the fibers, in a stoichiometric mixture of hydrogen and oxygen to ensure that water vapor is the only byproduct. Stainless steel gas lines introduce the hydrogen (red) and oxygen (green) to two Omega FMA 5400/5500 flow meters (9 in Fig. 2.1). The flow rates are set to 30 mL/min and 60 mL/min for oxygen and hydrogen respectively. Directly after the flow meters is a coarse particle filter (10 in Fig. 2.1), followed by a valve for safety (11 in Fig. 2.1). The gases mix in a tee after a flexible stainless steel tube (12 in Fig. 2.1). The gas

mixture is then filtered with a high quality 3 nm filter (13 in Fig. 2.1). Finally the hydrogen-oxygen mixture exits through a custom-made nozzle with 29 holes of 200 μm diameter in a $1 \times 2 \text{ mm}^2$ area (14 in Fig. 2.1, see Fig. 2.2). The nozzle serves as a flame arrestor, while still allowing for the gas flow to be in the laminar regime.

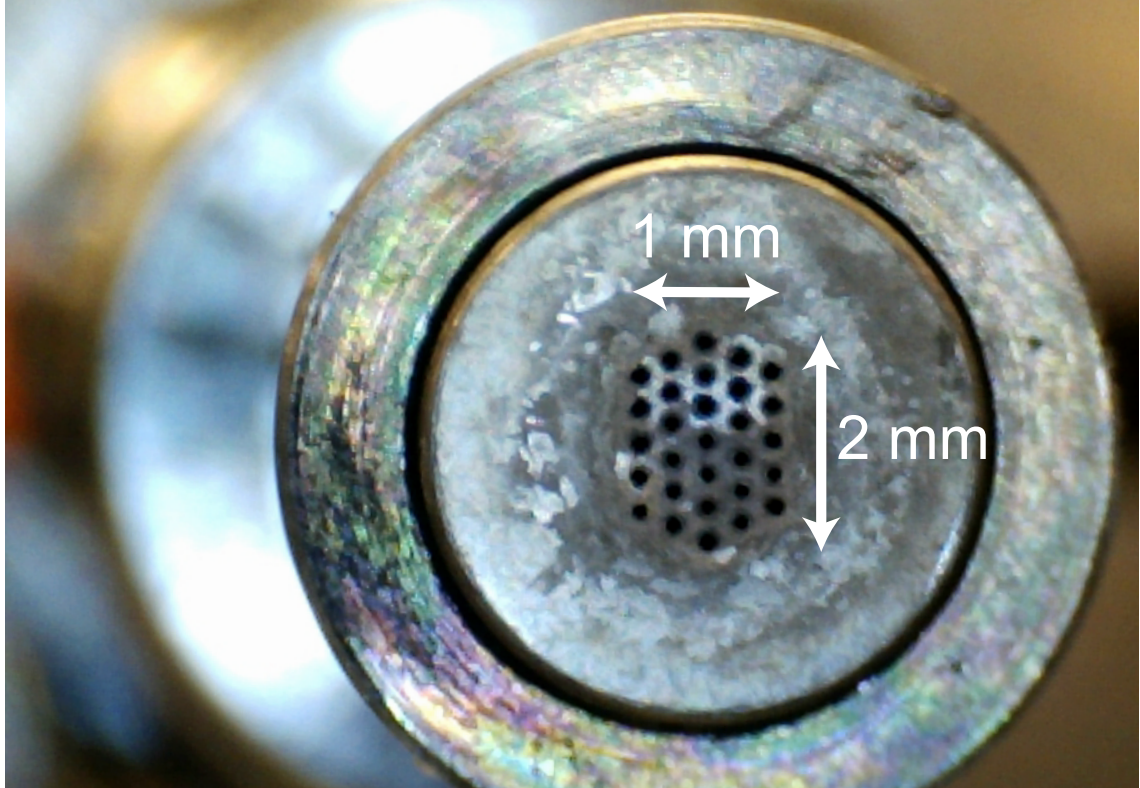


Figure 2.2: An image of the flame nozzle. The holes are arranged in a grid that is $1 \text{ mm} \times 2 \text{ mm}$.

We ignite the flame using a resistively-heated platinum wire as a catalyst. This process is clean and results in less deposition of particulate on the fiber. The nozzle is clamped to a Thorlabs DRV014 motor (16 in Fig. 2.1), the flame motor, that translates the flame in front of the fiber for the duration of the pulling process.

This flame motor introduces and removes the heat source to the fiber. During the pull we fix the distance between the nozzle and the front edge of the fiber to about 0.5 mm. We have found experimentally that a distance of 0.4-0.6 mm provides the proper heat distribution from our flame and does not result in the fiber breaking during the pulling process.

The entire pulling apparatus is inside a nominally specified ISO Class 100 cleanroom. If any fiber buffer remains or dust lands on the fiber at any time the transmission will degrade (see Sec. 2.7).

2.2.2 Transmission monitoring setup

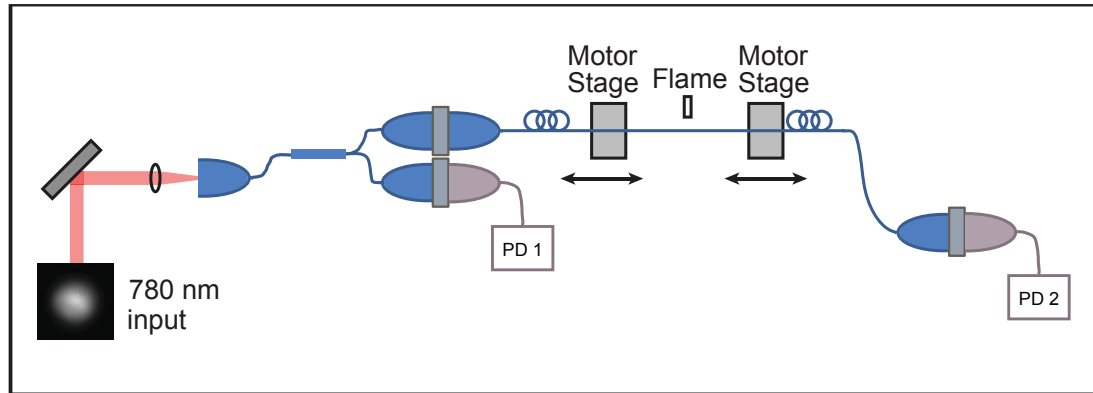


Figure 2.3: The experimental setup to monitor the transmission when launching the fundamental mode during ONF fabrication.

Figure 2.3 shows the transmission monitoring setup. Using a 780 nm Vortex laser, we launch light into a fiber and split the light with a 50/50 in-fiber beam

splitter. One output of the beam splitter goes to a Thorlabs DET36A photodetector and records the laser power. The other output is connected to a FC connectorized fiber that we fusion splice to Fibercore SM800 fiber. We then place the SM800 fiber in the fiber puller and record the power of light through the fiber at the output of the fiber puller using another DET36A. We record data for the duration of the pull on a DPO7054 Tektroniks oscilloscope in high resolution mode set to collect 10^7 samples. We normalize the signal through the fiber puller to the laser drift throughout the pull.

2.3 Algorithm

We pull our fibers using a flame brushing technique [107–109, 111]. A section of fiber, less than a millimeter in length, is brought to its softening point using a clean oxyhydrogen flame and then pulled by two high-precision motors.

To choose the parameters for a pull we developed an algorithm¹, based on the work of the originally Mainz and currently Vienna group [111], that calculates the trajectories of the motors needed to produce a fiber with the desired final radius, length of uniform waist, and taper geometry. The tapers are formed by a series of small fiber sections that are well approximated by lines, allowing us to form a linear taper with a given angle down to a radius of $6 \mu\text{m}$. This connects to an exponential section that smoothly reduces and connects to a uniform section with a

¹The program is available at the Digital Repository of the University of Maryland (DRUM) at <http://hdl.handle.net/1903/15069>.

submicron radius, typically 250 nm. The slope of the linear taper section generally varies between 0.3 and 5 mrad. The algorithm divides the pull into steps defined by their pulling velocity and the traveling length of the flame. It recursively calculates the parameters, starting from the desired final radius, r_w , until reaching the initial radius, r_0 .

Full details on the algorithm can be found in Ref. [120]. The key points are:

- The fiber volume is conserved during the pulling process so that the radius r_n of the fiber waist at step n , is related to the radius r_{n-1} of the waist at step $n - 1$, according to the equation

$$r_n = r_{n-1} \exp \left(\frac{-t_{0,n} v_{f,n}}{2L_0} \right), \quad (2.1)$$

where $t_{0,n}$ is the time during which the flame fully sweeps through a point on the fiber, $v_{f,n}$ is the velocity at which the fiber motors move apart, and L_0 is the length of the heating region.

- We assume that the fiber is pulled symmetrically with respect to the center of the flame and that the distribution of the pulling velocities inside the flame is linear. Using this assumption, we derive a differential equation that we can solve to find an expression for $t_{0,n}$:

$$t_{0,n} = \frac{L_0}{v_{f,n}} \ln \left(\frac{2v_{b,n} + v_{f,n}}{2v_{b,n} - v_{f,n}} \right). \quad (2.2)$$

With these results the ratio r_n/r_{n-1} is fixed by the geometric constraints we impose on our fiber. We fix the velocity of the burner $v_{b,n} = v_b$ and use Eqns. 2.1 and 2.2

to calculate $v_{f,n}$ and $t_{0,n}$. Typically we fix v_b at 2 mm / s while v_f can vary from 10 μm / s to more than 100 $\mu\text{m}/\text{s}$.

We want each subsection in the taper region to smoothly connect to neighboring sections. We achieve this by properly linking the taper in each consecutive step. The model requires that $v_{b,n} > v_{f,n}/2$ to ensure the flame can reach previously thinned points. Fig. 2.4 presents a physical picture of the taper linking process. Where Fig. 2.4(a) and (b) shows the evolution of the fiber taper and the flame in step n and $n + 1$ respectively.

Here we can identify three heating classes, which we distinguish by color: fiber sections that begin in the flame (light blue), fiber sections that are fully swept by the flame (green), and fiber sections that end in the flame (dark blue). The fiber sections that begin in the flame form the taper in step n . This occurs because each marker on the fiber is swept by the flame for a different period of time and therefore thinned differently. The ONF waist in step n forms when the flame fully sweeps through that section of fiber. Here each part of the glass sees the same integrated heat distribution of the flame and therefore thins uniformly. Finally, the region of fiber in which the flame ends forms the other side of taper in step n .

The dashed black line in Fig. 2.4 separates the evolution of the fiber and flame in step n from step $n + 1$. We note that the z-axis flips and zeroes between steps. Specifically, the outer edge of the flame in step n becomes the zero of the z-axis in step $n + 1$.

We link the tapers by tracking the evolution of the first section of glass that the flame fully sweeps in step n . In Fig. 2.4 we represent this marker with a thick

red line. This marker represents the taper-waist link in step n . By tracking the evolution of this section of glass from step n to step $n + 1$ and bringing the outer edge of the flame in contact with this point in step $n + 1$ we are able to link tapers.

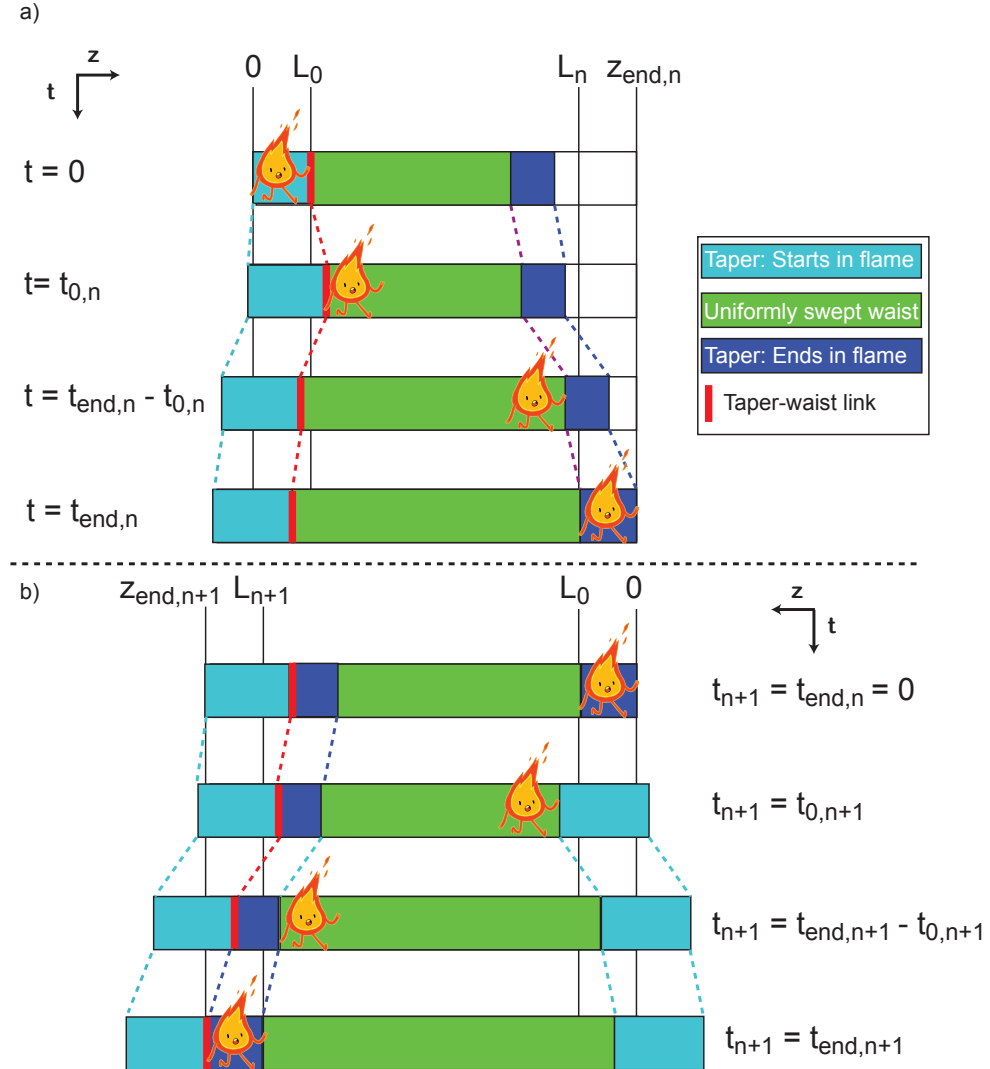


Figure 2.4: The taper linking process. a) The evolution of the flame and taper in step n . b) The flame evolution in step $n+1$. We note that the the horizontal axis flips between steps such that the outer edge of the flame in step n becomes the zero of the z -axis in step $n+1$. There are three heating classes in a given step: fiber sections that begin in the flame (light blue), fiber sections that are fully swept by the flame (green), and fiber sections that end in the flame (dark blue). These regions form the taper, waist, and taper, in step n respectively.

Using conservation of volume we relate the length of the waist $L_{w,n-1}$ in step $n-1$, to the length of the waist $L_{w,n}$ in step n :

$$r_{n-1}^2 L_{w,n-1} = r_n^2 L_{w,n} + r_{n-1}^2 \left(v_{b,n} - \frac{v_{f,n}}{2} \right) t_{0,n}. \quad (2.3)$$

This relates $L_{w,n}$ to the distance L_n , the distance the flame sweeps in step n , and also relates it to $L_{w,n}$, $v_{f,n}$, and $t_{0,n}$ by

$$(L_n - v_b t_{0,n}) (v_{b,n} - v_{f,n}/2) = v_{b,n} L_{w,n}. \quad (2.4)$$

Once we experimentally establish L_0 and v_b (see Sec. 2.3.2) and fix r_0 for a given fiber we specify the desired r_w , L_w and Ω for the given pull and the algorithm calculates the necessary parameters to produce a fiber with desired geometry.

2.3.1 Motor control

The model produces a velocity profile that is a square wave in time. Experimentally, we approximate the square wave in three parts:

1. A ramp up of the pulling motors to $v_{b,n} \pm v_{f,n}/2$
2. A constant pull velocity equal to $v_{b,n} \pm v_{f,n}/2$
3. A ramp down of both fiber motors to zero velocity.

Here $v_{b,n}$ is the velocity of the flame in step n and $v_{f,n}$ is the velocity that the fiber motors move apart. The addition of $v_{b,n}$ arises from the transformation to the rest frame of the flame. Typically, $v_{b,n}$ (2 mm/s) is an order of magnitude greater

than $v_{f,n}$ (0.01 mm/2 - 0.1 mm/s). When transforming to the rest frame of the flame, both motors move in the direction the flame would have swept in that step. The motor whose pull velocity is in the same direction as the flame motion will lead while the other motor will lag. We have verified this sequence using the position encoders on the motors. This allows us to record the trajectory of the motors. We have separately verified this by looking at the output of a Michelson interferometer with one arm spanning the two motorized stages.

2.3.2 Measurement of the flame width

One fundamental experimental parameter of the algorithm is the effective size L_0 of the flame. This corresponds to the effective length of the fiber inside the flame that melts and thins during the pulling process. The softening point for the fused silica used by Fibercore for the SM800 fiber occurs at 1585° C. The best way to estimate L_0 is to pull fibers measure the resulting geometry and compare to the algorithm, since our flame is not visible by eye.

For reproducible conditions, we need to working distance between the fiber and the nozzle. Ideally the fiber is always in the same part of the flame and always sees the same distribution of temperature. We set the distance from the end of the nozzle to the center of the fiber to $400 \pm 50 \mu\text{m}$ before each pull and verify the distance with a microscope.

We measure L_0 by fixing the flame and letting both motors move apart at a constant velocity. Conservation of volume leads to an exponential profile with a

waist of length L_0 , and the radius profile is given by :

$$r_w = r_0 \exp \left(-\frac{t_h v_f}{2L_0} \right), \quad (2.5)$$

where t_h is the heating time and r_0 the unmodified radius of the fiber. We use our imaging system (15 in Fig. 2.1) to measure the radius of the waist of the fiber for different values of $v_f t_h$, and fit $\ln(r_0/r_w)$ to extract L_0 . The measurement consists of fixing the pulling velocity at 0.05 mm/s, varying the heating time from 2 to 32 s, and then measuring the final radius of the waist. We limit ourselves to times less than 40 seconds to stay within the 2 μm resolution of our imaging system.

Plotting $\ln(r_0/r_w)$ as a function of $v_f t_h$ we obtain a fit (see Fig. 2.5) with a reduced χ^2 of 1.07. Here we extract the slope of the fit which corresponds to the effective width of the flame resulting in $L_0 = 0.753 \pm 0.014$ mm. This parameter should be checked from time to time as the pulling apparatus is used since it can vary by a small amount.

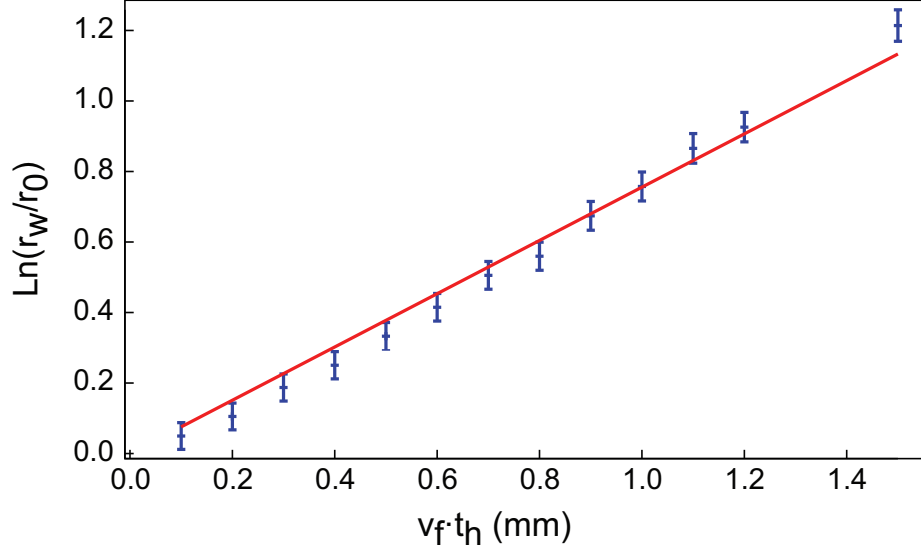


Figure 2.5: $\ln(r_w/r_0)$ as a function of $v_f t_h$. The blue markers are the experimental points, and the red line is the fit. From the slope of the fit we extract $L_0 = 0.753 \pm 0.014$ mm.

Measuring the length of the waist or fitting the profiles of the taper to an exponential are less accurate methods than the above procedure because Eq. 2.5 assumes a uniform hot zone, L_0 . In this measurement we keep the flame fixed, which means that our hot zone is not uniform. During the actual pulling procedure we sweep, which creates an effective uniform hot zone. Here, the section of fiber located at the central point of the flame is thinned the most, as a result it is more accurate to measure the profile of the fiber after tapering and find the smallest radius to extract the value of L_0 .

2.4 The pulling process

The setup for an ultrahigh transmission pull involves a series of cleaning and alignment steps. We outline this procedure in this section.

2.4.1 Cleaning procedure

Obtaining high transmission through an ONFr requires careful attention to the pre-pull cleanliness of the fiber. If any particulate remains from the fiber buffer or if dust arrives on the fiber before being introduced to the flame, the particulate will burn and greatly diminish the final transmission, see Sec. 2.7. Furthermore, we found that evaporation from solvents can decrease transmission.

Our cleaning procedure starts by mechanically removing the protective plastic buffer to expose the glass of the fiber to the flame. Then we use isopropyl alcohol on lens tissue to remove larger particulate. A few wipes of acetone² are then applied with class 10a cleanroom wipes from Ted Pella, in order to dissolve smaller remnants of the buffer. A final cleaning with methanol using class 10a cleanroom wipes removes evaporation left from the previous solvents. After, we carefully lay the fiber into the grooves of the fiber clamps on the pulling apparatus and image the entire

²We used acetone for the data shown here; however, we generally would not recommend its use because it can prolong the cleaning process. SM800 fibers have a buffer made of dual acrylate, which dissolves in acetone. Acetone is fine for chemical removal of the buffer when heated or paired with other chemicals, but when cleaning with a wipe, the acetone can spread small buffer particulate along the stripped portion of fiber, which can burn when introduced to the flame.

length of cleaned fiber using the optical microscope. If there is any visible dust, particulate, or evaporate, within the $2 \mu\text{m}$ resolution of the optical microscope, we repeat the cleaning procedure over. If the fiber is clean, we proceed to align it.

2.4.2 Alignment procedure

We start the alignment procedure by tensioning the fiber. We tension the fiber by moving the fiber motors apart in $200 \mu\text{m}$ increments until the fiber slides through the fiber clamps, which typically takes $800 \mu\text{m}$ of total displacement. This allows the fiber to reach a uniform tension. However, early measurements showed the fiber to be overtensioned: introducing the fiber to the flame will yield an immediate thinning, even if the motors are stationary. To prevent this, we then untension the fiber in $20 \mu\text{m}$ increments until the fiber buckles. We observe the buckling process (the fiber bending inwards and then straightening under the inward force from the motors) with a 2 MP USB digital microscope mounted orthogonally to the flame above the center of the fiber, see 17 in Fig. 2.1.

The buckling process results in no loss in transmission and no thinning visible through the optical microscope upon introducing the fiber to the flame, at least within the microscope's resolution of $\pm 2 \mu\text{m}$.

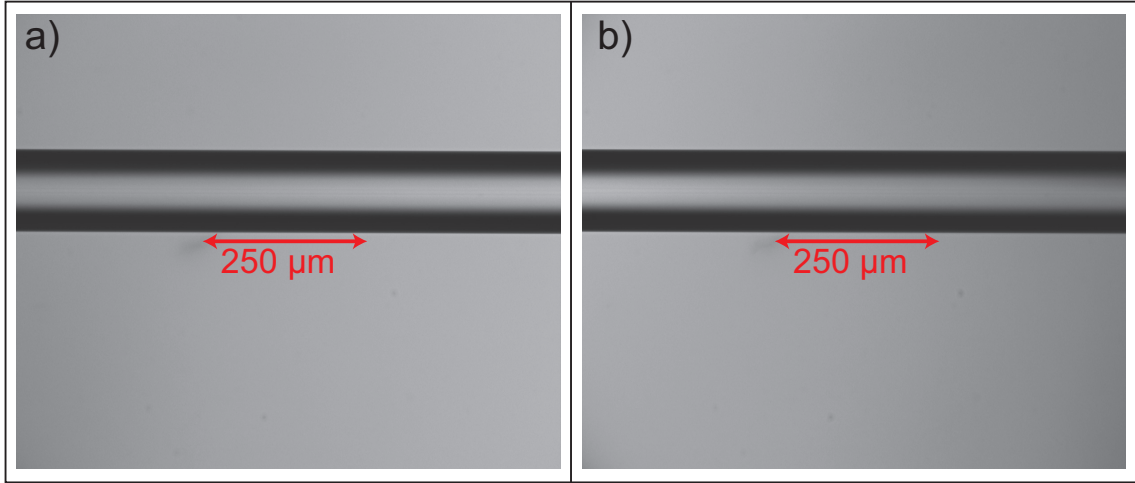


Figure 2.6: Images of fiber sections (a) next to the left and (b) right fiber clamps.

The two images are separated by 3 cm and show excellent lateral alignment.

Once the fiber is properly tensioned, we align the fiber such that the sections of fiber directly next to the left fiber clamp and right fiber clamp are equidistant from the optical microscope and at the same height. We translate each section of fiber in front of the optical microscope using the fiber motors, see Fig. 2.1, and align the height and focus of each fiber using the micrometers attached to the flexure stage until both images overlap. If we see a sag in the fiber caused by the buckling we carefully retension the fiber in $5 \mu\text{m}$ steps until the fiber is straight as in Fig. 2.6. The microscope objective has a $3 \mu\text{m}$ depth of field, so by matching the diameter of the lensed light from the cladding and core we ensure that the v-grooves of the fiber clamps on each motor are equidistant from the camera, and therefore the nozzle of the flame. This alignment is on the order of micrometers over a length of

centimeters. Once the images overlap, see Fig. 2.6, the fiber is ready to be pulled.

2.5 Results

Here we discuss the results obtained from following the procedures outlined above. First we validate the pulling algorithm and simulation of the taper geometry using microscopy. Then we present details on the transmissions achieved by following cleaning and alignment procedures. Finally, we detail methods to aid in understanding the entire modal evolution during the fiber pull as a final check on the quality of the ONFs we produce.

2.5.1 Microscopy validation

We validate the accuracy of our simulation of the expected fiber profile using both an *in situ* optical microscope and a scanning electron microscope (SEM) to examine fibers after pulling. Figure 2.7 (a) shows the measured (blue markers) and simulated profiles (red lines) of a fiber taper imaged optically. The taper profile is designed to have three angles, 5, 2, and 3 mrad, on sections that taper down to radii of 50, 35 and 25 μm , respectively. An exponential profile smoothly links the radius of 25 μm to the the final radius of 15 μm . The final radius is chosen to be well above the resolution of our optical microscope to allow it to be precisely measured. The length of the uniform waist is chosen to be 5 mm long.

The data in Fig. 2.7(a) is a compilation of optical microscope images taken of the entirety of the tapered fiber. We use an edge finding technique to measure the

profile of the fiber at different cuts. The error in the measured radius is dominated by a systematic error of $\pm 2.5 \mu\text{m}$ due to the finite resolution of the imaging system. We first use an image of the unmodified fiber, which has a known diameter of 125.1 μm , to determine the pixel to micron conversion. The number of pixels measured for an unmodified fiber has an error of a few pixels as a result of the resolution of the optical microscope. We then binarize the gray levels of the pixels and choose a threshold such that the diameter of the unmodified fiber matches the pixel count from the previous measurement. The edge finding technique itself has an error of about 0.5 pixels for a flat length of fiber resulting from the binarization process. Figure 2.7 (b) displays the relative difference between the measured image radius and the simulated radius normalized to the expected radius. The largest deviation is slightly larger than 2%, while the RMS value is 0.0187. This verifies the accuracy of our algorithm and pulling apparatus for larger radius tapers.

We use a SEM to measure the ONF profile below a micrometer to verify that our ONFs truly achieve the desired diameter. Figure 2.8, shows a SEM image of a ONF, coated with graphite, with an expected diameter of 500 nm, and a measured diameter of $536 \pm 12 \text{ nm}$. The error is systematic, coming from the scaling factor associated with the SEM calibration. We attribute this small disagreement to thermal air current forces that push the fiber away from the nozzle at the end of the pull when the fiber is thin. We could compensate for this in the algorithm by adjusting the effective hot zone as the fiber tapers, but we have not found it necessary to do so.

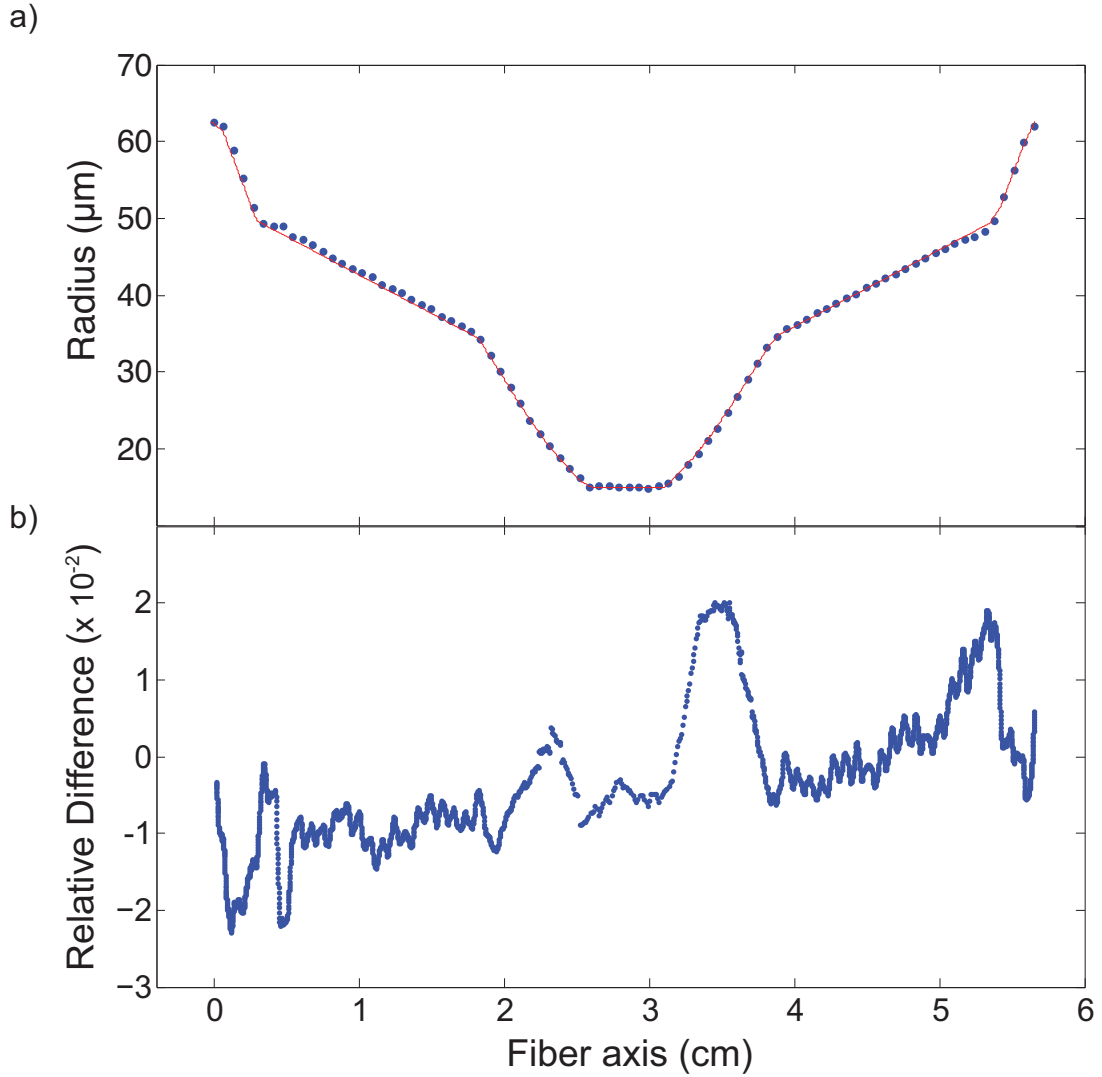


Figure 2.7: Profile of a multiple-angled, linearly tapered fiber. (a) The blue dots are measurements taken using the optical microscope and the red curve represents the intended profile shape from the fiber tapering simulation. The pull was for a final radius of 15 μm . The taper profile was designed to have three angles, 5, 2, 3 mrad, that taper down to radii of 50, 35 and 25 μm , respectively. The error in each measurement is dominated by a systematic error of $\pm 2.5 \mu\text{m}$. (b) The relative difference between the expected profile and the measured profile with an RMS value of 0.0187.

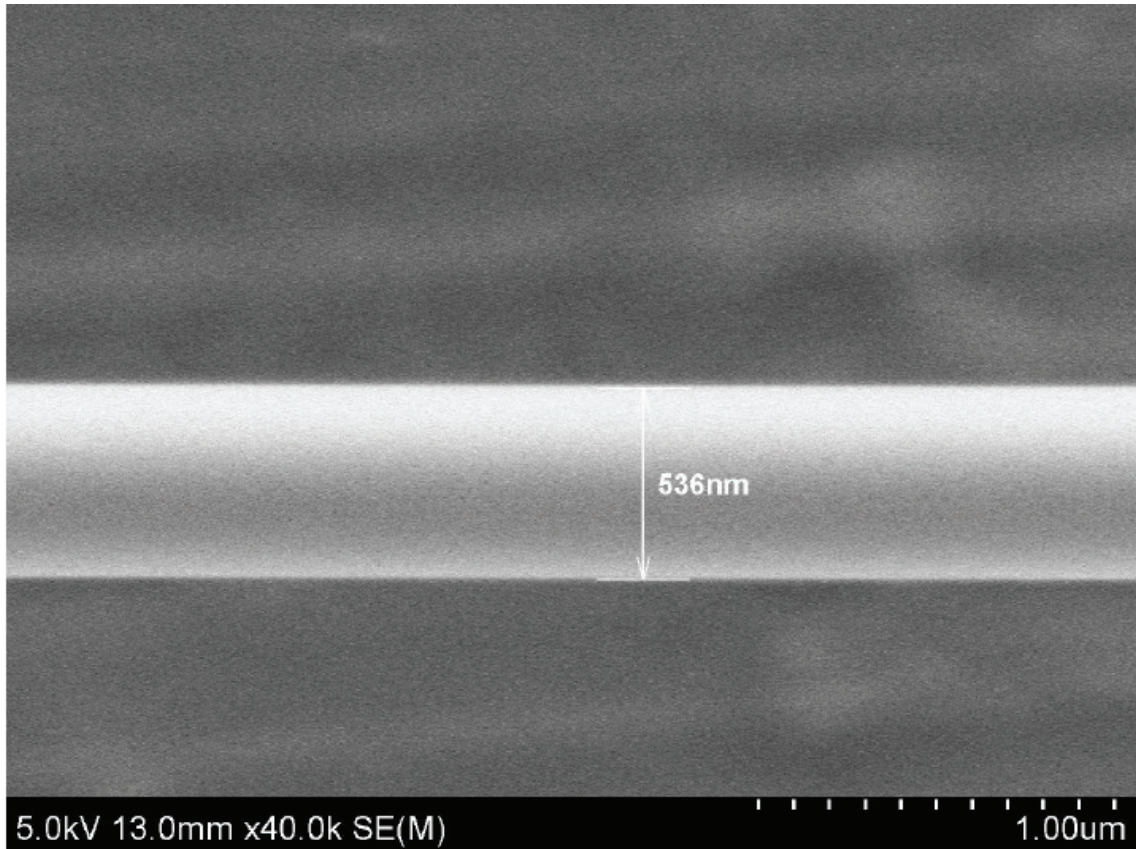


Figure 2.8: A SEM image taken in the Nanoscale Imaging Spectroscopy and Properties Laboratory (NISP) lab at UMD. We measure a radius of 536 ± 12 nm, the intended diameter of the waist is 500 nm. In order to image the fiber we coat it with a layer of graphite.

2.5.2 Transmission

Figure 2.9(a) shows the transmission as a function of time during the pull for an ONF with a 2 mrad angle taper to a radius of $6 \mu\text{m}$ and exponential profile to reach a final waist radius of 250 nm, with a fiber waist length of 5 mm. It achieves a

transmission of $99.95 \pm 0.02 \%$, corresponding to a loss of 2.6×10^{-5} dB/mm when taken over the entire stretch. The error listed in the transmission is the standard deviation. We see from Fig. 2.9 (b) and (c) a histogram of the data ranges we use to find the mean for the average value at the beginning of the pull and the average value at the end of the pull. We obtain a standard deviation of 1.0×10^{-4} for the data in Fig. 2.9 b) and 1.0×10^{-4} for the data in c). This leads to a standard deviation of the final transmission of 2.3×10^{-4} . There are possible systematic errors such as drifts in the amplifier gain, but we expect them to be of the same order or smaller than the quoted standard deviation.

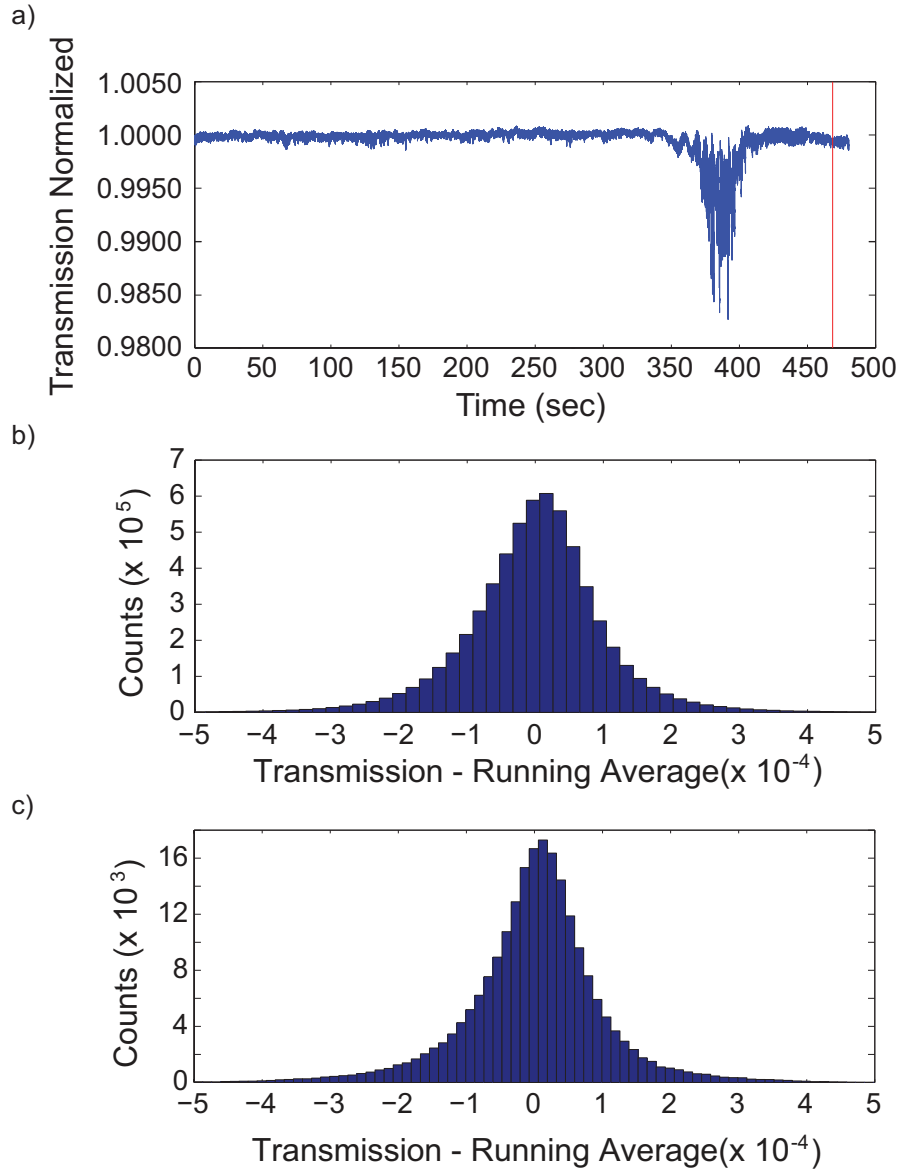


Figure 2.9: a) The normalized transmission as a function of time during the pull through an ONF with an angle of 2 mrad to a radius of $6 \mu\text{m}$ and exponential profile to a final waist radius of 250 nm. The length of the waist is 5 mm. The fiber has a final transmission of $99.95 \pm 0.02 \%$ or equivalently a loss of $2.6 \times 10^{-5} \text{ dB/mm}$. b) Histogram of data taken from the beginning of the pull before higher order mode excitation. c) Histogram of transmission data taken after the pull ended.

The final transmission is determined by taking the mean of the data after the pull ends, delineated by the red line in Fig. 2.9, and dividing by the value of the normalized signal at the beginning of the pull, which we must determine. We take a cumulative average of the transmission from the beginning of the pull until just before any higher order modes are excited, see Sec. 2.5.3. Using this we see that the transmission steadies at 99.95 %. We find this to be a fair method because there is no detectable loss over this range and no beating between modes in the signal since we have yet to excite any higher order modes, and by checking the cumulative average we show that the transmission listed is steady. We also note that this provides a lower bound on the transmission through the fiber.

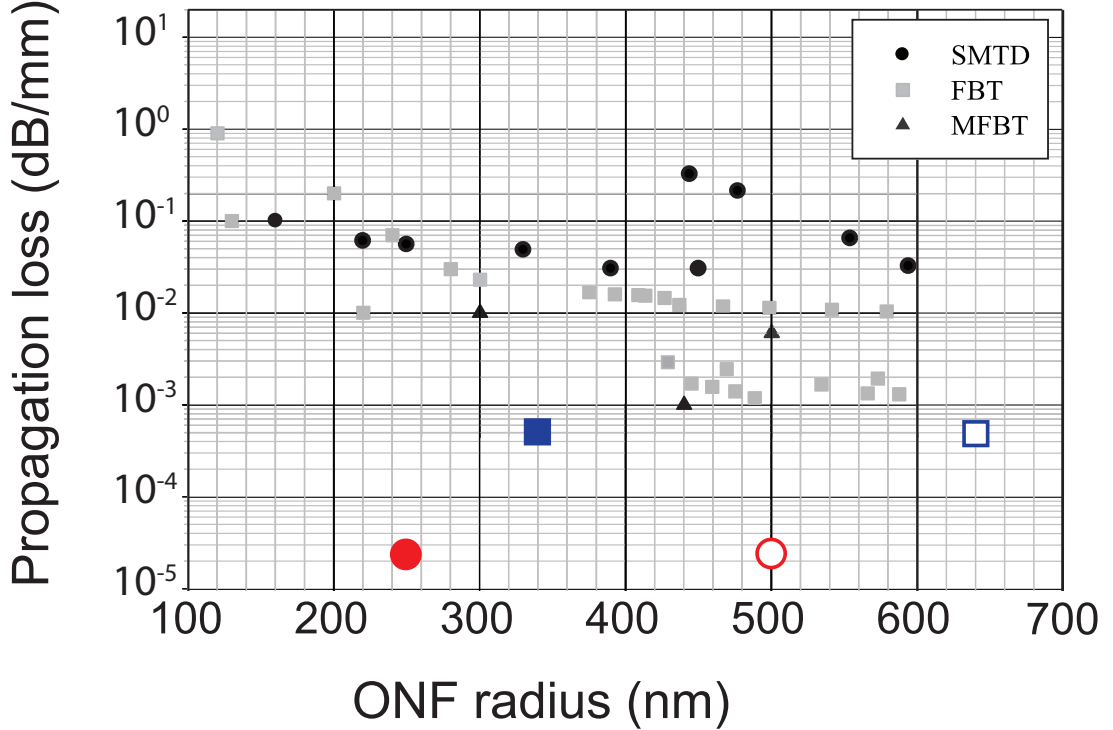


Figure 2.10: Propagation loss as a function of ONF radius as compiled in Ref. [84]

edited to include our results for optical ONF loss in dB/mm. The smaller, solid gray and black squares, circles, and triangles, represent previous results for different pulling techniques: self-modulated taper-drawing (SMTD), the flame-brushing technique (FBT), and the modified flame-brushing technique (MFBT). The solid red circle represents our result for loss when launching the fundamental mode. The open red circle scales the fundamental mode result to the effective radius to compare results with equivalent V numbers at 1550 nm. The solid blue square represents our loss when launching the higher-order modes. Similarly the open blue square scales the result to the effective radius.

Much previous work on high transmission ONFs was focussed on using telecom light at 1550 nm. In Fig. 2.10 we plot the propagation loss as a function of ONF radius for different pulling techniques as compiled from Ref. [84] and references therein. We extend the axes to overlay our results. Figure 2.10 shows that the lowest loss for previous work on the fundamental mode is on the order of 10^{-3} dB/mm at 1550 nm, with final radii of between 440-600 nm. Our result for the fundamental mode has a loss of 2.6×10^{-5} dB/mm when the loss is taken over the entire 84 mm stretch. If the loss is only attributed to the 5 mm waist this corresponds to 4.34×10^{-4} dB/mm. These results mark an improvement of two orders of magnitude over previous work [84, 121, 122]. For higher-order modes pulls, our loss of 5×10^{-4} dB/mm, when taken over the entire stretch, has less than the previous results for fundamental mode launches [84, 121, 122], see Chap 4 for more details. This loss exceeds the expected loss in an untapered fiber at 780 nm by more than an order of magnitude which is given by 3.3 dB/km.

Since the V number is proportional to the fiber radius divided by the input wavelength we compare our results at a wavelength of 780 nm to the results in Fig. 2.10 at 1550 nm by scaling our final radius by a factor of 2. The solid red circle and blue square in Fig. 2.10 represent the actual radius of the pull while the open red circle and blue square are designed to scale our results to equivalent V numbers for inputs at 1550 nm and represent an effective radius. This means our effective final radius for the fundamental mode is 500 nm and for the higher modes 640 nm. This ultra-high transmission is reproducible to better than 1% over time with the same fiber, when following the cleaning and alignment procedure outlined

in Sec. 2.4.

Using a numerical Maxwell's equations solver, FIMMPROP [123], we simulate the expected transmission through a fiber with the same profile as in our pulls. We find the expected transmission to be 99.97% [103], through a *one-sided* taper profile matching the 2 mrad pull depicted in Fig. 2.9, which is consistent with our experimental result that measures the transmission through the entire ONF. Furthermore, when launching the next family of modes through the fiber the FIMMPROP simulations were well-matched to the achieved transmissions [104]. This suggests that we are not limited by imperfections in the pulling apparatus.

2.5.3 Spectrogram analysis

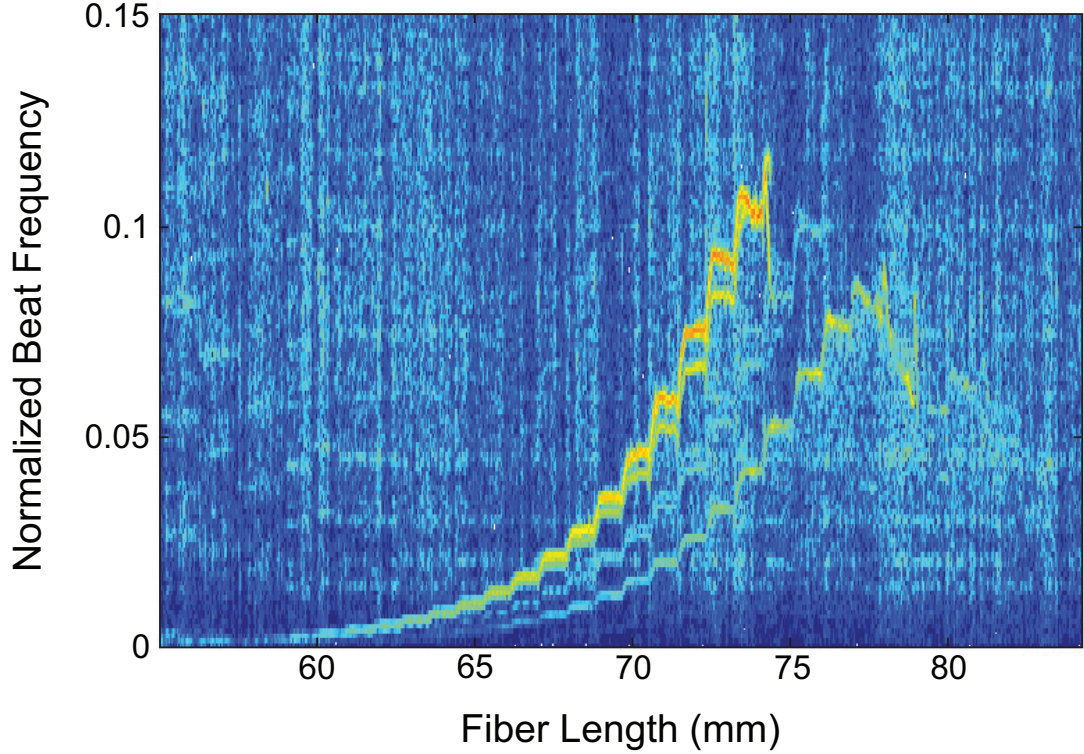


Figure 2.11: Spectrogram of the transmission data from Fig. 2.9. The curves correspond to higher-order mode excitations of the same symmetry as the fundamental mode: EH_{11} , HE_{12} , and HE_{13} .

We analyze the quality of the ONF using a spectrogram, a short-time Fourier transform of the transmission data, also sometimes referred to as the Gabor Transform. The spectrogram allows us to extract the entire modal evolution in the ONF during the pull. Each curve in the spectrogram corresponds to the evolution of the spatial beat frequency between the fundamental mode and excited modes propa-

gating in the fiber, while the contrast corresponds to the energy transferred from the fundamental mode to the higher-order mode. We use simulations to identify all modes that are excited during the pull. A detailed description and full theoretical background, can be found in Ref. [103] and in Chap. 3.

Figure 2.11 is a spectrogram of the transmission data from Fig. 2.9. We see that for a successful 2 mrad pull with SM800 fiber we expect to observe a few higher order mode excitations. If modes are excited that are asymmetric to the fundamental mode, we know the cylindrical symmetry of the fiber was broken during the pulling process [103], which can aid in identifying and fixing the error in the pulling apparatus.

It is worth noting that the modal excitation remains in the family of the same symmetry as the fundamental mode. To the best of our knowledge, this is the first report of modal excitation that remained purely in the symmetric family of modes. Previous work has seen asymmetric excitations to the TE_{01} , TM_{01} , and HE_{21} modes [112,124]. In Sec. 2.7, we demonstrate that such coupling to asymmetric modes can occur for an uncleaned fiber.

2.6 Power Measurements

Once the pull is complete the fiber is transferred to a HV chamber beneath a HEPA filter. Without keeping the fiber in a clean environment the transmission will degrade [102] as dust accumulates on the surface of the ONF waist and taper, which will cause the fiber to break under high optical powers in vacuum due to local

heating [125].

Ion pumps produce small leakage currents that can charge the ONF [126]. To prevent the leakage current from impinging on the ONF, we avoided having direct line of sight between the ion pump and the ONF by placing the ion pump on an elbow. Between the elbow and the ion pump we placed a grounding mesh to prevent the electric field from penetrating past the mesh. With this arrangement a 250 nm radius ONF has withstood the application of more than 400 ± 12 mW from a Ti:Sapphire laser at 760 nm in HV conditions. To the best of our knowledge, this is the highest optical power reported through an ONF.

2.7 Dust studies

We find that the presence of particulate on the optical fiber even before the pull begins can compromise the quality of the ONF: it will degrade the transmission, excite higher order modes, change the modal evolution, and scatter light. If any particulate accumulates on the fiber before the pull, the maximum possible transmission for a given taper geometry will not be achieved. Using FIMMPROP, as described in Sec. 2.5.2, we could estimate the ideal transmission for a given geometry, and if the observed transmission deviates, it could possibly be attributed to a lack of proper cleaning. If the ONF environment is not clean or has a high humidity the transmission will decrease after a pull is finished [102]. Furthermore, if dust accumulates on the ONF surface, the fiber will not withstand high optical powers when the fiber is transferred to vacuum.

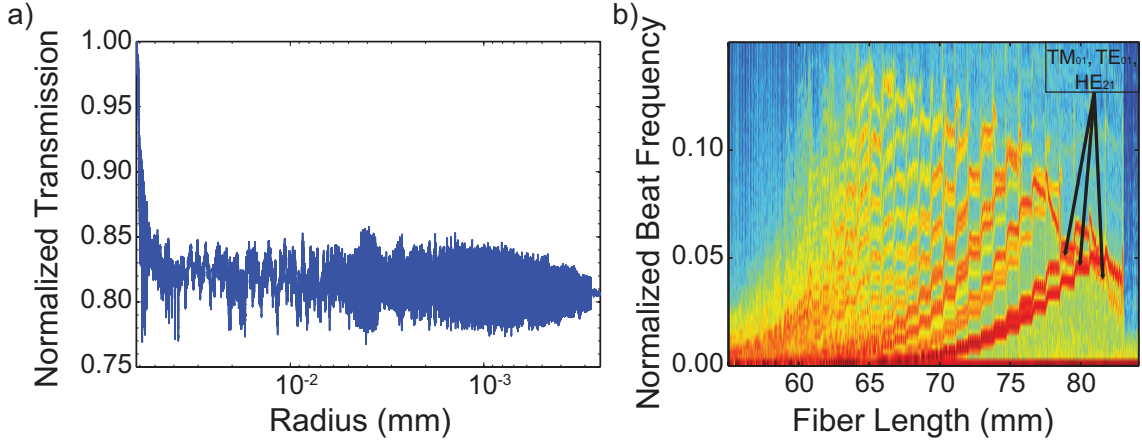


Figure 2.12: (a) Transmission signal for an uncleaned 2 mrad tapered fiber. The transmission of this fiber is 80.50 %. (b) Spectrogram of the transmission data. We can distinguish the excitation of many higher order modes. Of special interest are the curves identified, the asymmetric TE_{01} , TM_{01} , and HE_{21} modes.

We find that if the fiber is not properly cleaned before pulling, the final transmission can vary by a few percent. Figure 2.12 displays the extreme case of mechanically stripping the buffer and not cleaning the fiber at all before pulling. Here, the transmission is only 80.5% for a 2 mrad taper down to $r_w = 250$ nm, leading to more than a 19% loss in transmission when compared to a properly cleaned fiber. The spectrogram in Fig. 2.12 (b) shows excitation to an asymmetric mode: TE_{01} , TM_{01} , and HE_{21} , identified by arrows, that were not present when the fiber was properly cleaned. It is further interesting that there is more energy transferred to these asymmetric modes than any other modes.

Repeating what we stated above, before every pull, we follow the cleaning

procedure described in Sec. 2.4.1. After imaging the fiber, we decide whether or not we should start the pull or restart the cleaning process. We restart if anything is obstructing the light, which we shine perpendicular to the fiber axis, traveling through the fiber reaching the CCD. When there is particulate attached on top of or below the fiber, we use a wipe with methanol and remove it. If there is nothing observable within the resolution of the optical microscope we proceed with the pull. When we do not follow these criteria the reproducibility in the transmission will vary by a few percent from one pull to the next. When we apply this cleaning method, the variability between runs is better than 1 %.

Particulate can come in various forms: remnants of plastic buffer, residue left after the solvent evaporates, or the small dust particulate floating in the air. We believe the most common source to be the buffer. Since we use a mechanical fiber stripper to remove the buffer, micro or macroscopic pieces of buffer remain on the fiber after stripping. We apply wipes to remove the buffer remnants. This removal process can be imperfect because mechanical strippers are not designed to make contact with the actual glass of the fiber. Buffer remnants are a particularly insidious form of particulate because it is a plastic that is generally designed with a higher index of refraction than the cladding to help remove cladding modes. If the buffer remains it may burn into the fiber during the pulling process. This higher index irregularity can lead coupling to higher-order modes.

During the pull we find signatures if the fiber was not properly cleaned. These include a large decrease in transmission and the excitation of higher-order modes. If there is initially loss or beating in the transmission this is a sign that the fiber was

not properly cleaned; this is displayed in Fig. 2.12(a). The fiber starts with a single mode in the core and therefore there should be no beating between modes and negligible losses in the initial pulling process. Eventually the fundamental mode becomes a cladding mode, as the tapering process reduces the effective index of refraction below the index of refraction of the cladding.

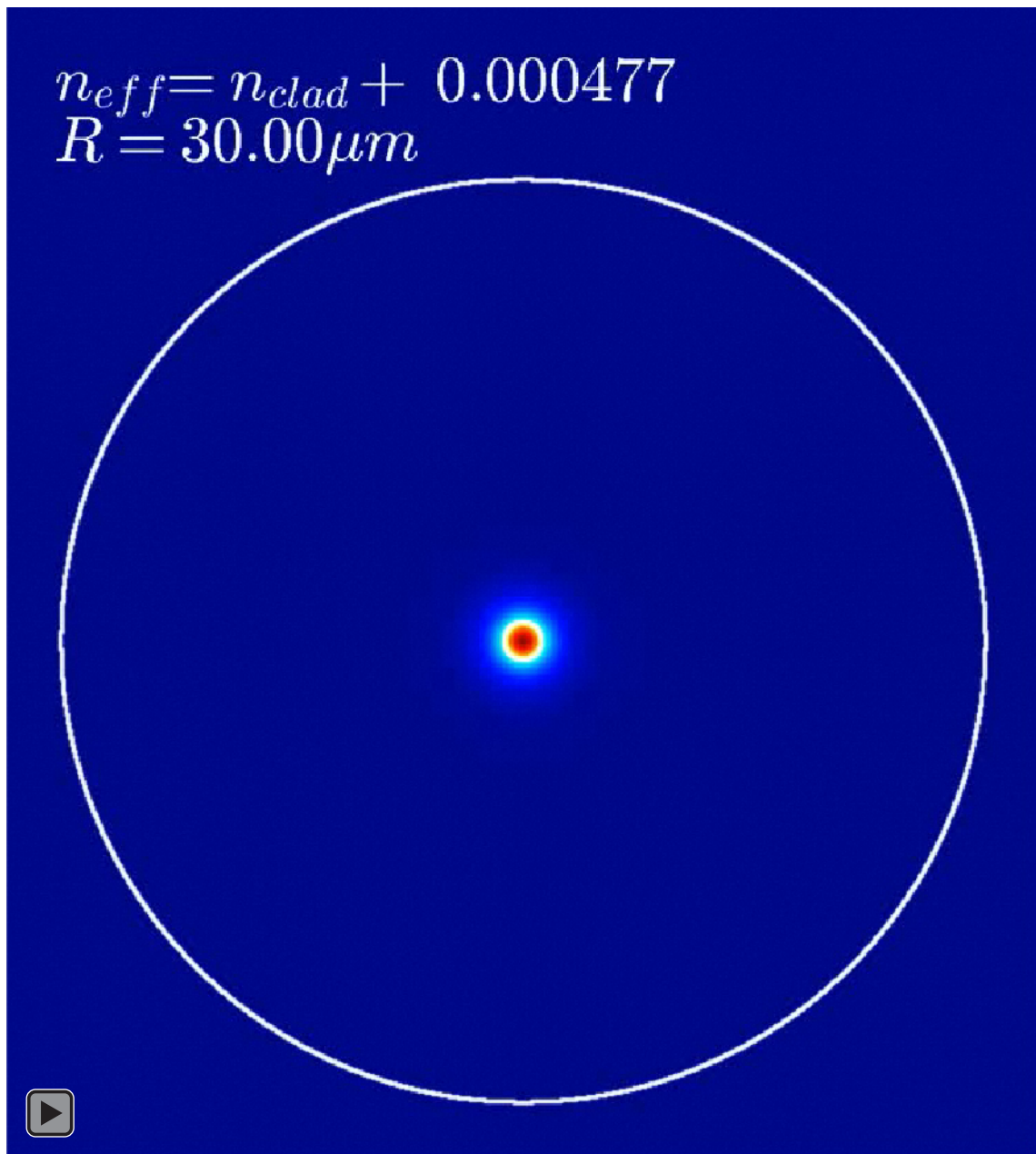


Figure 2.13: Multimedia View showing the transition of the intensity in the fundamental mode from a core to a cladding mode. The intensity of each frame is renormalized to aid visualization. The modes are obtained using the numerical solver FIMMPROP.

As the fiber tapers during a pull and the effective index of refraction of the fundamental mode approaches the index of refraction of the cladding, the mode begins to leak from the core. This is when the fundamental mode can couple to higher-order modes. For the SM800 fiber used in this study, the transition occurs at a radius of $19.4 \mu\text{m}$. Fig. 2.13 show a simulation of the fundamental mode as the fiber tapers. Here, we see that as the radius reduces, the effective index of refraction approaches the index of refraction of the cladding and we can see the mode starts to leak from the core. If the beating between higher order modes occurs before this point, this is evidence that the fiber was damaged. We typically found that an ONF with a 2 mrad geometry, if handled properly, only couples to three higher-order modes: EH_{11} , HE_{12} , and HE_{13} [103]. In contrast we can identify more than twenty excited modes as a result of the buffer remnants in Fig. 2.12(b).

We believe that chemically removing the buffer could be beneficial to the fiber transmission. In principle chemical removal can lead to less mechanical damage to the fiber and complete removal of the buffer. While this is not a critical issue, since our transmission is in good agreement with simulations from FIMMPROP, but it could improve reproducibility and ease the cleaning process. Preliminary tests using acetic acid to remove the buffer were promising.

2.8 Conclusion

We provide the necessary procedures to clean, prepare, and pull an ultrahigh transmission ONF in a reproducible way. The work is validated through microscopy,

and we present the transmission results of a standard 2 mrad pull yielding a transmission of $99.95 \pm 0.02\%$ or loss of 2.6×10^{-6} dB/mm, an improvement of two orders of magnitude for the fundamental mode over previous work. When launching higher-order modes we have losses of 5×10^{-4} dB/mm. The transmission results are in excellent agreement with transmission simulations, suggesting that the limiting factor in transmission comes from a lack of pre-pull cleanliness. The cleaning protocol greatly improves the reproducibility for ultrahigh transmission fibers and produces the first recorded tapers without asymmetric modal excitation. The pre-pull cleanliness is critical to achieving ultrahigh transmission ONFs. These fibers can achieve efficient guidance with short, controllable taper lengths and are usable for various atomic physics applications. During the manuscript writing process we became aware of similar independent work [127].

Chapter 3: Optical nanofiber spectrogram analysis

3.1 Introduction

Understanding mode coupling in an optical waveguide [128] is important for good control of transmission and proper design of optical connections between fibers. This is especially true for tapered optical fibers with sub-wavelength waists, where light propagates in a mode that exhibits a large evanescent component propagating outside the waveguide. ONFs are useful for probing nonlinear physics, atomic physics, and other sensing applications [69, 70, 121, 129]. As the light propagates through the taper, it successively encounters regimes where the fiber is single mode, multimode and then single mode again. Careful design of the tapers can lead to ultra-low loss fibers [130]. Adiabatic tapering criteria give an upper limit on how steep a taper can be, but are too vague for optimization of transmission. Here we are interested in giving quantitative bounds and constraints on the taper geometry.

Using a spectrogram analysis of the transmission signal through the fiber [124], we are able to identify the modes excited during the tapering process and extract the coupling to each of these modes. From this analysis, we show the importance of the geometry control and the fiber cleanliness to reach transmissions as high as 99.95% in commercial fibers at 780 nm. After reaching the cutoff radius, the excited

modes couple to radiative modes [131] and diffract outside of the fiber.

The analysis we describe here provides a full model the electromagnetic field evolution in an ONF. This is crucial for modeling the coupling between light on the ONF and atoms trapped around the fiber [68, 96]. When atoms are trapped in the evanescent field around ONF waist, we will need to know the coupling coefficients between the modes of the field and the atoms to understand the trap depth. This chapter details the modal evolution in the fiber and provides perspectives on the design of even more adiabatic fibers or other control protocols [132], making them usable in extreme conditions [105].

This chapter presents our diagnostics, and characterization on the fabricated ONFS. We first discuss the experimental motivation in Sec. 3.2. Section 3.3 presents the dynamics of the modal evolution in ONFs. We then study in Sec. 3.4 adiabaticity in tapered fibers. Section 3.5 analyzes the transmission signal in more detail. We introduce the spectrogram to analyze the transmission [124] in Sec. 3.6. In Sec. 3.7 we identify crucial elements to improve the transmission. Section 3.8 looks into the other losses present in the fiber. Finally, in Sec. 3.9 is the conclusion of the paper.

3.2 Motivation and construction overview

Controlling neutral atoms with optical dipole traps is a promising approach to implementing of a variety of applications [133]. These traps are based on producing a force from off-resonant interaction between light and atoms in the presence of an intensity gradient: detuning the light below an atomic resonance attracts atoms

to be attracted to the most intense region. This is the same effect used to produce optical tweezers [134, 135]. Applying light above resonance pushes the atoms to intensity minima, which requires more complicated geometries to implement a trap [136, 139–141]. One drawback of optical tweezers obtained by tightly focusing a laser beam comes from diffraction, which limits the trapping volume extension in the axial direction. One solution to this limitation is the use of ONFs [68, 69, 71]. ONFs allow confinement and guidance of trapped atoms over a few centimeters in the axial direction and appear to be well-suited for integration with other devices [88, 96, 142, 143].

3.3 Modal evolution

3.3.1 Modes in a cylindrical waveguide

The theoretical description of electromagnetic modes in a cylindrical waveguide using Maxwell equations can be found in several references *e.g.* [74, 131] and is described in detail in Appendix A. The modal fields vary as $\exp[i(\beta_{lm}z - \omega t)]$ where β_{lm} is the propagation constant of the mode of order (l, m) . Analysis reveals the propagation of light inside a two-layered step index fiber depends on the V -parameter of the fiber,

$$V = \frac{2\pi}{\lambda}a\sqrt{n_1^2 - n_2^2}, \quad (3.1)$$

where a is the core radius, n_1 is the core index of refraction, n_2 is index of refraction of the surrounding medium, and λ is the wavelength in free space. The relation between β_{lm} and the V -parameter is equivalent to the dispersion relation of mode (l, m) .

For our tapers, we can approximate the fiber as a two-layer step index cylindrical waveguide in two regions: At the beginning of the taper, the light is confined to the core and guided through the core-to-cladding interface. In the waist, what was initially the core in the center of the fiber is now negligible ($a_{core} \approx 10 \text{ nm} \ll \lambda$). The light is then guided through the cladding-to-air interface.

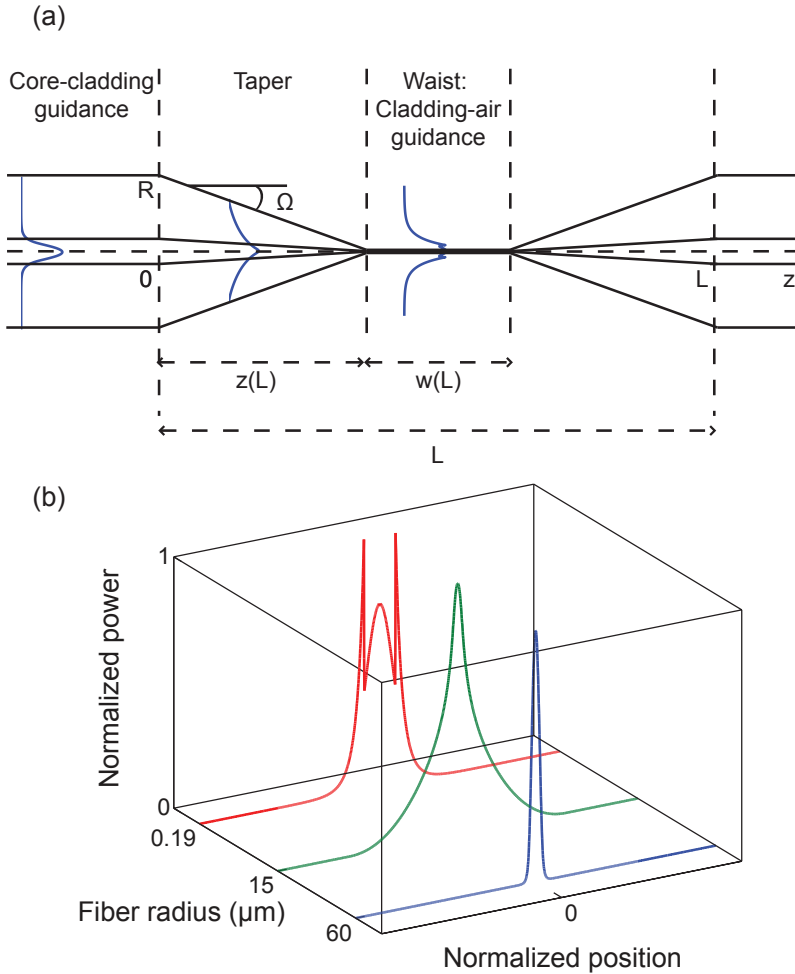


Figure 3.1: (a) Schematic of the stretched fiber. At a given time, the fiber is composed of two tapers and an uniform waist of radius r and length w . The total stretch is equal to L . (b) Calculated intensity profile versus radius for a fiber equal to 60 μm , 15 μm and 190 nm. Note that the position axes are not quantitative, and have been scaled to make the plots visible. The profiles are normalized to their maximum power.

As we continuously decrease the fiber radius during the pull, the fundamental mode leaks from the core to the cladding. In that region, the presence of the core,

the cladding, and the air influence the mode (see Fig. 3.1). A proper treatment has to take into account all of those interfaces. Accordingly, we model our fibers using a three-layered structure, and we calculate the dispersion relations for a series of modes using a commercial fully vectorial finite difference mode solver FIMMWAVE [123]. Figure 3.2 shows a plot of $n_{\text{eff}} = \beta/k_0$ as a function of the radius of the SM800 fiber described in Sec. 3.2.

We pull a SM800 fiber from Fibercore that has a numerical aperture of 0.12 and a cutoff wavelength of 794 nm. Using the Sellmeier coefficients provided by Fibercore, we determine the core ($n_{\text{core}} = 1.45861$) and the cladding ($n_{\text{clad}} = 1.45367$) indices of refraction. The pull is divided into approximately 100 steps, such that the taper is composed of a series of sections small enough to be considered linear, see Chap. 2. Our tapers are generally composed of a section with a constant few mrad taper angle that reduces the fiber to a radius of 6 μm , and then connects to an exponential section that gently reaches submicrometer radii (on the order of 250 nm). The central waist is uniform and its length can be between 5 mm and 10 cm. A pull generally lasts for a few hundreds of seconds.

We are interested in modes that are initially launched into the untapped core and guided by the core-to-cladding interface. Core modes have most of their energy contained in the core, and their effective indices of refraction satisfy $n_{\text{clad}} < n_{\text{eff}} < n_{\text{core}}$. Figure 3.2 shows that the HE_{11} mode effective index is initially greater than $n_{\text{clad}} = 1.45367$ (green curve indicated by an arrow). In typical optical fiber, the step index of refraction between the core and cladding is small. This small change in the index of refraction leads to an approximation to the fiber modes known as

Linear Polarized (LP) modes. Some higher-order modes from the LP11 family, a set of degenerate modes that are composed of the HE_{21} , TM_{01} , and TE_{01} modes, may be accepted in the core, close to the cutoff condition. We note that the fiber cutoff wavelength is 792 nm $>$ 780.24 nm, so strictly speaking, our fibers are not in the single mode regime. Experimentally, we filter higher-order modes that have been launched or excited with a 1.27 cm diameter mandrel, effectively placing us into the single mode regime.

When the fiber radius decreases, n_{eff}^{HE11} approaches n_{clad} . Around the point where $n_{eff}^{HE11} = n_{clad}$ ($R = 19.43$ μm in Fig. 3.2) the core becomes too small to support the fundamental mode. The mode progressively leaks into the cladding to be guided by the cladding-to-air interface. The characteristic length-scale of the waveguide is $R \gg \lambda$, and many modes can be guided by the cladding to air interface ($n_{air} < n_{eff} < n_{core}$), together with the fundamental mode. As long as $R \gg \lambda$, the air has little influence on the effective index of many of the accepted modes ($n_{eff} \approx n_{clad}$ for all the modes shown in Fig. 3.2). However, the effective indices of the modes are so close to each other that the modes interact and exchange energy easily. For that reason, this is the critical region of the taper, where the adiabaticity condition is the most stringent. By symmetry, for a fully cylindrical fiber intermodal energy transfer will only happen between modes of the same family (one color in Fig. 3.2). Energy transfers between modes from different families are a consequence of the azimuthal asymmetries in the fiber.

Further decreasing R , we observe that the modes effective indices approach $n_{air} = 1$. The dispersion curves separate, and adiabaticity can again be easily

achieved. When the index of refraction of a mode reaches n_{air} , the mode is not guided by the fiber anymore and radiates into the air. This radius, specific to each mode, is called its cutoff. The highly-excited modes leave the fiber first, and the number of modes allowed in the waveguide decreases progressively (see Fig. 3.2(c)). Under $0.3 \mu\text{m}$, the only mode that can propagate is the HE_{11} mode, whose index asymptotically approaches 1. The fiber is once again single-mode.

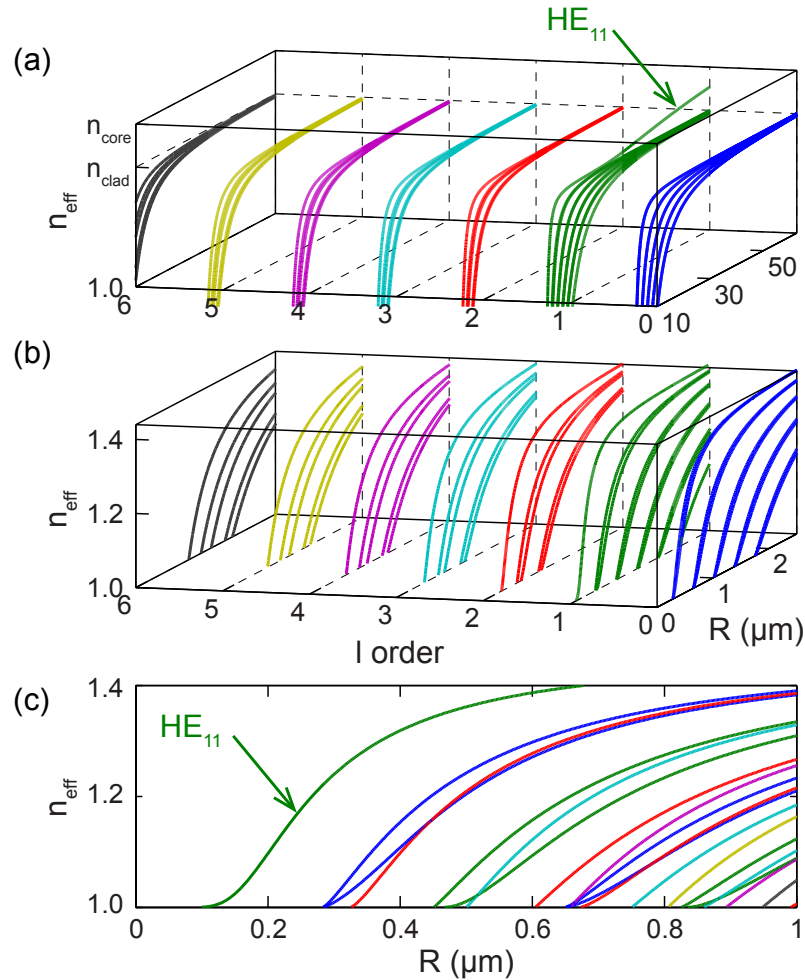


Figure 3.2: Dispersion relations for various modes TE_{0m} , TM_{0m} , HE_{lm} and EH_{lm} ($l = 1$ to 5) as a function of radius calculated for a three-layer model using FIMM-PROP. Here, $n_{\text{air}} = n_{\text{vacuum}} = 1$. We show the first few modes of each family. (a)-(b) Three dimensional representation of the dispersions for different mode families. (c) Plot showing smaller values of R .

3.4 Adiabaticity in fibers

Achieving high transmission in ONFs requires precise control of the fiber taper geometry. This is particularly critical in the part of the taper where the mode escapes from the core and leaks into the cladding before coupling back to the core [107, 131]. High transmission through ONFs is indicative of the quality of the taper section as well as the cleanliness of the fiber during and after the pull [102, 130].

3.4.1 Adiabaticity criterion

The taper geometry determines the mode conversion in a taper. If a taper is too short (taper angle too steep), the mode evolution is non-adiabatic, and we observe a drop in transmission. On the other hand, as the taper is lengthened, the mode conversion is more adiabatic. In the limit of a very shallow angle, the transmission can reach 100%, since all the energy remains in the fundamental mode throughout the evolution.

Following these ideas, we can derive an adiabaticity criterion [131, 137, 138] that relates the characteristic taper length z_t , to the characteristic beating length between two modes z_b . We define: z_t as the length associated with the tapering angle Ω at radius R , defined by:

$$z_t = \frac{R}{\tan(\Omega)}, \quad (3.2)$$

z_b as the beat length between two modes (the spatial frequency of the beating):

$$z_b = \frac{2\pi}{\beta_1 - \beta_2} = \frac{\lambda}{n_{eff,1} - n_{eff,2}}. \quad (3.3)$$

Here β_1 is the fundamental mode propagation constant at radius R and β_2 is the propagation constant at radius R of the first excited mode with the same symmetry as the fundamental mode (EH_{11}). Equation (3.3) relates the beat length to the inverse of the vertical distance between two curves in Fig. 3.2. Mode conversion in a taper is adiabatic when the fiber is long enough: $z_t \gg z_b$ [131]. We note that if the two modes have nearly the same n_{eff} , z_b is large, making the adiabaticity condition more difficult to satisfy. The choice of EH_{11} gives the most stringent condition on the fiber length, as it produces the shortest beat length between the fundamental mode and any mode with symmetry $l = 1$. Nevertheless, this condition remains too vague when one wants to optimize the taper geometry for a given transmission.

Using the dispersion relations from FIMMPROP, we can solve the equation $z_t = z_b$, to find when the taper angles for which the beat length equals the taper length. The blue curve in Fig. 3.3 separates the plane into two regions: in order to be adiabatic, taper angles need to be much smaller than the ones indicated on the curve. Above the curve, the angles correspond to non-adiabatic tapers.

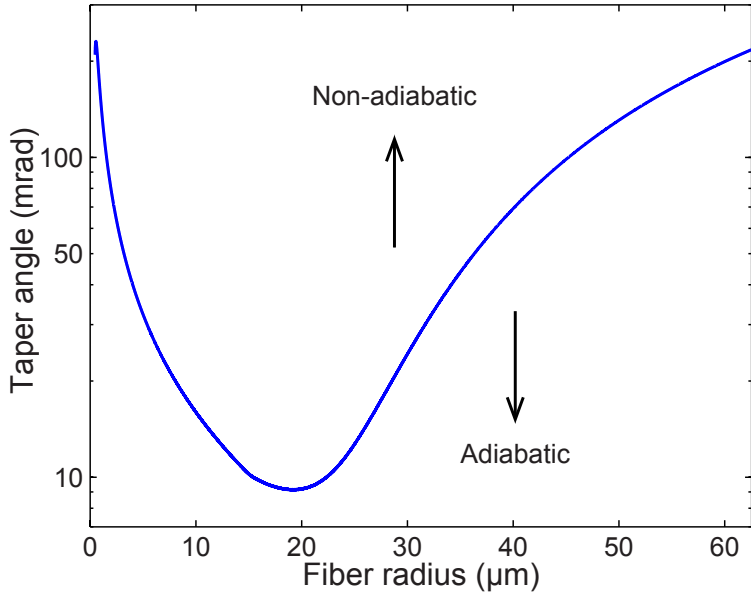


Figure 3.3: Upper boundary for the taper angle Ω as a function of the radius of the fiber set by $z_b = z_t$. Note the logarithmic scale for the vertical axis. The core to cladding diameter ratio for this fiber of 2.535/62.55 is fixed for the entirety of the pull. $n_{core} = 1.45861$ and $n_{clad} = 1.45367$.

Figure 3.3 gives an *upper* limit on the taper angle at a specific radius using the condition $z_b = z_t$ from Eqs. 3.2, 3.3. It does not provide any quantitative information on the intermodal energy transfers for a given taper: calculations in Sec. 3.4.4 show that the angles in Fig. 3.3 lead to large energy transfers. We are interested in producing fibers with high transmissions, greater than 99.90%, and we need to find the optimal geometry necessary to reach a specific transmission.

3.4.2 Transmission of a tapered fiber section

We perform numerical simulations with FIMMPROP to explore the parameter space and find the optimal adiabatic profile for a given transmission. For these numerical studies we assume fiber tapers from a $62.55\text{ }\mu\text{m}$ radius down to a 250 nm radius and use the indices of refraction for our SM800 fiber (see Sec. 3.2). We divide the taper into 32 discrete series of linear sections. At the end of each section we project the output field into the first family of modes (the 15 first modes of family 1) to obtain the transmitted amplitude and phase information in terms of the excited modes. The S -matrix, relating input and output, contains all the mode phases and amplitudes necessary to relate the input and output fields of each section.

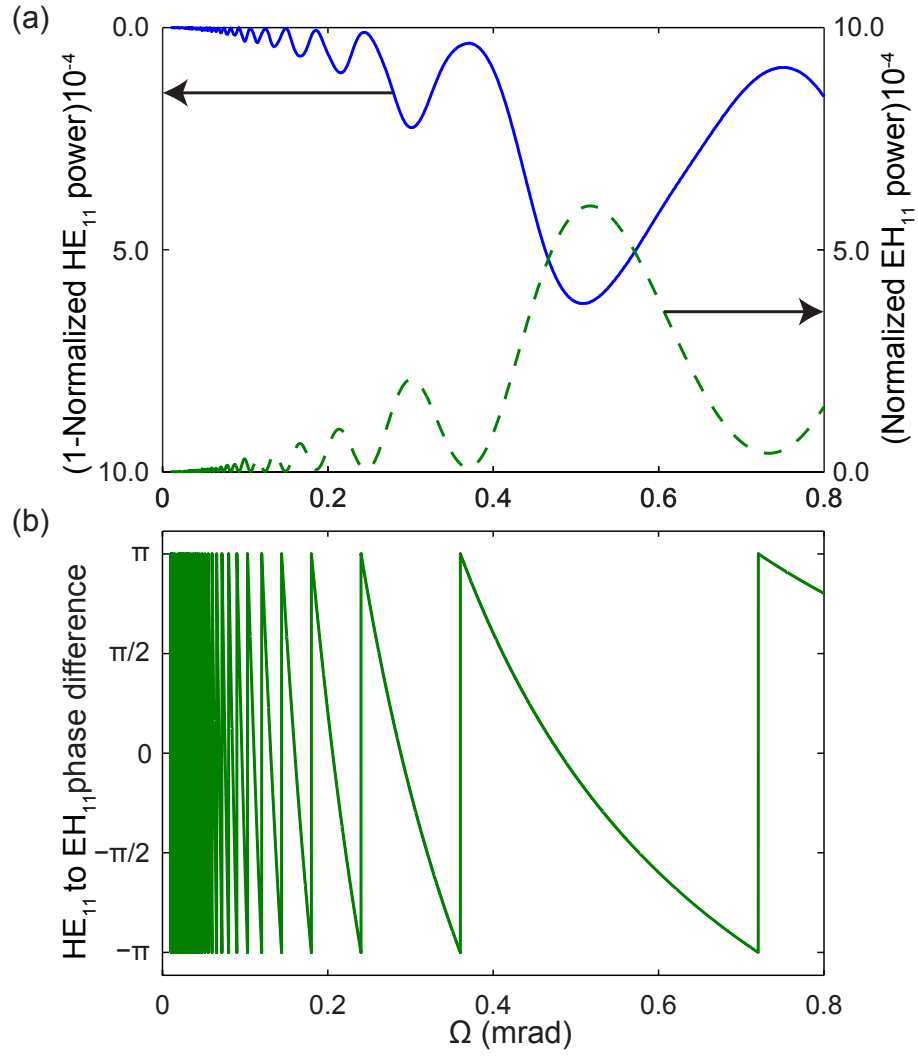


Figure 3.4: Transmission of one section (tapering from 25.5 to 23.5 μ m) as a function of angle when the input is the fundamental mode. (a) Amplitude of the fundamental HE_{11} (continuous blue) and the first higher-order mode EH_{11} (dashed green) (b) Phase difference between the fundamental and the first higher order mode.

Figure 3.4 shows the modal evolution in a tapered section when the input is in the fundamental mode. When Ω is small (or the L is large), the modal evolution is adiabatic and the transmission approaches unity for small taper angles, as seen

in the plot for the normalized power in the HE_{11} mode in Fig. 3.4(a). When Ω increases, some energy couples to higher-order modes, and the fundamental mode transmission decreases. For the small angles considered here, Fig. 3.4(a) shows energy transfer to one mode only (EH_{11} mode dashed green curve). Energy transfer to other modes (HE_{12} mode and higher) is negligible within the resolution of the plot. The oscillations in the transmission are due to modal dispersion in the fiber, which leads to spatial beating: two modes see different indices of refraction and accumulate a phase difference as they propagate through the fiber (see Sec. 4.2 and Chap. 5). The phase accumulation increases and can become large for small angles (or increased fiber length). In the particular situation of Fig. 3.4(b) where only two modes beat together, the EH_{11} power reaches a local maximum for phase differences of $2\pi n$, where n is an integer, and local minimum for phase differences of $n\pi$ where n is an odd integer.

The situation is more complex when more than two modes are excited. Consequently, there exist some situations where large intermode energy transfers during the propagation still results in good fundamental mode transmission. Thanks to mode spatial interferences, most of the energy can couple back to the fundamental mode during the propagation. In this case, one relies on interference to reduce the loss of transmission when the taper is non-adiabatic.

3.4.3 Genetic algorithm

To obtain the total transmission T , after calculating the projection on the fundamental mode of the full S -matrix, we find the product of the S -matrices for all the sections. Ideally we want to find the shortest tapered fiber that gives a target transmission. For this task, we use the genetic algorithm function from MATLAB to find an optimal solution. This approach is expected to be efficient for large problems and allows the use of information from previous runs to improve the computing time. This can be contrasted with naive unweighted MonteCarlo methods or other optimization techniques that use deterministic approaches.

We typically use a population size of 500, a crossover probability of 0.7, a mutation probability of 0.025 and a number of generations of 500 as parameters for the algorithm. The genetic algorithm can probe a large parameter space: for each section, we have calculated 1500 S -matrices, and use angles in the range between 10 μ rad and 1.57 rad. We run the algorithm more than 1000 times with different sets of parameters to try to find the global minimum.

3.4.4 Fully adiabatic fiber

We define total transmissions greater than $T = 0.9990$ as a fully adiabatic fiber. In this section, we discuss simulation results on fibers with limited intermode energy transfers during the pull. This means that the power contained in the fundamental mode never deviates much from T at any point in the taper. In this case, the interference between higher order modes plays a minimal role in the final trans-

mission. We note that we benefit from the robustness with respect to variation in parameters that is associated with an adiabatic process. We obtain the most strict condition on the angles that can be used to reach a specific transmission. We run the algorithm with the added condition that the transmission of each small taper section must be greater than the target in the total transmission T . That way, we make sure that the fundamental mode transmission is greater than T at 32 points in the taper. Between those points the fundamental mode power can oscillate, but remains constrained around T , limiting the intermode energy transfers in the taper.

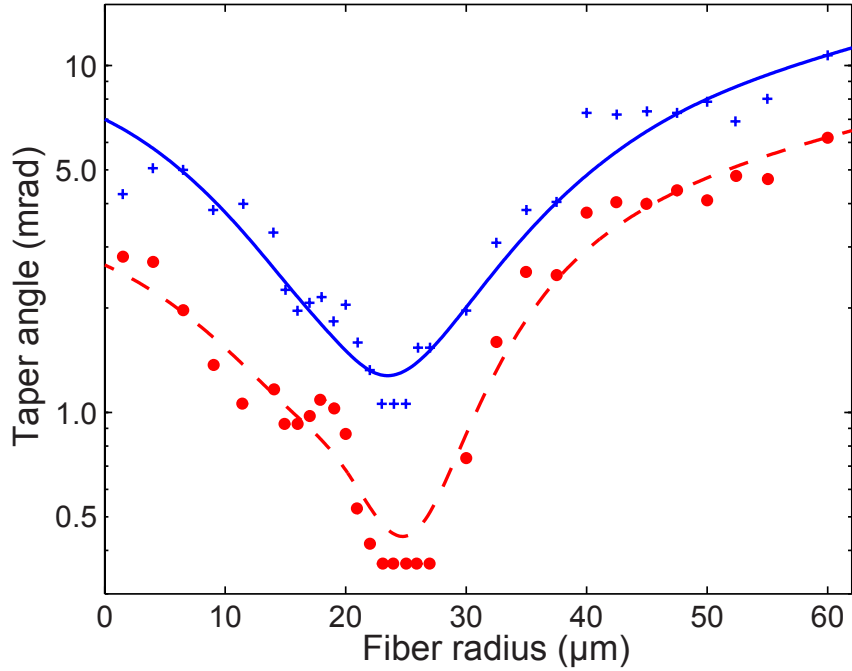


Figure 3.5: Simulation of optimal adiabatic tapers calculated with the genetic algorithm for $T = 99.90\%$ (blue crosses and continuous line) and $T = 99.99\%$ (red dots and dashed line), where the intermode energy transfers are limited. Each marker corresponds to the optimum angle for a section. The lines are guides for the eye.

Figure 3.5 shows results from the genetic algorithm for optimized adiabatic fiber tapers using target transmissions of 99.90% and 99.99%. Here we plot the taper angle as a function of the fiber radius. We observe similar behavior in Fig. 3.3: large taper angles are allowed for large fiber radii, there is a minimum around the transition region at $20 \mu\text{m}$, before the angle increases again at smaller radii. For $T = 0.9999$, the optimal taper in Fig. 3.5 (red dashed curve) shows angles as low as 0.4 mrad , 30 times smaller than the $z_b = z_t$ criteria. The results in Fig. 3.5 give

precise bounds on adiabaticity, with minimum power transmitted to higher-order modes. This last point ensures that this algorithm is insensitive to phase effects: the final transmission is not a consequence of constructive interference between several modes and will be independent of perturbation to the fiber geometry.

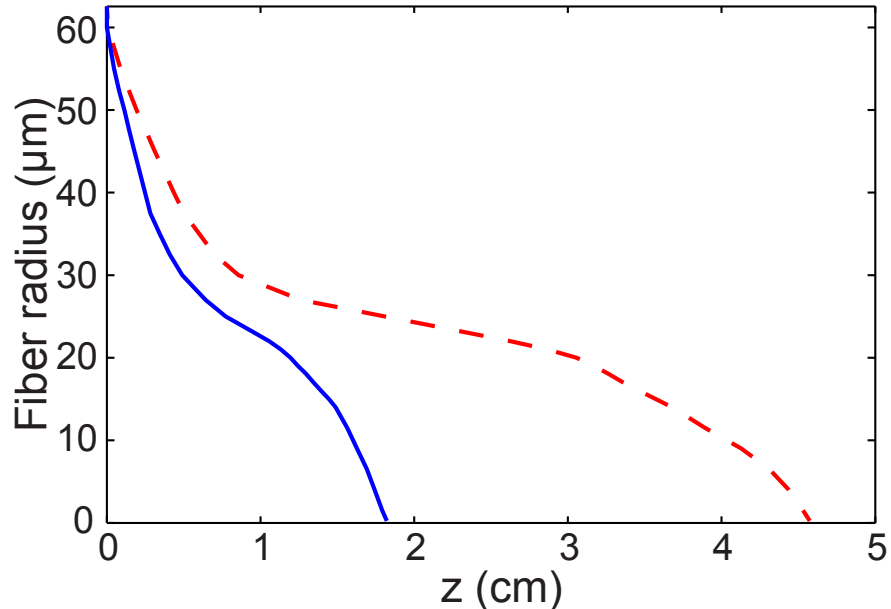


Figure 3.6: Simulation of optimal taper profiles for $T = 99.90\%$ (continuous blue line) and $T = 99.99\%$ (dashed red line). The profiles are only based on the dots from Fig. 3.5 and not on the continuous lines. Note that the horizontal axis scale is in centimeters whereas the vertical axis scale is in microns.

Figure 3.6 shows the corresponding optimized taper profiles corresponding to $T = 0.9990$ (blue continuous line) and $T = 0.9999$ (red dashed line). Strikingly, for $T = 0.9999$ the optimized adiabatic taper is only 4.5 cm long, on the order of typical non-adiabatic tapers lengths produced with a heat-and-pull method [144]. For example the 2 mrad taper presented in Sec. 3.5 is ≈ 6 cm long and still presents

non-adiabaticities. Note however that in Fig. 3.6, Ω varies continuously as a function of z , and can be large at the beginning of the pull. Experimentally, we show below (see Sec.3.7) that abrupt variations of Ω during the pull can induce detrimental asymmetries in the taper. With our apparatus, we have precise control of the taper geometry for linear and exponential profiles [144], see Sec. 2.3. Using only a single linear taper section in the same way as above would require a linear taper angle $\Omega \approx 0.5$ mrad, and a substantially increased length. One could chose to use smaller clad-fibers [103] or to chemically pre-etch fibers, in principle allowing shorter adiabatic tapers.

3.4.5 Utilizing non-adiabaticity

Limiting intermodal energy transfers in a taper to arbitrarily small values is possible, but can be impractical due to large taper lengths. An alternative approach consists of allowing large energy transfers, yet reaching high transmissions by careful design and phase control in the fiber. As we discuss in Sec. 4.2, different modes interfere together as they propagate in the taper. Taking advantage of this spatial beating, we can design fibers with particular phase combinations that allow high transmission, despite the presence of non-adiabaticities. In this section, we run the genetic algorithm with only a condition on the final transmission ($T \geq 0.9999$): intermodal energy transfers in each section is no longer limited. Using this non-adiabaticity, it is possible to produce short high-transmission tapers.

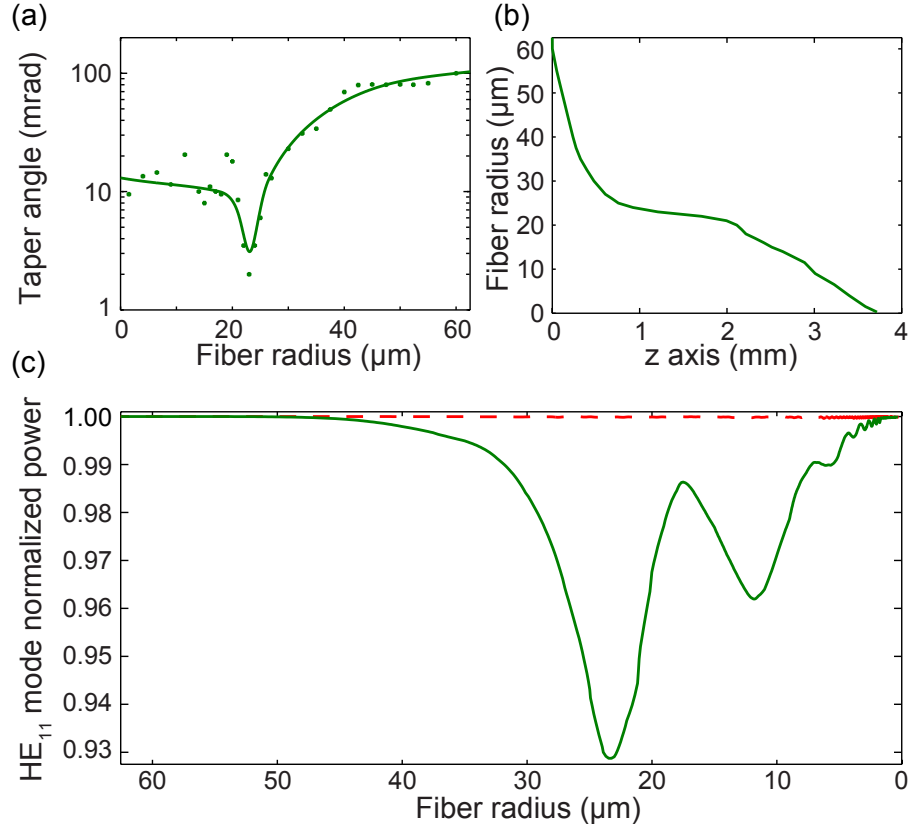


Figure 3.7: Simulation of fiber profile for 99.99% transmission with optimized length given by the genetic algorithm. (a) Taper angles and fiber radius, squares are from the simulation and the continuous curve is a guide for the eye. (b) Fiber radius and fiber length with a final length of 3.7 mm using the results in (a). (c) Fundamental mode transmission as a function of fiber radius for the optimized adiabatic fiber (red dashed line) and the optimized non-adiabatic fiber (green continuous line).

In this case we use the genetic algorithm to search for the profile with the shortest fiber length that has a 99.99% total transmission in the fundamental mode. Figure 3.7(a) shows that the taper angles allowed here are much larger than the ones presented above in the adiabatic case (Fig. 3.5). At large fiber radii, the taper

angle reaches ≈ 100 mrad. Closer to the transition region, the minimal taper angle can still be as large as 2 mrad. From the the taper angles used here, we know that the fundamental mode is not propagating adiabatically in this taper. Figure 3.7(b) shows the corresponding profile. Figure 3.7(c) shows the simulated transmission for this fiber as a function of position for a total transmission of a 99.99% (green continuous curve). This fiber would have a 3.7 mm length, a factor of 12 shorter than in the adiabatic case (red dashed curve) calculated using FIMMPROP. This greatly reduces the length requirements for high-transmission fibers, which could be useful for our application.

In the optimized adiabatic case (red dashed curve Fig. 3.7(b)), we confirm that the power contained in the fundamental mode is close to 99.99% throughout the taper. Higher-order modes excitations are negligible, and the evolution is adiabatic. However, for the non-adiabatic simulation (green curve Fig. 3.7(b)), we observe large energy transfers to higher-order modes. Around $R = 23 \mu m$, more than 7% of the energy has been transferred to higher-order modes. However, using this particular geometry, the resulting phase combinations lead to high-transmission in the fundamental mode.

The fact that non-adiabaticity can lead to high-transmission with shorter tapers is potentially useful for taper design. However, exploiting non-adiabaticity requires paying close attention to the geometry because there is sensitivity to the phases of the modes: deviations from the calculated profile might lead to situations where mode interference causes large losses, with less energy ending in the fundamental mode than initially expected. One would need to reproduce the calcu-

lated geometry as accurately as possible. As discussed above, producing the taper in Fig. 3.7 with a continuously varying angle is not the best option for us, due to the presence of large angles and possible experimental asymmetries. Moreover, this particular taper length (3.7 mm) is likely to be too small in comparison to the heating-zone size (0.75 mm in our experiment) to accurately produce such a profile. Our typical profiles start with a linear section (Ω of a few mrad) from 62.5 μm down to 6 μm radius, followed by an exponential section down to 250 nm radius. We calculate with FIMMPROP the HE_{11} mode evolution through such a taper ($\Omega = 2$ mrad) and show that it benefits from non-adiabatic effects, leading to high-transmission.

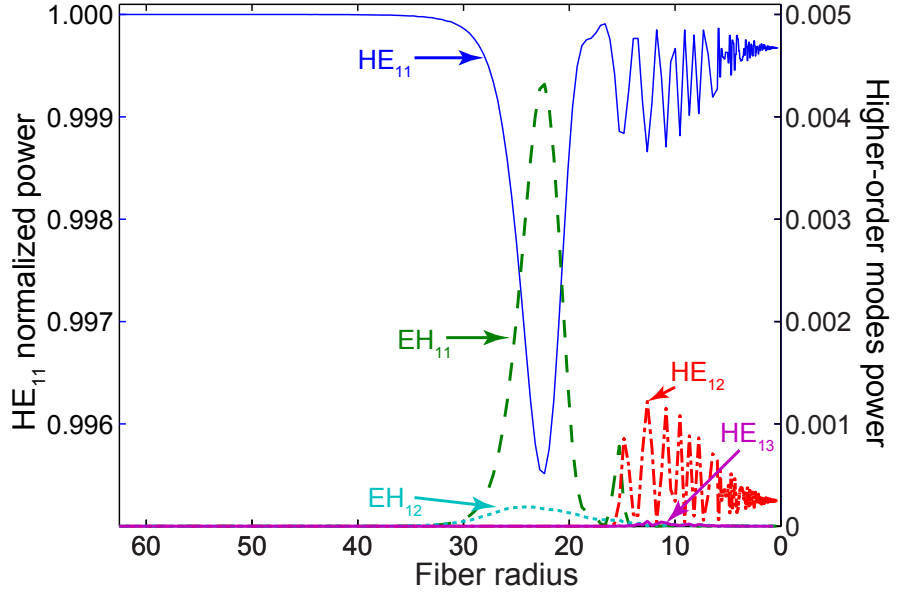


Figure 3.8: Mode evolution for a 2 mrad linear fiber down to 250 nm radius. During the propagation through the taper, some energy is transferred from the fundamental HE_{11} (blue thin continuous line) to 4 higher-order modes EH_{11} (green long dashed line), EH_{12} (light blue dotted line), HE_{12} (red dashed dot line), and EH_{13} (purple thick continuous line). The final transmission through one taper is 99.97% on the HE_{11} fundamental mode.

We start by using FIMMPROP to examine geometries we can produce with good accuracy using our fiber puller. Figure 3.8 shows the transmission of the first few modes of family $l = 1$ through a 2 mrad taper. We create a taper with FIMMPROP that reproduces the experimental profile, which has been validated with microscopy measurements [144], Sec. 2.5.1. Initially, all the power is contained in the fundamental mode. Around $R = 23 \mu\text{m}$, $\approx 0.4\%$ of the energy is transferred to higher-order modes because of non-adiabaticities (up to HE_{13} , the fifth mode

of family $l = 1$). This illustrates that non-negligible higher-order mode excitations can be observed below the $z_b = z_t$ limit (the taper angle $\Omega = 2$ mrad is at least a factor of five below the $z_b = z_t$ limit everywhere in the taper). Those modes beat together, and by the end of the taper, 99.97% of the energy is transmitted through the fundamental mode. For different taper angles, we observe that our typical tapers benefit from non-adiabaticity (see Sec. 3.5). Although there is still room for optimization, the simplicity of the linear geometry makes it the ideal candidate for our application.

3.5 Analysis of transmission signal

To test the results from FIMMPROP and the pulling algorithm we evaluate the quality of a pull by monitoring the transmission of a few mW from a 780.24 nm laser through a fiber during the pulling process following the setup described in Sec. 2.2.2. Figure 3.9(a) shows a plot of transmission as a function of time for a successful 2 mrad pull. The transmission and incident power fiber outputs are connected to two Thorlabs DET10A photodetectors that deliver a signal to a Stanford Research Systems SR570 low-noise differential preamplifier. A Tektronix DPO7054 digital oscilloscope set on high resolution mode and sample rate of 10-20 ksample/s records the data. The fiber is thinned during the pull, and as its radius decreases, we observe different notable features in the transmission signal. Figure 3.9(b) shows the relation between time and radius for the particular pull of Fig. 3.9(a) calculated using the algorithm for fiber pulling that was validated in

Sec. 2.5.1 with a deviation from the experimental measurements lower than 8% at all diameters.

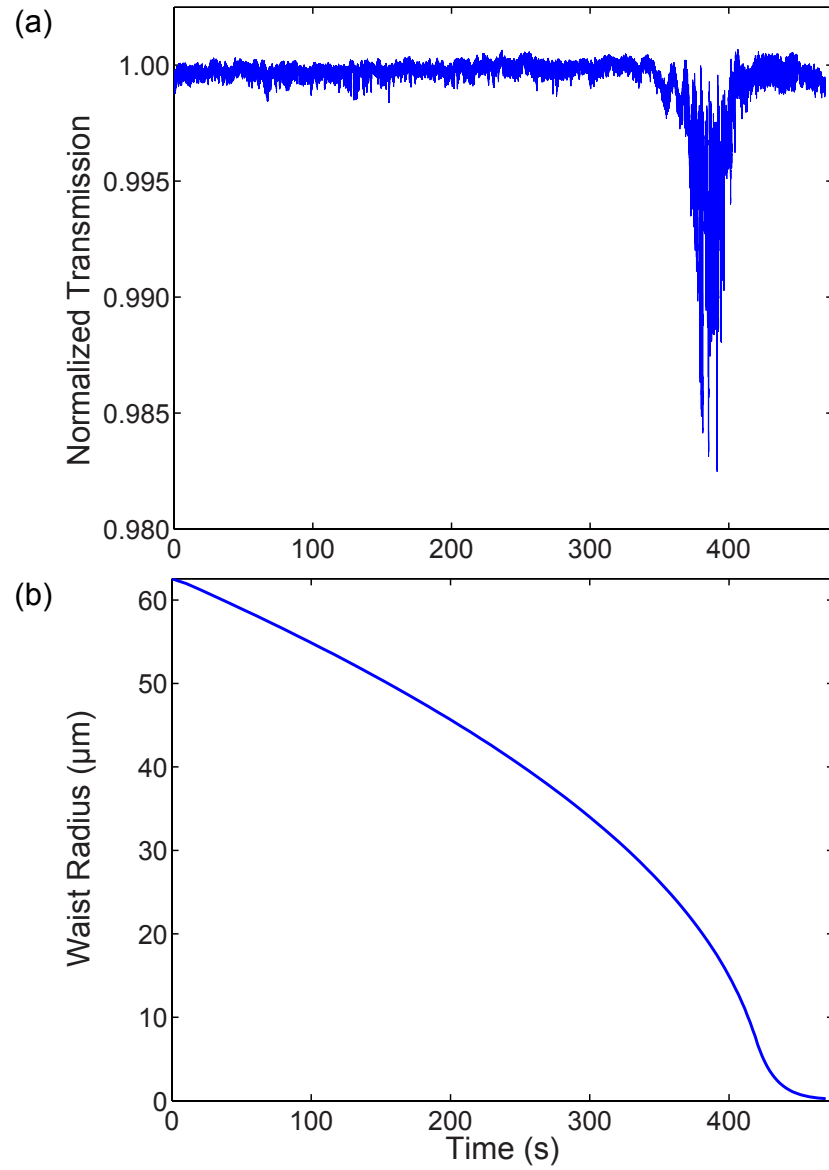


Figure 3.9: (a) Measure transmission through a 2 mrad fiber as a function of time during the manufacturing process. (b) Evolution of the waist radius during the pull, calculated from the algorithm described in [144]. The final radius is 250 nm.

3.5.1 Single mode section

We note that even before we pull the fiber it is not single mode ($V \approx 2.45$) at the light wavelength we use to measure the transmission. However, during the first 100 seconds (down to 25 μm radius), we observe a constant transmission. Thus a 2-mrad taper is completely adiabatic in this region (see Fig. 3.3) and we can conclude that the fundamental mode is confined to the core and does not couple to any other modes.

3.5.2 From single mode to multimode

As the fiber radius decreases, the fundamental mode effective index approaches the cladding index of refraction (see Fig. 3.2). The fiber core becomes too small to support the fundamental mode, which progressively leaks into the cladding to become guided by the cladding-to-air interface. The point where the fundamental mode leaks into the cladding is $n_{eff}^{HE11} = n_{clad}$, at $R = 19.43 \mu\text{m}$. At that point, the waveguide is so large in comparison to the wavelength of the light that the fiber is multimode ($V \approx 170$). The dispersion relation curves of all the modes are close to each other (see Fig. 3.2(a)), and the modes can easily interact. Figure 3.5 shows that the tapering angle has to be smaller than 0.3 mrad in order to be adiabatic in that region. The transmission signal shows mode beating (see Fig. 3.10).

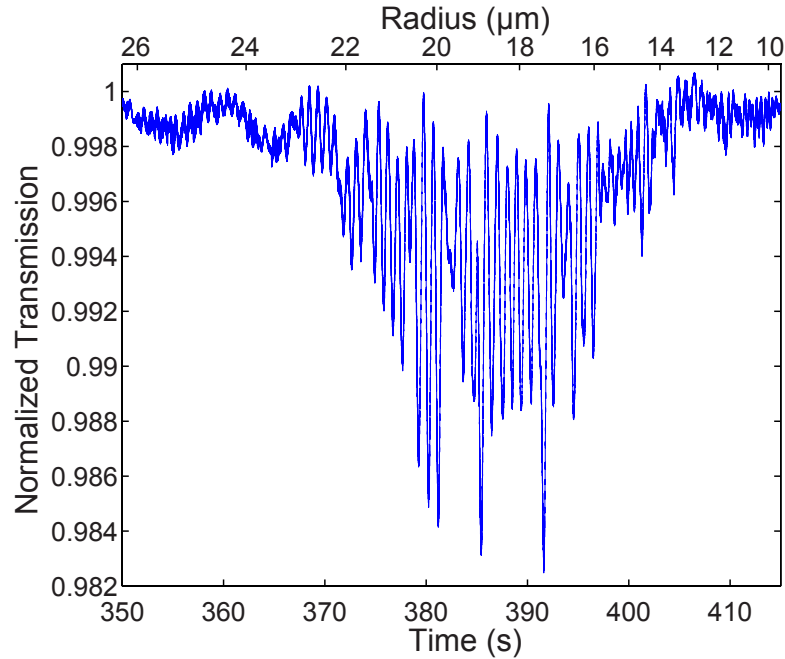


Figure 3.10: Detailed view of the transmission of the 2 mrad pull shown in Fig. 3.9, when the radius of the waist is near 20 μm . We see small oscillations in the transmission signal, due to the beating between the fundamental mode and higher-order modes excited at a radius of 20 microns. The top vertical scale is the fiber radius at the waist.

Energy transfers to higher-order modes occur during the transition from core to cladding because of this non-adiabaticity. For a cylindrically symmetric fiber, such a transfer of energy is only possible from the fundamental mode to other modes of order $l = 1$ (by symmetry). Once they have been excited in the fiber, those modes coexist and propagate together with different propagation constants, given by the dispersion relation curves (green curves in Fig. 3.2). The optical path length inside

the fiber is:

$$(L)_n = \int_{fiber} n_{eff}^n(z) dz. \quad (3.4)$$

According to Eqn. (3.4) different modes will accumulate different phase differences.

The modulation observed in the transmission signal around radius of 20 μm is a signature of the presence of higher-order modes beating together.

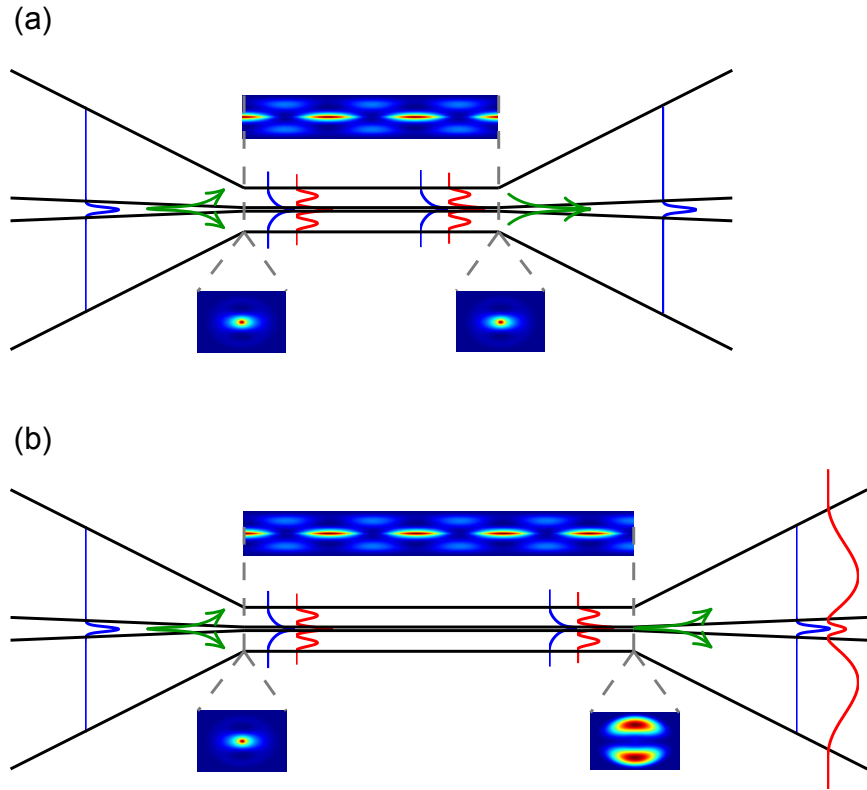


Figure 3.11: Schematic showing modal evolution in the transition region. All the power is initially contained in the fundamental mode (blue profile). When the core of the fiber becomes too small compared to the wavelength, the light escapes into the cladding (green arrows) and some higher-order modes can be excited (red profile). The radius of the waist is equal to $20 \mu\text{m}$, so that the excited modes do not experience any cutoff as they propagate through the waveguide. (a) The length of the fiber is an integer number of beating lengths. (b) Length of the fiber not an integer of beating lengths. The mode profiles were calculated with FIMMPROP.

The beating signal is related to the relative phases when light couples back into the fiber core as the R increases in the second taper. When R reaches $19.43 \mu\text{m}$

in the second taper, energy couples back into the core. Although the two tapers are identical, the presence of beating between modes breaks the symmetry (see Fig. 3.11). Depending on the fiber length, the phase accumulation between the modes leads to a different field distribution entering the core at $19.43\ \mu\text{m}$. The fraction of energy that can couple back into the core depends on the field distribution at this point. If the modes travel through an integer number of beat lengths, the field distribution returns to its initial input. The reciprocity theorem implies that all the energy couples back into the core. If the modes experience a non-integer number of beat lengths, the field distribution is different from what it was initially and only a fraction of energy can couple back into the core: the rest of the energy couples to cladding modes. The cladding light is not detected since we filter the higher-order modes placing a mandrel wrap in front of the detector. At the fiber output, we only observe on the detector the light that coupled back into the fiber core.

3.5.3 Single mode again

As we continue to thin the fiber, the modes' effective indices approach the air index of refraction. When R (equivalently, the V -parameter) becomes small enough, the excited modes cut off and couple to radiation modes in air. On the other hand, the fundamental mode's effective index asymptotically approaches n_{air} without reaching a cutoff. A small enough fiber can consequently be single mode again after all the higher-order modes cutoff. For the SM800 fiber, the single-mode

cutoff occurs at 300 nm radius as we can calculate in Appendix A. After this cutoff, we should not see beating and the transmission should be steady again.

We measure a transmission of 99.950(23)% where the dispersion of the distribution is 5.8×10^{-3} and the dispersion on the mean is 1.2×10^{-5} . Possible systematic effects related to the fiber cleanliness and the detectors and amplifiers long term stability prevent us from giving a better bound than 0.023% to the measured uncertainty in the transmission, but T is close to unity, both in the measurement and in the simulation. Note that the simulation Sec. 3.4.5 looks at the propagation through a single taper. In the present case, light goes through two tapers, supporting one reason why the measured transmission of 99.95% is slightly smaller than the simulated one of 99.97%.

3.6 Spectrograms

Much additional information about the mode evolution during a pull can be obtained from a spectrogram plot. A spectrogram is a local, windowed Fourier transforms of the transmission signal as a function of time. We use the spectrogram function in MATLAB with a window of 8192 points and an overlap of 7000 points.

Figure 3.13 shows an example of a spectrogram found from the transmission data in Fig. 3.9(a)). The modulation in the transmission does not have a single frequency. The frequency is chirped for various reasons. First, the stretch of the fiber is not a linear function of time.

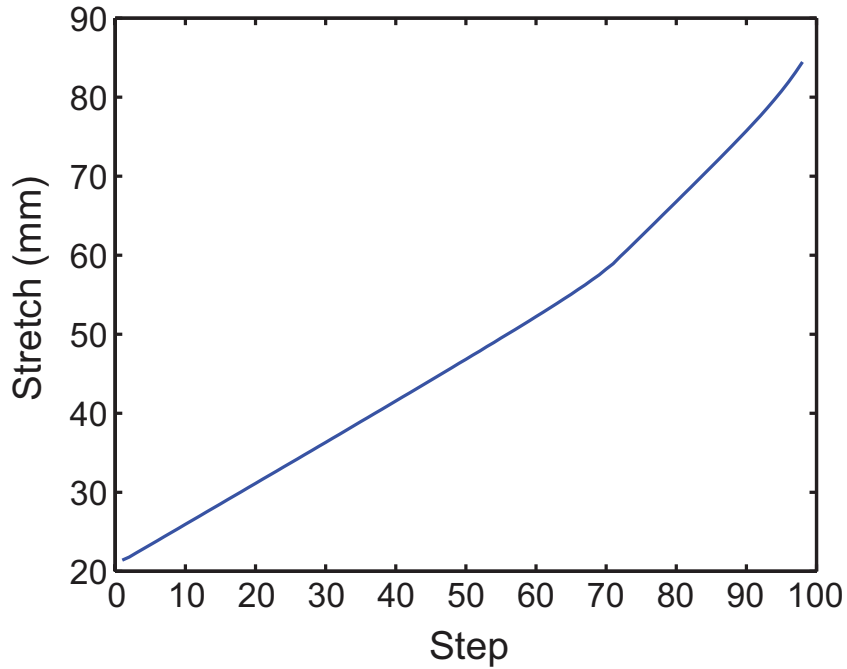


Figure 3.12: Simulation of the stretch as a function of step for fiber sample 1.a.

Fiber sample 1.a has the following properties: $\Omega = 2$ mrad, $L_w = 5$ mm, and $r_w = 250$ nm.

Its form depends on the chosen pulling parameters, and can be calculated using our algorithm, see Fig. 3.12. Second, the propagation constants of the modes are not only radius-dependent but the way they evolve also depends on the mode. The difference between two curves varies as a function of R , which means that the phase does not accumulate at a constant rate.

stretchvssstep.eps

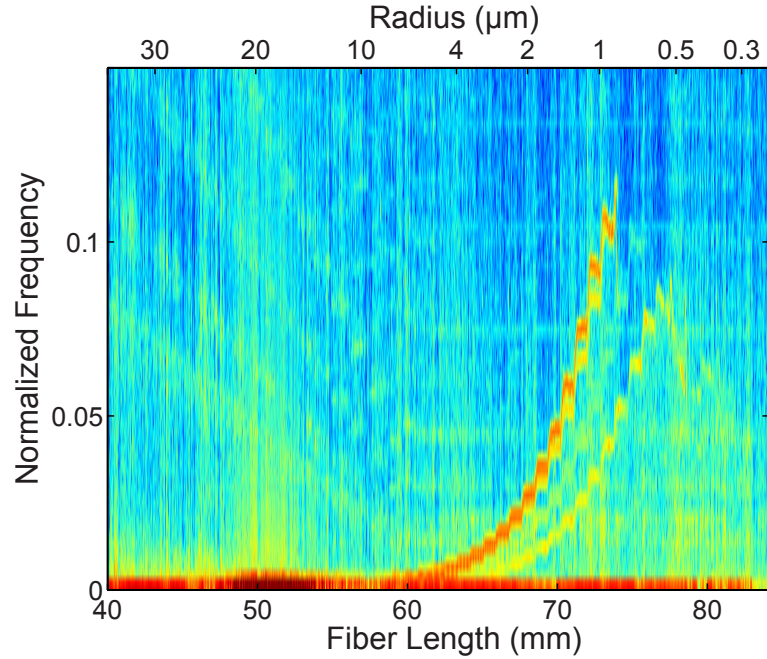


Figure 3.13: Transmission spectrogram of a 2 mrad pull (see the time evolution in Fig. 3.9) as a function of the stretch L of the fiber, showing the chirp of the beating frequency and the abrupt end of the beating. The top vertical scale shows the waist radius calculated from the algorithm. The colormap corresponds to the power spectral density (PSD).

Each curve in the spectrogram signals the interaction between two modes beating at a given frequency. They all appear when the fiber enters the multimode regime ($R \approx 19.43 \mu\text{m}$). The presence of these curves indicates non-adiabaticities in the pull. The curves terminate before the end of the pull, at a point that corresponds to the cutoff of one of the two beating modes. We now have the task to identify which modes are excited, how they are excited, and if there is a way to suppress their excitation. Given the specificity of the phase accumulation for a couple of modes,

it is possible to label the modes excited during the pull and use the spectrogram as a diagnostic to evaluate the adiabaticity and symmetry of the fibers.

3.6.1 Modeling the pull

The phase accumulation between two modes is a function of their optical path length, which depends on the geometry of the fiber at a time t (see Eq. (3.4) above). Let the stretch at a time t be L , then the phase accumulation between two modes is:

$$\Phi_{i,j}(L) = \int_0^L [\beta_i(r(z)) - \beta_j(r(z))] \, dz. \quad (3.5)$$

We can then define the with spatial frequency $K_{i,j}$ [124] due to modes i and j .

$$K_{i,j}(L) = \frac{1}{2\pi} \frac{d\Phi_{i,j}}{dL}. \quad (3.6)$$

Typically we will be interested in the case where mode i is the fundamental mode and we will need to simulate $K_{1,j}$ for higher-order modes.

3.6.2 Identifying the modes

Fig. 3.14 outlines the procedure we use to identify the modes in producing a spectrogram.

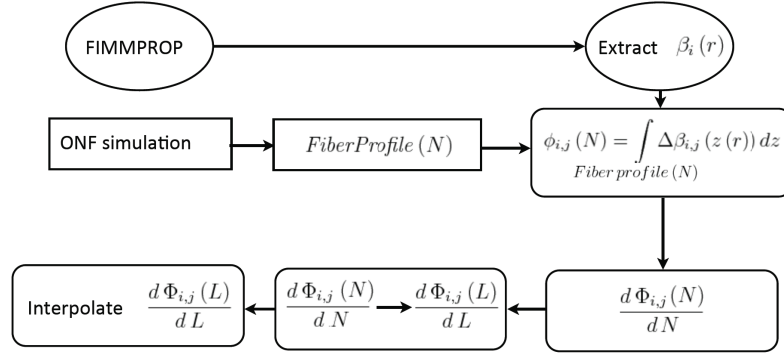


Figure 3.14: Flow chart of the spectrogram outline. Ellipses represented simulations from FIMMPROP. Rectangles are taken from the fiber pulling simulation. Rounded rectangles implies a combination of the two simulations.

We start with the simulated profile at the end of a step from the pulling algorithm described in [144] and in Sec. 2.3, and Fig. 3.15. We use the dispersion relations obtained with FIMMPROP to calculate the differences, $\Delta\beta_{i,j}$, in propagation constants for mode i and mode j .

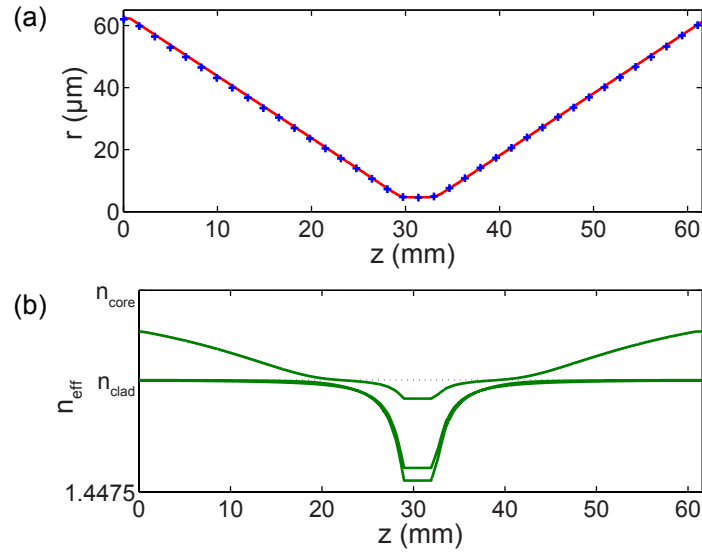


Figure 3.15: a) Simulated taper profile from pulling algorithm. b) Plot of n_{eff} from FIMMPROP as a function of the profile for multiple modes.

By integrating numerically $\Delta\beta_{i,j}(z)$ at each step, we obtain $\Phi_{i,j}(L)$. A numerical differentiation of $\Phi_{i,j}$ with respect to L gives us the evolution of the spatial frequency as a function of step (see Fig. 3.16). From our simulation of the pull, we know the stretch as a function of time, and we can plot the evolution of the spatial frequency as a function of time.

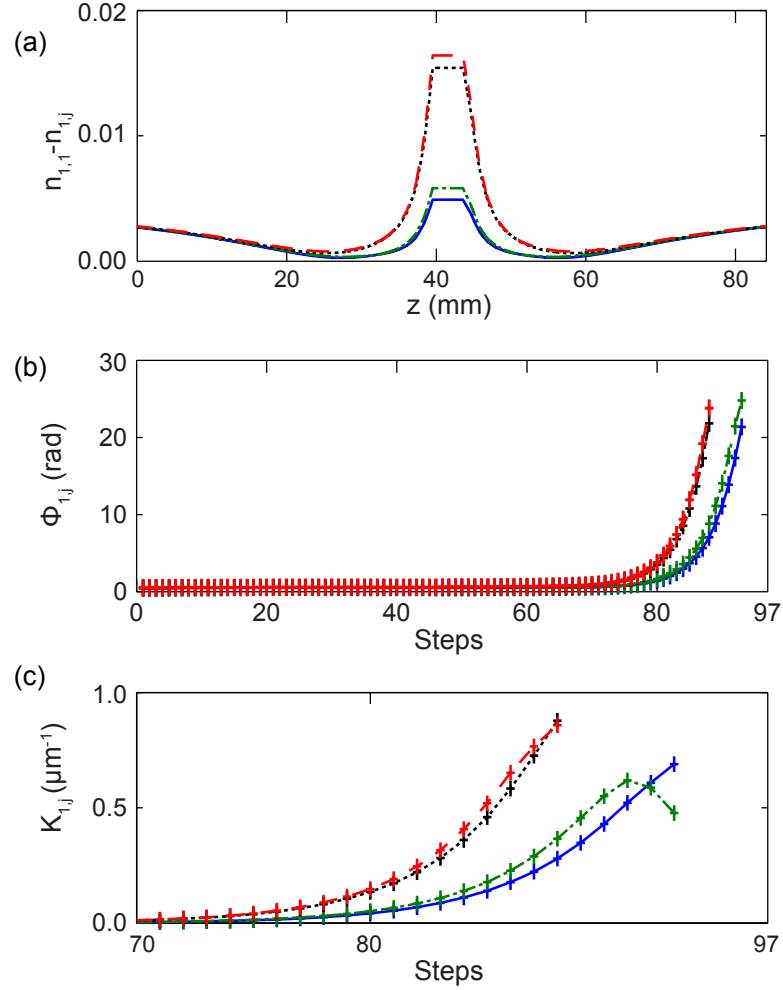


Figure 3.16: Simulation of the differences between the fundamental mode and the first four excited modes of family one for a 2mrad taper profile to r_w of 250 nm.

(a) $\Delta\beta_{1,j}$ as a function of length along the fiber axis (difference between the indices of refraction at step 75). (b) Phase accumulation $\Phi_{1,j}$ as a function of step. (c) Spatial frequency $K_{1,j}$ of the beating as a function of step. The lines (long dashed red, continuous blue, short dash black and long-short dash green) join the calculated points.

We calculate the spatial frequency for a thousand pairs of modes with different

radial symmetry ($l = 1$ to 6) and azimuthal order ($m = 1$ to 20), and we map them on a measured spectrogram, see Fig. 3.17. Using the overlap, we can then identify and label the curves observed on the spectrogram by looking for their overlap with the experimental curves. Figure 3.17 shows excellent matching without any scale adjustments.

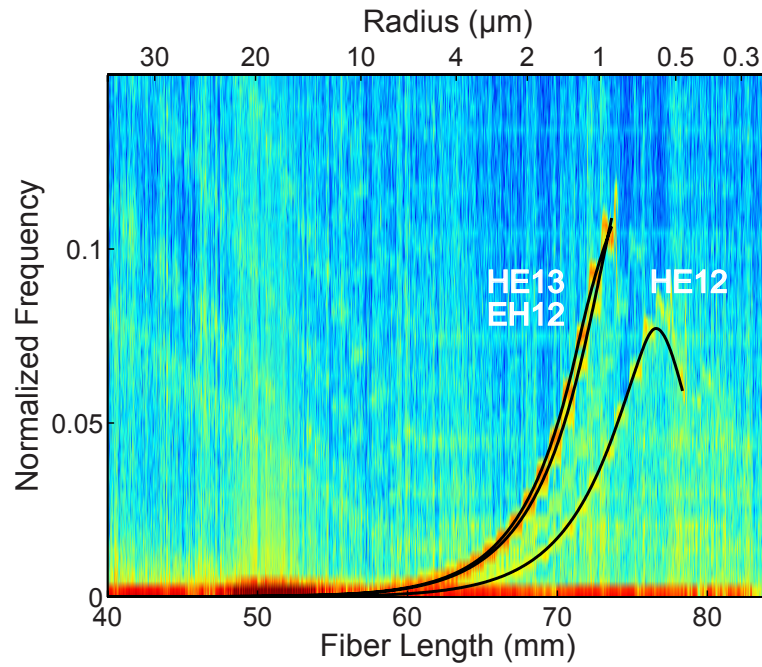


Figure 3.17: Identification of the modes responsible for the beating in the 2 mrad tapered fiber spectrogram shown in Fig. 3.13. Only modes from family one are beating.

We can identify in the spectrogram (2-mrad tapered fiber) the signature of beating between four modes. All those modes have the symmetry $l = 1$ (see Fig. 3.2) as expected for a cylindrically symmetric fiber. We observe higher-order mode excitation up to the fifth mode of family $l = 1$, which is consistent with the simulations

(Sec. 3.4.5). The total HE_{11} transmission is 0.9995, meaning that 0.05% of the energy has been transferred to the other modes. If we assume that all the losses come from the transfer of power to other modes, this power would radiate into the air when those modes reach cut off. The contribution of other losses like Rayleigh scattering are expected to be much smaller. The power spectral density (PSD), which defines the colormap in a spectrogram, gives a representation of how the remaining power is distributed between the higher-order modes as a function of time. By plotting the PSD at different times, we evaluate the power contained in each branch contributing to the beating. Below $R = 4 \mu\text{m}$, those contributions are almost constant, and the higher-order mode relative power is distributed as follow: $5.5 \pm 0.5\%$ in HE_{12} , $9 \pm 0.5\%$ in EH_{12} and $85.5 \pm 0.5\%$ in HE_{13} . Note that we only resolve the beating between the fundamental mode and one excited mode. The beating between excited modes exists, but this second order effect is too weak to be visible in the spectrogram.

3.7 Applications of the quality of the pull

We can use the spectrogram analysis to design and diagnose its quality while pulling a fiber. The number of modes excited and which modes are excited give us information about the adiabaticity, asymmetries and the quality of the fiber after the pull.

3.7.1 Internal parameters: algorithm input parameters

The beating amplitude and higher-order modes excitations seen in Fig. 3.9 and Fig. 3.13 show that the angle of tapering near the critical region at $19.43 \mu\text{m}$, is non-adiabatic. A shallower taper angle around that region could lead to a more adiabatic transition. Following this idea, we study a fiber with a 2 mrad angle until a radius of $20 \mu\text{m}$, and then decrease the angle to 0.75 mrad. After $R = 6 \mu\text{m}$, the pull is exponential down to $R = 250 \text{ nm}$.

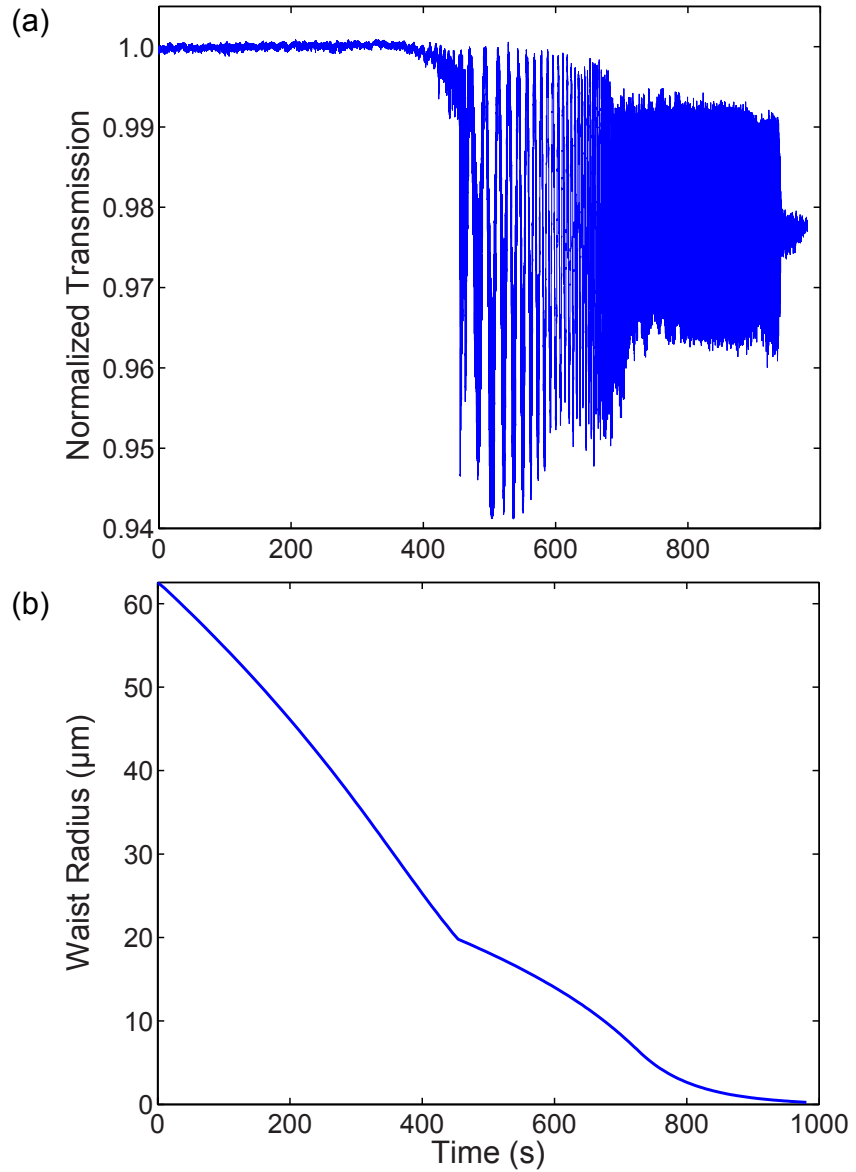


Figure 3.18: (a) Measure of normalized transmission through the fiber as a function of time during the manufacturing process. (b) Evolution of the radius of the waist during the pull. Based on the algorithm, we initially taper the fiber with a 2 mrad angle until a radius of $20 \mu\text{m}$; the angle changes to 0.75 mrad until the radius of the fiber is equal to $6 \mu\text{m}$, where the radius exponentially decreases down to 250 nm.

We see that the transmission at the end of the pull is only 97.850% from

Fig. 3.18. This corresponds to a transfer of energy to the higher-order modes larger than 3%, a factor of sixty worse than in the linear 2 mrad pull (Fig. 3.9). The beating amplitude is much larger than in the 2 mrad case. This is surprising since this pull is designed to be more adiabatic, and simulations with FIMMPROP confirm that we still expect a transmission $T \geq 99.90\%$.

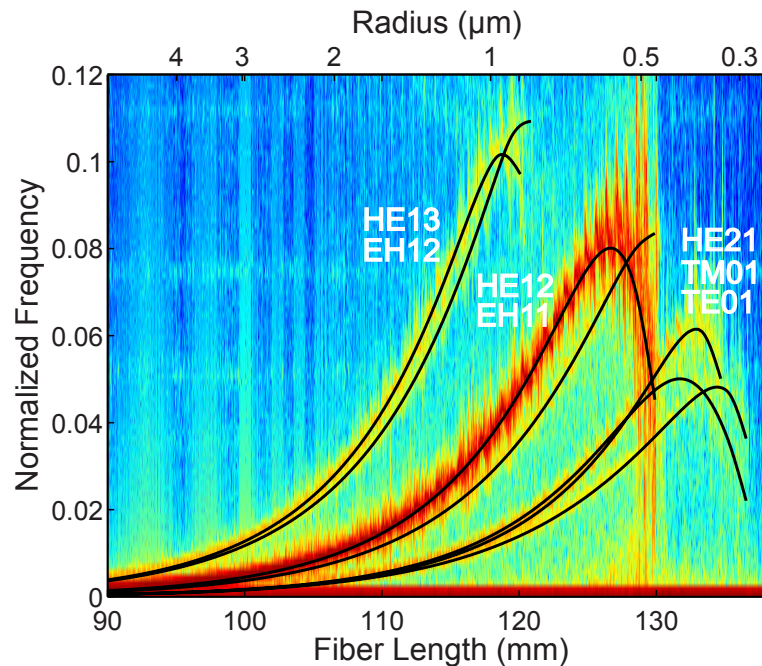


Figure 3.19: Spectrogram of the transmission data shown in Fig. 3.18. The solid black curves are the one given by the simulation. The modes are labeled on the figure. The total transmission in the fundamental is 0.97850. For $R \leq 2 \mu\text{m}$ we calculate from the PSD that the remaining energy is distributed between seven higher-order modes as follow: TE_{01} (0.08%), TM_{01} (0.05%), EH_{11} (0.35%), EH_{12} (0.05%), HE_{12} (98.4%), HE_{13} (0.2%) and HE_{21} (0.87%).

The spectrogram in Fig. 3.19 shows coupling to the TE_{01} , TM_{01} , and HE_{21}

modes, which do not belong to the family of the fundamental mode. The largest transfer is still to the same family, with a different distribution. Coupling to other families should not be observed for a fiber with cylindrical symmetry. This suggests that our multiple angle tapers introduce some asymmetries in the fiber. We imaged the fiber using an optical microscope near the angle change regions (see Fig. 3.20) to further investigate the decrease of transmission.

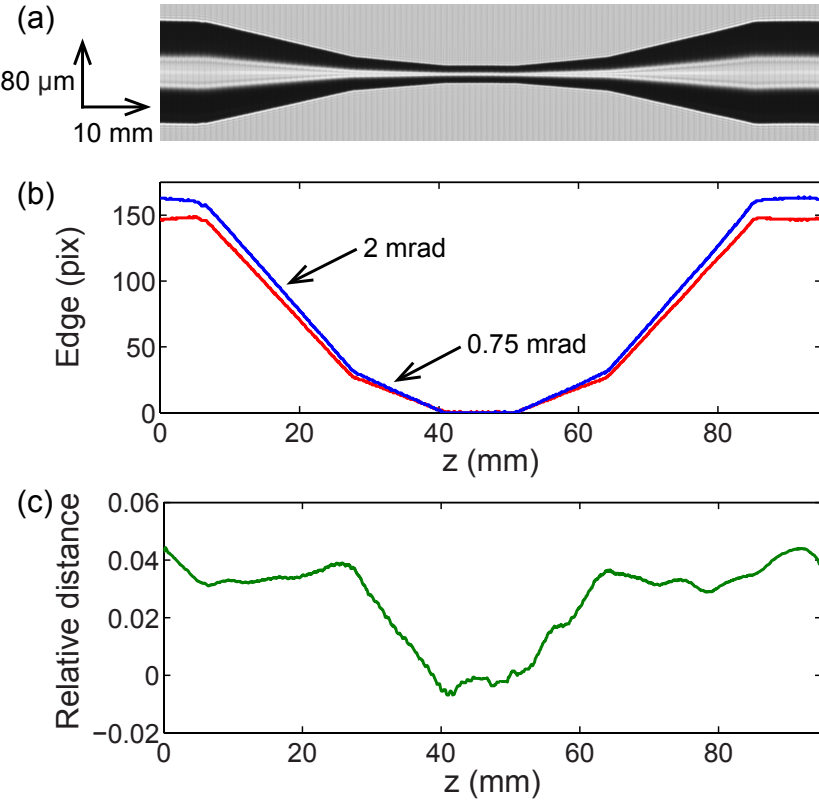


Figure 3.20: Study of the asymmetry of a pulled fiber. The fiber has a $10 \mu\text{m}$ radius with an angle change from 2 mrad to 0.75 mrad at $20 \mu\text{m}$. (a) 100 images taken with an optical microscope stacked and horizontally compressed to enhance any asymmetries. (b) Profile of the bottom edge (blue curve) and top edge (red curve) of the fiber. The abrupt change in angle at $20 \mu\text{m}$ introduces an asymmetry at this radius. (c) Relative difference between the two edges (normalized by the diameter of the fiber) as a function of z .

Figure 3.20 shows that the bottom angle of the fiber exceeds the top angle. Although the measured diameters are as expected, superimposed plots of the top and bottom edges show that there are imperfections around the transition. We observe

a peak at the transition radius ($R \approx 20 \mu\text{m}$) in the distance between the edges. We believe that the excitation of higher-order modes at this radius is a consequence of this asymmetry. We do not observe the same imperfection around the transition region for a 2 mrad flat fiber. The abrupt change in angle exacerbates imperfections in the pulling process by introducing some asymmetries. This results further support that single-angle linear tapers are good candidates for our application. Further increasing adiabaticity would require to decrease Ω , leading to large taper lengths. Because of geometrical and handling constraints, we find it ideal to work with 2 mrad tapers. To work with steep and multiple angles might require a smaller flame or a more symmetric heating.

3.8 Understanding the losses

3.8.1 Losses

Understanding the losses in ONFs is important for our future applications [105], see Chap. 1 and Chap. 6, which require knowledge of such photon loss. We identify two main loss mechanisms that contribute to the final losses: coupling to higher-order modes through non-adiabaticities and scattering around the ONF waist [131]. Systematic effects like the presence of impurities on the fiber surface, or asymmetries in the pull, enhance the losses through those mechanisms.

3.8.2 Coupling to higher-order modes

We observe beating in the transmission doing the fiber pulls due to the effect of non-adiabaticities in the taper. The presence of the beats is a signature of energy transfer to higher-order modes. As we reach the single mode regime, the higher-order modes cut off. They can not be guided by the fiber anymore, and they diffract out as radiative modes. In a plane transverse to the fiber, one can observe a characteristic diffraction pattern further supporting that this effect is the most important for the pulls considered in this study.

3.8.3 Rayleigh scattering

Rayleigh scattering is present in any real glass due to local defects and inhomogeneities, leading to scattering of light and attenuation of the transmitted signal [131]. The attenuation coefficient due to Rayleigh scattering for a fused silica optical fiber is small at a wavelength of 780.24 nm. However by imaging a fiber that is carrying 1 mW of optical power, it is possible to directly observe the scattered light. Experimentally, it is particularly visible on the fiber waist, but the resulting attenuation is on the order of 3 dB/km. This is small enough that we could neglect it when discussing profile optimization. Further study of Rayleigh scattering is presented in Chap. 5.

3.8.4 Systematic effects

The transmission varies drastically with the surface condition of an ONF. When the fiber is initially dirty, the spectrogram analysis during a pull shows the excitation of more modes corresponding to more losses, see Sec. 2.7. We attribute this to the presence of impurities on the surface of the fiber at the beginning or during the pull. Particulate on the fiber waist leads to losses through coupling to higher-order modes or scattering. The cleanliness of the fiber is critical before and during the pull. Such imperfections are avoidable by properly cleaning the fiber and imaging the fiber prior to a pull as explained in [144], see Sec. 2.4. All the pulls presented in this work were done after applying the cleaning procedure described in [144], see Sec. 2.4.

3.9 Conclusion

Reaching high transmissions is important for many ONF applications. In this chapter, we described an algorithm for calculating the optimum taper profile and length for a given transmission, or equivalently the optimum transmission for a given taper length. This approach gives more precise bounds for achieving adiabaticity and yields design for a suitable taper geometry. We found that in our experiments, the transition from the single-mode regime to the multimode regime is non-adiabatic, inducing excitations of higher-order modes during the tapering. Having a good control of the taper geometry is crucial for limiting losses and the propagation of different modes during the pull leads to a characteristic beating pat-

tern in the transmission. Plotting the spectrogram of the transmission signal and using a model of the fiber pulling process, we were able to identify the modes excited during the pull. This gives information for the analysis of the quality of a fiber and the understanding of loss factors. This technique can be applied to the manufacturing of even more adiabatic fibers.

Chapter 4: Efficient guidance of higher-order modes

4.1 Introduction

ONFs with a waist diameter smaller than the wavelength of the guided light are currently used for non-linear optics, atomic physics, sensing, and fiber coupling [69, 70, 121]. The intense evanescent field outside of an ONF is particularly interesting for atom trapping and strong atom-photon coupling. Tapering standard optical fiber down to submicron diameters has been a successful fabrication technique for a variety of applications [88, 107, 130, 142, 143], in which transmissions of the fundamental mode of the waveguide reaching more than 99 % have been achieved [122, 130, 144], see Chap 2. Until now, the efficient guidance of higher-order modes has not been observed, due to the ease with which they couple to other modes, leading to large losses. This restricts most work with ONFs to the single mode regime, where the diameter is small enough to only support the fundamental mode HE_{11} [69, 96].

This chapter reports measurements with ONFs using the first excited TE_{01} , TM_{01} , and HE_{21} modes, which have azimuthal, radial, and hybrid polarization states, respectively. Prior work on HOM propagation has shown $\approx 30\%$ transmission of this LP_{11} family of modes [145], with a mode purity at the fiber output of $\approx 70\%$,

which gives a total transmission of only 20 %. Here, by carefully controlling the taper geometry, and by choosing a commercially available 50 micron reduced-cladding-diameter fiber we demonstrate transmissions greater than 97% for 780 nm light in the first excited LP_{11} family of modes through fibers with a 350 nm waist. Furthermore, we present a setup that enables us to efficiently launch these three modes with exceedingly high purity at the output, where less than 1% of the light is coupled to the fundamental mode [146]. We follow the work of Ref. [111] to fabricate the ONFs and use a series of diagnostics during the pull to monitor the quality of the fiber described in Chap. 2 and Chap. 3. We record the total transmission of the light and image the mode exiting the fiber for the duration of the pull. Analysis of the transmission as a function of time for different types of fibers allows us to estimate which modes are excited during the pull as well as their relative energies of excitation through the use of spectrograms [103], see Chap. 3.

These results open the way to efficiently use HOMs in ONFs. Unlike the HE_{11} mode, HOMs experience a cutoff at a finite radius. This allows improved control of the evanescent field extent at large radii, enabling stronger fibers and improved handling characteristics. Our work enables the usage of HOMs for atomic physics applications. In particular, the spatial interference between several of those modes can create unique evanescent field distributions on the waist, providing an easy and self-consistent way to break the symmetry along the propagation axis, suppressing the need to create a standing wave. This is particularly relevant to atomic physics applications for the realization of a one color, blue-detuned and state insensitive trapping potential for atoms [85].

4.2 Mode propagation in an optical fiber

We describe the modes in a cylindrical waveguide using Maxwell's equations in Chap 3 and Appendix A.

The propagation of light inside a two-layered step-index fiber, consisting of a core of radius a and refractive index n_{core} surrounded by a cladding of radius R and refractive index n_{clad} , depends on V , given by Eqn. 3.1.

V plays an important role in our tapers, since the radius, a in Eqn. 3.1, varies enough that the interfaces seen by the modes change as they propagate through the taper. At the beginning of the taper, the light is confined in the core, and guided by the core-to-cladding interface with V_{core} as in Eqn. 3.1, and $n_{clad} < n_{eff} < n_{core}$. At the end of the taper, the core is negligible ($a_{core} \approx 10 \text{ nm} \ll \lambda$) and the light is guided by the cladding-to-air interface with $n_{air} < n_{eff} < n_{clad}$. Between these two regimes, the light leaves the core, and the relevant radius in Eq. 1 becomes R , which is much larger than a . Due to this radius increase, and the large index difference between n_{clad} and n_{air} , $V \gg 1$. The fiber becomes highly multimode, as the number of bound modes is proportional to $V^2/2$ [131]. Maintaining adiabaticity through this transition is critical.

4.2.1 First family of excited modes

Figure 4.1 (a) shows the effective index of refraction vs V for several low-order modes in an ONF. When $V < 2.405$, the fiber supports only the HE_{11} mode. For a typical ONF, $n_{core} \approx 1.5$ and $n_{clad} = 1$. The TE_{01} and TM_{01} modes are allowed

for $V > 2.405$, and the HE_{21} mode is allowed for $V > 2.8$. As long as V remains lower than 3.8, only the four modes mentioned above are allowed. In the weakly guided regime¹, the modes of interest are known as the LP_{11} family. Prior work has emphasized propagation of the HE_{11} mode, where $V \leq 2.405$ [69, 96, 143]. We are interested in selectively exciting and guiding the LP_{11} family through an ONF, in a regime where $2.405 \leq V \leq 3.8$. When expanded to free space, these modes have the intensity and polarization profiles shown in Fig. 4.1 (b).

¹We initially launch into the *actual* LP_{11} family, because at the entrance, the fiber is weakly guided. The taper takes us into the strong guiding regime where the LP_{11} splits into TE_{01} , TM_{01} , and HE_{21} . We will refer to the set of modes (TE_{01} , TM_{01} , and HE_{21}) during the entirety of the pull as the LP_{11} family. This simplifies discussions when referring to the full set of modes, especially in reference to excitations to modes or families with the same symmetry, i.e. LP_{12} for TE_{02} , TM_{02} , and HE_{22} .

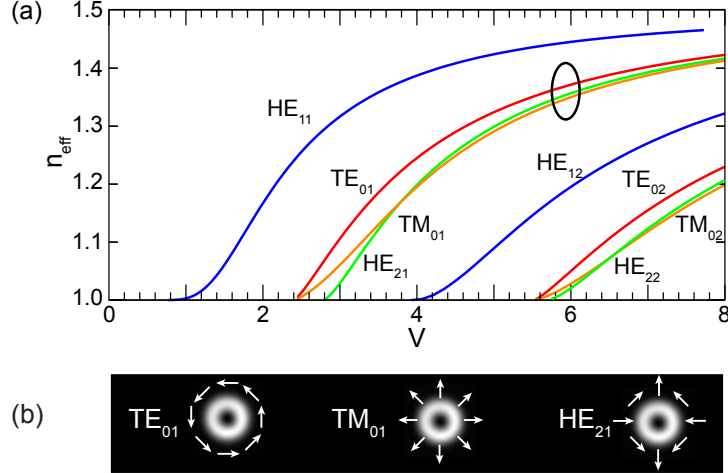


Figure 4.1: (a) n_{eff} indices of several low-order modes in an ONF with $n_{clad} = 1.5$, surrounded by vacuum ($n_{air} = 1$). Below $V \approx 3.8$, two families of modes exist. In this work, we are emphasizing the LP_{11} family (circled). By symmetry, modes in this family can interfere with the TM_{02} , TE_{02} , HE_{22} family, which may be excited through non-adiabatic processes. (b) Intensity and polarization profiles of the LP_{11} family of modes considered in this work.

4.2.1.1 Adiabaticity condition

Using the adiabatic criterion described in Sec. 3.4, we calculate a minimum Ω of a few milliradian for the limiting case of $z_t = z_b$ for the HOMs. This implies that a taper requires sub-milliradian Ω to achieve adiabaticity in the region where light leaves the core of the fiber and becomes a cladding mode. We note that this is a more stringent condition than for the fundamental mode as shown in Fig. 3.3. Therefore, choosing an optical fiber with a small R_i and thus a reduced V_{clad} is highly advantageous to maintaining adiabaticity [145]. Additionally, such a fiber

reduces the overall drawing time, length requirements of the pulling apparatus, and the overall length of the taper.

4.2.2 Experimental setup

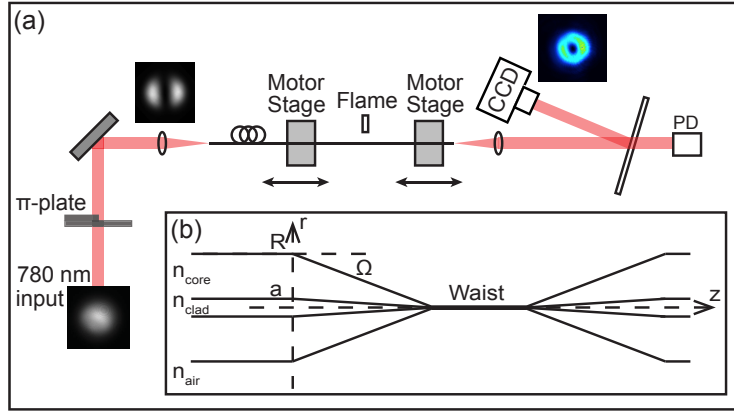


Figure 4.2: (a) Simplified diagram of the experimental setup. A Gaussian beam passes through a π -phase plate and is coupled into the fiber to be drawn. On the output of the fiber, a photodetector (PD) and camera (CCD) monitor the transmission. Typical beam images are shown. (b) Schematic of an OFN.

Figure 4.2 shows a diagram of our experimental setup. Here, we review the mode preparation, the pulling process, and the detection and analysis. We efficiently excite the TM_{01} , TE_{01} , and HE_{21} modes using a fiber-based Cylindrical Vector Beam (CVB) generation method [146, 147]. The fiber is drawn using a heat-and-pull method [111, 116, 144], described in Chap 2. We measure the transmission while pulling, recording simultaneously the output of the photodiode to a digital storage oscilloscope and beam profiles on a Charge-Couple Device (CCD) camera.

A New Focus Vortex laser delivers a TEM_{00} Gaussian beam at $\lambda=780.24$ nm. We spatially filter this beam using a polarization-maintaining optical fiber, and collimate with an asphere to a $1/e^2$ diameter of 630 microns. The Gaussian beam passes through a phase plate that imparts a π phase shift on half of the beam, producing a two-lobed beam that approximates a TEM_{01} free-space optical mode. Fig. 4.2 shows profiles of the beam before and after the phase plate. We couple the beam into the fiber using a matched asphere. The coupling coefficients to the fiber modes are determined by the beam symmetry. The inversion of the polarization over half the incident beam allows us to selectively excite with high efficiency TM_{01} , TE_{01} , and HE_{21} , which have cylindrically symmetric intensity profiles [146]. The fundamental HE_{11} mode is only excited through aberrations in the beam. To achieve efficient coupling into the LP_{11} family, we wrap the fiber with two or three windings around a 4-mm diameter mandrel that attenuates any modes higher than the LP_{11} family. Fig. 4.2(a) shows typical input (black and white) and output (color) modes.

We follow the same ONF pulling process described in Chap. 2 and Chap. 3. To observe all possible mode cutoffs, the fibers are typically drawn to $R \approx 280$ nm, at which point only the fundamental HE_{11} mode propagates. We vary Ω from 0.4 mrad to 4 mrad, resulting in pull times lasting between 100 to 1000 seconds. The output side of the fiber is held straight with no mode filtering. We follow the mode evolution for the duration of the pull by monitoring the transmission of a few mW of laser power through the fiber. The transmitted beam is monitored both by a CCD and by a photodetector (PD). The beamsplitter shown in the figure is tilted to as small an angle as possible to eliminate polarization-dependent reflections. Another

PD, not shown in Fig. 4.2 (a), measures the input laser power during the pull to normalize the transmission signal. We record PD signals with a Tektronix DPO7054 oscilloscope with 16-bit resolution and a sample rate of 1-10 ksamples/s.

4.2.3 Results

We first analyze the improvements gained by choosing a fiber with a reduced cladding radius. Ref. [145] looked at the improvement obtained by reducing the initial R from 125 μm to 80 μm . Moving from 80 μm to 50 μm fibers, we improve the transmission from 10 % to 51 % for a 2-mrad taper. A spectrogram analysis depicts fewer and weaker excitations of higher-order modes. Second, we demonstrate an improvement in adiabaticity through the control of the taper geometry. Our ability to vary Ω allows for marked improvement in guidance efficiency through the ONF, increasing from 16 % at 4 mrad up to 97.8 % at 0.4 mrad.

4.2.3.1 Varying the fiber type

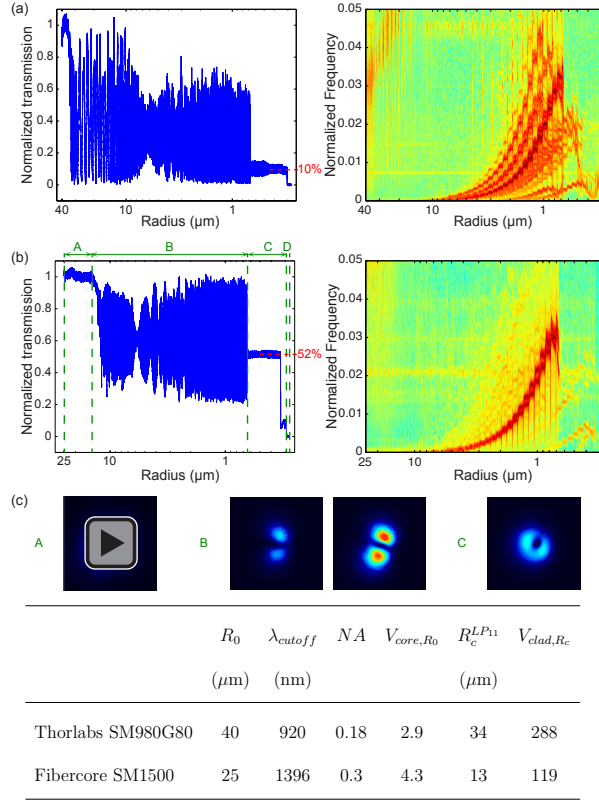


Figure 4.3: Evolution while tapering of the transmission through fibers with a half angle of 2 mrad as a function of the radius of the waist. (a) Fiber with an initial diameter of 80 μm . (b) Fiber with an initial diameter of 50 μm . The spectrograms associated with those transmission curves give a clear picture of the power transfers during the pull. Note the logarithmic scales on the horizontal axis. (c) (1.0 MB) Movie of the evolution of the beam transmitted through the fiber measured on the CCD during a 2 mrad pull of the 50 μm fiber. We record one frame every second, and display them at a 7 frames per second speed. Sections A, B, C, and D are described in the text. The properties of the fibers used are summarized in the table.

4.2.3.2 Transmission measurements

Figure 4.3 shows typical transmissions obtained when exciting the fiber with a combination of LP_{11} modes. We plot the normalized transmission during a single pull as a function of the fiber waist radius. We identify four distinct regimes in Fig. 4.3. The modes are initially confined to the core (regime *A* in Fig. 4.3). Adiabaticity can easily be achieved, and the transmission is steady. Because this fiber initially also supports the LP_{02} and LP_{21} modes and because our launch can weakly excite these modes, we observe a slight drop in transmitted power near $R = 20 \mu\text{m}$, when these modes become cladding modes. Regime *B* occurs after the light has escaped from the core to the cladding. Because the cladding is typically much larger than the core ($R/a > 10$), and because $n_{\text{clad}} - n_{\text{air}} \gg n_{\text{core}} - n_{\text{clad}}$, V increases by over two orders of magnitude ($V_{\text{clad}} \approx 200$). If the core-cladding transition is not adiabatic, modes of similar symmetry are excited. In particular, we observe transfers of energy to the LP_{12} family which contains the modes TE_{02} , TM_{02} , and HE_{22} . The interaction between those modes results in mode beating inside the fiber, and an oscillation in the amount of output light. The oscillations continue to $R \approx 0.7 \mu\text{m}$ (regime *C*), where for a typical silica fiber, $V_{\text{clad}} \approx 6$. From this cutoff location, it is clear that much of the beating behavior is due to the LP_{12} modes which have been excited through non-adiabatic transitions. The pull extends through the TM_{01} , TE_{01} , HE_{21} cutoffs (regime *D*). After reaching the cutoff radius near $R = 290 \text{ nm}$, very little light reaches the photodetector - typically less than 1-2% - indicating low population of the fundamental mode. Removing the phase

plate to restore the HE_{11} mode shows that losses were negligible in our tapers for this mode, meaning that we reach a mode purity of 98-99%. Mode purity is of fundamental importance for ONF applications, and in particular for atomic physics where polarization control and stability are required.

We have compared the transmissions obtained using fibers of diameter 80 μm and 50 μm , and observed the beneficial effects of smaller clad fibers for $\Omega = 2$ mrad. This taper angle is chosen because it is non-adiabatic and highlights the effect of fiber diameter on adiabaticity. The improvement in adiabaticity is clear in Fig. 4.3, with a transmission of 52% obtained for the 50- μm fiber, compared to the 10% transmission of the 80- μm fiber. The table in Fig. 4.3 compares the properties of the 80- μm and 50- μm fibers. Note that the SM1500 fiber initially supports the LP_{01} , LP_{11} as well as the next families of excited modes LP_{02} and LP_{21} ($V_{core,R_0} = 4.3$). These modes are substantially filtered, though not completely, by winding the fiber around a 4 mm-diameter rod. It is worth noting the substantial difference in adiabaticity for the HOMs compared to the fundamental mode. Fig. 2.9 shows a transmission of 99.95% for the fundamental mode with the same 2 mrad taper angle.

Using the numerical aperture (NA) and the cutoff wavelength provided by Thorlabs and Fibercore, we are able to derive using Eq. 3.1 the initial V value V_{core,R_0} , the radius at which the LP_{11} family escapes from the core to the cladding $R_c^{LP_{11}}$ and the corresponding V -number at that radius V_{clad,R_c} for a wavelength of 780 nm. From those numbers, we see that reducing the radius of the cladding allows the LP_{11} family to leak from the core to the cladding at a smaller radius in the fiber. This results in a significantly reduced V_{clad} when the modes escape from the core:

By reducing the cladding diameter from 80 μm to 50 μm , the number of available modes decreases by more than an order of magnitude.

4.2.3.3 Spectrograms

In non-adiabatic propagation, the LP_{11} modes couple to higher-order modes of the same symmetry, belonging to families LP_{1m} ($m \geq 2$). Because they propagate with different propagation constants during the pull, they accumulate a phase difference leading to interference in the amount of light recoupled into the core. Since the photodetector only measures core light, this interference leads to oscillations in the transmission (Fig. 4.3). Plotting the spectrogram of the transmission signal [103, 124], we directly observe the contribution of various pairs of modes in the beating. Fig. 4.3 shows the spectrograms for the 80- μm and 50- μm diameter fiber pulls. Each line in the spectrogram is specific to the beating between a LP_{01} or LP_{11} mode and another mode of similar symmetry excited during the pull. The curve ends when one of the modes reaches its cutoff: the energy is then lost via coupling to radiative modes.

The number of lines observed in a spectrogram is directly related to the excitation of higher-order modes through non-adiabatic processes from a single launched mode: the more lines present in the spectrogram, the less adiabatic the pull is. Moreover, the colormaps in Fig. 4.3 are normalized in such a way that the intensity of each red line gives the strength of the energy transferred. It is clear from Fig. 4.3 that more intense lines are present in the 80- μm fiber than in the 50- μm , further

supporting our observation of more stringent adiabaticity requirements for fibers with a large cladding radius. Improvements could be achieved by pre-etching the fiber to a smaller diameter so that the initial core clad ratio R/a is further reduced.

4.2.3.4 Imaging the fiber output

We monitor the transmitted beam with a CCD, and obtain Movie 1 showing both the core and cladding light as a function of time throughout the tapering process. Using a microscope objective, we first image the end of the fiber to observe the core-guided light (Movie 1 in Fig. 4.3). The movie shows oscillations that result from mode competition, which modulates the amount of light that exits the fiber in the core.

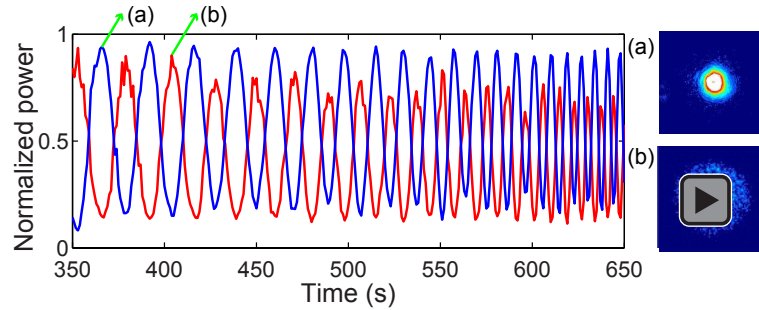


Figure 4.4: Amount of light (normalized) exiting the fiber from the core (blue curve) and from the cladding (red curve). The signals are out of phase, confirming the transfer of energy between modes during the tapering. We observed the two simultaneously by using the two reflections from a thick beamsplitter. (a)-(b) (1.1 MB) Movie 2 shows the evolution of the beam transmitted through an ONF during a portion of a pull, where the power is high enough to observe the cladding light.

Movie 2 in Fig. 4.4 (a) also depicts the transfer of energy from the core to the cladding. We image both the core and the cladding light simultaneously by using strong and weak reflections from a thick beamsplitter plate with an AR-coated front surface. Fig. 4.4 shows the normalized fractions of energy exiting the fiber from the cladding and from the core. The two signals are out of phase. We note that the sum of the energy contained in the core and the energy contained in the cladding does not add up to the total energy input in the fiber. Outside the taper region, cladding light becomes highly scrambled and lost through the fiber buffer, resulting in both the speckle observed in Movie 2 and the reduced total transmitted power. Residual cladding light is spatially filtered from hitting the photodetector, so that the observed oscillations Fig. 4.3 are due only to core-guided light.

4.2.3.5 Varying the angle

The measurements in this section use the reduced-cladding Fibercore SM1500. For this fiber, the LP_{11} modes transition to cladding modes near $R = 13 \mu\text{m}$. By using a reduced-diameter fiber, we observed a drastic improvement of the transmission of the LP_{11} modes. To further improve the adiabaticity, it is necessary to look into more details of the tapering process itself. We have lowered Ω to improve the transmission over what is observed in the previous section. Fig. 4.5 shows the results of draws using $\Omega = 4, 2, 1, 0.75$ and 0.4 mrad . Although each plot shows the same qualitative behavior as described for the 2-mrad pull, the strength of the features depends on Ω .

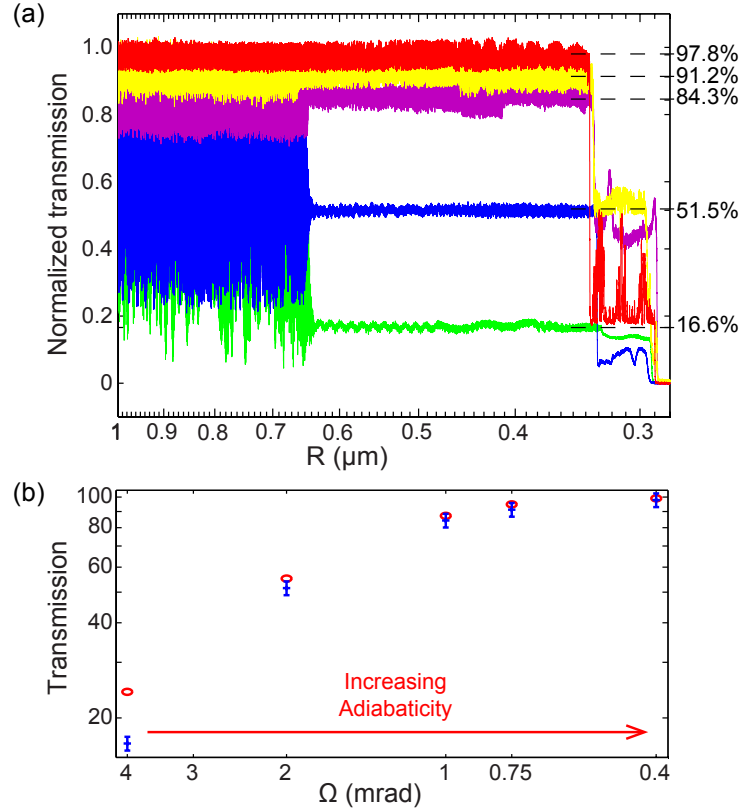


Figure 4.5: (a) Transmission through a SM1500 ONF for $\Omega = 4, 2, 1, 0.75, 0.4$ mrad depicted in green, blue, purple, yellow, and red respectively. The transmission plots have the fundamental mode subtracted out (typically about 1 %) to accurately describe the total transmission of the LP_{11} modes. The horizontal axis for the 4 mrad pull was renormalized to take into account extra tension in the fiber due to the rapidity of the pull. (b) Simulated (red circles) and experimental (blue lines) final transmissions through the fiber as a function of angle. Decreasing Ω enables us to improve the transmission of the LP_{11} family up to 97.8 %.

The free-space mode at the fiber input has a spatial polarization that is an equal superposition of HE_{21} and TM_{01} (or TE_{01}). However, mode conversion occurs where the fiber is wound around the mode-filtering mandrel so that the distribution

entering the ONF is unknown. Within the ONF waist, which is held fixed and straight, mode conversion is unlikely to occur so that the desired mode profile can be achieved after the pull [146]. By $R = 0.45 \mu\text{m}$, only the TM_{01} , TE_{01} , and HE_{21} modes are confined, with a small contribution in the fundamental HE_{11} . The HE_{12} mode achieves cutoff at $V_{clad} = 2.8$ ($R \approx 330 \text{ nm}$), earlier than the TM_{01} and TE_{01} modes, which reach cutoff at $V = 2.4$ ($R \approx 290 \text{ nm}$). At $R \approx 330 \text{ nm}$, the power is reduced by the HE_{21} content, which is determined by the initial superposition of states entering the ONF.

The transmitted power in the LP_{11} mode family is 16.6 % for $\Omega = 4 \text{ mrad}$. The transmitted power drops sharply near $R = 13 \mu\text{m}$, and undergoes strong oscillations between 10-80 %. For $\Omega = 2 \text{ mrad}$, the oscillations below $R = 13 \mu\text{m}$ are reduced, with the transmission fluctuating between 30-90 %, and the transmitted power improves to 51.5%. Further decreasing the angle to $\Omega = 1, 0.75$ and 0.4 mrad , improves the transmission to 84.3 %, 91.2 % and 97.8 % respectively, where uncertainty is dominated by systematic effects that should be less than 1 %. Fig. 4.5 also shows excellent agreement between the experimental results and those obtained using commercial waveguide propagation software [123]. For those calculations, the propagation was modeled using the targeted fiber geometry. In our transmission measurements, the scaling between time and radius is made using a separate algorithm that models the dynamics of the pull based on conservation of volume [144], see Chap. 2. For $\Omega = 0.4$ to 2 mrad , the mode cutoff positions we obtain using the scaling from the algorithm correspond directly to what is expected theoretically. We also observe excellent agreement between the experimental transmission measure-

ments and the calculations, confirming the accuracy of our pulling procedure. We were not limited by systematic effects that might include accumulation of contaminants for longer pulls, and asymmetric profiles for faster ones. For the fastest pull (4 mrad), we observed a discrepancy due to systematic effects, and we must apply a different scaling to match the theoretical cutoffs.

For $\Omega = 0.4$ mrad, the most shallow angle studied, the amplitude of the oscillations, which is directly related to the energy transfer to undesired modes, is reduced to a few percent. The observed transmissions are due to losses into and out of the waist. Because the fiber is symmetric, the normalized transmitted power is the square of that in the waist. For $\Omega = 0.4$ mrad, this leads to 98.9 % power in the waist. We believe that such a fiber is usable for various applications involving HOMs. We note that reaching adiabaticity for HOMs requires fibers that are substantially longer than for the fundamental mode. For the HE_{11} mode, transmissions greater than 99% can easily be achieved for Ω up to 5 mrad [103], see Chap. 3. We also observed that when we remove the π -phase plate from the launch, the transmission in the fundamental mode is essentially equal to the transmission before pulling, as adiabaticity is strongly satisfied for this mode. During the tapering process, the higher-order modes escape from the core earlier than the fundamental HE_{11} mode. When the HE_{11} mode finally transitions to a cladding mode, R has decreased, so that V and the number of available modes to couple to is smaller. The reduction in R also leads to an increase in the difference between adjacent propagation constants, allowing less mode interaction and a steeper Ω . Mode conversion also occurs throughout the fiber and not just at the core-cladding transition point, of course,

but this region has the most stringent adiabatic criterion.

4.2.4 Conclusion

We have demonstrated propagation of higher-order modes in ONFs using the TE_{01} , TM_{01} , and HE_{21} modes. By tapering the fiber with angles near 0.4 mrad and using a commercial, off-the-shelf fiber with 50 μm diameter, we have achieved transmission efficiency of 97.8% with excellent mode purity, a factor of four higher than previous work, and more than one order of magnitude improvement on mode purity. Critical to this work was a spectrogram analysis of the modes present during the pulling. Our experimental results agree with simulations of the propagation through the taper. High transmissions of LP_{11} modes with high purity is a promising tool for atomic physics, expanding the possible intensity and polarization configurations of evanescent fields surrounding the ONF.

Chapter 5: Higher-order mode identification and control

5.1 Introduction

We demonstrate efficient guidance of higher-order modes through an ONF in Chap. 4 . The identification and control of the modes propagating on the ONF waist is crucial for excellent atom trapping and other applications of ONFs [85] . This chapter shows our successful control of the propagation modes where we can launch a pure mode or a superposition of the LP11 family.

5.2 IDIOM

The first attempt at modal identification was to use Interferometric Decomposition Into Optical Modes (IDIOM) [148], a method developed at the Naval Research Laboratories (NRL). This technique is used to decompose the output of a multimode fiber into its constituent modes and identify the relative occupancy of each mode by beating the output of the fiber with a reference gaussian beam. Here we wanted to use IDIOM to show that a pure mode input resulted as a pure mode output. The premise being if a mode superposition is preserved from input to output, we know the mode composition on the ONF waist.

In the first tests we pulled past the cutoff of the LP_{11} family, hoping to see the spectral weight of each mode drop off as the radius moved below its cutoff radius. But the decomposition showed components of the HE_{21} mode even after cutoff. The implication is that there is mode conversion somewhere along the fiber taper. In further tests, even when we launch a pure mode, the fiber leads to mode conversion.

Whether this is an issue inherent to ONFs or a technical issue requires more study. There are technical issues with the fiber clamps and fiber bends that could potentially lead to mode conversion. In addition our experimental setup has limited space since all the optics must fit on a breadboard that can sit on the fiber pulling motors, see Fig. 2.1. For these reasons, we decided it necessary to pursue other means to identify the modes on the ONF waist.

5.3 Rayleigh scattering measurements

Since the ONF appears to behave as a bulk optic, converting a pure mode input to a superposition of modes output, it is necessary to probe the ONF on the fiber waist itself to gain information about the mode distribution. The Rayleigh scattering in fibers arises from induced dipole radiation dependent on the polarization of the mode [149, 150], we can use the radiated light from the ONF waist to ascertain information about the local modal distribution.

5.3.1 Theory

We work with Fibercore SM1500 fiber, which is multi-mode with input light at 795 nm initially admitting not only the fundamental mode but the next family of modes known as the LP_{11} family. These modes are labelled the TE_{01} , TM_{01} , and HE_{21} modes. An unfortunate consequence of working with SM1500 fiber is that the V number exceeds 3.8. From Fig. 4.2.1 we see that the fiber also admits the next family of modes. Therefore, a clean launch of the LP_{11} family requires careful alignment.

Upon launching a mode into a fiber, if we could spatially resolve the transverse profile of the Rayleigh scattering, we could identify the modes [151]. However, given that we typically pull to waist radius below 400 nm, we do not have the optical resolution. It is also possible that since the surface scattering dominates it could obscure the bulk scattering in the image 5.3.4.

The Rayleigh scattered power is proportional to the local intensity. Therefore, by observing the modulation in the Rayleigh scattered power along the fiber as a function of position, resulting from the beating between modes, we can identify the modes present in the fiber. In Chap. 2 we observed the phase accumulation from this beating. Here we can directly measure and determine the sets of beat lengths as a function of position. Using the data from Fig. 4.2.1 and reparametrizing the horizontal axis in terms of radius, we can obtain the propagation constants as a function of radius. Then using Eqn. 3.3, we plot beat lengths for the modes of interest as a function of fiber radius in Fig. 5.1. We see that for an ONF with a

waist radius of 390 nm we can expect the beat length to vary from a few microns for any HOM beating with the fundamental mode, to tens of microns for HOMs beating together. Note, that due to the orthogonality of the polarizations at all points in space the TE_{01} and TM_{01} will never interfere.

To extract the beat lengths we perform the following procedure:

1. Image the entire length of an ONF over the tapered region and waist.
2. Align and concatenate the images.
3. Sum over the transverse profile creating data representing power scattered vs position along the fiber axis.
4. Take a spectrogram of the power scatter vs position data.

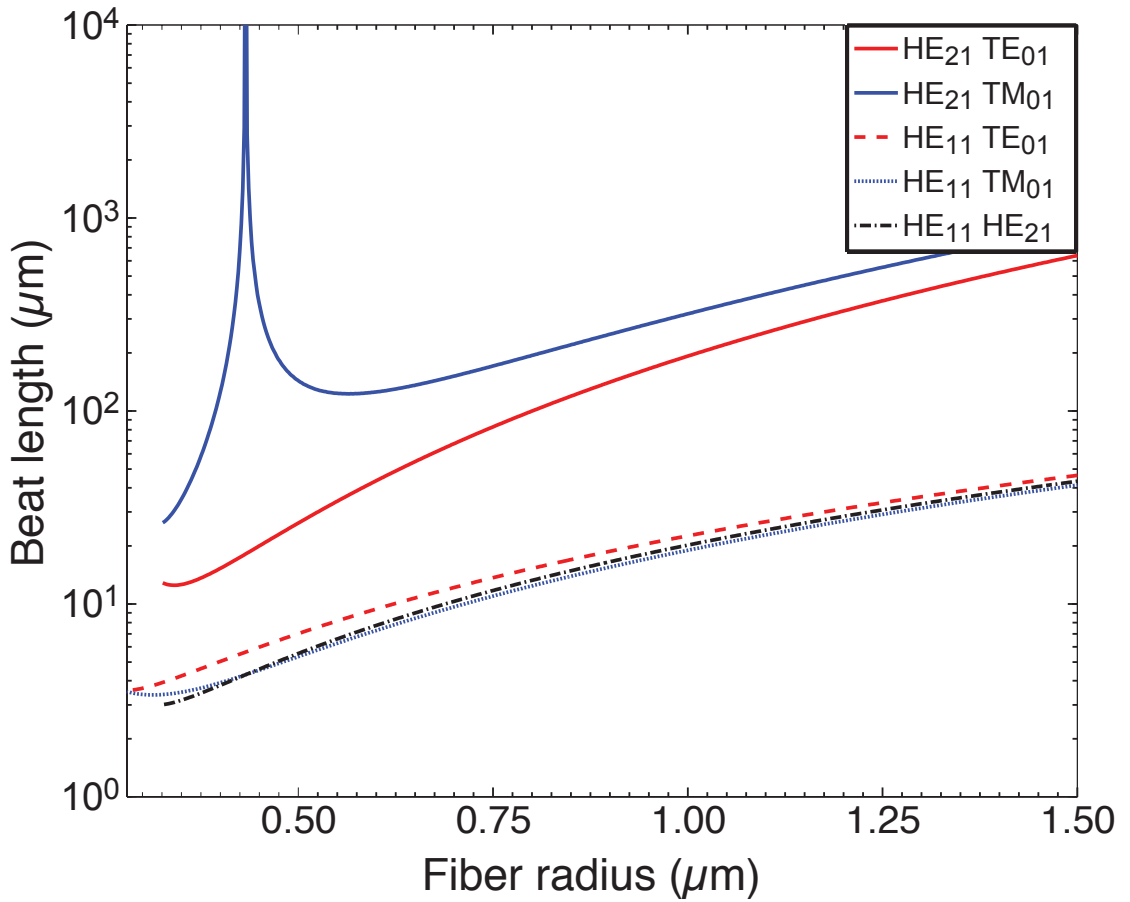


Figure 5.1: The beat length between various modes as a function of fiber radius for a fiber with indices of refraction $n_{Core} = 1.48693$; $n_{Clad} = 1.45424$, and $n_{Air} = 1.0$ simulated using FIMMPROP.

The spectrogram will show all the spatial frequencies that are changing as a function of position in the fiber. These are the inverse spatial angular beat lengths given by $1/\text{beat length}$. Figure 5.2 shows the inverse beat lengths as a function of radius, displaying the value we actually expect to extract from the spectrogram. We can then overlap the observed beat lengths with the difference in propagation

constants and identify the modes that are in the fiber as a function of position.

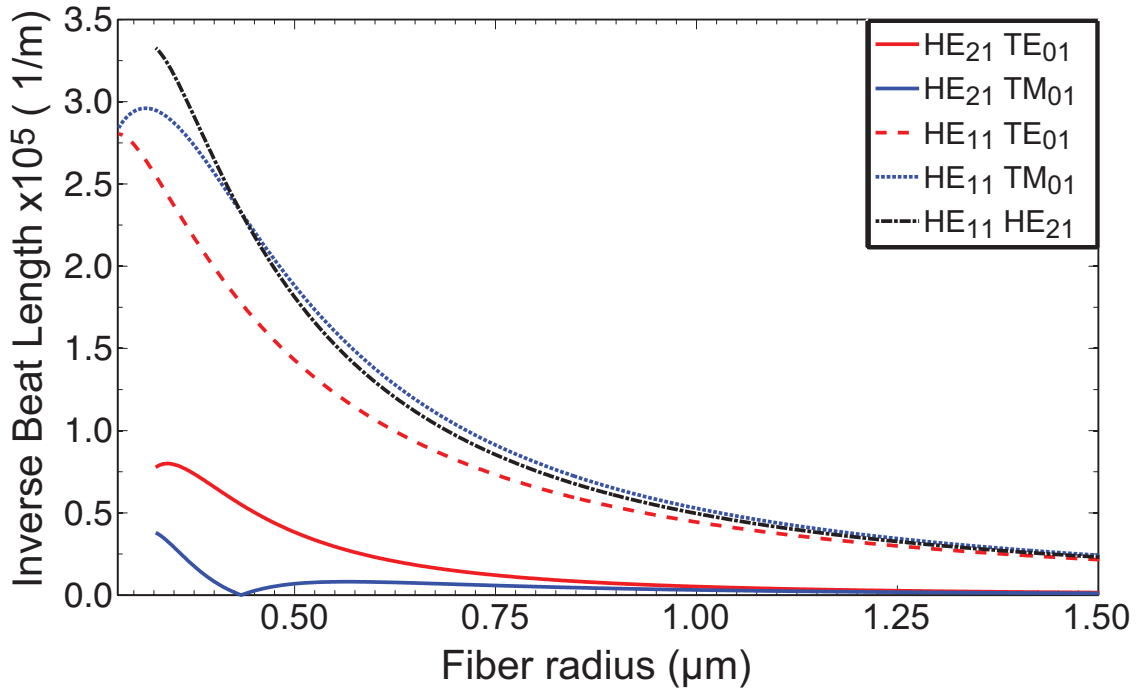


Figure 5.2: The inverse beat length between the modes in Fig. 5.1 as a function of fiber radius.

Using the above method we can identify the modes on the waist.

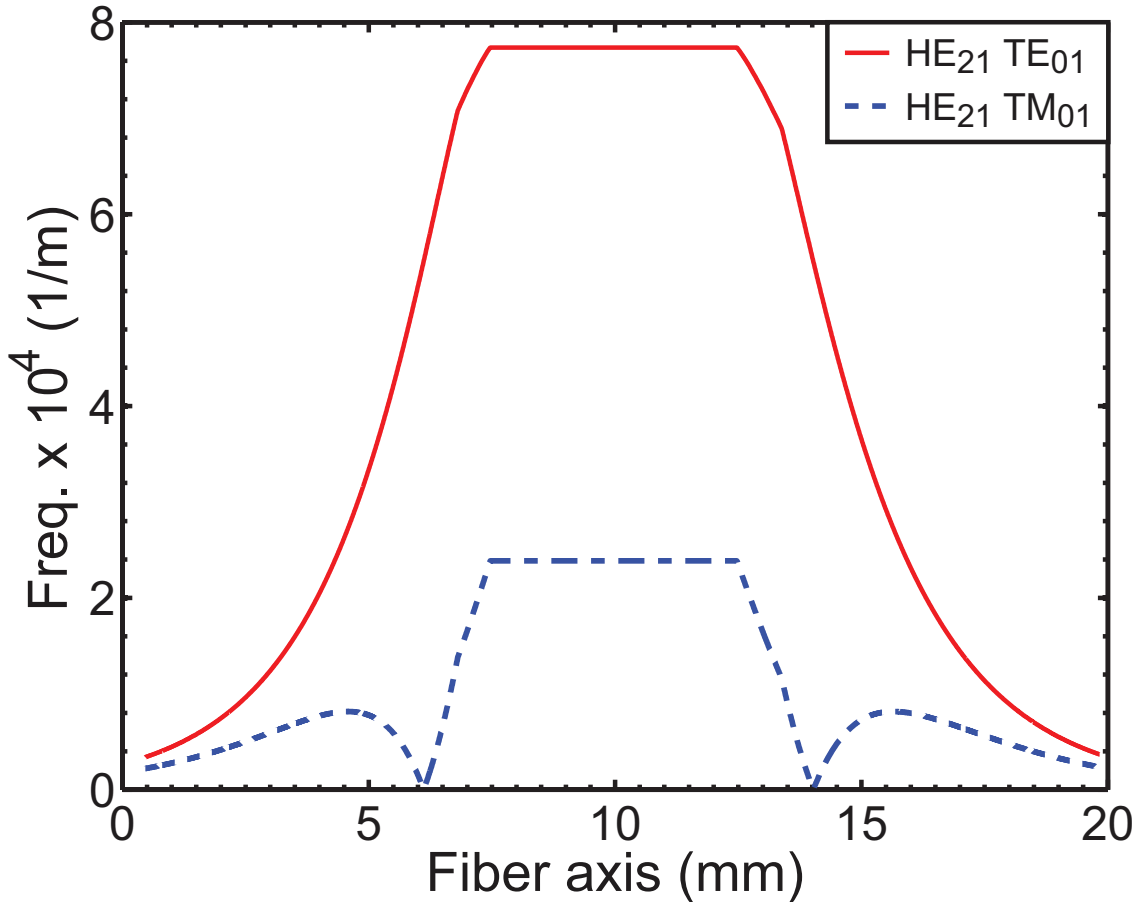


Figure 5.3: Inverse beat frequency simulation for $r_w = 390 \text{ nm}$ with $\Omega = 1 \text{ mrad}$ taper and $L_w = 10 \text{ mm}$.

We can use the simulation of the ONF profile, see Chaps. 2 and 3, and the inverse beat frequencies to simulate the inverse beat frequency as a function of position for a given ONF. Figure 5.3 shows such a simulation for the HE_{21} mode beating with the TE_{01} (red) and TM_{01} (blue) modes for a fiber with a 1 mrad taper to a waist radius of 390 nm and 10 mm length waist.

To demonstrate control we need to launch and manipulate the manifold of

HOMs in a controllable and efficient manner. Following Ref. [146] we use a vector beam generator described in Sec. 5.3.2 and bulk optics to rapidly manipulate the input mode launched into the ONF and therefore the mode propagating on the ONF waist.

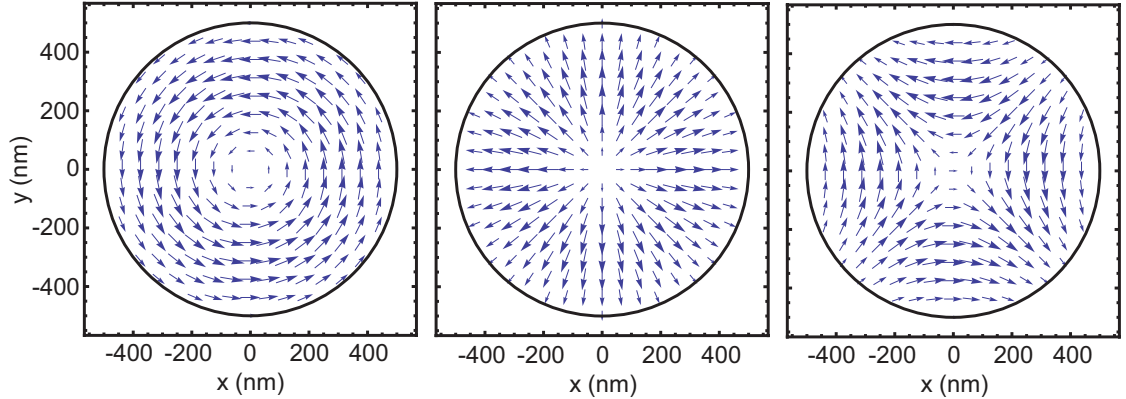


Figure 5.4: The vector profile inside a 450 nm radius fiber for the transverse components of the TE_{01} , TM_{01} and HE_{21} modes respectively. The black circle represents the cladding air interface at 450 nm. The indices of refraction are chosen to be 1.45 and 1 for the cladding and air respectively.

Figure 5.4 displays the vector profile for the transverse components of a 450 nm radius fiber for the HOMs. By placing two HWPs with a relative angle of 45 degrees between their fast axes in front of a TM_{01} mode will output a pure TE_{01} mode in the fiber, which can be seen in Fig. 5.4.

Similarly, when launching a superposition of the HE_{21} and TM_{01} , which produces a two lobed mode with polarization perpendicular to the null, we can completely convert to a superposition of HE_{21} and TE_{01} using a HWP with a relative

angle of 45 degrees. Fig. 5.5 shows the transverse profiles of the HE_{21} and TM_{01} modes interfering together and the HE_{21} and TE_{01} modes interfering respectively.

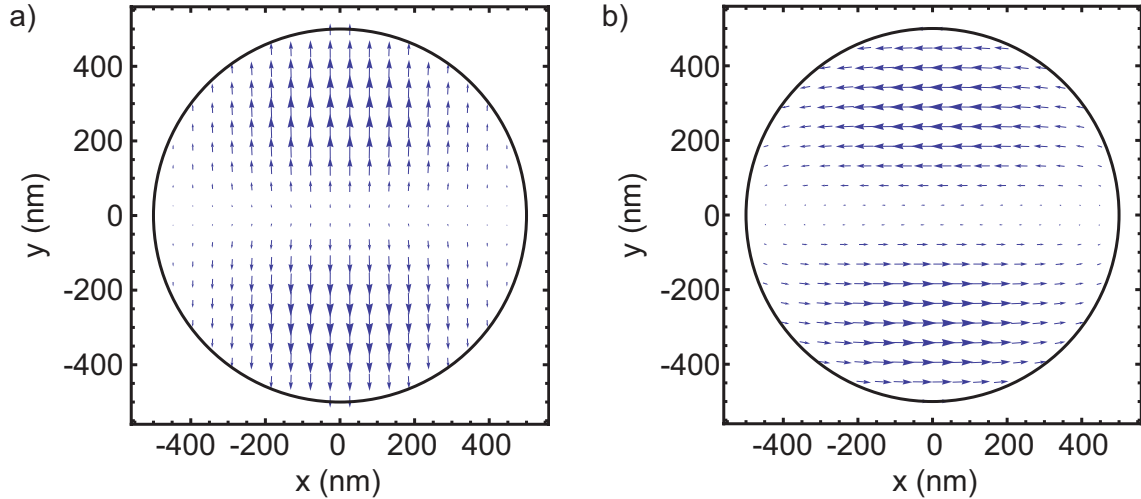


Figure 5.5: The vector profile inside the fiber for the transverse component HOM interfering. a) HE_{21} and TM_{01} modes interfering b) HE_{21} and TE_{01} modes interfering. The black circle represents the cladding of the fiber with a radius of 450 nm.

These calculations confirm what we had stated earlier in this chapter that by launching a known mode and using bulk optics we should be able to rapidly convert the mode on the waist to any desired superposition of states.

5.3.2 Experimental setup

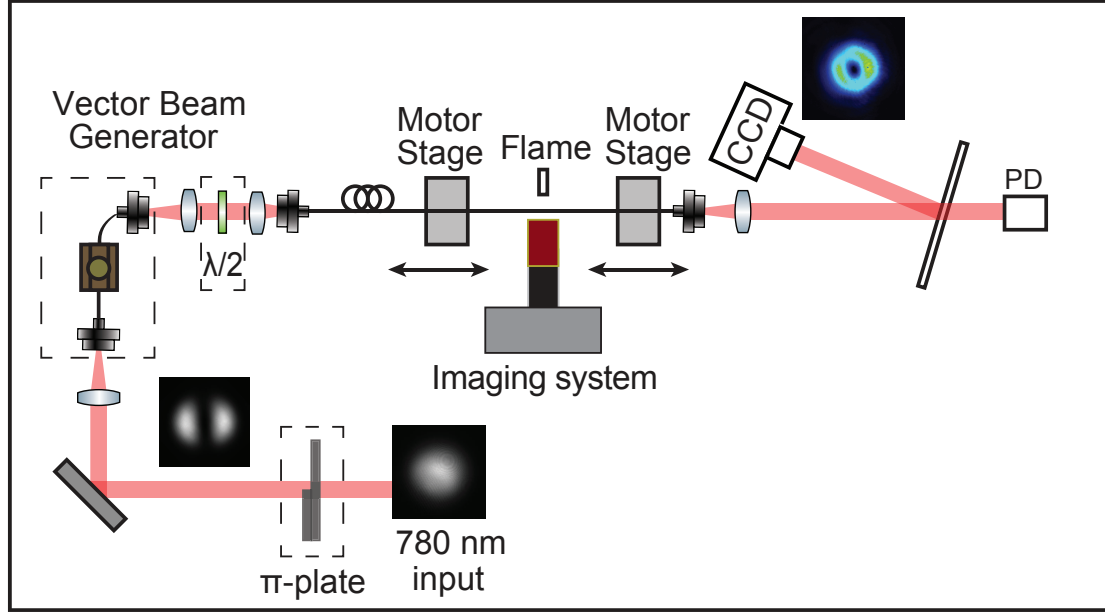


Figure 5.6: The experimental setup to measure the Rayleigh scattering from an ONF.

The experimental setup, as depicted in Fig. 5.6, has three components: the ONF fiber launch and vector beam generation setup, the ONF Rayleigh scattering imaging setup, and the ONF output imaging setup. The HOM generation differs from Sec. 4.2.2. Here we generate a desired mode instead of an unknown superposition. First we launch light from a 795 nm laser into a polarization maintaining fiber. This spatially filters the mode and sets the polarization. The output of the polarization maintaining fiber travels through a phase plate. The phase plate imparts a π phase shift onto half of the beam. This phase shift creates a two lobed

mode that when projected onto the fiber basis will excite a superposition of either HE_{21} and TE_{01} modes or HE_{21} and TM_{01} modes. The next step is to launch this superposition into the vector beam generator.

The vector beam generator consists of HI1060 fiber that we thread through a Thorlabs In-Line Fiber Polarization Controller (PC). The HI1060 fiber has a V number below 3.8 and admits only the HE_{11} , TE_{01} , TM_{01} , and HE_{21} modes. The PC then allows us to control the output mode of the HI1060 fiber. We can then produce a pure mode, or any superposition of modes from the vector beam generator. The output of the vector beam generator is then carefully coupled into the ONF.

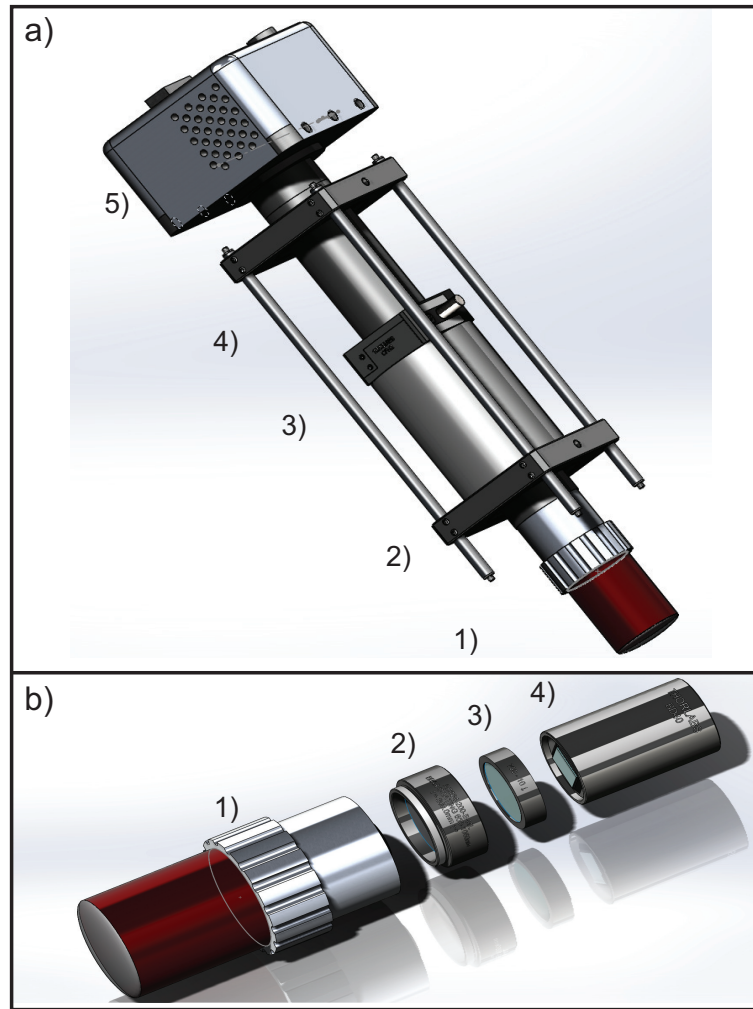


Figure 5.7: (a) The imaging system used for Rayleigh scattering measurements. (b) The optics for the imaging system as detailed in Tab. 5.1

Item	Description
1	Mitutoyo NIR 10X objective
2	Achromatic Doublet, $f=200$ mm
3	795 nm Bandpass filter
4	Mounted Calcite Beam Displacer
5	Luca Andor EMCCD

Table 5.1: List of equipment parts for the Rayleigh scattering imaging system.

Once a pull is completed we use the fiber motors to step along and image the Rayleigh scattering from the ONF using the imaging system depicted in Fig. 5.7 (see Tab. 5.1). The Rayleigh scattering imaging system is composed of a Mitutoyo M Plan Apo NIR optimized infinity corrected objective, either 10x or 50x with NAs of 0.26 and 0.65 respectively. This allows us to choose a shorter or longer depths of field, or use the minimum spatial resolution necessary depending on the topic of study. The objective collects and collimates the Rayleigh scattering from the ONF. The light then passes through a 200 mm achromat doublet (part number here). Then we place a 795 nm bandpass filter to prevent any room light from adding unwanted background to the images. Finally we use a calcite polarizer as a walk off to separate the longitudinal and transverse polarization of the radiated light. The light is then imaged on an Andor Luca EMCCD. The calcite walk-off limits the spatial resolution of the imaging system to $3 \mu\text{m}$. Since the transverse resolution is worse than a few microns we cannot observe HOMs beating with the fundamental,

as shown in Fig. 5.1.

The ONF output is collimated with an asphere and then imaged on a Thorlabs Beam Profiler. We control the focus of the Rayleigh scattering image system with micrometers. While we control the positioning of the ONF relative to the imaging system along the fiber axis using the two high precision XML 210 fiber motors. This allows us to precisely move the fiber, image the entire fiber length, and calibrate the Rayleigh scattering imaging system.

To control the mode [146] we use bulk optics: by placing combinations of HWPs and QWPs we can efficiently convert modes.

5.3.3 Experimental results

5.3.3.1 Mode identification

Using the experimental setup described in Sec. 5.3.2 we launch a HOM into an ONF and step the fiber motors in set increments to take a series of images of the Rayleigh scattering. We then align and concatenate the images together. Figures 5.8 displays approximately 300 concatenated images taken with a Mitutoyo 50X M Plan Apo NIR optimized infinity corrected objective. Each individual image captures a $200 \mu\text{m}$ field of view which we then crop to $150 \mu\text{m}$. We use the XML 210 motors to move in controlled $150 \mu\text{m}$ steps and use features from different images to calibrate the length scales. Figure 5.8 displays the transverse polarization of the Rayleigh scattering. We adjust the gain, exposure time and averaging so that we can image the ONF without saturating the pixels.

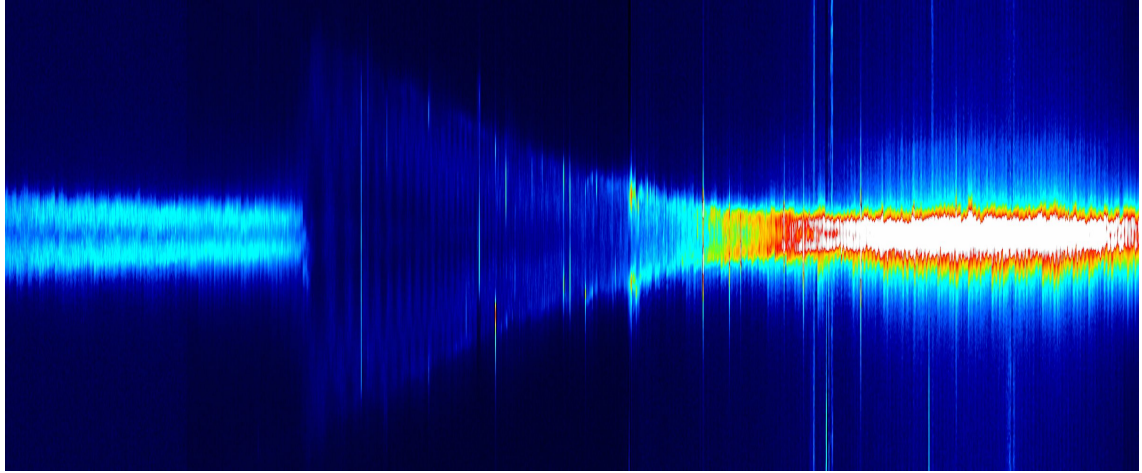


Figure 5.8: HOM 50x montage transverse polarization with the power scale in arbitrary units.

Tracing Fig. 5.8 from the left edge to the right we observe that the mode starts as a core mode. As described in Sec. 3.5, the mode is initially guided by the core-cladding interface. The imaging system has the resolution to actually observe the Rayleigh scattering focusing along the fiber axis as the core mode follows the tapering core. The null in the center of the scattering is an expected consequence of HOM Rayleigh scattering. Superpositions of HOMs can have a two-lobed intensity pattern that when scattering and imaged on a plane can have a null in the center. As the fiber continues to taper and reduces below a radius of $13 \mu\text{m}$ we see that the mode can no longer be supported by the core and leaks into the cladding. Here we observe a beautiful oscillation pattern indicative of modes interfering. The interference pattern increases in spatial frequency as the fiber tapers and traces out the diameter of the cladding as the mode focuses down to the ONF waist in

which the power scattered increases as surface scattering begins to dominate the bulk scattering.

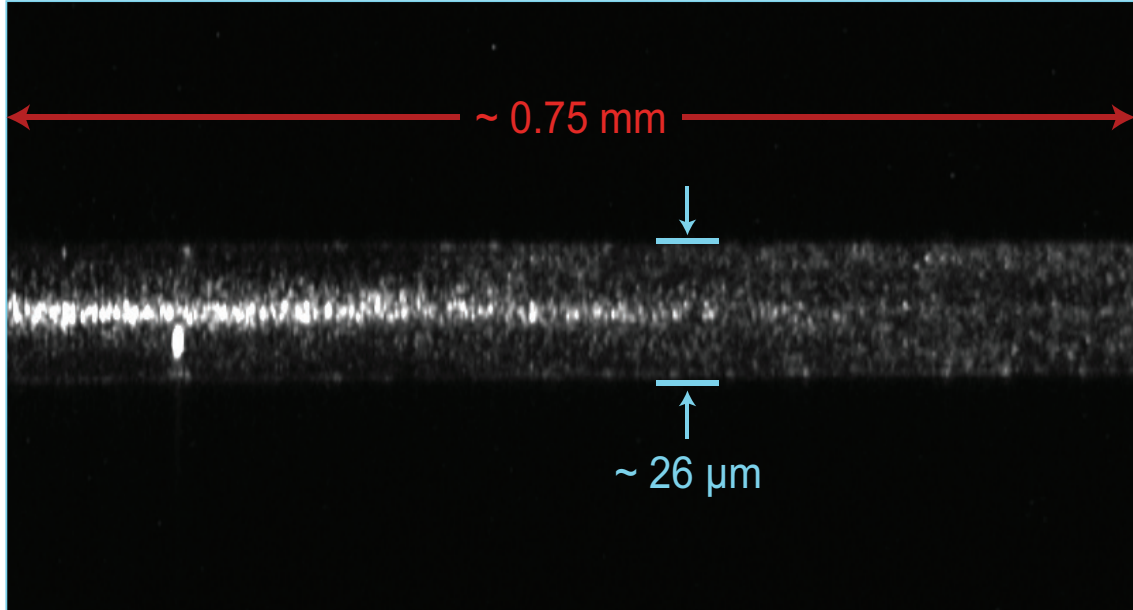


Figure 5.9: Rayleigh Scattering depicting HOMs transitioning from core to cladding modes.

Fig. 5.9, captures in a single image, a HOM superposition leaking from core to cladding guidance in a fiber taper using SM1500 fiber. Using the Mitutoyo 10X objective the field of view of the image is $750 \mu\text{m}$. We see that the mode starts as a core mode and leaks into the cladding. The transition occurs at a radius of $13 \mu\text{m}$ in Fig. 5.9, which is consistent with the transmission data in Sec. 4.2.3.1.

We can spatially resolve transverse modal information from the Rayleigh scattering when the mode is a core mode. Once the mode escapes into the cladding the imaging system can resolve the transverse profile until a diameter of about $2\text{-}3 \mu\text{m}$.

If we were able to spatially resolve the transverse Rayleigh scattering on the ONF waist we could follow the work done in [151]. Unfortunately, we do not have the spatial resolution. Therefore, as described in Sec. 5.3.1 we average out the transverse scattering information by summing over the columns. When we sum the columns we are able to observe variations in scattered power along the fiber axis as in Fig. 5.10. Figure 5.1 displays the expected beat lengths as a function of radius and since we expect the signal to be chirped we take a spectrogram. A typical spectrogram of the data is displayed in Fig. 5.10.

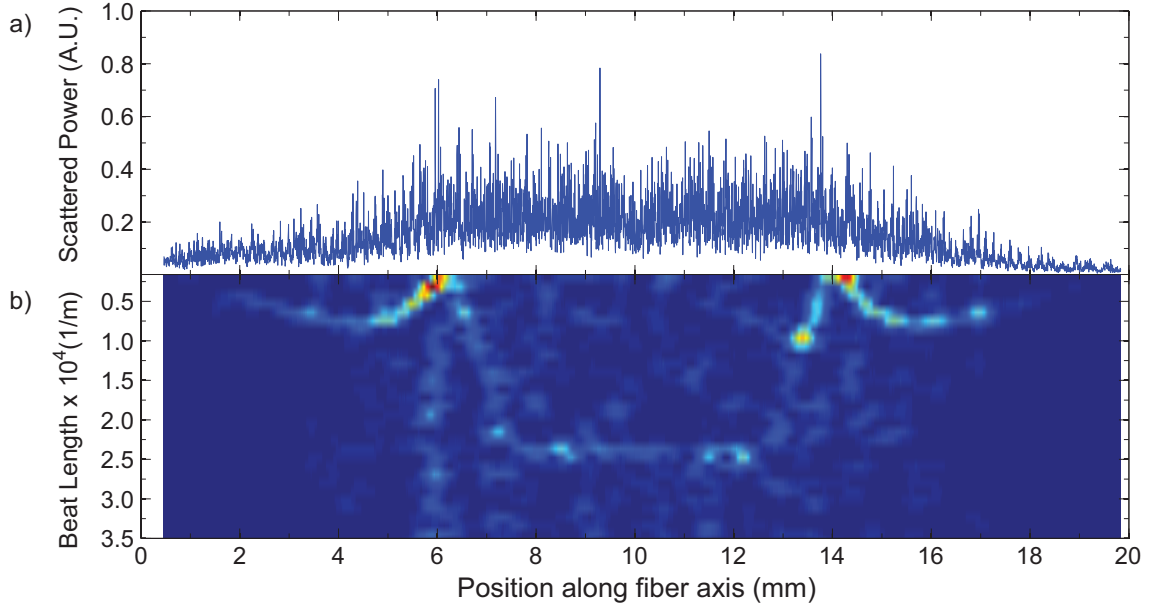


Figure 5.10: a) Scattered power along the ONF waist after summing over the columns. b) A spectrogram of aligned concatenated images displaying the HE_{21} mode beating with the TM_{01} mode.

Fig. 5.10 (a) shows the power scattered as a function of position near the ONF

waist for a 1 mrad pull with $r_w = 390$ nm. The change in oscillation frequency in scattered power is quantified in the spectrogram in Fig. 5.10 (b). We see that the inverse beat frequency first increases, then decreases implying a long beat length. The inverse beat frequency reaches a steady value along the fiber waist, and then reproduces the symmetric pattern on the other side of the taper.

Using Figs. 5.2 and 5.3 we can identify that the only inverse beat frequency that matches near 390 nm is the value for the HE_{21} mode beating with the TM_{01} . We can also see that r_w for this fiber is slightly smaller than predicted at about 360 nm. Furthermore, the general shape of the mode profile is qualitatively the same as the shape of the blue curve in Fig. 5.3. This distinct shape arises from the crossing of the n_{eff} curves for the HE_{21} mode and TM_{01} at around 430 nm, which is identifiable in Fig. 4.2.1. Fig. 5.2 comes from the sum of the transverse and longitudinally polarized scattered light. If we were to plot the scattered power for the transverse and longitudinal components and take each respective spectrogram we would see the same profile in either image. Therefore, it is easy to see that this signal must arise from the TM_{01} mode beating with the H_{21} since the TE_{01} mode should have no longitudinal component ¹.

5.3.3.2 Mode control

To demonstrate mode control on the ONF waist we launch an input mode that projects onto a superposition of the HE_{21} and TM_{01} modes, see Fig. 5.5. Rotating

¹We are never actually able to completely eliminate the longitudinal component of the scattering.

a HWP converts the superposition into a sum of HE_{21} and TE_{01} . We image the longitudinally and transversally polarized Rayleigh scattering across the waist and then take the Fourier transform of the power scattered vs position for various HWP angles. Figure 5.11 (a) displays the power scattered as a function of position along the ONF waist when launching a superposition of the HE_{21} and TM_{01} modes. We note that the offset between the blue curve, the launching of a superposition of HE_{21} and TM_{01} , and the red curve, the launching of a superposition of the HE_{21} and TE_{01} , is added to ease the visualization of the profiles. We changed the mode by rotating a HWP at the input of the ONF launch by 44 degrees.

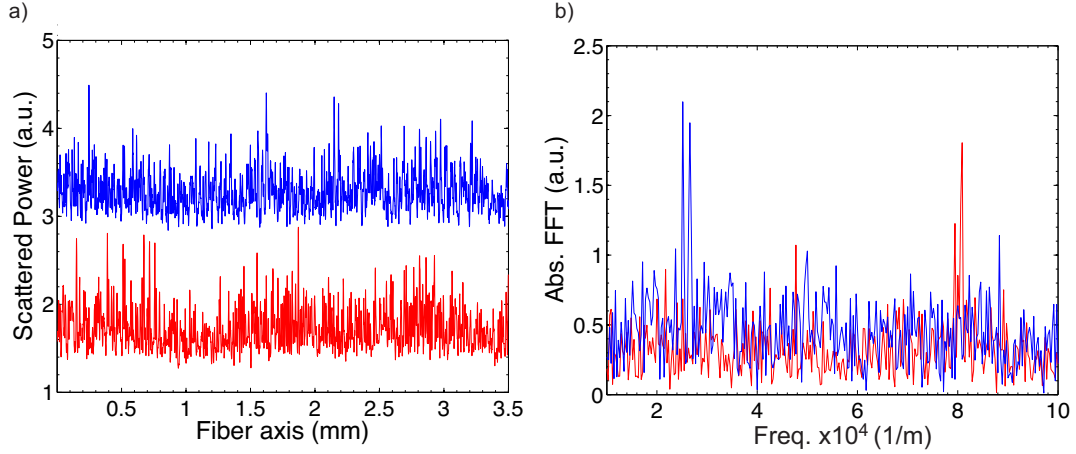


Figure 5.11: (a) Scattered power vs position along the fiber axis with HWP angle offset by 44 degrees. This converts the mode from a HE_{21} and TM_{01} superposition (blue) to a HE_{21} and TE_{01} superposition (red). The offset is added for visualization. (b) Absolute value of the Fourier transform for the Rayleigh scattering. We see the HE_{21} and TM_{01} peak at about 2.5×10^4 1/m in the blue curve (and not in the red curve) and we observe the HE_{21} and TE_{01} peak at about 8×10^4 1/m in the red curve (and not in the blue curve) indicating we have fully converted the superposition of modes.

Figure 5.11 (b) shows Absolute value of the Fourier transform for the Rayleigh scattering. We see the HE_{21} and TM_{01} peak at about 2.5×10^4 1/m in the blue curve (and not in the red curve) and we observe the HE_{21} and TE_{01} peak at about 8×10^4 1/m in the red curve (and not in the blue curve) indicating we have fully converted the superposition of modes.

Figure 5.12 shows a more detailed description of the above process for the

longitudinally and transversely scattered light. We now collect the scatter over the ONF waist for 2 degree rotations of HWP. Then we take the absolute value of the Fourier transform squared and plot each of these curves as a vertical slice in Fig. 5.12.

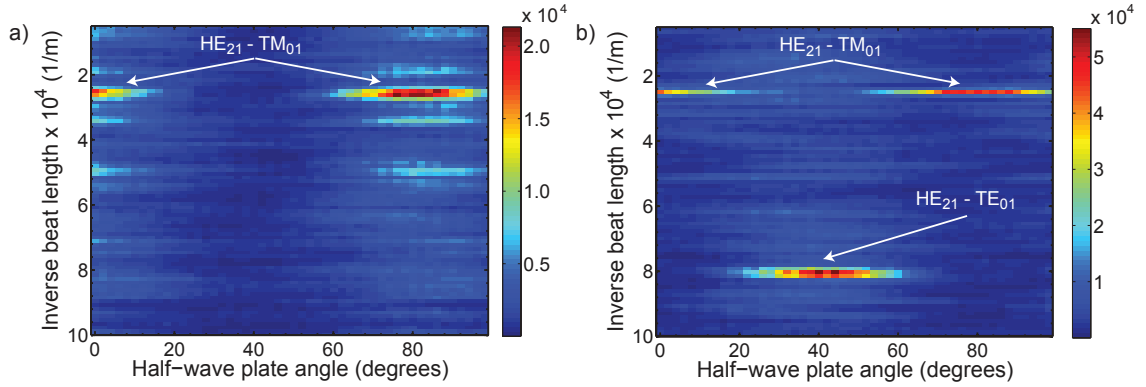


Figure 5.12: Conversion of HE_{21} and TM_{01} to HE_{21} and TE_{01} as a function of half-wave plate angle a) Longitudinal component only. b) Transverse component only.

We see that at a HWP angle of zero we start with the HE_{21} and TM_{01} modes beating together since the signal occurs in the longitudinal plot. As the HWP angle rotates we see that the the magnitude of the Fourier transform drops for the HE_{21} and TM_{01} while it grows for the the HE_{21} and TE_{01} . At a 40 degree rotation we see that a superposition of HE_{21} and TE_{01} occupies the ONF waist while there is no TM_{01} within the contrast of the Fourier transform. This conversion occurs at 40 degrees rather than 45 because the a HWP angle of 0 does not correspond to a maximum in the absolute value of the Fourier transform in the HE_{21} and TM_{01}

frequency band. Rotating the HWP another 45 degrees to 85 degrees brings in a maximum in the HE_{21} and TM_{01} frequency band and a minimum in the HE_{21} and TE_{01} frequency band, completely as expected.

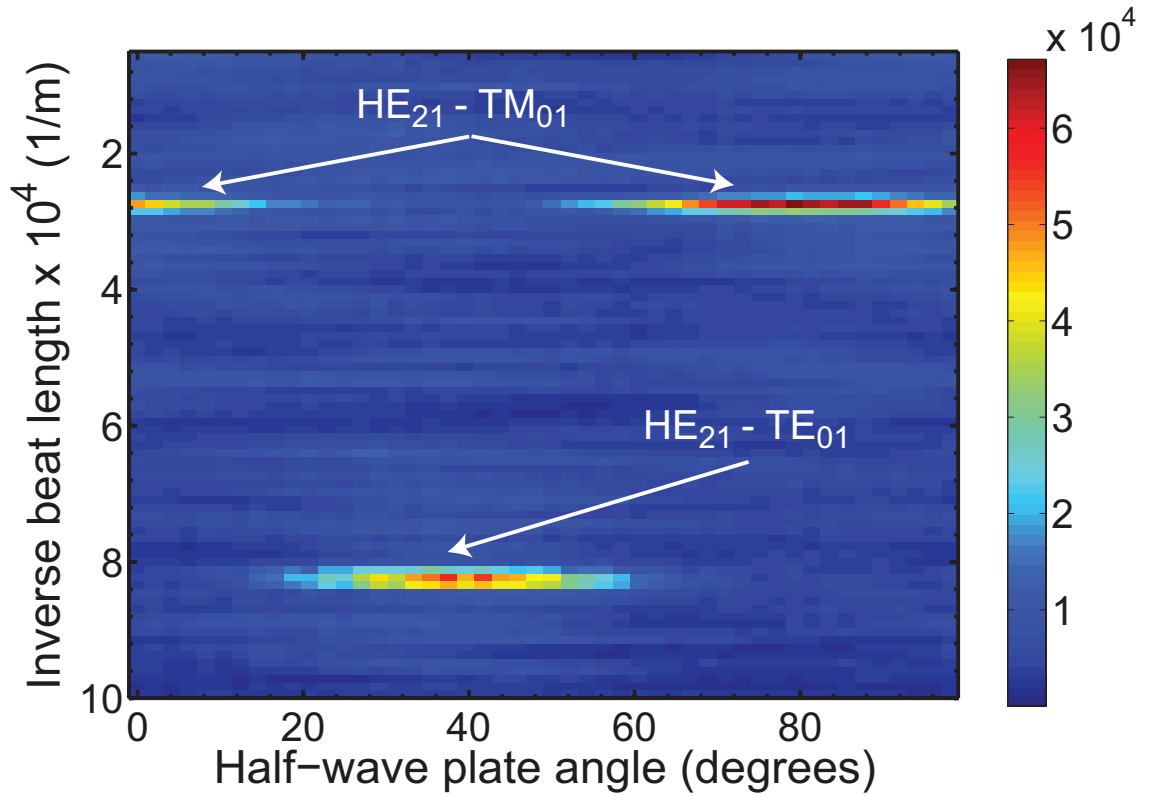


Figure 5.13: Conversion of HE_{21} and TM_{01} to HE_{21} and TE_{01} with longitudinal and transverse components summed.

Figure 5.13 is the sum of the longitudinal and transverse components in Fig. 5.12. It is clearer here that the background in the other frequencies is more uniform than in the individual longitudinal and transverse components.

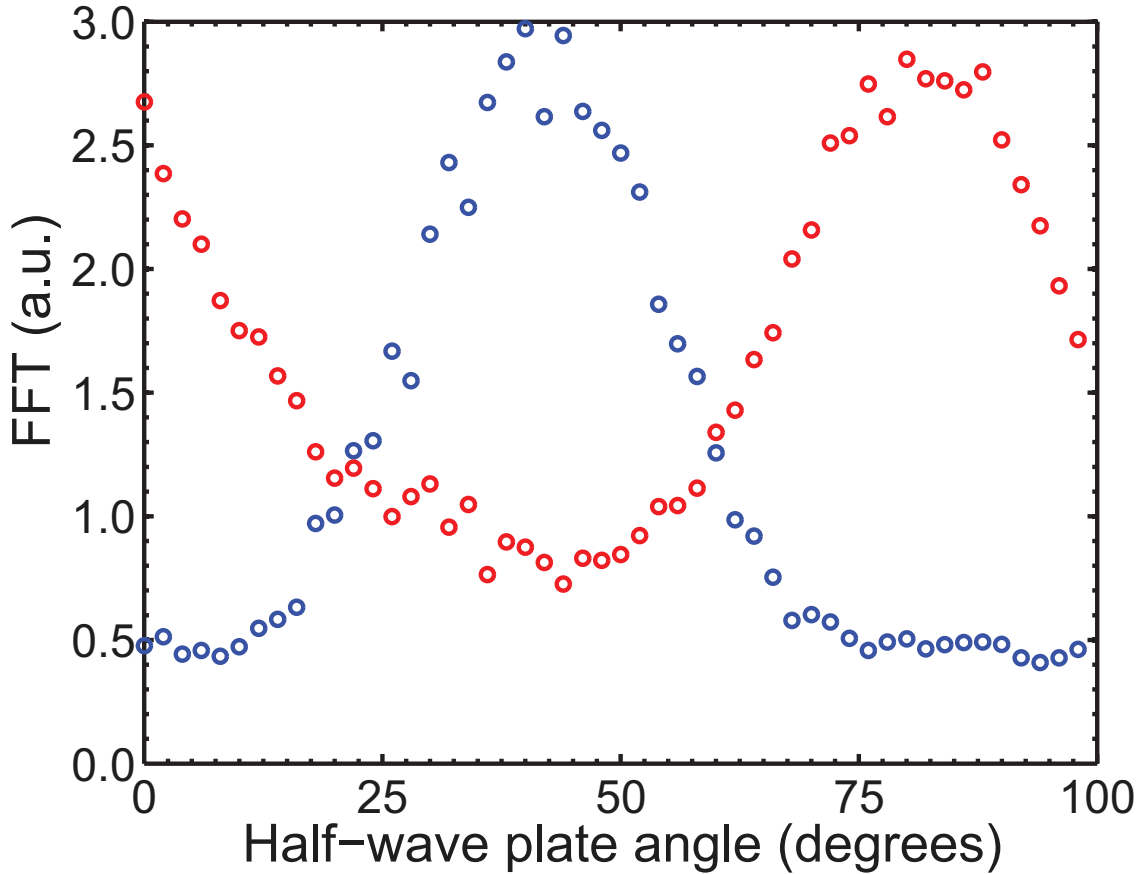


Figure 5.14: Conversion of HE_{21} and TM_{01} to HE_{21} and TE_{01} specifically in the proper frequency bands.

Fig. 5.14 displays the absolute value of the Fourier transform from Fig. 5.13 in the relevant frequency bands for the inverse beat. The red circles represent the presence of the HE_{21} and TM_{01} modes, while the blue circles depict the HE_{21} and TE_{01} modes. We see that the two signals are 90 degrees out of phase (45 degrees in HWP angle) as expected.

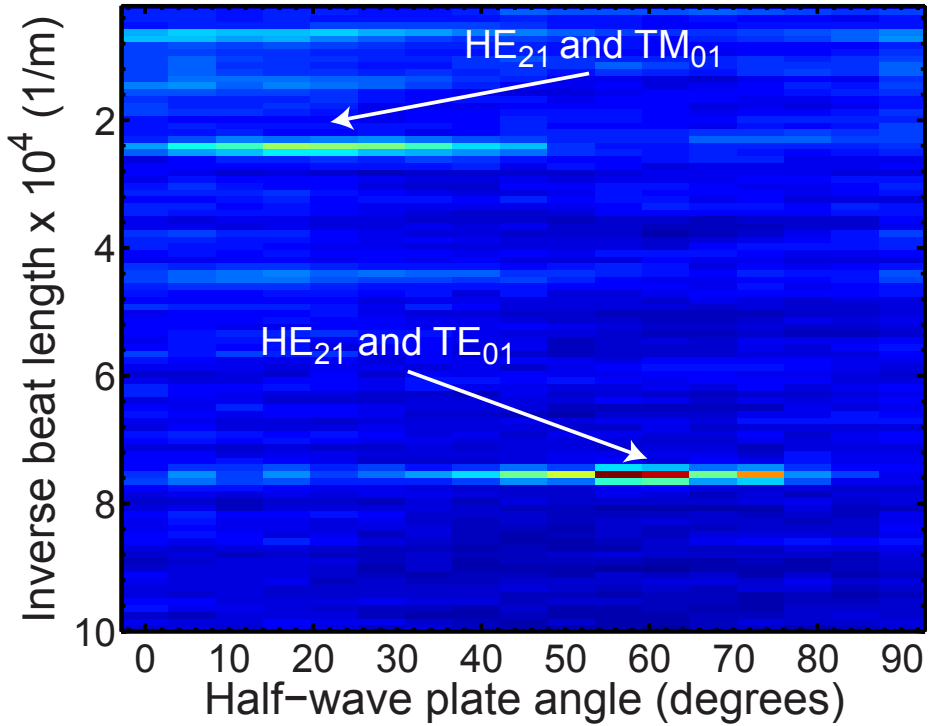


Figure 5.15: Pure mode conversion as a function of half-wave plate angle

The last step necessary to demonstrate modal control on the ONF waist is to send in a pure mode. If there is a pure mode, there should be no frequency spectrum in the spectrogram or Fourier transform. Since a pure mode input undergoes mode conversion through the ONF we cannot simply launch a pure mode into the fiber. Instead, we image the waist and look at the Fourier transforms in real time and tweak the input until there is no peak in the frequency spectrum. We place QWP and HWP in front of the fiber launch and adjust the PC to change the fiber launch into the ONF. Fig. 5.15 demonstrates the result of this arbitrary input. At a HWP angle of zero degrees there is a small signal from the HE_{21} and TM_{01} modes. As

the HWP is rotated the TM_{01} mode comes in and out as the TE_{01} mode is excited.

Finally at 90 degrees we see that there is no beat signal at all. Implying a pure mode on the waist.

This technique does not uniquely identify the mode on the ONF waist nor does it express the determine the distribution of modes, without some further calibrations. It seems within reason, that if we could spatially resolve and identify the mode at a radius of a few microns the mode conversion would be minimal to the waist. Furthermore, if we were able to both identify the mode at a few microns on input and output of the waist it is likely that the mode on the ONF waist is identical.

5.3.4 Surface scattering and mode cutoffs

When tapering a fiber below 325 nm, we pass the HE_{21} cutoff. Fig. 5.16 shows the longitudinal, transverse, and total Rayleigh scattering from the ONF as a function of position with a 1 mrad angle tapered to a 300 nm radius waist that is 1 cm long. Here we observe a number of phenomena.

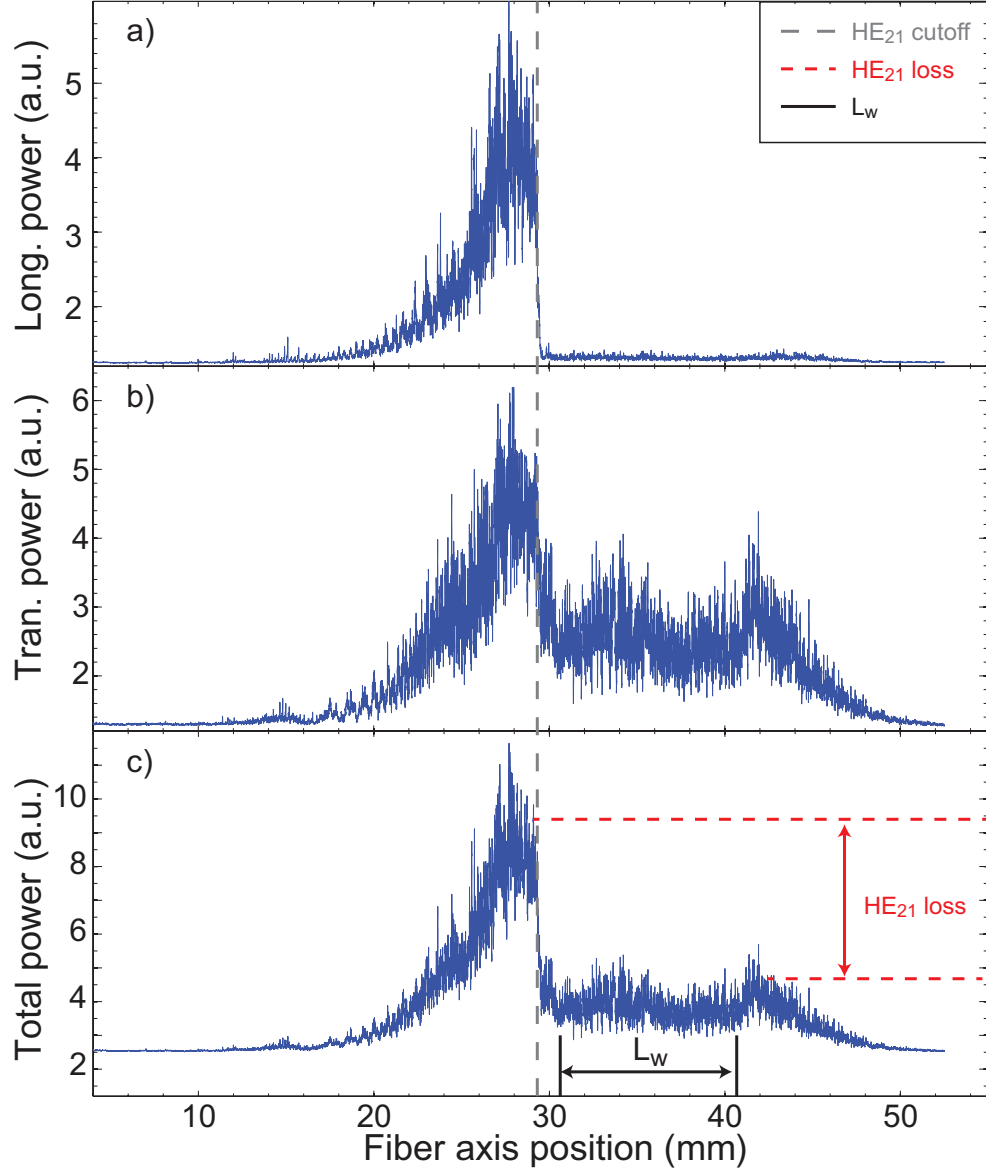


Figure 5.16: Launching a superposition of HOMs into a fiber with $\Omega = 1$ mrad, $r_w = 300$ nm, and $L_w = 1$ cm. The three panels correspond to scattering collected with (a) longitudinal polarization, (b) transverse polarization, and (c) total scatter as a function of length respectively. The long dashed gray line denotes the HE_{21} cutoff and from that point we observe only the propagation of the TE_{01} mode. The short dashed red lines show the power loss from the HE_{21} mode ejecting from the ONF. Finally, the continuous black lines designate the ONF waist.

First, from a position of 4 mm to 14 mm on the fiber axis we see that the total power is steady. That this region, a taper section, has a steady scattering rate, is indicative of bulk scattering and is consistent with Lambert-Beer law. The fact that there is a steady increase in the scattering rate as the fiber continues to taper, from 14 mm to 29 mm is consistent with surface scattering effects. The intensity of the mode at the fiber surface increases as the radius decreases and surface imperfections begin to dominate over bulk scattering.

The next interesting behavior occurs at 29 mm on the abscissa, denoted by the dashed gray line in Fig. 5.16. This is the point that the HE_{21} mode cuts off at a radius of 325 nm. We see an immediate drop in the Rayleigh scattering, most pronounced in the longitudinal component in panel (a) of Fig. 5.16.

In each panel of Fig. 5.16 we see a flat region between 30.5 mm and 40.5 mm in the scattering. This region, denoted L_w corresponds to the ONF waist. We see that it is 10 mm long, consistent with the length specified by the pulling algorithm for the ONF.

The difference in height between the red dashed lines in the total scattered power plot represents the power loss from the HE_{21} mode ejection as observed in the decrease in scattered light. We choose two symmetric regions on opposite sides of the waist, such that we are looking at similar radii, to make the comparison.

Interestingly, the scattering stays fairly consistent along the the rest of the ONF . The data is consistent with having the HE_{21} and TE_{01} modes excited. Since the HE_{21} mode is ejected from the waveguide, and we see that scattering still exists in the transverse direction, we know there are other modes left in the fiber. The

only mode that can propagate with no z-component in the mode profile is the TE_{01} mode at that radius. Therefore, only the TE_{01} mode is left in the waveguide from the point of the HE_{21} cutoff. Note there is still scattering along the ONF waist in the longitudinal component. This could be caused by a small TM_{01} or HE_{11} background that is not observable in the spectrogram. Ref. [151] notes that the longitudinal scattering was never fully eliminated even in unmodified fibers.

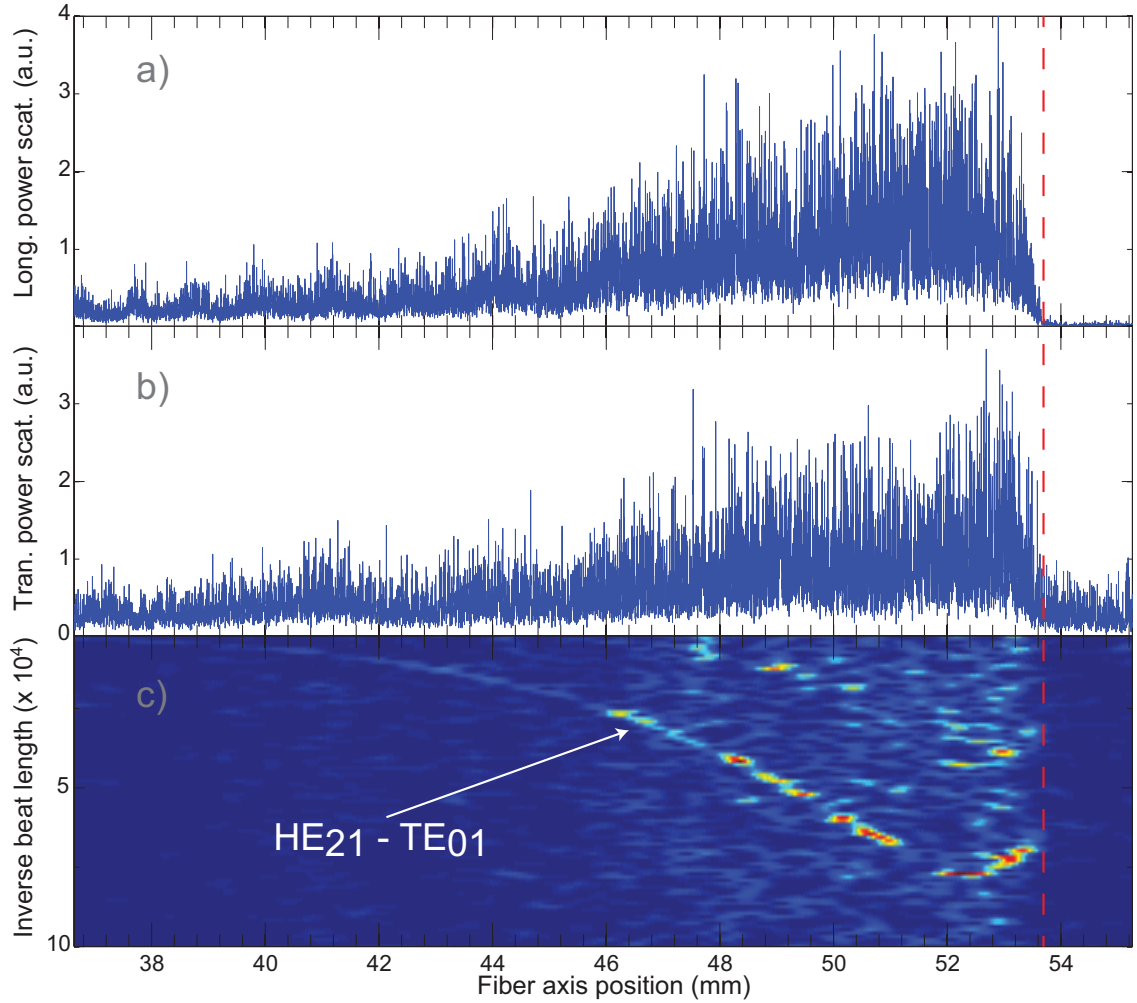


Figure 5.17: (a) Longitudinally polarized scattered power vs position. (b) Transversally polarized scattered power vs position. (c) Spectrogram of power scattered. The red dashed line at 53 mm represents the HE_{21} mode cutoff.

Using the spectrogram we can extract the radius of the fiber as a function of position. Fig. 5.17 shows the longitudinal and transverse power scatter and the spectrogram of the total power scattered for an ONF with a taper geometry of $\Omega = 0.5$ mrad and $r_w = 300$ nm. We see at 53.6 m that the HE_{21} mode cuts off as

represented by the red dashed line in Fig. 5.17. This is observable in not only the longitudinal and transverse power scatter but also in the spectrogram in which the signal disappears. Similar to Fig. 5.16 we see that the magnitude of the longitudinal scatter decreases significantly in Fig. 5.17 implying only the TE_{01} mode propagating in the waveguide from that point. From the inverse beat length in spectrogram at the cutoff we know exactly what modes are beating and identify them as the HE_{21} and TE_{01} modes.

Here we extract the radial profile as a function of position along the fiber axis in various ways:

1. Use the simulated profile for the fiber in regions where the beating in the spectrogram is clean and overlap the expected beat lengths for that profile with the spectrogram.
2. Manually extract the beat length from the spectrogram and from there invert the beat lengths to obtain the radius as a function of position.
3. Suppose an exponential taper with an unknown coefficient and vary the coefficient until the overlap with the spectrogram is optimized.

The taper profile occasionally deviates from the simulation enough to make 1 an imperfect choice. It helps to identify the mode but not necessarily extract the radius as a function of position. Commonly the fiber is thinned and stretched farther than our simulation predicts. So that using the fiber pulling simulation leads to decent overlaps on one side of the taper but not both. The issue then becomes

in defining the zero. The simulated profile seems to fit either side of the taper well locally when varying the origin of the taper. When overlapping the simulation with the experimental data, there is an error in where we define our zero. That is we do not know exactly the radius of the fiber from our measurements. We know how far we have moved and the pixel conversion, but not the radius of the fiber as a function of position. Therefore, we need to redefine the zero of the simulated radius vs position to overlap with the scattered power.

2 is both time consuming and difficult to automate for pulls that do not have clean spectrograms. The speckle in the scattering leads to frequency components that obfuscate the inverse beat frequencies we wish to extract. This broadband signal in the Fourier transform makes it difficult to automate the process of inverse beat length extraction.

We have found that 3 is the easiest to implement in practice. Fig. 5.18 demonstrates the overlap, in white, of the spectrogram. Here we use four separate exponential sections and vary the coefficients in each until the overlap appears to agree.

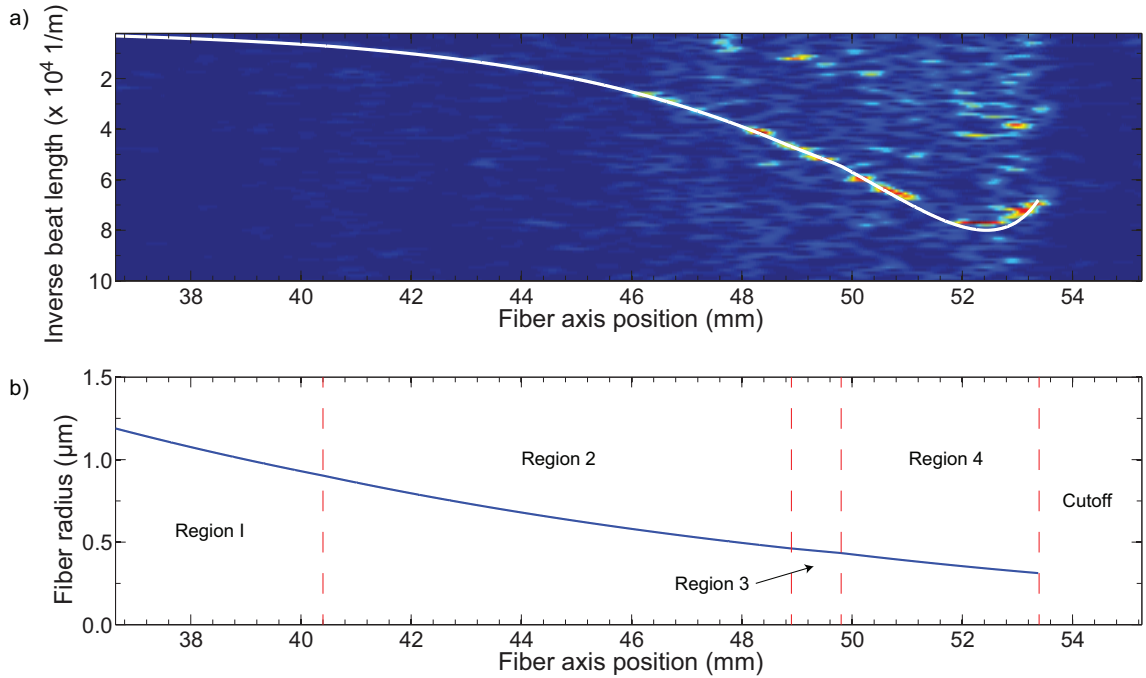


Figure 5.18: (a) A spectrogram of the data from Fig.5.17 with a white line representing the expected beat length for an extracted radius profile. (b) The extracted radius as a function of position along the fiber axis from stitching together four exponential geometries. Each region with a different coefficient is marked with red dashed lines.

Fig. 5.18 (b) shows the corresponding extracted radius as a function of position. With the extracted radius information, it could be possible to perform further studies of the power scattered as a function of radius for various modes.

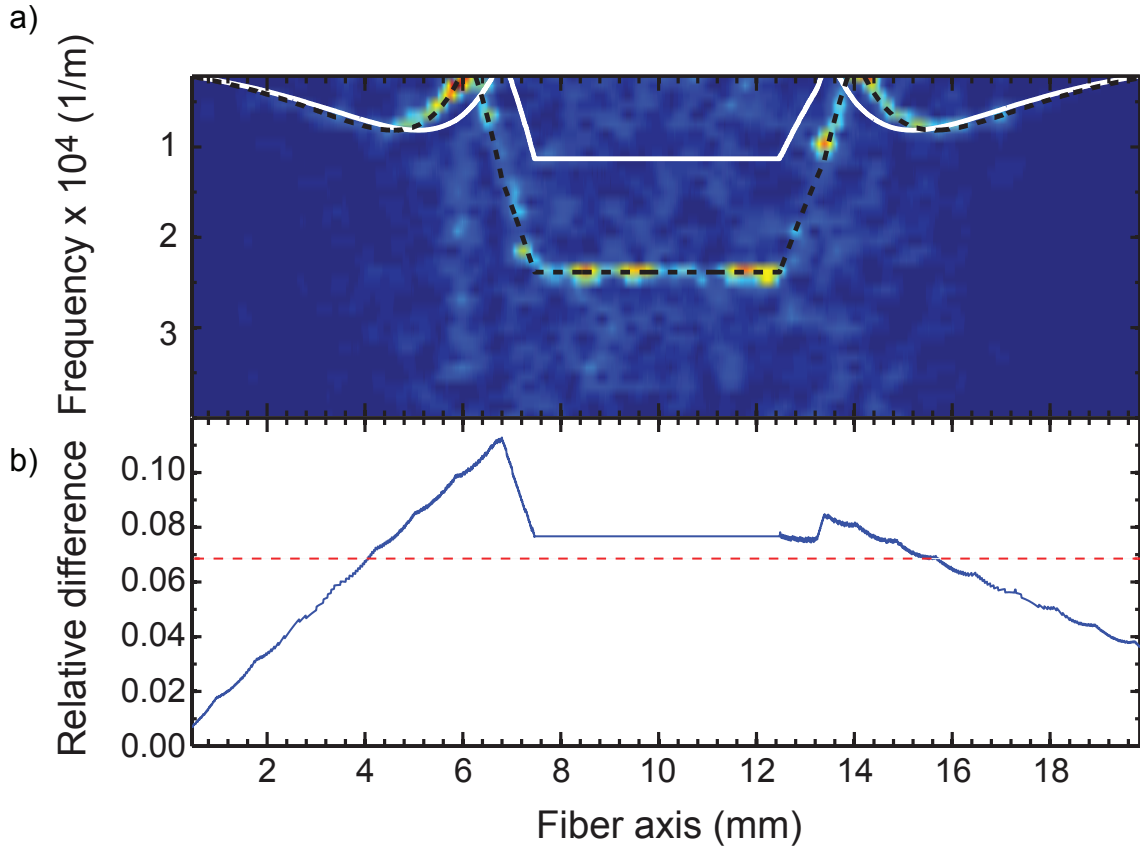


Figure 5.19: (a) Spectrogram overlaid with fiber simulation (solid white line) and four exponential taper sections (dashed black line). (b) The deviation in the measured overlap of extract radius to the simulation normalized to the simulated radius. The red line marks the RMS value.

Fig. 5.19 displays a similar means of extracting the fiber radius, this time for a fiber intended to have a 390 nm radius waist. Therefore, the HOMs do not cutoff in the spectrogram and we can clearly see the section that corresponds to the waist. We employ a similar technique as done before: start with the simulated fiber profile, fit the profile with an exponential, vary the coefficient in multiple exponential sections

until the overlap matches nicely. Despite, the 10^4 (1/m) difference on the fiber waist between the measured and simulated fiber this is only equal to a 30 nm difference in radius. Therefore on the fiber waist, with a HWHM (3 dB point) of about 1000 (1/m) this leads to an error in diameter of ± 5 nm.

Fig. 5.19 (b) displays the deviation in the extracted radius from the simulation. The red line denotes the RMS value of 0.069.

It is worth noting that this is an *in situ* method of measuring the radius of the ONF. We do not require a high NA imaging system and can extract the radius of the fiber waist down to about 640 nm diameter. If we were able to resolve the beating of the fundamental mode with HOMs, see Sec. 5.3.5, we could measure the radius of fibers down to 560 nm diameter. This is all for 780 nm light. If we were to scale to the equivalent V number using 405 nm input light we should be able to use this technique to measure the radii of ONFs down to a waist diameter of 290 nm without requiring high NA optics.

5.3.5 Optical fiber probe

The Rayleigh scattering provides an efficient means of measuring the modes on the ONF waist but the speckle leads to noise in the spectrogram observable in Fig. 5.12. These frequencies in the Fourier transform obscure the signal we wish to extract. Another means of detecting the mode information is to directly access the evanescent field. The Rayleigh scattering occurs from a radiating dipole polarized in the direction of the mode field. If we directly measure the variation in the evanescent

field intensity along the fiber axis the signal could be improved. To achieve this we use a tapered fiber probe.

Here, we use evanescent coupling from the ONF waist under study to the field of the fiber probe. For example, we produce a tapered fiber with a $3\ \mu\text{m}$ radius waist and directly bring the probe fiber into contact with the ONF waist from below. Some of the light propagating along the ONF waist will couple into the fundamental mode of the probe fiber. We then image the output of the fiber probe with a 5X Mitutoyo objective and 795 nm bandpass filter on an Andor Luca EMCCD.

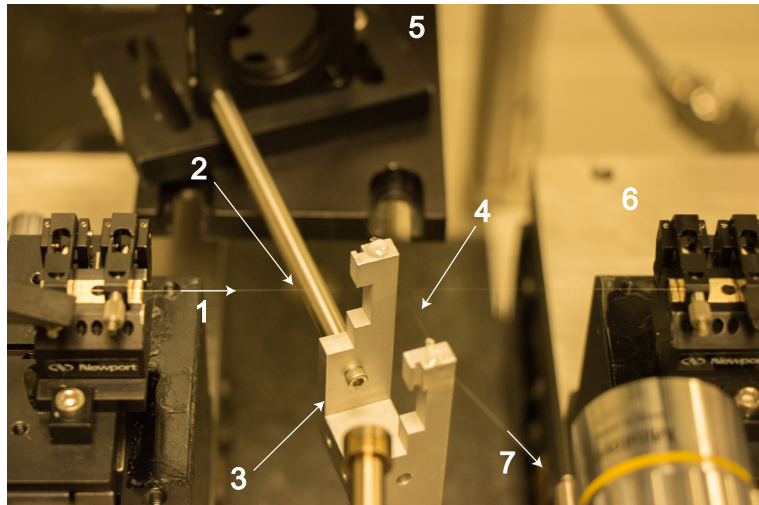


Figure 5.20: The fiber probe setup. 1) Direction of the input HOM beam. 2) ONF. 3) Aluminum fiber holder. 4) Probe fiber. 5) DRV014 stepper motors for positioning probe fiber. 6) XML 210 motors for positioning the ONF. 7) Output beam from the probe fiber to EMCCD.

Fig. 5.20 shows the experimental setup for the fiber probe measurement. A $3\ \mu\text{m}$ radius waist fiber probe (4 in Fig. 5.20) is epoxied onto an aluminum fiber holder (3 in Fig. 5.20). Two DRV014 Thorlabs stepper motors (fiber probe motors)

bring the fiber probe into contact with the ONF of interest(5 in Fig. 5.20). The fiber probe motors allow us to bring the fiber probe into contact from below the ONF and position the waist of the fiber probe in contact with the ONF (2 in Fig. 5.20). We raise the fiber probe motors in $50 \mu\text{m}$ steps until we observe light output from the fiber probe on the EMCCD. Then using the XML 210 pulling motors (6 in Fig. 5.20) we can step the ONF along the fiber probe, typically in $0.5 \mu\text{m}$ steps, and measure the collected power as a function of fiber position.

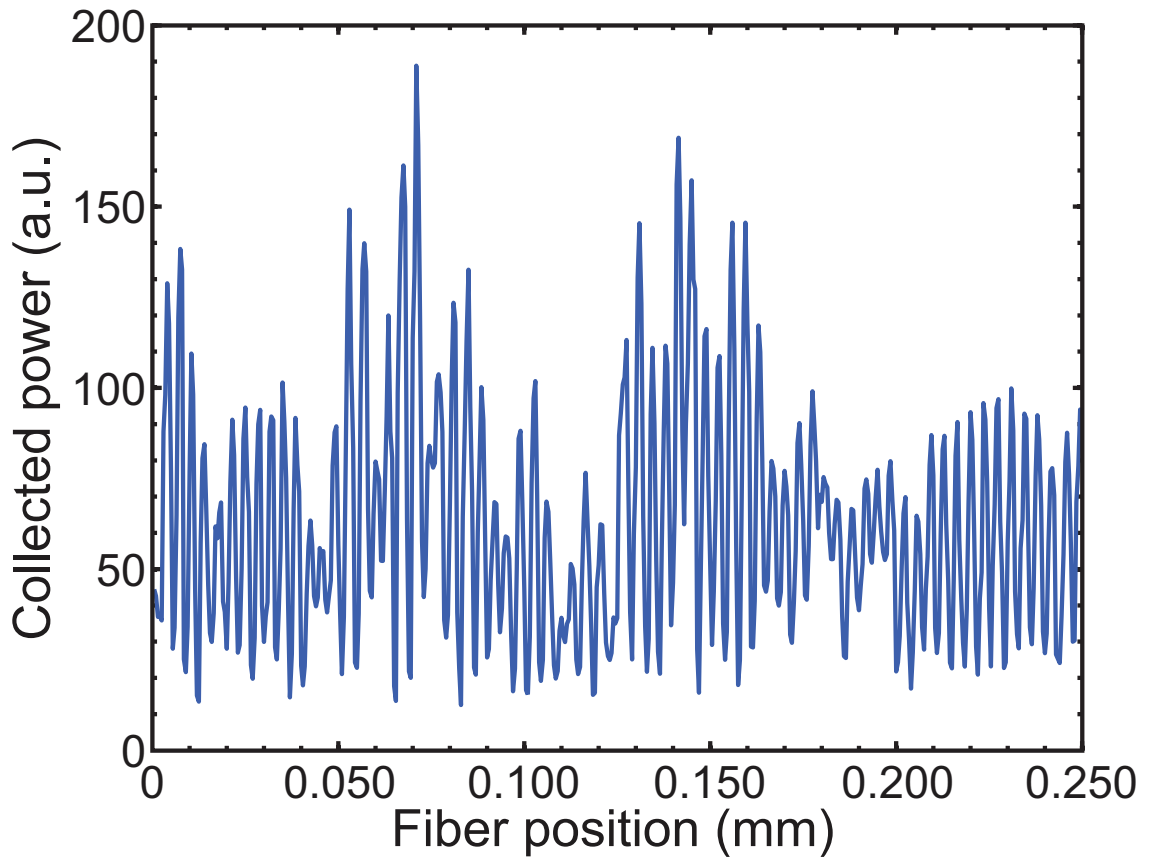


Figure 5.21: Power collected through the fiber probe as a function of position along ONF waist. The data is collected in 500 nm steps.

Fig. 5.21 shows the power collected as a function of fiber position in which we collected data in steps of 500 nm through the probe fiber. The dimensions of the ONF are $r_w = 400$ nm, $\Omega = 1$ mrad, and $L_w = 10$ mm. Here we intentionally launched the fundamental mode to test the resolution of the technique. The signal shows multiple modes beating together with a few wavelengths on the order of $4 \mu\text{m}$ and a longer wavelength on the order of $100 \mu\text{m}$.

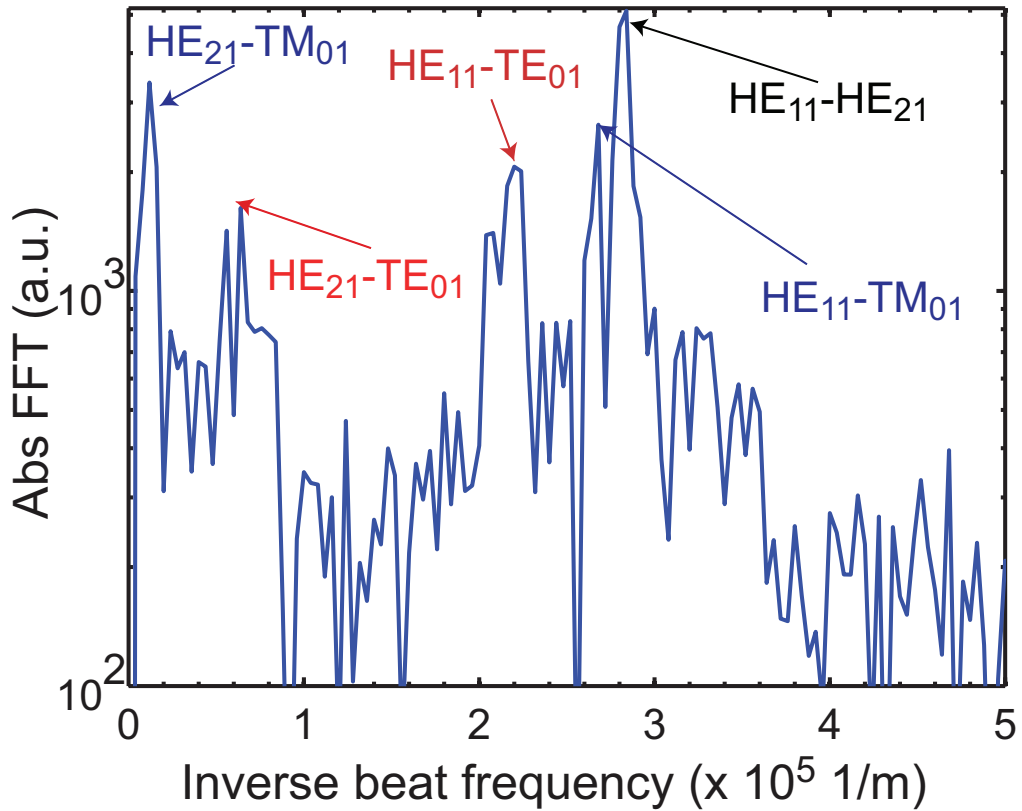


Figure 5.22: FFT of optical power collected using the fiber probe from Fig. 5.21. Here we can identify five frequencies detailed in Tab. 5.2. We note the y-axis is a log scale.

Figure 5.22 show the absolute value of the Fourier transform of the data from Fig. 5.21. Here we observe five peaks corresponding to the $HE_{21} - TM_{01}$, $HE_{21} - TE_{01}$, $HE_{11} - TE_{01}$, $HE_{11} - TM_{01}$, and $HE_{21} - HE_{11}$ modes beating together.

Mode	Sim. freq.(1/m)	Exp. freq. (1/m)
$HE_{11} - HE_{21}$	2.80×10^5	$2.84 \times 10^5 \pm 0.06 \times 10^5$
$HE_{11} - TM_{01}$	2.66×10^5	$2.68 \times 10^5 \pm 0.06 \times 10^5$
$HE_{11} - TE_{01}$	2.09×10^5	$2.20 \times 10^5 \pm 0.07 \times 10^5$
$HE_{21} - TE_{01}$	0.70×10^5	$0.64 \times 10^5 \pm 0.10 \times 10^5$
$HE_{21} - TM_{01}$	0.13×10^5	$0.12 \times 10^5 \pm 0.08 \times 10^5$

Table 5.2: Table comparing simulated inverse beat frequencies for a 380 nm ONF with extracted. The error bars correspond to the HWHM (3 dB point) relative to each peak.

Table 5.2 compares the inverse beat frequencies simulated in Fig. 5.2 to the frequencies extracted from Fig. 5.22. The values for the simulated frequency were chosen for an ONF with a 380 nm radius waist using the largest highest frequency peak in Fig. 5.22 to identify the radius and mode. The error bars correspond to the HWHM from the maximum of each peak. We see that the frequencies are in excellent agreement for a 380 nm fiber and note that this method has a finer resolution than the optics of the Rayleigh scattering method. Here we can both observe and identify the fundamental mode interfering with HOMs which was beyond the resolution of the Rayleigh scattering method.

5.3.6 Photodiode motor jog

We employ a more efficient means of data collection using a transimpedance amplifier set to a gain of 10^9 V/A to amplify the power collected on a photodiode (PD) from the fiber probe. This method allows us to observe the mode profile on an oscilloscope in real time as we sweep the motors. Using the jog mode of the motors, we are able to set a fixed velocity for both fiber pulling motors, and we sweep the ONF across the fiber probe. We typically sweep with velocities from 1 to 50 micrometers per second. The data is collected on a DPO7054 for hundreds to thousands of seconds, with a one sample collected per ms.

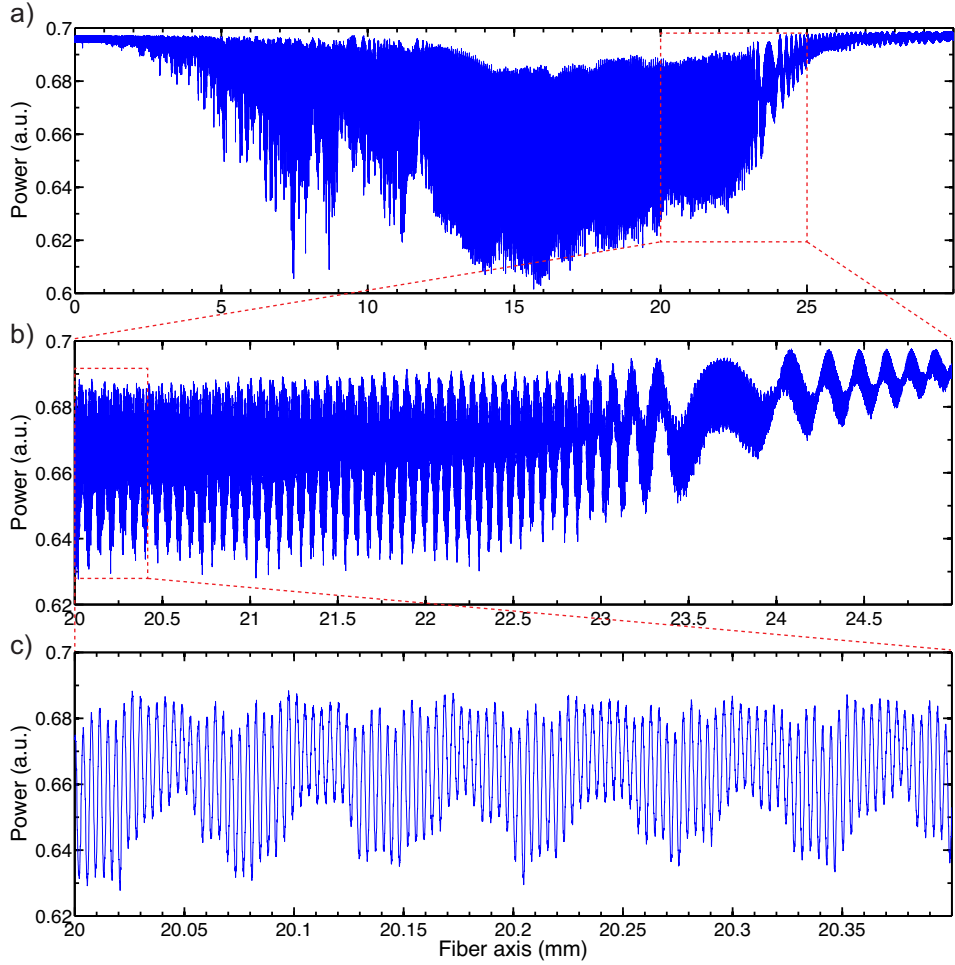


Figure 5.23: Probe power collected using a PD while jogging the pulling motors at $20 \mu\text{m/s}$. (a) Power collected while sweeping from the input taper across the ONF waist and output taper. (b) A zoom in along 20 mm to 25 mm. (c) A magnification of 20 mm to 20.35 mm.

Fig. 5.23 displays the probe power collected using the above method while jogging the motors at $20 \mu\text{m/s}$. Fig. 5.23 (a) shows a sweep from the input taper (0-12 mm), where we can see many modes interacting. The next two panels are magnifications show the beating from a $3 \mu\text{m}$ scale to tens of micrometers.

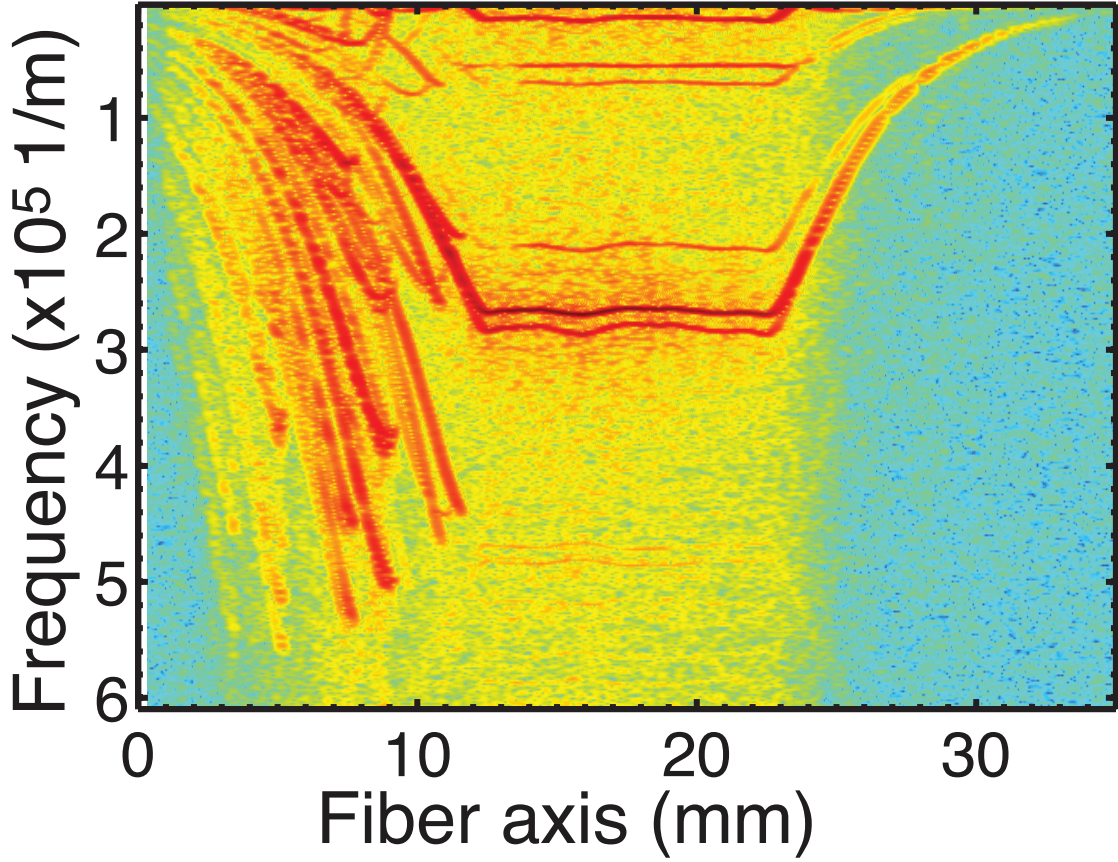
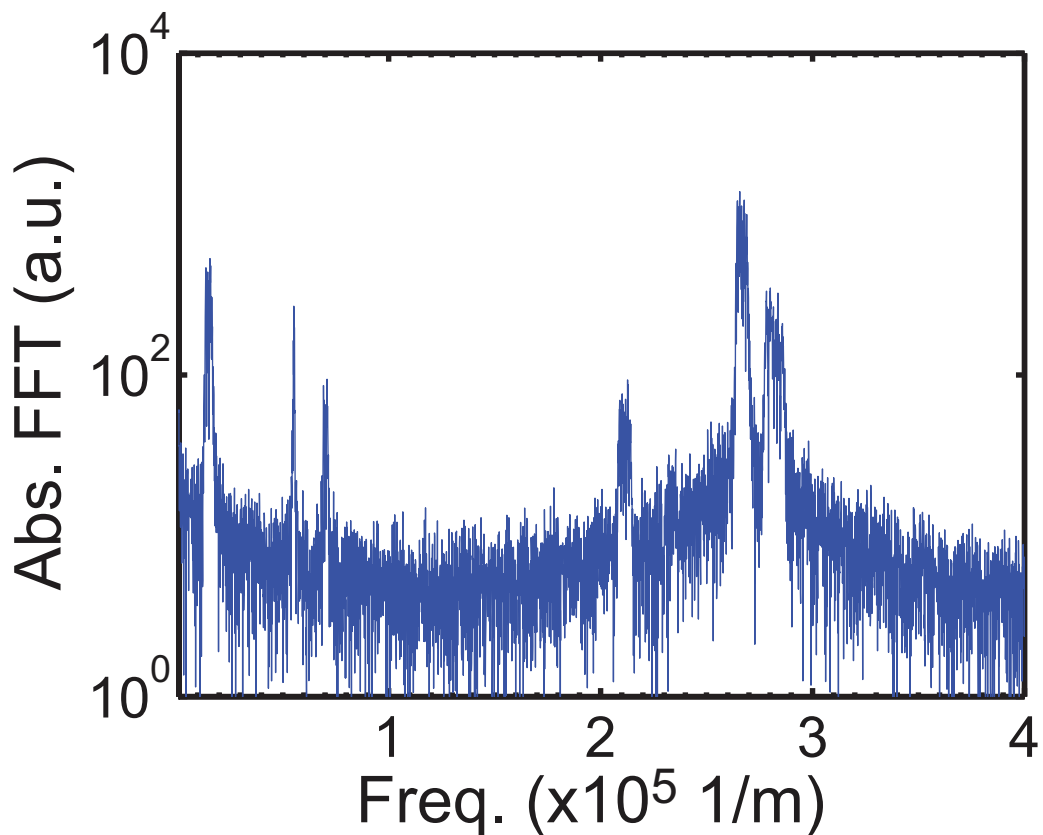


Figure 5.24: Spectrogram of data from Fig. 5.23 taken with the

Fig. 5.24 shows a spectrogram of the data from Fig. 5.23. We use a bin of 1024 points and overlap of 1019 points which is equivalent to 20.48 mm bins with a 20.38 mm overlap. It is clear that this 1 mrad taper was lossy since we can observe many modes cutting off on the input taper. On the ONF waist we observe 6 peaks: 5 corresponding to known modes and 1 occurring from a nonlinearity. At the taper output we observe a cleaner signal since the higher-order mode excitations were cutoff before the waist.



Mode	Measured freq. (1/m)
$HE_{11} - HE_{21}$	$2.82 \times 10^5 \pm 0.04 \times 10^5$
$HE_{11} - TM_{01}$	$2.65 \times 10^5 \pm 0.025 \times 10^5$
$HE_{11} - TE_{01}$	$2.11 \times 10^5 \pm 0.02 \times 10^5$
$HE_{21} - TE_{01}$	$7.0 \times 10^4 \pm 0.125 \times 10^4$
$HE_{21} - TM_{01}$	$1.50 \times 10^4 \pm 0.125 \times 10^4$

Figure 5.25: FFT of power collected from ONF waist from 5.23 and table of extracted beat frequencies.

Fig. 5.25 displays the absolute value of the FFT of the power collected corresponding to the ONF waist from Fig. 5.23. The error bars are extracted from the HWHM from the peak. We observe the peaks for each of the allowed modes of propagation, all in excellent agreement with simulated frequencies for a 380 nm radius fiber, see Table. 5.2.

We follow the same method described earlier for extracting the radius. This time we vary two exponentials for either side of the taper and overlap for each of the five modes, see Fig. 5.26.

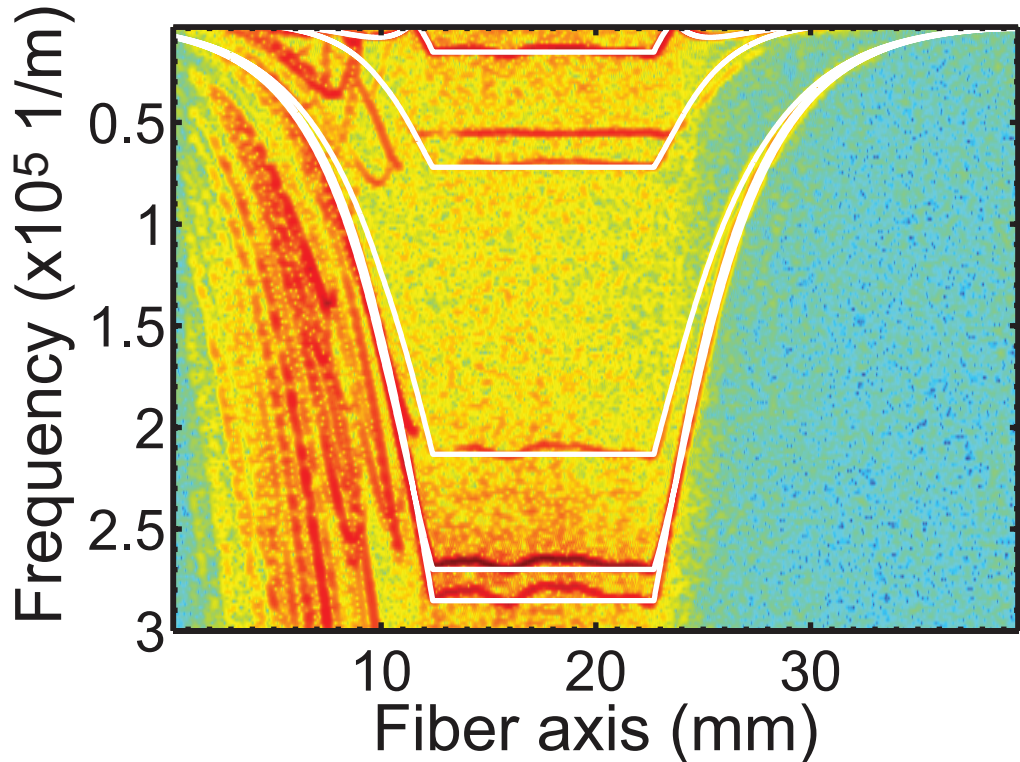


Figure 5.26: Spectrogram of data from Fig. 5.23 with radius extraction overlap (white curves).

We compare measured radius to the expected radius from simulation in Fig. 5.27.

Here we see that the agreement is slightly better with an RMS value of 0.06. The waist radius of 380 nm is closer to the expected radius of 400 nm.

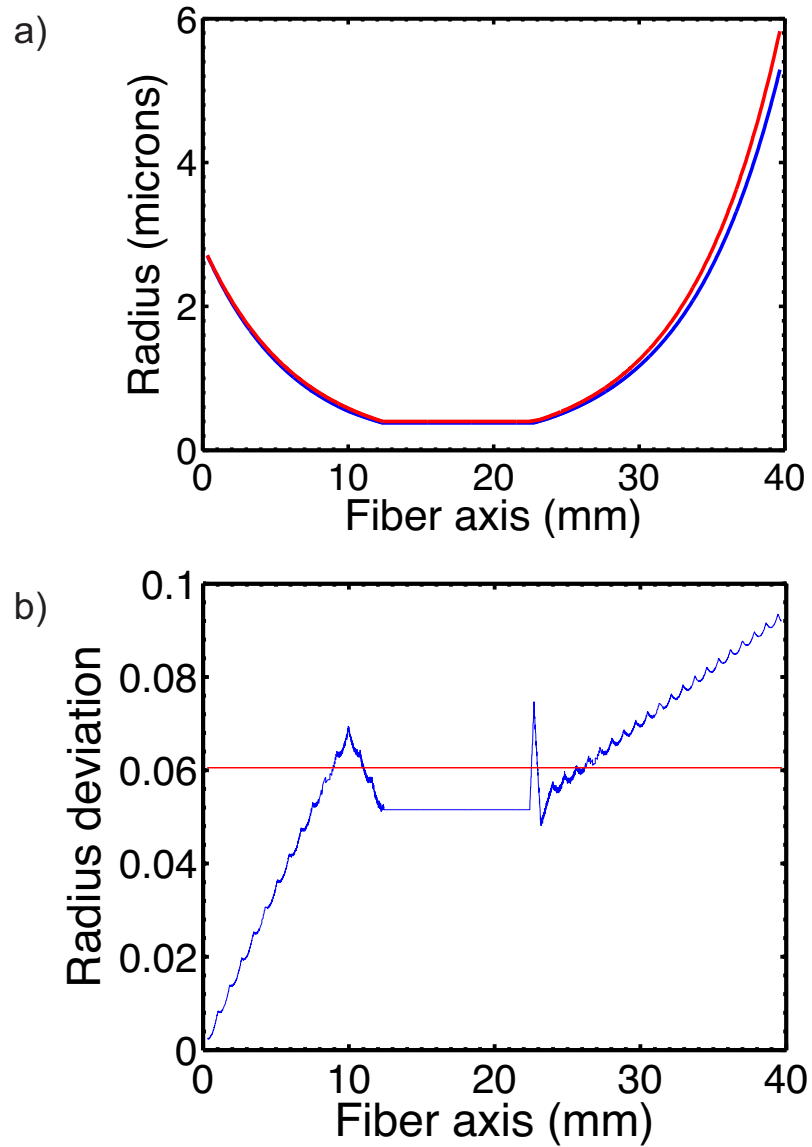


Figure 5.27: a) Measured radius (blue) and simulated radius (red) vs position. b) Deviation of the simulated radius with the red line representing the RMS value of 0.06.

Using the HWHM frequency range for the HE_{21} mode beating with TM_{01} mode we arrive at an error of ± 6 nm. Once again it is worth reiterating that these beat frequency measurements allow for nondestructive precise measurements of the fiber radius.

5.4 Conclusion

We demonstrated the ability to identify and control the mode on the ONF waist in this chapter. We use two different techniques: Rayleigh scattering and evanescent coupling with a fiber probe. We note that the ONF appears to act as a mode converter when light propagates through the waveguide. Whether this is a fundamental property of the ONF or simply a technical constraint imposed by working with fiber clamps and in tight confines inside the clean room is still up for debate. Further study is required using IDIOM on microfibers to better understand this phenomena. Rayleigh scattering measurements inherently have more noise than the fiber probe technique, but provide a faster real time analysis on the mode distribution. The fiber probe provides an improved resolution compared to the Rayleigh scattering technique and is capable of distinguishing between the fundamental mode beating with any of the HOMs. It is worth noting that these techniques are accurate means of measure the fiber radius.

Chapter 6: Conclusions and Outlook

In the preceding five chapters, we have described the fabrication and analysis of ONFs usable for a hybrid quantum system composed of a superconducting resonator and cold trapped ^{87}Rb atoms.

In Chapter 2 we outlined the fabrication process providing details on the cleaning, alignment, and full pulling process. We also provided details on the derivation of the pulling algorithm. Using microscopy we have verified that our pulling geometry is in excellent agreement with simulation. We have also report the lowest loss ONFs with 2.6×10^{-5} dB/mm marking an improvement of 2 orders of magnitude when compared to previous work. When following the pulling and transfer procedures outlined we report the highest transmission reported through an ONF with 400 mW of optical power transferred through.

Chapter 3 details an analysis of the modal evolution in an ONF taper. We were able to identify the higher-order modes the fundamental mode couples to during the tapering process Using a genetic algorithm we are able to provide better bounds on ONF geometries to produce desired transmission given specified length constraints.

In Chapter 4 we demonstrate the highest reported transmissions through ONFs when intentionally launching HOMs. Here, we are able to demonstrate comparable

losses when launching HOMs to losses reported through ONFs when launching the fundamental mode. Finally in Chapter 5 we provide a detailed analysis identifying the mode structure on the ONF waist using both Rayleigh scattering and evanescent coupling.

Below we describe the outlook and next steps.

6.1 Hybrid System

Fig. 6.1 shows our groups current vision of the setup for the hybrid quantum system. The Rayleigh scattering from an ONF, while approximately parts in a million, will still form quasiparticles in the SC. Therefore we want to minimize the cross section of scattered light from the ONF by using the SC resonator geometry to our advantage. With this in mind, we polish the Sapphire substrate to the inductor edge. This allows us to place the ONF in the plane of the chip, parallel to the 100 nm-400 nm layer of deposited Al rather than above the entire chip. This reduces the light scattered cross section by at least a factor of 20.

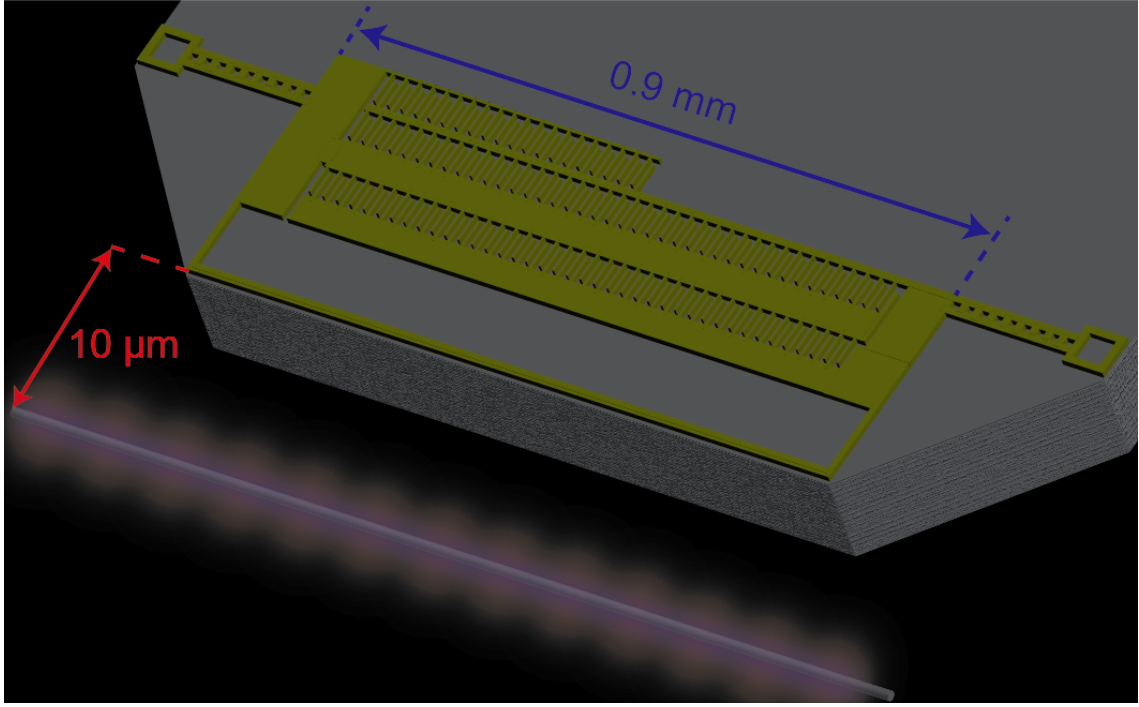


Figure 6.1: The setup of the hybrid quantum system. The superconducting lumped-element LC resonator was fabricated from a thin-film of Al deposited on a sapphire chip. The sapphire chip was polished by Nesco Lettsome at Neocera so that the edge of the sapphire chip was at the edge of the inductor. The ONF is in the plane of the SC resonator and is $10 \mu\text{m}$ from the edge of the inductor. Atoms are trapped in standing wave maxima approximately every 500 nm .

The ONF trap requires that atoms are cooled for efficient loading. Therefore the atoms will need to be cooled and trapped elsewhere in the setup. One approach that the group has pursued is using a pyramid-type MOT [153, 154] in a chamber anchored to the 3.5 K stage of the dilution refrigerator which has Watts of cooling power. Here we can place the necessary magnetic coils away from the supercon-

ducting chip. However, this means that we will need an optical conveyor belt to transport the atoms from the MOT along the ONF waist to the chip. We need to determine the maximum distance we can transport the atoms while minimizing atomic loss. This process will require great care, for example using adiabatic protocols [155] or dynamic controls [132]. The atomic transport process is an important design consideration. Fortunately we can study this process at room temperature.

To introduce atoms into the dilution refrigerator one approach the group is currently developing is a 2D MOT atomic beam source [156]. The 2D MOT would attach to one of the ports on the vacuum jacket of the dilution refrigerator and will be used to load the pyramid MOT. A room temperature 2D MOT, could in theory, be directly attached to the dilution refrigerator as a separate module.

6.2 ONF studies

There are many other interesting ONF issues that we did not explore in this thesis. For example it would be interesting to optimize an ONF to maximize the spontaneous emission back into the fiber, a term known as Γ_{1D} . Fig. 6.2 shows a parameter search calculating Γ_{1D} as a function of ONF radius and atomic displacement from the ONF surface.

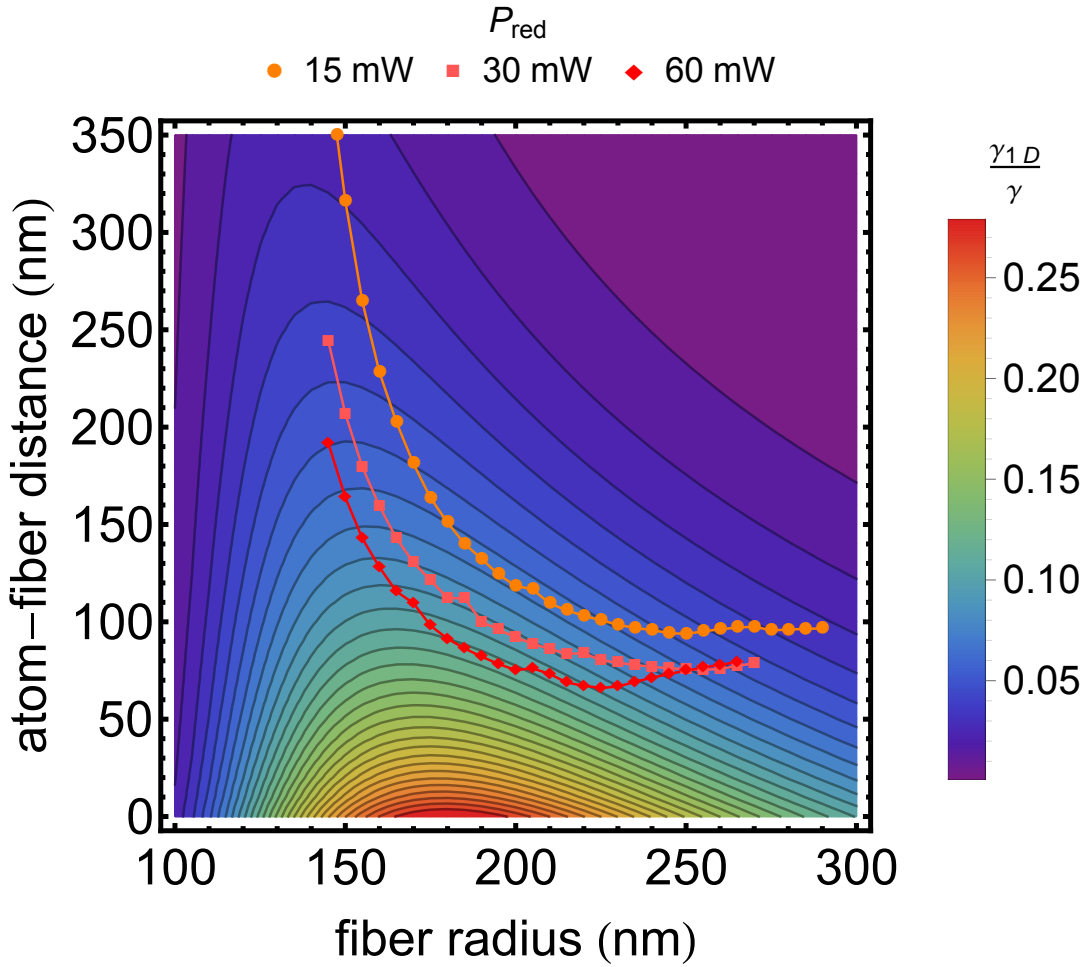


Figure 6.2: Γ_{1D} calculated in the parameter space of fiber radius and distance from the fiber surface. This space is then searched for a $300 \mu\text{K}$ trap depth for 15 mW (circle), 30 mW (square), and 60 mW (diamond) in the red-detuned trapping beam.

Using the information in Fig. 6.2 we could pull a fiber that maximizes Γ_{1D} for atoms located at realistic trapping sites. With an ONF maximized for Γ_{1D} it will be possible to pursue self-organization of atoms into crystalline structures [82].

This work opens new avenues for the studies of HOMS in ONFS using the interference of HOMs we can create unique trapping geometries. A possible next steps would be to design and fabricate an ONF system capable of loading and trapping atoms using the HOMs that such an ONF supports. This would reduce the level of optical power in the atom trap and reduce the Rayleigh scattering from the ONF, two important parameters in the pursuit of coupling atoms to superconducting devices.

Appendix A: Fiber Modes

Here we derive the bound modes for a step index fiber. We generally follow the work of Refs. [74, 131, 157, 158].

A.1 Cylindrical coordinates

$$\nabla \cdot \mathbf{A} = \frac{1}{r} \partial_r [r A_r] + \frac{1}{r} \partial_\phi A_\phi + \partial_z A_z \quad (\text{A.1})$$

$$\nabla \times \mathbf{A} = \left(\frac{1}{r} \partial_\phi A_z - \partial_z A_\phi \right) \hat{r} + (\partial_z A_r - \partial_r A_z) \hat{\phi} + \frac{1}{r} (\partial_r [r A_\phi] - \partial_\phi A_r) \hat{z} \quad (\text{A.2})$$

$$\nabla^2 = \partial_r^2 + \frac{1}{r} \partial_r + \frac{1}{r^2} \partial_\phi^2 + \partial_z^2 \quad (\text{A.3})$$

A.2 Maxwell's Equations

Maxwell's equations in a material with dielectric constant ϵ and magnetic permeability μ are given by

$$\nabla \cdot \mathbf{E} = \frac{\rho}{\epsilon} \quad (\text{A.4})$$

$$\nabla \cdot \mathbf{B} = 0 \quad (\text{A.5})$$

$$\nabla \times \mathbf{E} = -\mu \partial_t \mathbf{H} \quad (\text{A.6})$$

$$\nabla \times \mathbf{H} = \epsilon \partial_t \mathbf{E} \quad (\text{A.7})$$

Using the curl equations we arrive at six separate equations

$$\epsilon \partial_t E_r = \frac{1}{r} \partial_\phi H_z - \partial_z H_\phi \quad (\text{A.8})$$

$$\epsilon \partial_t E_\phi = \partial_z H_r - \partial_r H_z \quad (\text{A.9})$$

$$\epsilon \partial_t E_z = \frac{1}{r} (\partial_r [r H_\phi] - \partial_\phi H_r) \quad (\text{A.10})$$

$$-\mu \partial_t H_r = \frac{1}{r} \partial_\phi E_z - \partial_z E_\phi \quad (\text{A.11})$$

$$-\mu \partial_t H_\phi = \partial_z E_r - \partial_r E_z \quad (\text{A.12})$$

$$-\mu \partial_t H_z = \frac{1}{r} (\partial_r [r E_\phi] - \partial_\phi E_r) \quad (\text{A.13})$$

$$(\text{A.14})$$

A.3 Cylindrically symmetric dielectric waveguide

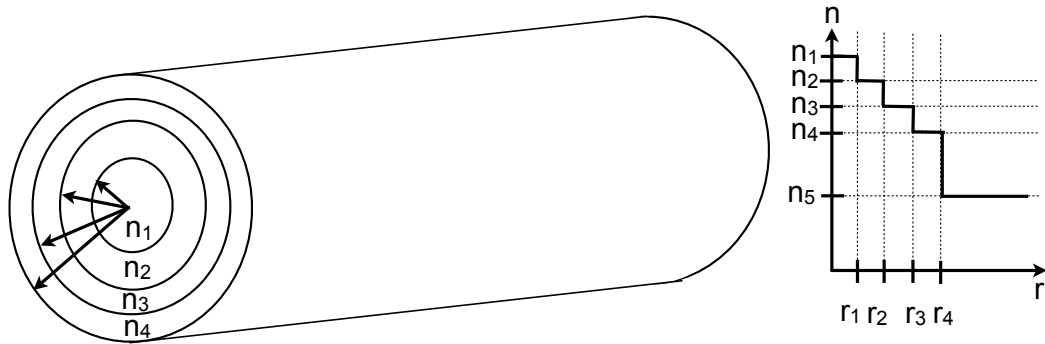


Figure A.1: Cylindrically symmetric waveguide, with constant layers of index of refraction.

For the moment, we envision a waveguide with radial layers of azimuthally symmetric dielectric functions and free space magnetic permeability, see Fig A.1. This symmetry implies solutions of the form,

$$\mathbf{E} = \mathbf{E}_0(\mathbf{r}, \phi) \exp[i(\omega t - \beta z)]$$

$$\mathbf{H} = \mathbf{H}_0(\mathbf{r}, \phi) \exp[i(\omega t - \beta z)]$$

inside each radial layer. Using the above it is clear that

$$\partial_t \mathbf{E} = i\omega \mathbf{E}$$

$$\partial_t \mathbf{H} = i\omega \mathbf{H}$$

$$\partial_z \mathbf{E} = -i\beta \mathbf{E}$$

$$\partial_z \mathbf{H} = -i\beta \mathbf{H}$$

Applying the above to equations A.8 we find

$$i\omega\epsilon E_r = \frac{1}{r} \partial_\phi H_z + i\beta H_\phi$$

$$i\omega\epsilon E_\phi = -i\beta H_r - \partial_r H_z$$

$$i\omega\epsilon E_z = \frac{1}{r} (\partial_r [r H_\phi] - \partial_\phi H_r)$$

$$-i\omega\mu H_r = \frac{1}{r} \partial_\phi E_z + i\beta E_\phi$$

$$-i\omega\mu H_\phi = -i\beta E_r - \partial_r E_z$$

$$-i\omega\mu H_z = \frac{1}{r} (\partial_r [r E_\phi] - \partial_\phi E_r)$$

which we can now use to solve for the transverse components of the field.

$$\begin{aligned} i\omega\epsilon E_r &= \frac{1}{r} \partial_\phi H_z + i\beta H_\phi \\ &= \frac{1}{r} \partial_\phi H_z + i\beta \frac{1}{-i\omega\mu} (-i\beta E_r - \partial_r E_z) \\ &= \frac{1}{r} \partial_\phi H_z + \frac{\beta}{\omega\mu} \partial_r E_z + \frac{i\beta^2 E_r}{\omega\mu} \\ E_r &= \frac{-i}{\epsilon\omega - \frac{\beta^2}{\mu\omega}} \left(\frac{1}{r} \partial_\phi H_z + \frac{\beta}{\omega\mu} \partial_r E_z \right) \\ E_r &= \frac{-i\beta}{\mu\epsilon\omega^2 - \beta^2} \left[-\frac{\mu\omega}{\beta r} \partial_\phi H_z + \partial_r E_z \right]. \end{aligned}$$

Similarly, we arrive at

$$E_r = \frac{-i\beta}{\mu\epsilon\omega^2 - \beta^2} \left[\frac{\mu\omega}{\beta r} \partial_\phi H_z + \partial_r E_z \right] \quad (\text{A.15})$$

$$E_\phi = \frac{-i\beta}{\mu\epsilon\omega^2 - \beta^2} \left[-\frac{\mu\omega}{\beta} \partial_r H_z + \frac{1}{r} \partial_\phi E_z \right] \quad (\text{A.16})$$

$$H_r = \frac{-i\beta}{\mu\epsilon\omega^2 - \beta^2} \left[-\frac{\epsilon\omega}{\beta r} \partial_\phi E_z + \partial_r H_z \right] \quad (\text{A.17})$$

$$H_\phi = \frac{-i\beta}{\mu\epsilon\omega^2 - \beta^2} \left[\frac{\epsilon\omega}{\beta} \partial_r E_z + \frac{1}{r} \partial_\phi H_z \right]. \quad (\text{A.18})$$

Solving for the complete modal equations is reduced to finding the fields in the longitudinal direction. We take $\mu = \mu_0$ and $k = \mu_0\epsilon\omega$, using the wave equation we find that

$$\left[\partial_r^2 + \frac{1}{r} \partial_r + \frac{1}{r^2} \partial_\phi + (k^2 - \beta^2) \right] \begin{bmatrix} E_z(r, \phi) \\ H_z(r, \phi) \end{bmatrix} = 0. \quad (\text{A.19})$$

Separation of variables yields solutions of the form

$$\begin{bmatrix} E_z(r, \phi) \\ H_z(r, \phi) \end{bmatrix} = \begin{bmatrix} R_E(r) \\ R_H(r) \end{bmatrix} \text{Exp}(\pm l\phi) \quad (\text{A.20})$$

where l is a nonnegative number. This leads to the differential equation

$$\left[\partial_r^2 + \frac{1}{r} \partial_r + \left(k^2 - \beta^2 - \frac{l^2}{r^2} \right) \right] \begin{bmatrix} R_E(r) \\ R_H(r) \end{bmatrix} = 0. \quad (\text{A.21})$$

The above is Bessel's differential equation, which has solutions of the form,

$$R(r) = \begin{cases} c_1 J_l(hr) + c_2 Y_l(hr), & k^2 - \beta^2 > 0 \\ c_1 I_l(qr) + c_2 K_l(qr), & k^2 - \beta^2 < 0 \end{cases} \quad (\text{A.22})$$

where we define $h = \sqrt{k^2 - \beta^2}$ and $q = \sqrt{\beta^2 - k^2}$.

Now we apply these types of solutions to a two layer step index fiber.

A.4 Two layer step index fiber

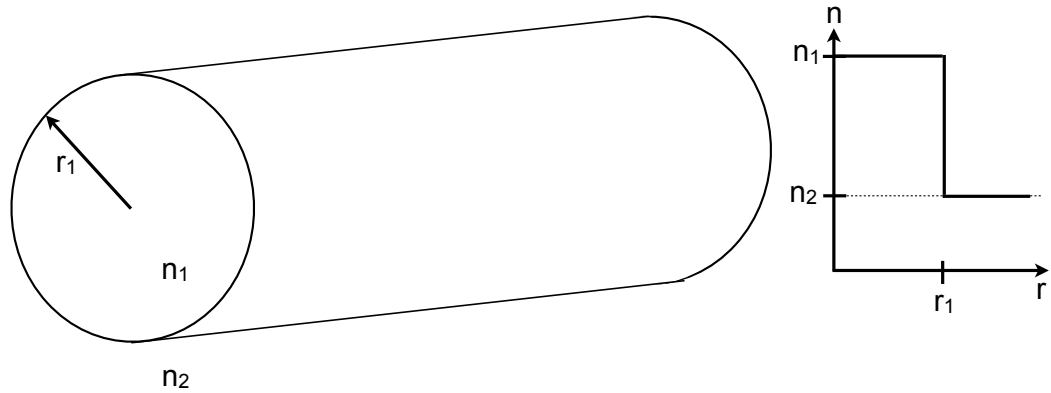


Figure A.2: Cylindrically symmetric waveguide, with a core of index of refraction n_1 out to radius of r_1 and an infinite cladding with index of refraction n_2 , where $n_1 > n_2$.

The fiber waveguide in the two layer model is composed of a core with constant dielectric ϵ_1 out to a radius $r = a$, and an infinite cladding from $r = a$ to ∞ with dielectric constant ϵ_2 . These boundary conditions reduce the longitudinal

components to

$$\begin{aligned}
E_z(r, \phi) &= AJ_l(hr) \text{Exp}[i(\omega t - \beta z \pm l\phi)], \quad r < a \\
H_z(r, \phi) &= BJ_l(hr) \text{Exp}[i(\omega t - \beta z \pm l\phi)], \quad r < a \\
E_z(r, \phi) &= CK_l(qr) \text{Exp}[i(\omega t - \beta z \pm l\phi)], \quad r > a \\
H_z(r, \phi) &= DK_l(qr) \text{Exp}[i(\omega t - \beta z \pm l\phi)], \quad r > a.
\end{aligned} \tag{A.23}$$

As a result of the azimuthal symmetry, there exist two degenerate solutions corresponding to $\pm l\phi$. These solutions correspond to a left or right circulating solution as the mode advances along the fiber axis. We have the freedom to choose either set as our solution; however, for the moment we will keep the solutions as general as possible.

Applying equation A.23 to equation A.15 we find for $r < a$

$$E_{r,\pm} = \frac{-i\beta}{h^2} \left[\pm \frac{i\mu_0\omega l}{\beta r} BJ_l(hr) + AhJ'_l(hr) \right] \text{Exp}[i(\omega t - \beta z \pm l\phi)] \tag{A.24}$$

$$E_{\phi,\pm} = \frac{-i\beta}{h^2} \left[\pm \frac{il}{r} AJ_l(hr) - \frac{\mu_0\omega h}{\beta} BJ'_l(hr) \right] \text{Exp}[i(\omega t - \beta z \pm l\phi)] \tag{A.25}$$

$$E_{z,\pm} = AJ_l(hr) \text{Exp}[i(\omega t - \beta z \pm l\phi)] \tag{A.26}$$

$$H_{r,\pm} = \frac{-i\beta}{h^2} \left[\mp \frac{i\epsilon_1\omega l}{\beta r} AJ_l(hr) + BhJ'_l(hr) \right] \text{Exp}[i(\omega t - \beta z \pm l\phi)] \tag{A.27}$$

$$H_{\phi,\pm} = \frac{-i\beta}{h^2} \left[\frac{\epsilon_1\omega}{\beta} AhJ'_l(hr) \pm \frac{il}{r} BJ_l(hr) \right] \text{Exp}[i(\omega t - \beta z \pm l\phi)] \tag{A.28}$$

$$H_{z,\pm} = BJ_l(hr) \text{Exp}[i(\omega t - \beta z \pm l\phi)] \tag{A.29}$$

$$(A.30)$$

and for $r > a$

$$E_{r,\pm} = \frac{i\beta}{q^2} \left[\pm \frac{i\mu_0\omega l}{\beta r} DK_l(qr) + CqK'_l(qr) \right] \text{Exp}[i(\omega t - \beta z \pm l\phi)] \quad (\text{A.31})$$

$$E_{\phi,\pm} = \frac{i\beta}{q^2} \left[\pm \frac{il}{r} CK_l(qr) - \frac{\mu_0\omega q}{\beta} DK'_l(qr) \right] \text{Exp}[i(\omega t - \beta z \pm l\phi)] \quad (\text{A.32})$$

$$E_{z,\pm} = CK_l(hr) \text{Exp}[i(\omega t - \beta z \pm l\phi)] \text{Exp}[i(\omega t - \beta z \pm l\phi)] \quad (\text{A.33})$$

$$H_{r,\pm} = \frac{i\beta}{q^2} \left[\mp \frac{i\epsilon_2\omega l}{\beta r} CK_l(qr) + DqK'_l(qr) \right] \text{Exp}[i(\omega t - \beta z \pm l\phi)] \quad (\text{A.34})$$

$$H_{\phi,\pm} = \frac{i\beta}{q^2} \left[\frac{\epsilon_2\omega}{\beta} CqK'_l(qr) \pm \frac{il}{r} DK_l(qr) \right] \text{Exp}[i(\omega t - \beta z \pm l\phi)] \quad (\text{A.35})$$

$$H_{z,\pm} = DK_l(qr) \text{Exp}[i(\omega t - \beta z \pm l\phi)] \quad (\text{A.36})$$

$$(\text{A.37})$$

where, $J'_l(hr) = \frac{\partial J_l(hr)}{\partial(hr)}$, $K'_l(qr) = \frac{\partial K_l(qr)}{\partial(qr)}$.

A.4.1 Boundary Conditions

The parallel E and H fields must be continuous across the boundary at $r=a$.

This implies that E_z , H_z , E_ϕ and H_ϕ must be continuous across the boundary at $r=a$. This results in

$$AJ_l(ha) - CK_l(qa) = 0 \quad (\text{A.38})$$

$$BJ_l(ha) - DK_l(qa) = 0 \quad (\text{A.39})$$

$$\pm \frac{\beta l}{h^2 a} AJ_l(ha) + \frac{i\mu_0\omega}{h} BJ'_l(ha) \pm \frac{\beta l}{q^2 a} CK_l(qa) + \frac{i\mu_0\omega}{q} DK'_l(qa) = 0 \quad (\text{A.40})$$

$$\frac{-i\epsilon_1\omega}{h} AJ'_l(ha) \pm \frac{\beta l}{h^2 a} BJ_l(ha) - \frac{i\epsilon_2\omega}{q} CK'_l(qa) \pm \frac{l\beta}{q^2 a} DK_l(qa) = 0 \quad (\text{A.41})$$

which can be recast in the form,

$$\begin{bmatrix} J_l(ha) & 0 & -K_l(qa) & 0 \\ 0 & J_l(ha) & 0 & -K_l(qa) \\ \pm \frac{\beta l}{h^2 a} J_l(ha) & \frac{i\mu_0\omega}{h} J'_l(ha) & \pm \frac{\beta l}{q^2 a} K_l(qa) & \frac{i\mu_0\omega}{q} D K'_l(qa) \\ \frac{-i\epsilon_1\omega}{h} J'_l(ha) & \pm \frac{\beta l}{h^2 a} J_l(ha) & -\frac{i\epsilon_2\omega}{q} K'_l(qa) & \pm \frac{l\beta}{q^2 a} D K_l(qa) \end{bmatrix} \begin{bmatrix} A \\ B \\ C \\ D \end{bmatrix} = 0. \quad (\text{A.42})$$

The determinant of the above equation must vanish in order for there to be a nontrivial solution for A, B, C, D . This results in an eigenvalue problem for β ,

$$\left[\frac{1}{ha} \frac{J'_l(ha)}{J_l(ha)} + \frac{1}{qa} \frac{K'_l(qa)}{K_l(qa)} \right] \left[\frac{n_1^2}{ha} \frac{J'_l(ha)}{J_l(ha)} + \frac{n_2^2}{qa} \frac{K'_l(qa)}{K_l(qa)} \right] = l^2 \left[\left(\frac{1}{ha} \right)^2 + \left(\frac{1}{qa} \right)^2 \right]^2 \frac{\beta^2}{k_0^2} \quad (\text{A.43})$$

Now that we know a nontrivial solution exist we use the boundary conditions to solve for the constants,

$$\frac{C}{A} = \frac{J_l(ha)}{K_l(qa)} \quad (\text{A.44})$$

$$\frac{B}{A} = \pm \frac{il\beta}{\mu_0\omega} \left[\left(\frac{1}{ha} \right)^2 + \left(\frac{1}{qa} \right)^2 \right] \left[\frac{J'_l(ha)}{ha J_l(ha)} + \frac{K'_l(qa)}{qa K_l(qa)} \right]^{-1} \quad (\text{A.45})$$

$$\frac{D}{A} = \frac{BC}{A^2} = \frac{B}{A} \frac{J_l(ha)}{K_l(qa)} - \frac{l^2 \beta^2}{k_0^2} \left[\left(\frac{1}{ha} \right)^2 + \left(\frac{1}{qa} \right)^2 \right]^2. \quad (\text{A.46})$$

Once we obtain A , the power normalization coefficient (see Sec. A.5), we have a complete set of solutions for the Electromagnetic fields for a given fiber with radius, a , and indices of refraction, n_1 and n_2 .

A.4.2 The propagation constant and fiber modes

We rewrite Eqn. A.43 as

$$0 = n_1^2 \left[\frac{J'_l(ha)}{haJ_l(ha)} \right]^2 + \left((n_1^2 + n_2^2) \frac{K'_l(qa)}{qaK_l(qa)} \right) \left[\frac{J'_l(ha)}{haJ_l(ha)} \right] + \left(n_2^2 \frac{K'_l(qa)}{qaK_l(qa)} - \frac{l^2\beta^2}{k_0^2} \left[\left(\frac{1}{ha} \right)^2 + \left(\frac{1}{qa} \right)^2 \right]^2 \right).$$

Solving for $\left[\frac{J'_l(ha)}{haJ_l(ha)} \right]$, we obtain

$$\left[\frac{J'_l(ha)}{haJ_l(ha)} \right] = -\frac{(n_1^2 + n_2^2)}{2n_1^2} \left[\frac{K'_l(qa)}{qaK_l(qa)} \right] \pm R \quad (\text{A.47})$$

$$R = \sqrt{\frac{(n_1^2 - n_2^2)^2}{(2n_1^2)^2} \left[\frac{K'_l(qa)}{qaK_l(qa)} \right]^2 + \frac{l^2\beta^2}{k_0^2} \left[\left(\frac{1}{ha} \right)^2 + \left(\frac{1}{qa} \right)^2 \right]^2}. \quad (\text{A.48})$$

Recalling the recursion relations,

$$\begin{aligned} J'_l(x) &= J_{l-1}(x) - \frac{l}{x} J_l(x) \\ K'_l(x) &= -\frac{1}{2} [K_{l-1}(x) + K_{l+1}(x)], \end{aligned}$$

we find

$$\frac{J_{l-1}(ha)}{haJ_l(ha)} = \frac{(n_1^2 + n_2^2)}{4n_1^2} \left[\frac{K_{l-1}(qa) + K_{l+1}(qa)}{qaK_l(qa)} \right] + \frac{l}{(ha)^2} \pm R \quad (\text{A.49})$$

$$R = \sqrt{\frac{(n_1^2 - n_2^2)^2}{(4n_1^2)^2} \left[\frac{K_{l-1}(qa) + K_{l+1}(qa)}{qaK_l(qa)} \right]^2 + \frac{l^2\beta^2}{n_1^2 k_0^2} \left[\left(\frac{1}{ha} \right)^2 + \left(\frac{1}{qa} \right)^2 \right]^2}. \quad (\text{A.50})$$

The $(\pm) R$ solutions correspond to the EH and HE modes, respectively. These are hybrid modes in which all components of the field $E_r, E_\phi, E_z, H_r, H_\phi$, and H_z exist. The distinction between EH and HE depends on whether the electric (EH) or magnetic (HE) field dominates at a chosen reference point.

Two special cases of solutions arise when $l = 0$,

$$\frac{J_1(ha)}{ha J_0(ha)} = \begin{cases} -\frac{n_2^2}{n_1^2} \frac{K_1(qa)}{qa K_0(qa)}, & (+) \text{TM} \\ -\frac{K_1(qa)}{qa K_0(qa)}, & (-) \text{TE} \end{cases} \quad (\text{A.51})$$

We see that when $l = 0$ for the (+) solution both A and C vanish yielding a TM mode. The (-) solution leads to B and D vanishing, resulting in a TE mode.

A.4.3 Solving for the propagation constants

To find the propagation constant for the HE, EH, TE or TM modes we must solve their respective transcendental equations, A.49 or A.51. In Fig. A.3 we plot the left hand side (blue) and right hand side (red) of each equation with a fixed V number and l value and look for their crossings. Where the V number is given by $V = a k \sqrt{n_1^2 - n_2^2}$. It is worth noting that we can recast qa as a function of ha and V number.

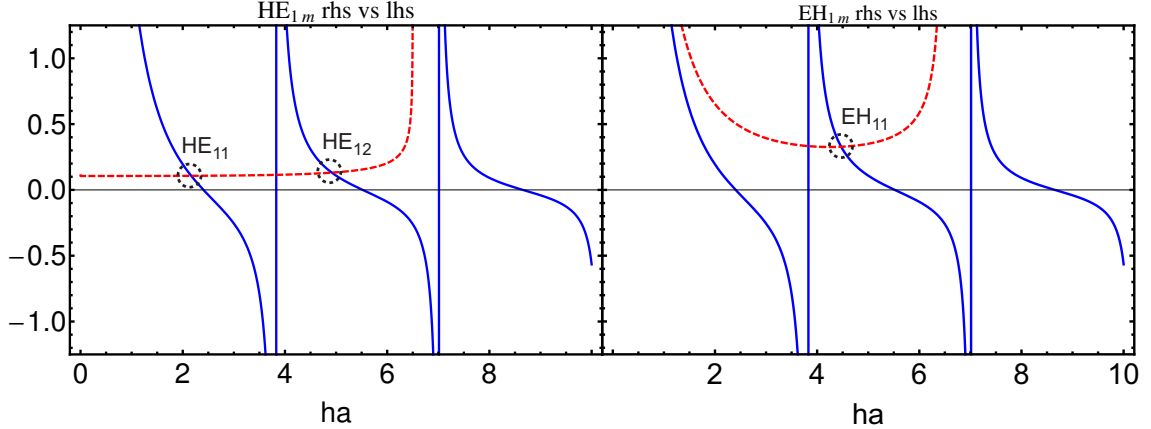


Figure A.3: We plot the left hand side (blue) and right hand side (red) of Eqn. A.49.

There exist two solutions circled with dashed black line for $(-R)$ with $l = 1$ and the normalized frequency $V=6.5$. These solutions correspond to the HE_{11} and HE_{12} modes. We see that for any V value, there will always be a crossing for the HE_{11} mode and therefore it is guided mode for and radius fiber. Unlike the HE modes, the EH modes have only one solution to Eqn. A.49 for $(+R)$ with $l = 1$ and the normalized frequency $V=6.5$. This solution corresponds to the EH_{11} mode.

The multiple crossings for a given l value yield families of the same symmetry. Modes are labeled by HE_{lm} where l corresponds to the radial symmetry or oscillations of the mode and m the azimuthal symmetry. The intersections in the plot yield higher m numbers for the HE_{1m} modes which correspondingly have higher propagation constants. This procedure can be repeated to find EH_{lm} , TE_{0m} , and TM_{0m} , see Figs. A.3 and A.4. Figure A.3 shows that for any V number there always exists a crossing for the HE_{11} mode. This means that no matter how small the waveguide radius, the HE_{11} mode is always guided. All other modes have cutoffs

and will radiate their energy into free space, or couple back to other modes in the fiber, as the radius decreases.

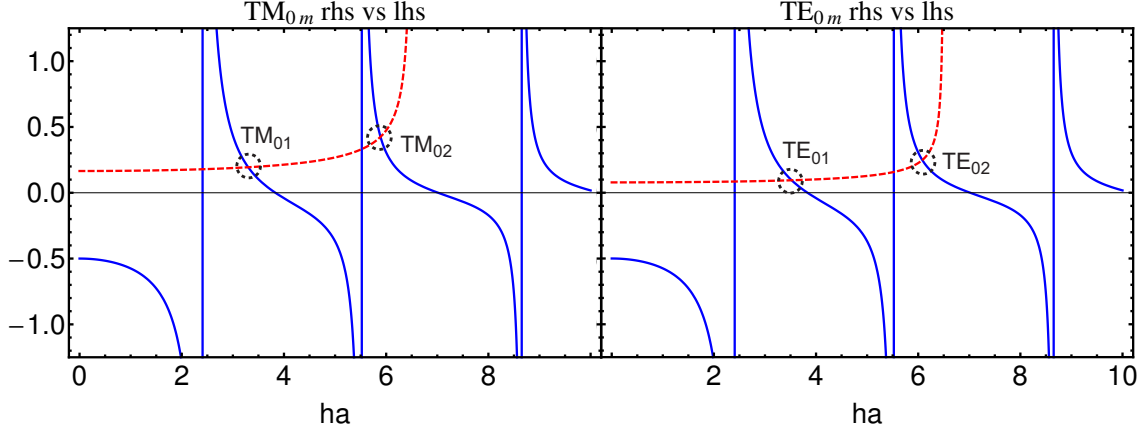


Figure A.4: We plot the left hand side (blue) and right hand side (red) of Eqn. A.51 with $l=0$ and $V=6.5$. From the crossings of the curves we find that the TE_{01} , TE_{02} , TM_{01} , and TM_{02} modes can propagate in a fiber with $V = 6.5$.

These plots are all for a $V=6.5$. If we vary V , which is effectively changing the radius of the fiber, we can arrive at dispersion relations. The dispersion relations describe the effective index of refraction, the propagation constant normalized to the free space wave vector, each mode experiences for fibers with various core radii. This effective index, n_{eff} is bounded by the indices of refraction of the core and the infinite cladding. In the limit that V goes to infinity, n_{eff} of all modes approaches n_{core} , and in the limit as V goes to zero, all modes cut off and radiate, except the fundamental mode which asymptotically approaches $n_{cladding}$.

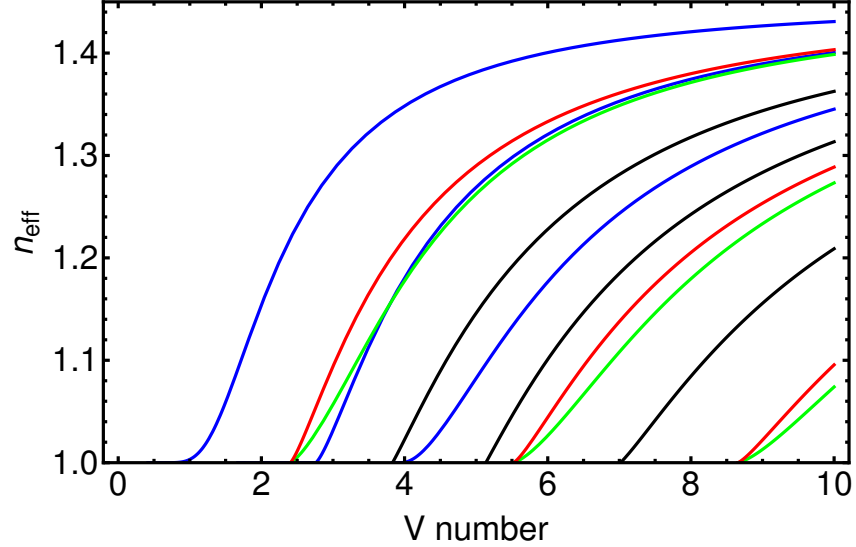


Figure A.5: The effective indices of refraction vs V number. Where $n_{core} = 1.45$ and $n_{cladding} = 1$

Figure A.5 shows that as the V number of a fiber increases, or, for fixed indices of refraction and k_0 , as the radius of the core of the fiber increases, the fiber becomes highly multimode. A fiber is single mode, in the core, when the V number is less than 2.405. Therefore, the first family of excited modes is cutoff and can no longer propagate.

When working with a single mode fiber designed for propagation of 780 nm light, such as SM800 from Fibercore, there is a finite core and finite cladding, unlike in the two layer model. These fibers, typically have a core radius of 2-5 μm and cladding radius of 62.5 μm . As a fiber is tapered the radius decreases, which naively would imply that modes get cutoff. But, in a single mode fiber there exists only one mode, the fundamental, in the core. There are no other modes to cutoff and no modes to couple to as the eigenbasis changes. As the fiber tapers, this would

seem to imply that no other modes could get excited; however, modes can exist in the cladding. This implies two regimes, core modes and cladding modes. Core modes have indices of refraction that satisfy $n_{core} > n_{eff} > n_{cladding}$. While cladding modes satisfy $n_{cladding} > n_{eff} > n_{air}$. A real ONF is not adequately represented by the two layer model. Light initially guided by the core-cladding interface, leaks into the cladding as n_{eff} drops below the index of refraction of the cladding and is then guided by the cladding-air interface. Although the fundamental mode always exists in this fiber, there is a discontinuity in the two layer model. If one plots the dispersion relation for the fundamental mode for core-cladding and cladding-air guidance as a function of radius we find that these two curves approach each other at radius of $20\mu\text{m}$, see Fig. A.6.

These dispersion relations are necessary in understanding the modal evolution in a fiber during a taper.

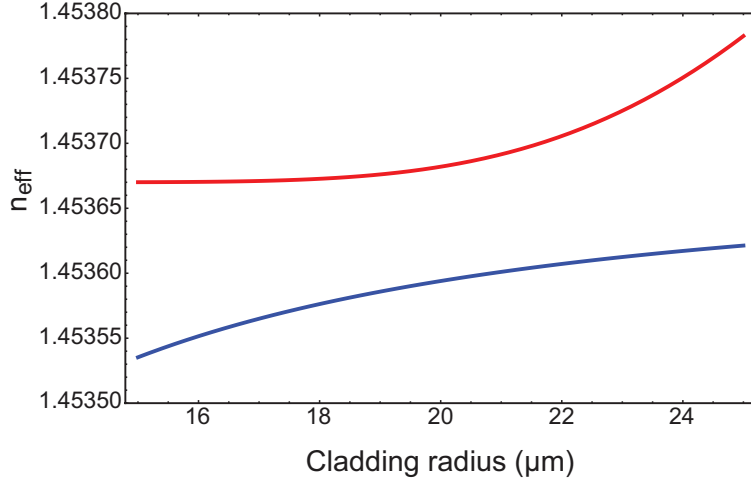


Figure A.6: A magnification of the region of closest approach for the dispersion relation of the HE_{11} mode for core-cladding (red) and cladding-air (blue) guidance. These curves do not connect, exhibiting a limitation of the two layer model.

A.4.4 Quasilinear polarization

When we launch linearly polarized light into a fiber it will excite both the $\pm l\phi$ solutions. We can represent the mode in what we call a quasilinear basis, as represented below.

$$\mathbf{E}_{\text{lin}} = \frac{1}{\sqrt{2}} [\mathbf{E}_+ \pm \mathbf{E}_-] \quad (\text{A.52})$$

$$\mathbf{H}_{\text{lin}} = \frac{1}{\sqrt{2}} [\mathbf{H}_+ \pm \mathbf{H}_-]. \quad (\text{A.53})$$

It is useful to think of this as analogous to representing linearly polarized light as a superposition of left and right circularly polarized.

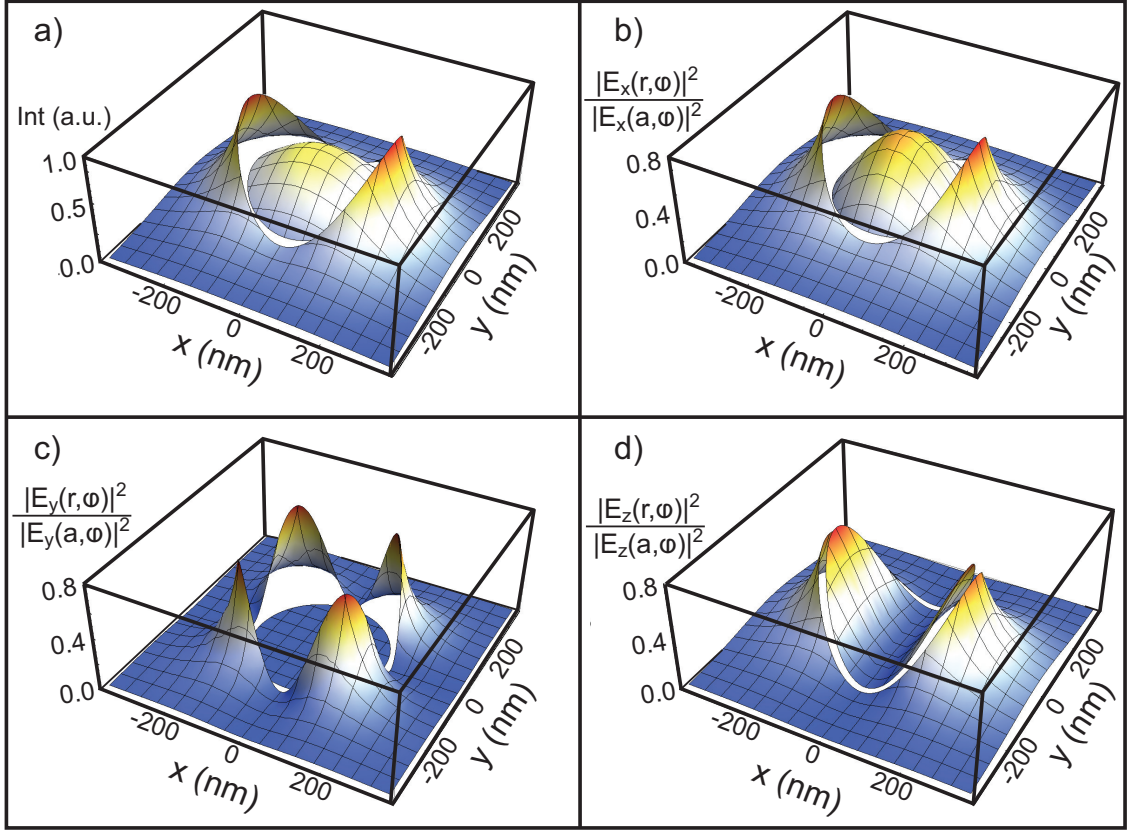


Figure A.7: The HE_{11} mode for a 180 nm radius fiber with 780 nm light input with indices of refraction $n_1 = 1.45367$ and $n_2 = 1.0$. (a) The Intensity profile. (b) $|E_x|^2$ normalized to the field at the fiber surface. (c) $|E_y|^2$ normalized to the field at the fiber surface. (d) $|E_z|^2$ normalized to the field at the fiber surface.

Fig. A.7 (a) shows the Intensity profile of the fundamental mode with a radius of 180 nm and for light with a 780 nm wavelength. We observe a discontinuity across the cladding-air boundary with about 60% of the power propagating outside the fiber tightly confined near the fiber surface, see Fig. A.8. Fig. A.7 (b-d) shows $|E_i(r, \phi)|^2/|E_i(a)|^2$ for $i = x, y, z$ polarizations. There is a sizable longitudinal com-

ponent for the fundamental mode of the fiber. This longitudinal component can lead to vector light shifts [75]. There are trapping regimes that minimize the longitudinal component and therefore its deleterious effects [71]. Alternatively, there are means of cleverly using the longitudinal component to ones advantage and selectively addressing arrays of trapped atoms on either side of the ONF [76], since the sign of E_z is different on opposite sides of the fiber.

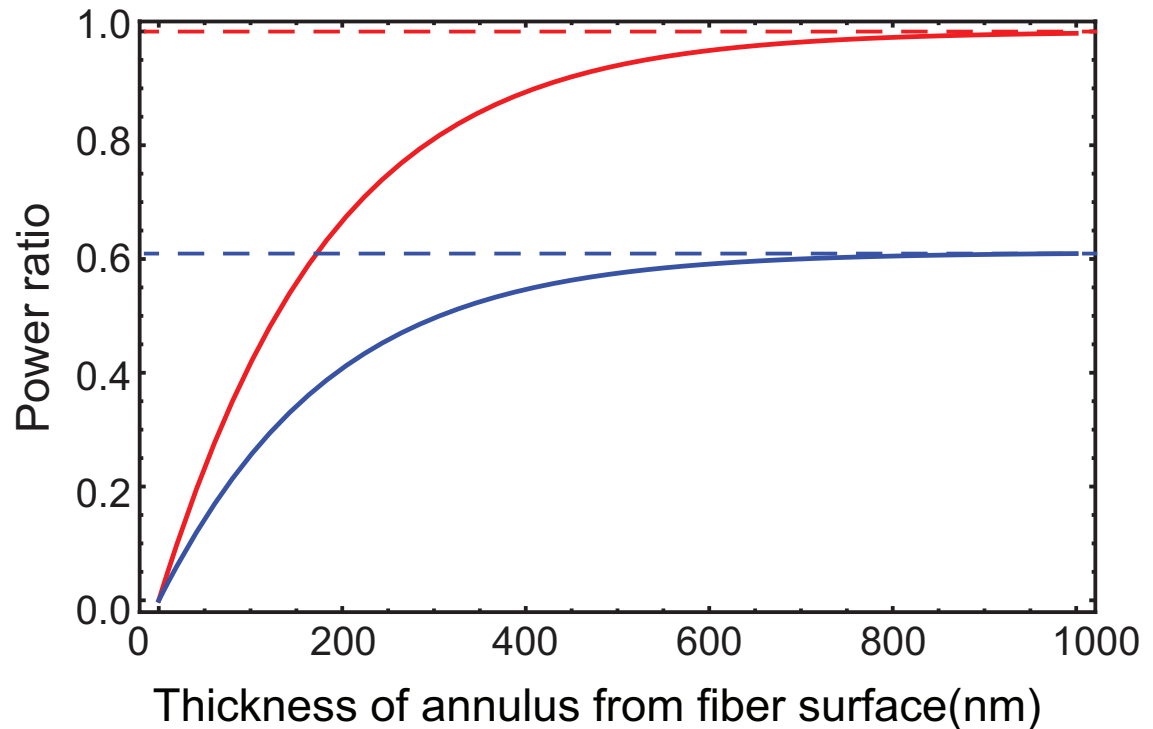


Figure A.8: Power ratio as a function of the annulus thickness from the ONF surface. Red: normalized (to power propagating outside the fiber) power contained in an annulus of a given thicknesses from the fiber surface. Blue: same but with the normalization to the total power propagating thorough the fiber. The dashed lines are the asymptotic values.

Fig. A.8 displays the ratio of integrated power propagating through an ONF with a 180 nm radius as a function of distance from the fiber surface. The red curve is normalized to the power outside the fiber and the blue curve is normalized to the total power. We see the red curve asymptotically approaches one while the blue curve asymptotically approaches 0.61, the power outside the fiber.

A.5 Power Normalization

We have not yet determined all the coefficients to fully describe the modes of the fiber. The missing coefficient, A , is derived by normalizing the modes to the input power propagating through the fiber. In other words, the energy flux traveling in the z direction is conserved:

$$P = \langle S \rangle_{z,t} \quad (\text{A.54})$$

$$\langle S \rangle_{z,t} = \frac{1}{2} \int (\mathbf{E} \times \mathbf{H}^*) \cdot \mathbf{z} r dr d\phi \quad (\text{A.55})$$

$$= \frac{A^2}{2} \int E_r H_\phi^* - E_\phi H_r^* r dr d\phi. \quad (\text{A.56})$$

Specifically, the time averaged Poynting vector is a constant given by the input power. We can solve analytically for the exact normalization. We note that the integral is independent of ϕ and that we can break the integral into two components:

$$\begin{aligned} \langle S \rangle_{z,t} &= A^2 \pi \int_0^a E_r^{(in)} H_\phi^{*(in)} - E_\phi^{(in)} H_r^{*in} r dr d\phi \\ &\quad + A^2 \pi \int_a^\infty E_r^{(out)} H_\phi^{*out} - E_\phi^{(out)} H_r^{*out} r dr d\phi \\ &= A^2 \pi (D_{in} + D_{out}) \end{aligned} \quad (\text{A.57})$$

Where D_{in} and D_{out} represent the power inside and outside the fiber carried by the guided mode. Once we solve for D_{in} and D_{out} we can use Eqn. A.57 to solve for A.

A.5.1 HE_{lm} and EH_{lm} mode normalizations

Here we outline how to solve analytically for D_{in} and D_{out} for the HE_{lm} and EH_{lm} modes.

$$\begin{aligned}
D_{out} &= \pi \int_a^\infty (E_r H_\phi^* - E_\phi H_r^*) r dr \\
D_{out} &= \pi \int_a^\infty \left(\frac{i\beta}{q^2} \left[\frac{i\mu_0\omega l}{\beta r} DK_l(qr) + CqK_l'(qr) \right] \frac{-i\beta}{q^2} \left[\frac{\epsilon_2\omega}{\beta} CqK_l'(qr) + \frac{il}{r} DK_l(qr) \right] \right. \\
&\quad \left. - \frac{i\beta}{q^2} \left[\frac{il}{r} CK_l(qr) \frac{\mu_0\omega q}{\beta} DK_l'(qr) \right] \frac{-i\beta}{q^2} \left[\frac{i\epsilon_2\omega l}{\beta r} CK_l(qr) - DqK_l'(qr) \right] \right) r dr \\
D_{out} &= \pi \frac{\beta^2}{q^2} C^2 \int_a^\infty \left(\left[\frac{i\mu_0\omega l}{\beta} B \frac{K_l(qr)}{qr} + K_l'(qr) \right] \left[\frac{\epsilon_2\omega}{\beta} K_l'(qr) + ilB \frac{K_l(qr)}{qr} \right] \right. \\
&\quad \left. - \left[il \frac{K_l(qr)}{qr} - \frac{\mu_0\omega}{\beta} BK_l'(qr) \right] \left[\frac{i\epsilon_2\omega l}{\beta} \frac{K_l(qr)}{qr} - BK_l'(qr) \right] \right) r dr
\end{aligned}$$

Defining s as

$$s = \frac{\mu_0\omega}{il\beta} B = \left[\left(\frac{1}{ha} \right)^2 + \left(\frac{1}{qa} \right)^2 \right] \left[\frac{J_l'(ha)}{haJ_l(ha)} + \frac{K_l'(qa)}{qaK_l(qa)} \right]^{-1}$$

we can rewrite D_{out} in the form

$$\begin{aligned}
D_{out} &= \pi \frac{\beta^2}{q^2} C^2 \int_a^\infty \left(\left[-l^2 s \frac{K_l(qr)}{qr} + K_l'(qr) \right] \frac{il\beta}{\mu_0\omega} (-il) \left[\frac{\epsilon_2\mu_0\omega^2}{l^2\beta^2} K_l'(qr) - s \frac{K_l(qr)}{qr} \right] \right. \\
&\quad \left. - il \left[\frac{K_l(qr)}{qr} - sK_l'(qr) \right] \frac{il\beta}{\mu_0\omega} \left[\frac{\epsilon_2\mu_0\omega^2}{\beta^2} \frac{K_l(qr)}{qr} - sK_l'(qr) \right] \right) r dr \\
D_{out} &= \pi \frac{\beta^2}{q^2} \frac{l^2\beta}{\mu_0\omega} C^2 \int_a^\infty \left(\left[-l^2 s \frac{K_l(qr)}{qr} + K_l'(qr) \right] \left[\frac{\epsilon_2\mu_0\omega^2}{l^2\beta^2} K_l'(qr) - s \frac{K_l(qr)}{qr} \right] \right. \\
&\quad \left. + \left[\frac{K_l(qr)}{qr} - sK_l'(qr) \right] \left[\frac{\epsilon_2\mu_0\omega^2}{\beta^2} \frac{K_l(qr)}{qr} - sK_l'(qr) \right] \right) r dr.
\end{aligned}$$

Then, we can define N_2 as

$$N_2 = \sqrt{\epsilon_2 \mu_0 \frac{\omega^2}{\beta^2}} = \sqrt{\frac{n_2^2 k^2}{\beta^2}} = \frac{n_2 k}{\beta}$$

which is the ratio of the free-space wavevector and that of the guided mode.

We also define

$$Z = \pi \frac{\beta^2}{q^2} \frac{l^2 \beta}{\mu_0 \omega} C^2$$

which yields the following

$$\begin{aligned} D_{out} &= Z \int_a^\infty \left(\left[-l^2 s \frac{K_l(qr)}{qr} + K'_l(qr) \right] \left[\frac{N_2^2}{l^2} K'_l(qr) - s \frac{K_l(qr)}{qr} \right] \right. \\ &\quad \left. + \left[\frac{K_l(qr)}{qr} - s K'_l(qr) \right] \left[N_2^2 \frac{K_l(qr)}{qr} - s K'_l(qr) \right] \right) r dr \\ D_{out} &= Z \int_a^\infty \left(\begin{array}{l} -s N_2^2 \frac{K_l(qr)}{qr} K'_l(qr) + l^2 s^2 \left(\frac{K_l(qr)}{qr} \right)^2 + \frac{N_2^2}{l^2} (K'_l(qr))^2 - s \frac{K_l(qr)}{qr} K'_l(qr) \\ + N_2^2 \left(\frac{K_l(qr)}{qr} \right)^2 - s \frac{K_l(qr)}{qr} K'_l(qr) - s N_2^2 \frac{K_l(qr)}{qr} K'_l(qr) + s^2 (K'_l(qr))^2 \end{array} \right) r dr \\ D_{out} &= Z \int_a^\infty \left(-2s \frac{K_l(qr)}{qr} K'_l(qr) [1 + N_2^2] + \left(\frac{K_l(qr)}{qr} \right)^2 [N_2^2 + l^2 s^2] \right. \\ &\quad \left. + (K'_l(qr))^2 \left[\frac{N_2^2}{l^2} + s^2 \right] \right) r dr \\ D_{out} &= Z \int_a^\infty \left(-2s \frac{K_l(qr)}{qr} K'_l(qr) [1 + N_2^2] + \left[l^2 \left(\frac{K_l(qr)}{qr} \right)^2 + (K'_l(qr))^2 \right] \left[\frac{N_2^2}{l^2} + s^2 \right] \right) r dr. \end{aligned}$$

Using the Bessel function relation

$$\begin{aligned} K_l(qr) &= \frac{qr}{2l} (K_{l+1}(qr) - K_{l-1}(qr)) \\ K'_l(qr) &= -\frac{1}{2} (K_{l+1}(qr) + K_{l-1}(qr)) \end{aligned}$$

we arrive at

$$\begin{aligned}
D_{out} &= Z \int_a^\infty \left(\frac{s}{2l} [K_{l+1}^2(qr) - K_{l-1}^2(qr)] [1 + N_2^2] \right. \\
&\quad \left. + \frac{1}{4} [[K_{l+1}(qr) - K_{l-1}(qr)]^2 + [K_{l+1}(qr) + K_{l-1}(qr)]^2] \left[\frac{N_2^2}{l^2} + s^2 \right] \right) rdr \\
D_{out} &= Z \int_a^\infty \left(\frac{s}{2l} [K_{l+1}^2(qr) - K_{l-1}^2(qr)] [1 + N_2^2] \right. \\
&\quad \left. + \frac{1}{2} [K_{l+1}^2(qr) + K_{l-1}^2(qr)] \left[\frac{N_2^2}{l^2} + s^2 \right] \right) rdr \\
D_{out} &= \frac{Z}{2l^2} \int_a^\infty \left([sl [1 + N_2^2] + N_2^2 + l^2 s^2] K_{l+1}^2(qr) \right. \\
&\quad \left. + [-sl [1 + N_2^2] + N_2^2 + l^2 s^2] K_{l-1}^2(qr) \right) rdr \\
D_{out} &= \frac{Z}{2l^2} \int_a^\infty \left((1 + sl) (N_2^2 + sl) K_{l+1}^2(qr) + (1 - sl) (N_2^2 - sl) K_{l-1}^2(qr) \right) rdr.
\end{aligned}$$

Now we perform a change of variable $r \rightarrow r_q = qr$,

$$D_{out} = \frac{Z}{2l^2 q^2} \left[(1 + sl) (N_2^2 + sl) \int_{qa}^\infty K_{l+1}^2(r_q) r_q dr_q + (1 - sl) (N_2^2 - sl) \int_{qa}^\infty K_{l-1}^2(r_q) r_q dr_q \right]$$

and applying the relation

$$\int_{qa}^\infty K_l^2(r_q) r_q dr_q = -\frac{1}{2} (qa)^2 [K_l^2(qa) - K_{l-1}(qa) K_{l+1}(qa)]$$

we arrive at

$$\begin{aligned}
D_{out} &= \frac{-Z a^2}{4l^2} \left[(1 + sl) (N_2^2 + sl) [K_{l+1}^2(qa) - K_l(qa) K_{l+2}(qa)] \right. \\
&\quad \left. + (1 - sl) (N_2^2 - sl) [K_{l-1}^2(qa) - K_l(qa) K_{l-2}(qa)] \right] \\
D_{out} &= \frac{-\pi a^2 \beta \beta^2}{4\mu_0 \omega} \left(\frac{J_l(ha)}{K_l(qa)} \right)^2 \left[(1 + sl) (N_2^2 + sl) [K_{l+1}^2(qa) - K_l(qa) K_{l+2}(qa)] \right. \\
&\quad \left. + (1 - sl) (N_2^2 - sl) [K_{l-1}^2(qa) - K_l(qa) K_{l-2}(qa)] \right].
\end{aligned}$$

For the fundamental mode of the fiber, $l = 1$, this yields,

$$D_{out} = \frac{-\pi a^2 \beta \beta^2}{4\mu_0 \omega} \frac{1}{q^2} \left(\frac{J_1(ha)}{K_1(qa)} \right)^2 \left[(1+s) (N_2^2 + s) [K_2^2(qa) - K_1(qa) K_3(qa)] \right. \\ \left. + (1-s) (N_2^2 - s) [K_0^2(qa) - K_1^2(qa)] \right]$$

We can similarly solve for D_{in} , which results in

$$D_{in} = \frac{\pi a^2 \beta \beta^2}{4\mu_0 \omega} \frac{1}{h^2} \left[(1+sl) (N_1^2 + sl) [J_{l+1}^2(ha) - J_l(ha) J_{l+2}(ha)] \right. \\ \left. + (1-sl) (N_1^2 - sl) [J_{l-1}^2(ha) - J_l(ha) J_{l-2}(ha)] \right]. \quad (A.58)$$

Setting $l = 1$ we arrive at

$$D_{in} = \frac{\pi a^2 \beta \beta^2}{4\mu_0 \omega} \frac{1}{h^2} \left[(1+s) (N_1^2 + s) [J_2^2(ha) - J_1(ha) J_3(ha)] \right. \\ \left. + (1-s) (N_1^2 - s) [J_0^2(ha) + J_1(ha)^2] \right]. \quad (A.59)$$

Finally following the same procedure we can derive the power inside and outside the fiber for the TE_{01} and TM_{01} modes

$$D_{TE-OUT} = \frac{-\pi a^2}{4} \mu_0 \omega \frac{\beta}{q^2} \left(\frac{J_1(qa)}{K_1(ha)} \right)^2 [K_2^2(qa) - K_1(qa) K_3(qa) + K_0^2(qa) - K_1^2(qa)]$$

$$D_{TE-IN} = \frac{\pi a^2 \mu_0 \omega \beta}{4} \frac{1}{h^2} [J_2^2(ha) - J_1(ha) J_3(ha) + J_0^2(ha) + J_1^2(ha)]$$

$$D_{TM-OUT} = \frac{-\pi a^2 \epsilon_2 \omega \beta}{4} \left(\frac{J_1(ha)}{K_1(qa)} \right)^2 [K_2^2(qa) - K_1(qa) K_3(qa) + K_0^2(qa) - K_1^2(qa)]$$

$$D_{TM-IN} = \frac{\pi a^2 \epsilon_1 \omega \beta}{4 h^2} [J_2^2(ha) - J_1(ha) J_3(ha) + J_0^2(ha) + J_1^2(ha)].$$

We have implemented a Mathematica notebook in the lab that allows us to calculate all of these parameters. We also obtain similar results when using a commercial software, FIMMPROP [123].

Bibliography

- [1] R. Feynman, *Int. J. Theor. Phys.* **21**, 467 (1982).
- [2] D. Deutsch and R. Jozsa, "Rapid Solution of Problems by Quantum Computation," *Proc. R. Soc. London Ser. A* **439**, 553 (1992).
- [3] P. W. Shor, Proceedings of the 35th Annual Symposium on the Foundations of Computer Science, Los Alamitos, IEEE Computer Society Press, New York (1995).
- [4] P. W. Shor, "Scheme for reducing decoherence in quantum computer memory," *Phys. Rev. A* **52** (1995).
- [5] A. Steane, *Proc. R. Soc. London Ser. A*, "Multiple-Particle Interference and Quantum Error Correction," **452** 2551 (1996)
- [6] E. Knill and R. Laflamme, "Theory of quantum error-correcting codes," *Phys. Rev. A* **55**, 900 (1997).
- [7] D. Gottesman, "Stabilizer Codes and Quantum Error Correction," Thesis (1997)
- [8] L. K. Grover, "A fast quantum mechanical algorithm for database search," Proceedings, 28th Annual ACM Symposium on the Theory of Computing (STOC), pages 212-219, (1996).
- [9] S. Lloyd, "Universal Quantum Simulators," *Science* **273**, 1073 (1996).
- [10] I. Bulata and F. Nori, "Quantum Simulators," *Science* **326**, 108 (2009).

- [11] J. I. Cirac and P. Zoller, "Goals and opportunities in quantum simulation," *Nature Physics* **8**, 264266 (2012).
- [12] J. Simon, W. S. Bakr, R. Ma, M. E. Tai, P. M. Preiss, and M. Greiner, "Quantum simulation of antiferromagnetic spin chains in an optical lattice," *Nature* **472**, 307 (2011).
- [13] E. E. Edwards, S. Korenblit, K. Kim, R. Islam, M.-S. Chang, J. K. Freericks, G.-D. Lin, L.-M. Duan, and C. Monroe, "Quantum simulation and phase diagram of the transverse-field Ising model with three atomic spins," *Phys. Rev. B* **82**, 060412 (2010).
- [14] K. Kim, M.-S. Chang, S. Korenblit, R. Islam, E. E. Edwards, J. K. Freericks, G.-D. Lin, L.-M. Duan, and C. Monroe, "Quantum simulation of frustrated Ising spins with trapped ions," *Nature* **465**, 590 (2010).
- [15] R. Islam, C. Senko, W. C. Campbell, S. Korenblit, J. Smith, A. Lee, E. E. Edwards, C. C. J. Wang, J. K. Freericks, and C. Monroe, "Emergence and Frustration of Magnetism with Variable-Range Interactions in a Quantum Simulator," *Science* **340**, 583 (2013).
- [16] M. C Beeler, M. E. W Reed, T. Hong, and S. L. Rolston, "Disorder-driven loss of phase coherence in a quasi-2D cold atom system," *New Journal of Physics* **14** 073024 (2012).
- [17] Z. Hadzibabic, P. Kruger, M. Cheneau, B. Battelier, and J. Dalibard, "BerezinskiiKosterlitzThouless crossover in a trapped atomic gas," *Nature* **441** 11181121 (2006)
- [18] A. M. Rey, R. Sensarma, S. Filling, M. Greiner, E. Demler, and M. D. Lukin, Controlled preparation and detection of d-wave superfluidity in two-dimensional optical superlattices, *EPL* vol. **87**, p. 60001, (2009).
- [19] P. Treutlein, P. Hommelhoff, T. Steinmetz, T. W. Hnsch, and J. Reichel, "Coherence in Microchip Traps," *Phys. Rev. Lett.* **92**, 203005 (2004).
- [20] D. Jaksch, J. I. Cirac, P. Zoller, S. L. Rolston, R. Ct, and M. D. Lukin, "Fast Quantum Gates for Neutral Atoms," *Phys. Rev. Lett.* **85**, 2208 (2000).
- [21] W. S. Bakr, J. I. Gillen, A. Peng, S. Foelling, and M. Greiner, "A quantum gas microscope for detecting single atoms in a Hubbard-regime optical lattice," *Nature* **462**, 74-77 (2009).

- [22] J. I. Cirac and P. Zoller, "Quantum computations with cold trapped ions," *Phys. Rev. Lett.* **74**, (1995).
- [23] C. Monroe, D. M. Meekhof, B. E. King, W. M. Itano, D. J. Wineland, "Demonstration of a Fundamental Quantum Logic Gate," *Phys. Rev. Lett.* **75**, 47144717 (1995).
- [24] D. Leibfried, B. DeMarco, V. Meyer, D. Lucas, M. Barrett, J. Britton, W. M. Itano, B. Jelenkovic, C. Langer, T. Rosenband, and D. J. Wineland, "Experimental demonstration of a robust, high-fidelity geometric two ion-qubit phase gate," *Nature* **422**, 412-415 (2003).
- [25] D. I. Schuster, A. Fragner, M. I. Dykman, S. A. Lyon, and R. J. Schoelkopf, "Proposal for Manipulating and Detecting Spin and Orbital States of Trapped Electrons on Helium Using Cavity Quantum Electrodynamics," *Phys. Rev. Lett.* **105**, 040503 (2010).
- [26] Y. Makhlin, G. Schn, and A. Shnirman, "Quantum-state engineering with Josephson-junction devices," *Rev. Mod. Phys.* **73**, 357 (2001).
- [27] M. H. Devoret and R. J. Schoelkopf, "Superconducting Circuits for Quantum Information: An Outlook," *Science* **339** 1169-1174(2013).
- [28] P. C. Maurer, G. Kucsko, C. Latta, L. Jiang, N. Y. Yao, S. D. Bennett, F. Pastawski, D. Hunger, N. Chisholm, M. Markham, D. J. Twitchen, J. I. Cirac, and M. D. Lukin, "Room-Temperature Quantum Bit Memory Exceeding One Second," *Science* **336**, 1283 1286 (2012).
- [29] K Saeedi, S. Simmons, J. Z. Salvail, P. Dluhy, H. Riemann, N. V. Abrosimov, P. Becker, H. J. Pohl, J. J. L. Morton and M. L. W. Thewalt, "Room-Temperature Quantum Bit Storage Exceeding 39 Minutes Using Ionized Donors in Silicon-28," *Science* **342**, 830 (2013);
- [30] Y. Nakamura, C. D. Chen, and J. S. Tsai, "Coherent control of macroscopic quantum states in a single-Cooper-pair box," *Nature* **398**, 786-788 (1999).
- [31] M. Martinis, S. Nam, J. Aumentado, and C. Urbina, "Rabi Oscillations in a Large Josephson-Junction Qubit," *Phys. Rev. Lett.* **89**, 117901 (2002).
- [32] Y. Yu, S. Han, X. Chu, S.-I. Chu, and Z. Wang, "Coherent Temporal Oscillations of Macroscopic Quantum States in a Josephson Junction," *Science* **296**, 889-892 (2002).

- [33] F. W. Strauch, P. R. Johnson, A. J. Dragt, C. J. Lobb, J. R. Anderson, F. C. Wellstood, Quantum Logic Gates for Coupled Superconducting Phase Qubits, *Phys. Rev. Lett.* **91**, 167005 (2003).
- [34] A. O. Caldiera and A. J. Leggett, "Quantum tunnelling in a dissipative system," *Ann. Phys.* **149**, 374 (1983).
- [35] J. R. Friedman, V. Patel, W. Chen, S. K. Tolpygo, and J. E. Lukens, "Quantum superposition of distinct macroscopic states," *Nature* **406**, 43 (2000).
- [36] C. H. van der Wal, A. C. J. ter Haar, F. K. Wilhelm, R. N. Schouten, C. J. P. M. Harmans, R. P. Orlando, S. Lloyd, and J. E. Mooij, "Quantum Superposition of Macroscopic Persistent-Current States," *Science* **290**, 773 (2000).
- [37] A. Wallraff, D. I. Schuster, A. Blais, L. Frunzio, R.-S. Huang, J. Majer, S. Kumar, S. M. Girvin and R. J. Schoelkopf, "Strong coupling of a single photon to a superconducting qubit using circuit quantum electrodynamics," *Nature* **431**, 162 (2004).
- [38] A. A. Houck, J. A. Schreier, B. R. Johnson, J. M. Chow, J. Koch, J. M. Gambetta, D. I. Schuster, L. Frunzio, M. H. Devoret, S. M. Girvin, and R. J. Schoelkopf, "Controlling the Spontaneous Emission of a Superconducting Transmon Qubit," *Phys. Rev. Lett.* **101**, 080502 (2008).
- [39] V. E. Manucharyan, J. Koch, L. Glazman, M. H. Devoret, "Fluxonium: Single Cooper-Pair Circuit Free of Charge Offsets," *Science* **326**, 113-116 (2009).
- [40] H. Paik, D. I. Schuster, L. S. Bishop, G. Kirchmair, G. Catelani, A. P. Sears, B. R. Johnson, M. J. Reagor, L. Frunzio, L. I. Glazman, S. M. Girvin, M. H. Devoret, and R. J. Schoelkopf, "Observation of High Coherence in Josephson Junction Qubits Measured in a Three-Dimensional Circuit QED Architecture," *Phys. Rev. Lett.* **107**, 240501 (2011),
- [41] D. P. DiVincenzo, Topics in Quantum Computers, Mesoscopic Electron Transport NATO ASI Series Volume **345**, pp 657-677, (1997).
- [42] D. P. DiVincenzo, "The Physical Implementation of Quantum Computation," *Fortschritte der Physik* **48**, 771 (2000).
- [43] L. Tian, P. Rabl, R. Blatt, and P. Zoller, "Interfacing Quantum-Optical and Solid-State Qubits," *Phys. Rev. Lett.* **92**, 247902 (2004).
- [44] J. E. Mooij, T. P. Orlando, L. Levitov, L. Tian, C. H. van der Wal, and S. Lloyd, "Josephson Persistent-Current Qubit," *Science* **285**, 1036 (1999).

- [45] T. L. Robertson, B. L. T. Plourde, P. A. Reichardt, T. Hime, C.-E. Wu, and J. Clarke, "Quantum theory of three-junction flux qubit with non-negligible loop inductance: Towards scalability," *Phys. Rev. B* **73**, 174526 (2006).
- [46] Y. Nakamura, Decoherence in Superconducting Quantum Systems Conference (Berkeley, 2007).
- [47] F. Yoshihara, K. Harrabi, A. O. Niskanen, Y. Nakamura, and J. S. Tsai, "Decoherence of Flux Qubits due to 1/f Flux Noise," *Phys. Rev. Lett.* **97**, 167001 (2006).
- [48] F. G. Paauw, A. Fedorov, C. J. P. M. Harmans, and J. E. Mooij, "Tuning the Gap of a Superconducting Flux Qubit" *Phys. Rev. Lett.* **102**, 090501 (2009).
- [49] D. I. Schuster, A. P. Sears, E. Ginossar, L. DiCarlo, L. Frunzio, J. J. L. Morton, H. Wu, G. A. D. Briggs, B. B. Buckley, D. D. Awschalom, and R. J. Schoelkopf, "High-Cooperativity Coupling of Electron-Spin Ensembles to Superconducting Cavities," *Phys. Rev. Lett.* **105**, 140501 (2010).
- [50] D. I. Schuster, L. S. Bishop, I. L. Chuang, D. DeMille, and R. J. Schoelkopf, "Cavity QED in a molecular ion trap," *Phys. Rev. A* **83**, 012311(2011).
- [51] A. S. Sorensen, C. H. van der Wal, L. I. Childress, and M. D. Lukin, "Capacitive Coupling of Atomic Systems to Mesoscopic Conductors," *Phys. Rev. Lett.* **92**, 063601 (2004).
- [52] J. Verdú, H. Zoubi, Ch. Koller, J. Majer, H. Ritsch, and J. Schmiedmayer, "Strong Magnetic Coupling of an Ultracold Gas to a Superconducting Waveguide Cavity," *Phys. Rev. Lett.* **103**, 043603 (2009).
- [53] P. Rabl, D. DeMille, J. M. Doyle, M. D. Lukin, R. J. Schoelkopf, and P. Zoller, "Hybrid Quantum Processors: Molecular Ensembles as Quantum Memory for Solid State Circuits," *Phys. Rev. Lett.* **97**, 033003 (2006).
- [54] A. André, D. DeMille, J. M. Doyle, M. D. Lukin, S. E. Maxwell, P. Rabl, R. J. Schoelkopf, and P. Zoller, "A coherent all-electrical interface between polar molecules and mesoscopic superconducting resonators," *Nature Physics* **2**, 636 (2006).
- [55] A. Imamoğlu, "Cavity QED Based on Collective Magnetic Dipole Coupling: Spin Ensembles as Hybrid Two-Level Systems," *Phys. Rev. Lett.* **102**, 083602 (2009).

- [56] D. Marcos, M. Wubs, J. M. Taylor, R. Aguado, M. D. Lukin, and A. S. Sorensen, "Coupling Nitrogen-Vacancy Centers in Diamond to Superconducting Flux Qubits," *Phys. Rev. Lett.* **105**, 210501 (2010).
- [57] Y. Kubo, F. R. Ong, P. Bertet, D. Vion, V. Jacques, D. Zheng, A. Dréau, J.-F. Roch, A. Auffeves, F. Jelezko, J. Wrachtrup, M. F. Barthe, P. Bergonzo, and D. Esteve, "Strong Coupling of a Spin Ensemble to a Superconducting Resonator," *Phys. Rev. Lett.* **105**, 140502 (2010).
- [58] F. Jessen, M. Knufinke, S. C. Bell, P. Vergien, H. Hattermann, P. Weiss, M. Rudolph, M. Reinschmidt, K. Meyer, T. Gaber, D. Cano, A. Guenther, S. Bernon, D. Koelle, R. Kleiner, and J. Fortgh, "Trapping of ultracold atoms in a 3He/4He dilution refrigerator," *Appl. Phys. B*, 1432-0649 (2013).
- [59] S. Bernon, H. Hattermann, D. Bothner, M. Knufinke, P. Weiss, F. Jessen, D. Cano, M. Kemmler, R. Kleiner, D. Koelle, and J. Fortgh, "Manipulation and coherence of ultra-cold atoms on a superconducting atom chip," *Nature Communications* **4**, 2380 (2013).
- [60] S. Minniberger, F. Diorico, S. Haslinger, C. Hufnagel, C. Novotny, N. Lippok, J. Majer, S. Schneider, and J. Schmiedmayer, "Magnetic conveyor belt transport of ultracold atoms to a superconducting atomchip," *Applied Physics B*, 0946-2171, 1-5 (2014).
- [61] Z. Kim, C. P. Vlahacos, J. E. Hoffman, J. A. Grover, K. D. Voigt, B. K. Cooper, C. J. Ballard, B. S. Palmer, M. Hafezi, J. M. Taylor, J. R. Anderson, A. J. Dragt, C. J. Lobb, L. A. Orozco, S. L. Rolston, and F. C. Wellstood, "Thin-film superconducting resonator tunable to the ground-state hyperfine splitting of ^{87}Rb ," *AIP Advances* **1**, 042107 (2011).
- [62] Y. B. Ovchinnikov, I. Manek, and R. Grimm, "urface Trap for Cs atoms based on Evanescent-Wave Cooling," *Phys. Rev. Lett.* **79**, 2225 (1997).
- [63] H. J. Metcalf and P. van der Straten, "Laser Cooling and Trapping," (Springer, New York, 1999).
- [64] R. P. Budoyo, *et. al.* In progress
- [65] J. Gao, J. Zmuidzinas, A. Vayonakis, P. Day, B. Mazin, and H. Leduc, "Equivalence of the Effects on the Complex Conductivity of Superconductor due to Temperature Change and External Pair Breaking," *J. Low Temp. Phys.* **151**, 557-563 (2008).

- [66] R. Barends, J. Wenner, M. Lenander, Y. Chen, R. C. Bialczak, J. Kelly, E. Lucero, P. O'Malley, M. Mariantoni, D. Sank, H. Wang, T. C. White, Y. Yin, J. Zhao, A. N. Cleland, J. M. Martinis, and J. J. A. Baselmans, "Minimizing quasiparticle generation from stray infrared light in superconducting quantum circuits," *Appl. Phys. Lett.* **99**, 113507 (2011).
- [67] A. D. Corcoles, J. M. Chow, J. M. Gambetta, C. Rigetti, J. R. Rozen, G. A. Keefe, M. Beth Rothwell, M. B. Ketchen, and M. Steffen, "Protecting superconducting qubits from external sources of loss and heat," *Appl. Phys. Lett.* **99**, 181906 (2011).
- [68] V. I. Balykin, K. Hakuta, F. Le Kien, J. Q. Liang, and M. Morinaga, "Atom trapping and guiding with a subwavelength-diameter optical fiber," *Phys. Rev. A* **70**, 011401 (2004).
- [69] E. Vetsch, D. Reitz, G. Sagué, R. Schmidt, S. T. Dawkins, and A. Rauschenbeutel, "Optical interface created by laser-cooled atoms trapped in the evanescent field surrounding an optical nanofiber," *Phys. Rev. Lett.* **104**, 203603 (2010).
- [70] F. L. Kien, J. Liang, K. Hakuta, and V. Balykin, "Field intensity distributions and polarization orientations in a vacuum-clad subwavelength-diameter optical fiber," *Optics Communications* **242**, 444-445 (2004).
- [71] A. Goban, K. Choi, D. J. Alton, D. Ding, C. Lacroûte, M. Pototschnig, T. Thiele, N. P. Stern, and H. J. Kimble, "Demonstration of a State-Insensitive, Compensated Nanofiber Trap," *Phys. Rev. Lett.* **109**, 033603 (2012).
- [72] F. Le Kien, V. I. Balykin, and K. Hakuta, "Atom trap and waveguide using a two-color evanescent light field around a subwavelength-diameter optical fiber," *Phys. Rev. A* **70**, 063403 (2004).
- [73] C. Lacroûte, K. S. Choi, A. Goban, D. J. Alton, D. Ding, N. P. Stern, and H. J. Kimble, "A state-insensitive, compensated nanofiber trap," *New J. Phys.* **14** 023056 (2012).
- [74] A. Yariv, "Optical Electronics," The Oxford Series in Electrical and Computer Engineering Series Oxford University Press, (1990).
- [75] I. H. Deutsch, and P. S. Jessen, "Quantum control and measurement of atomic spins in polarization spectroscopy ,," *Opt. Commun.* **283**, 681-694 (2010).
- [76] R. Mitsch, C. Sayrin, B. Albrecht, P. Schneeweiss, and A. Rauschenbeutel, "Exploiting the local polarization of strongly confined light for sub-micrometer-

resolution internal state preparation and manipulation of cold atoms," Phys. Rev. A **89**, 063829 (2014).

- [77] H. Katori, T. Ido, and M. Kuwata-Gonokami, "Optimal design of dipole potentials for efficient loading of Sr atoms," J. Phys. Soc. Jpn. **668**, 2479-2482 (1999).
- [78] J. Ye, D. W. Vernooy, and H. J. Kimble, "Trapping of Single Atoms in Cavity QED," Phys. Rev. Lett. **83**, 4987 (1999).
- [79] M. Boustimi, J. Baudon, P. Candori, and J. Robert, "van der Waals interaction between an atom and a metallic nanowire," Phys. Rev. B **65**, 155402 (2002).
- [80] J.-Y. Courtois, J.-M. Courty, and J. C. Mertz, "Internal dynamics of multilevel atoms near a vacuum-dielectric interface," Phys. Rev. A **53**, 1862 (1996).
- [81] A. Landragin, J.-Y. Courtois, G. Labeyrie, N. Vansteenkiste, C. I. Westbrook, and A. Aspect, "Measurement of the van der Waals Force in an Atomic Mirror," Phys. Rev. Lett. **77**, 1464 (1996).
- [82] D. E. Chang, J. I. Cirac, and H. J. Kimble, "Self-Organization of Atoms along a Nanophotonic Waveguide," Phys. Rev. Lett. **110**, 113606 (2013).
- [83] M. J. Morrissey, K. Deasy, M. Frawley, R. Kumar, E. Prel, L. Russell, V. G. Truong, and S. Nic Chormaic, "Spectroscopy, manipulation and trapping of neutral atoms, molecules, and other particles using optical nanofibers: A review," *Sensors* **13**, 10449 (2013).
- [84] G. Brambilla, "Optical fibre nanowires and microwires: a review," Journal of Optics **12**, 043001, (2010).
- [85] G. Sagué, A. Baade, and A. Rauschenbeutel, "Blue-detuned evanescent field surface traps for neutral atoms based on mode interference in ultrathin optical fibres," New Journal of Physics **10**, 113008 (2008).
- [86] D. Reitz and A. Rauschenbeutel. "Nanofiber-based double-helix dipole trap for cold neutral atoms," Optics Communications **285**, 4705-4708, (2012).
- [87] F. L. Kien, S. D. Gupta, V. I. Balykin, and K. Hakuta, "Spontaneous emission of a cesium atom near a nanofiber: Efficient coupling of light to guided modes," Phys. Rev. A **72**, 032509 (2005).

- [88] C. Wuttke, M. Becker, S. Brückner, M. Rothhardt, and A. Rauschenbeutel, "Nanofiber fabry-perot microresonator for nonlinear optics and cavity quantum electrodynamics" *Opt. Lett.* **37**, 1949-1951, (2012).
- [89] D. J. Alton, N. P. Stern, Takao Aoki, H. Lee, E. Ostby, K. J. Vahala, and H. J. Kimble, "Strong interactions of single atoms and photons near a dielectric boundary," *Nat. Phys.* **7**, 159-165, (2011).
- [90] K. P. Nayak, P. N. Melentiev, M. Morinaga, F. L. Kien, V. I. Balykin, and K. Hakuta, "Optical nanofiber as an efficient tool for manipulating and probing atomic fluorescence," *Opt. Express* **15**, 5431-5438 (2007).
- [91] J. C. Knight, G. Cheung, F. Jacques, and T. A. Birks, "Phase-matched excitation of whispering-gallery-mode resonances by a fiber taper," *Opt. Lett.* **22**, 1129-1131 (1997).
- [92] M. J. Morrissey, K. Deasy, Y. Wu, S. Chakrabarti and S. Nic Chormaic, "Tapered optical fibers as tools for probing magneto-optical trap characteristics," *Rev. Sci. Instrum.* **80**, 053102 (2009).
- [93] G. Kakarantzas, T. A. Birks, and P. S. J. Russell, "Structural long-period gratings in photonic crystal fibers," *Opt. Lett.* **27**, 1013-1015 (2002).
- [94] Y. Louyer, D. Meschede, and A. Rauschenbeutel. "Tunable whispering-gallery-mode resonators for cavity quantum electrodynamics," *Phys. Rev. A* **72**, 031801(2005).
- [95] M. Fujiwara, T. Noda, A. Tanaka, K. Toubaru, H.-Q. Zhao, and S. Takeuchi, "Coupling of ultrathin tapered fibers with high-q microsphere resonators at cryogenic temperatures and observation of phase-shift transition from under-coupling to overcoupling," *Opt. Express* **20**, 19545-19553 (2012).
- [96] S. M. Spillane, T. J. Kippenberg, O. J. Painter, and K. J. Vahala, "Ideality in a Fiber-Taper-Coupled Microresonator System for Application to Cavity Quantum Electrodynamics," *Phys. Rev. Lett.* **91**, 043902 (2003).
- [97] T. Schröder, M. Fujiwara, T. Noda, H.-Q. Zhao, O. Benson, and S. Takeuchi, "A nanodiamond-tapered fiber system with high single-mode coupling efficiency," *Opt. Express* **20**, 10490-10497 (2012).
- [98] K. P. Nayak and K. Hakuta. "Photonic crystal formation on optical nanofibers using femtosecond laser ablation technique," *Opt. Express* **21**, 2480-2490 (2013).

- [99] J. D. Thompson, T. G. Tiecke, N. P. de Leon, J. Feist, A. V. Akimov, M. Gullans, A. S. Zibrov, V. Vuletić, and M. D. Lukin, "Coupling a single trapped atom to a nanoscale optical cavity," *Science* **340**, 1202-1205 (2013).
- [100] M. Sadgrove, R. Yalla, K. P. Nayak, and K. Hakuta, "Photonic crystal nanofiber using an external grating," *Opt. Lett.* **38**, 2542-2545 (2013).
- [101] H. J. Kimble, "The quantum internet," *Nature* **453**, 1023-1030 (2008).
- [102] M. Fujiwara, K. Toubaru, and S. Takeuchi, "Optical transmittance degradation in tapered fibers," *Opt. Express* **19**, 8596-8601 (2011).
- [103] S. Ravets J. E. Hoffman P. R. Kordell J. D. Wong-Campos S. L. Rolston and L. A. Orozco, "Intermodal energy transfer in a tapered optical fiber: optimizing transmission," *J. Opt. Soc. Am. A* **30**, 2361-2371 (2013).
- [104] S. Ravets, J. E. Hoffman, L. A. Orozco, S. L. Rolston, G. Beadie, and F. K. Fatemi, "A low-loss photonic silica nanofiber for higher-order modes," *Opt. Express* **21**, 18325-18335, (2013).
- [105] J. E. Hoffman, J. A. Grover, Z. Kim, A. K. Wood, J. R. Anderson, A. J. Dragt, M. Hafezi, C. J. Lobb, L. A. Orozco, S. L. Rolston, J. M. Taylor, C. P. Vlahacos, and F. C. Wellstood, "Atoms talking to SQUIDs," *Revista Mexicana De Fisica* **57**,1-5 (2011).
- [106] M. Hafezi, Z. Kim, S. L. Rolston L. A. Orozco, B. L. Lev, and J. M. Taylor, "Atomic interface between microwave and optical photons," *Phys. Rev. A* **85**, 020302 (2012).
- [107] T. Birks and Y. Li, "The Shape of Fiber Tapers," *Journal of Lightwave Technology* **10**, 432-438 (1992).
- [108] F. Bilodeau, K. O. Hill, S. Faucher, and D. C. Johnson, "Low-loss highly overcoupled fused couplers: fabrication and sensitivity to external pressure," *Journal of Lightwave Technology*, **6**, 1476 -1482, (1988).
- [109] F. Warken, E. Vetsch, D. Meschede, M. Sokolowski, and A. Rauschenbeutel. "Ultra-sensitive surface absorption spectroscopy using sub-wavelength diameter optical fibers," *Opt. Express*, **15**, 11952-11958, (2007).
- [110] R. Garcia-Fernandez, W. Alt, F. Bruse, C. Dan, K. Karapetyan, O. Rehband, A. Stiebeiner, U. Wiedemann, D. Meschede, and A. Rauschenbeutel, *Applied Physics B* **105**, 3 (2011).

- [111] F. Warken, Ultra thin glass fibers as a tool for coupling light and matter, Ph.D. thesis, Rheinische Friedrich-Wilhelms Universitat, Mainz, Germany (2007).
- [112] L. Ding, C. Belacel, S. Ducci, G. Leo, and I. Favero, "Ultra-low loss single-mode silica tapers manufactured by a microheater," <http://arxiv.org/abs/1001.3076>, (2010).
- [113] Patrick Lambelet, Abdeljalil Sayah, Michael Pfeffer, Claude Philipona, and Fabienne Marquis-Weible. "Chemically etched fiber tips for near-field optical microscopy: A process for smoother tips," *Appl. Opt.* **37**, 7289- 7292, (1998).
- [114] Hani J. Kbashi. "Fabrication of submicron-diameter and taper fibers using chemical etching," *Jour. of Mat. Sci. & Tech.* **28**, 308-312 (2012).
- [115] H. Yokota, E. Sugai, and Y. Sasaki. "Optical irradiation method for fiber coupler fabrications," *Optical Review* **4**, A104–A107 (1997).
- [116] T. E. Dimmick, G. Kakarantzas, T. A. Birks, and P. S. J. Russell, "Carbon dioxide laser fabrication of fused-fiber couplers and tapers," *Appl. Opt.* **f38**, 6845-6848 (1999).
- [117] J. M. Ward, D. G. O'Shea, B. J. Shortt, M. J. Morrissey, K. Deasy, and S. G. Nic Chormaic, "Heat-and-pull rig for fiber taper fabrication," *Rev. of Sci. Instr.* **77**, 083105 (2006).
- [118] A. Stiebeiner, R. Garcia-Fernandez, and A. Rauschenbeutel, "Design and optimization of broadband tapered optical fibers with a nanofiber waist," *Opt. Express* **18**, 22677(2010).
- [119] Corning Incorporated. "HPFS fused silica standard grade semiconductor optics," Spec sheet.
- [120] The program is available at the Digital Repository of the University of Maryland (DRUM) at <http://hdl.handle.net/1903/15069>.
- [121] S. Leon-Saval, T. Birks, W. Wadsworth, P. S. J. Russell, and M. Mason, "Supercontinuum generation in submicron fibre waveguides," *Opt. Express* **12**, 2864-2869 (2004).
- [122] G. Brambilla, V. Finazzi, and D. Richardson, "ltra-low-loss optical fiber nanotapers," *Opt. Express* **12**, 2258-2263 (2004).
- [123] Photon Design Ltd, "FIMMWAVE/FIMMPROP," <http://www.photond.com>.

- [124] F. Orucevic, V. Lefèvre-Seguin, and J. Hare, "Transmittance and near-field characterization of sub-wavelength tapered optical fibers," *Opt. Express* **15**, 13624-13629 (2007).
- [125] C. Wuttke and A. Rauschenbeutel. "Thermalization via heat radiation of an individual object thinner than the thermal wavelength," *Phys. Rev. Lett.* **111**, 024301 (2013).
- [126] Michael Tandecki private communication (2012).
- [127] J. M. Ward, A. Maimaiti, V. H. Le, and S. N. Chormaic, "Optical Micro- and Nanofiber Pulling Rig," arxiv preprint (2014).
- [128] A. Yariv, "Coupled-mode theory for guided-wave optics," *IEEE J. Quant. Electron.* **9**, 919 – 933 (1973).
- [129] J. Bures and R. Ghosh, "Power density of the evanescent field in the vicinity of a tapered fiber," *J. Opt. Soc. Am. A* **16**, 1992-1996 (1999).
- [130] L. Tong, R. R. Gattass, J. B. Ashcom, S. He, J. Lou, M. Shen, I. Maxwell, and E. Mazur, "Subwavelength-diameter silica wires for low-loss optical wave guiding," *Nature* **426**, 816-819 (2003).
- [131] A. W. Snyder and J. D. Love, "Optical Waveguide Theory," Chapman and Hall, London, (1983).
- [132] P. Solano, Candidacy paper, UMD (2014).
- [133] R. Grimm, M. Weidemuller, and Y. B. Ovchinnikov, "Optical dipole traps for neutral atoms," *Adv. At. Mol. Opt. Phys.* **42**, 95-170 (2000).
- [134] A. Ashkin, "Trapping of atoms by resonance radiation pressure," *Phys. Rev. Lett.* **40**, 729-732 (1978).
- [135] S. Chu, J. E. Bjorkholm, A. Ashkin, and A. Cable, "Experimental observation of optically trapped atoms," *Phys. Rev. Lett.* **57**, 314-317 (1986).
- [136] R. J. Cook and R. K. Hill, "An electromagnetic mirror for neutral atoms," *Opt. Commun.* **43**, 258 - 260 (1982).
- [137] J. Love and W. Henry, *Electronics Letters* **22**, 912 (1986).

- [138] J. D. Love, W. M. Henry, W. J. Stewart, R. J. Black, S. Lacroix, and F. Gonthier, IEE Proceedings **138**, 343 (1991).
- [139] K.-H. Yang, W. C. Stwalley, S. P. Heneghan, J. T. Bahns, K.-K. Wang, and T. R. Hess, "Examination of effects of TEM_{01}^* -mode laser radiation in the trapping of neutral potassium atoms," Phys. Rev. A **34**, 2962-2967 (1986).
- [140] N. Davidson, H. J. Lee, C. S. Adams, M. Kasevich, and S. Chu, "Long atomic coherence times in an optical dipole trap," Phys. Rev. Lett. **74**, 1311-1314 (1995).
- [141] S. Kulin, S. Aubin, S. Christe, B. Peker, S. L. Rolston, and L. A. Orozco, "A single hollow-beam optical trap for cold atoms," J. Opt. B. Quantum Semiclass. Opt. **3**, 353 (2001).
- [142] X. Jiang, L. Tong, G. Vienne, X. Guo, A. Tsao, Q. Yang, and D. Yang, "Demonstration of optical microfiber knot resonators," App. Phys. Lett. **88**, 223501-223501 (2006).
- [143] K. P. Nayak, F. L. Kien, Y. Kawai, K. Hakuta, K. Nakajima, H. T. Miyazaki, and Y. Sugimoto, "Cavity formation on an optical nanofiber using focused ion beam milling technique," Opt. Express **19**, 14040-14050 (2011).
- [144] J. E. Hoffman, S. Ravets, J. Grover, P. Solano, P. R. Kordell, J. D. Wong-Campos, S. L. Rolston, and L. A. Orozco, "Ultrahigh transmission optical nanofibers," AIP Advances **4**, 067124 (2014) (2014).
- [145] M. C. Frawley, A. Petcu-Colan, V. G. Truong, and S. N. Chormaic, Optics Communications **285**, 4648 - 4654 (2012).
- [146] F. K. Fatemi, Opt. Express **19**, 25143-25150 (2011).
- [147] J. A. Pechkis and F. K. Fatemi, "Cold atom guidance in a capillary using blue-detuned, hollow optical modes," Opt. Express **20**, 13409-13418 (2012).
- [148] F. K. Fatemi and G. Beadie, "Rapid complex mode decomposition of vector beams by common path interferometry," Opt. Express **21**, 32291-32305 (2013).
- [149] E. Vetsch, S. T. Dawkins, R. Mitsch, D. Reitz, P. Schneeweiss, and A. Rauschenbeutel, "Nanofiber-based optical trapping of cold neutral atoms," IEEE Journal of Selected Topics in Quantum Electronics **18**, 1763–1770 (2012).
- [150] D. Marcuse, "Principles of optical fiber measurement," Academic Press 1981.

- [151] F. K. Fatemi and G. Beadie. "In progress"
- [152] F. Zhou and L. Spruch, "van der Waals and retardation (Casimir) interactions of an electron or an atom with multilayered walls," *Phys. Rev. A* **52**, 297 (1995).
- [153] V. Matthieu, P. Griffin, E. Riis, and A. S. Arnold, "Laser cooling with a single laser beam and a planar diffractor," *Opt. Lett.* **35**, 3453 (2010).
- [154] J. Lee, J. A. Grover, L. A. Orozco, and S. L. Rolston, "Sub-Doppler cooling of neutral atoms in a grating magneto-optical trap," *J. Opt. Soc. Am. B* **30**, 2869 (2013).
- [155] S. Kuhr, W. Alt, D. Schrader, M. Mauilm, V. Gomer, and D. Meschede, "Deterministic Delivery of a Single Atom," *Science* **293**, 278 (2001).
- [156] J. Schoser, A. Batr, R. Lw, V. Schweikhard, A. Grabowski, Yu. B. Ovchinnikov, and T. Pfau, "Intense source of cold Rb atoms from a pure two-dimensional magneto-optical trap," *Phys. Rev. A* **66**, 023410 26 (2002).
- [157] G. Sagué, "Cold atom physics using ultra-thin optical fibres," Ph.D. thesis, University of Bonn, (2008).
- [158] E. Vetsch, "Optical Interface Based on a Nanofiber Atom-Trap," Ph.D. thesis, Johannes Gutenberg University of Mainz, (2010).